Amorphous calcium phosphate nanoparticles for biomedical cargo delivery

William David Thom

Queens' College, University of Cambridge

Biomineral Research Group, Department of Veterinary Medicine

May 2020

This thesis is submitted for the degree of Doctor of Philosophy

Preface

This thesis is the result of my own work and includes nothing which is the outcome of work done in collaboration except as declared in the preface and specified in the text. It is not substantially the same as any work that has already been submitted before for any degree or other qualification. It does not exceed the prescribed word limit for the Degree Committee for the Faculties of Clinical and Veterinary Medicine.

Much of the early work presented in this thesis was carried out at the Medical Research Council Human Nutrition Research unit in Cambridge before my research group relocated to the Department of Veterinary Medicine within the University of Cambridge — where the majority of the subsequent work was carried out. The work was supervised, at both institutions, by Dr Jonathan Powell and Dr Nuno Faria. During the course of my PhD, I have collaborated with other members of the Biomineral Research group, as well as individuals at the Department of Immunology at the University of Toronto, the School of Chemical and Process Engineering at the University of Leeds, the Department of Earth Sciences at the University of Cambridge, and the Cavendish Laboratory at the University of Cambridge. In Chapter 2, the instrumental contributions to peak shape(s) in the reported X-ray diffraction data were determined by Dr Giulio Lampronti, using a LaB_6 standard. In Chapter 3, one of the implementations of the impinging jet reactor was machined by Mr Adrian Ison. In Chapter 4, the electron microscopy analyses were performed by Dr Andy Brown and the plunge-freezing of samples by Dr Nicole Hondow, both at the Leeds Electron Microscopy and Spectroscopy Centre. Also in Chapter 4, a python script to calculate the resolvent kernel used in centrifugal size analysis was written by Mr Stephen Farr of the Cavendish Theoretical Condensed Matter group. In Chapter 4 and Chapter 5, cell culture and imaging flow cytometry was performed by Dr Rachel Hewitt, and immunohistochemistry and confocal microscopy by Dr Jack Robertson. The animal work presented in Chapter 5 was carried out by Dr Ivan Tattoli and Miss Elaine Tam in Professor Dana Philpott's group at the Department of Immunology in Toronto.

This thesis contains a general introduction, including literature review and project aims, followed by four experimental chapters, and then a general conclusion. Results chapters are structured with a short introduction, followed by a combined results and discussion section, brief conclusions, and then materials and methods. Appendix material is structured by the sequence of experimental chapters such that Appendix A corresponds to Chapter 2, and Appendix B to Chapter 3 etc. Computer code (Matlab and Python) is the exception to this, being collated in Appendix D.

Abstract

Oral delivery of intact biomolecules is desirable but challenging. This thesis presents a potential approach, using amorphous calcium phosphate (ACP) nanoparticles as carriers of organic cargo. ACP is widely used as an *in vitro* delivery vehicle but similar in vivo use has not been realised. This PhD encompasses development of a practical synthetic route to stable ACP colloids of suitable size alongside their characterisation, formulation, and proof-of-principle in vivo testing. After reviewing the relevant literature, experimental and theoretical methods were employed to consider the solubility and stability of bulk ACP and its magnesium substituted counterpart. These findings subsequently informed the synthesis of functionalised ACP nanoparticles via an impinging jet reactor that I developed for this purpose. Particle size was tuneable, varying with reactor parameters, particularly flow rate and impingement angle. Surface chemistry could also be tailored, via coating selection. Process optimisation led to disperse ACP colloids of 50–300 nm at concentrations of up to 1% (w/v). The lead material proved to be size stable in complex media and was amenable to loading with diverse cargo – from soluble dyes and quantum dots to protein conjugates. Efficient *in vitro* delivery of a FRET pair (calcein & TRITC-BSA) was demonstrated with murine RAW cells. Finally, the particles were formulated in novel gastro-protective gels and tested, orally, in a murine model. This demonstrated proof-of-principle cargo delivery to intestinal lymphoid tissue. The materials and methods developed in this thesis make a significant contribution to the promising application of colloidal minerals to oral delivery of bio-active molecules.

Amorphous calcium phosphate nanoparticles for biomedical cargo delivery

William David Thom

Acknowledgements

Firstly, I would like to thank my supervisors Dr Jonathan Powell and Dr Nuno Faria for all their support, thought, and mentorship on this journey; but most of all for their enthused engagement and humour. I would also like to express my gratitude to Dr Jonathan Powell for supporting and championing my studies as a full-time employee in his research group, and to the Medical Research Council for funding that research programme.

This work benefited hugely from the technical expertise of colleagues and collaborators. I would like to thank Dr Nuno Faria and Dr Carlos Bastos for sharing their particle sizing wisdom and mastery of bucket chemistry. Special thanks also go to Dr Giulio Lampronti who taught me the dark art of Rietveld refinement; Dr Ravin Jugdaosingh for his ICP-whispering prowess; Dr John Wills for his sage MATLAB advice; and Dr Jonathan Powell and Dr Rachel Hewitt for their gastrointestinal and immunological expertise — without which I would have been lost at sea. I would also like to thank Dr Rachel Hewitt for performing cell culture experiments and imaging flow cytometry analyses; Dr Jack Robertson for performing immunohistochemistry and confocal microscopy; Dr Andy Brown for his genius at electron microscopy; Dr Nicole Hondow for plunge-freezing my troublesome samples; and Mr Stephen Farr for lending me his mathematical muscles when I was outmatched. Part of this work was carried out in collaboration with the University of Toronto, Canada, and I would like to thank Professor Dana Philpott and her research group for conducting the in vivo experiments, and LifeArc (formerly MRCT) for funding that collaboration.

The camaraderie in my research group has been important to the completion of this thesis; humour being the best balm to failed experiments, special thanks go to Carlos, my brother in arms, and to Kat, Ale, and Michelle, for bringing light and laughter to my time at the oars. Thanks also to John for sharing and indulging a glorious addiction to outdoor sports' cinematography. Furthermore, I would like to thank the wider research community in Cambridge for nourishing my mind, the city's many purveyors of fast food for nourishing my body, and my friends in the climbing and kayak clubs for nourishing my soul. I would also like to thank the rest of my friends, old and new, for the respite of their good company. My parents, I thank for a lifetime of love, support, and care — but most of all, for encouraging annoying levels of curiosity in their children; huge thanks go to my beloved brother, Dr Schneibler, for his unique combination of serious thought and deranged levity.

Last. And first. Laura — you are my magnesium. Thank you.

Table of Contents

Table of figures

Table of tables

List of abbreviations

	Mineral Phases
ACP	Amorphous Calcium Phosphate
ACP_1	Amorphous Calcium Phosphate Isomorph 1
ACP_2	Amorphous Calcium Phosphate Isomorph 2
DCPD	DiCalcium Phosphate Dihydrate
HAp	Hydroxyapatite
OCP	Octacalcium Phosphate
β-TCP	Beta-Tri-Calcium Phosphate
	General Terms
AMCP	Amorphous Magnesium substituted Calcium Phosphate
ATCC	American Type Culture Collection
BODIPY	Boron-dipyrromethane
BSA	Bovine Serum Albumin
CD	Crohn's Disease
CMC	Carboxymethycellulose
CNT	Classical Nucleation Theory
CoP	Co-precipitation
D_n	(particle size) Distribution by Number
D_v	(particle size) Distribution by Volume
DVLO	Derjaguin–Landau–Verwey–Overbeek
DLS	Dynamic Light Scattering
EDX	Energy Dispersive X-Ray
FCS	Fetal Calf Serum
FDA	US Food and Drug Administration
FRET	Förster Resonance Energy Transfer

FTIR	Fourier Transform Infra-Red (Spectroscopy)
GRAS	Generally Recognised as Safe
HAADF	High Angle Annular Dark Field
HEC	Hydroxy-Ethyl-Cellulose
IAEDANS	5-({2-[(iodoacetyl)amino]ethyl}amino)naphthalene-1-sulfonic acid
IC	Integral Centrifugation
ICP-OES	Inductively Coupled Plasma Optical Emission Spectroscopy
IJR	Impinging Jet Reactor
K_{sp}	Solubility Product Constant
NP	NanoParticles
OVA	Ovalbumin
PAA	Polyacrylic Acid
PBMC	Peripheral Blood Mononuclear Cells
PE	Polyelectrolyte
PFA	Paraformaldehyde
PLG	Poly-L-Glutamate
PLL	Poly-L-Lysine
QS	Quillaja Saponin
RI	Refractive Index
SI	Saturation Index
SPA	Single Phase Association
STEM	Scanning Transmission Electron Microscopy
STPP	Sodium TriPolyPhosphate
TEM	Transmission Electron Microscopy
TL	Triple Layer
TRITC	Tetramethylrhodamine
UV-Vis	Ultraviolet-Visible spectroscopy
XRD	X-Ray Diffraction

Chapter 1 General introduction

This thesis concerns amorphous calcium phosphate nanoparticles, their synthesis, formulation, and ultimately their bio-clinical application as oral delivery vehicles for macromolecular cargo. This introduction summarises the relevant state of art with respect to my findings, and then outlines the specific aims of the thesis.

1.1 Background

Biopharmaceuticals — therapeutics comprised from biomolecule actives — are invaluable to modern medicine (Mitragotri, Burke and Langer, 2014), accounting for almost 30% of new drug approvals by the US Food and Drug Administration (FDA) between 2015 and 2018 (Anselmo, Gokarn and Mitragotri, 2018). High selectivity and potency of action have made them the drugs of choice for numerous diseases (Morishita and Peppas, 2006), from follicular lymphoma (Fanale and Younes, 2007) to non-responsive Crohn's disease (Frédéric *et al.*, 2010).

Given their appeal and increasingly wide usage, it is perhaps surprising that few biopharmaceuticals can be delivered orally (Wang *et al.*, 2015). Almost all of the current biotechnology products are intravenous (IV), which is invasive and carries a multitude of disadvantages for chronic treatment (Drucker, 2020). Most seriously, intravenous administration of biologicals can lead to a range of potentially lethal immune reactions, such as anaphylaxis (Hansel *et al.*, 2010), and cytokine storms — the latter caused by non-specific activation of circulating T-cells (Green and Brendsel, 2006). In the case of TGN1412 (a humanised monoclonal antibody), all six of the phase 1 trial volunteers were hospitalised, four with multiple organ failure (Ganesh *et al.*, 2006).

Encouragingly, proof of concept oral delivery has been demonstrated with a number of biologicals in animal models (Zhang *et al.*, 1991; Faria and Weiner, 2005). Notably, Weiner and colleagues demonstrated that oral administration of (CD3) monoclonal antibodies was as effective (as the traditional IV route) at reversing experimental autoimmune encephalomyelitis, whilst having fewer side effects (Ochi *et al.*, 2006). This success, and clinical studies showing oral efficacy of peptides including insulin (Melmed *et al.*, 2015; Halberg *et al.*, 2019), are a spur to further work, but the challenge of more 'general' delivery remains. The main impediment is poor bioavailability, which stems from two issues. First, biochemicals are degraded by gastric acid and enzymes found in

pancreatic juices and the mucus-layer (Borchard, 2001). Second, permeation of the intestinal epithelium by large molecules is limited, thus their uptake is low (Morishita and Peppas, 2006).

Of these hurdles, gastric protection (in man) is relatively trivial; formulations can be coated with acid-insoluble 'enteric' polymers that provide a physical barrier through the stomach and rapidly disintegrate upon reaching a designated pH to release their payload. This was demonstrated elegantly in a radio-isotope study conducted by Cole et al (2002), wherein doses of ^{153}Samarium were encapsulated with hydroxypropyl methylcellulose and orally administered to volunteers. Images obtained by gamma scintigraphy revealed marked capsule disintegration in the small bowel after having remained intact through the stomach. Enzymatic protection is more problematic, being required in the intestinal lumen — where cargo must also be available for uptake. One solution is to 'scale-down' the protection by encapsulating biological payloads with polymeric (micro or nano) particles (Truong-Le, Lovalenti and Abdul-Fattah, 2015). Thus far, the polymers used have only offered partial protection (Škalko-Basnet, 2014) and further work is needed. Perhaps the greatest challenge to oral delivery of biologicals is effective uptake — which has been the subject of considerable effort (Drucker, 2020). Strategies have ranged from peptide permeation enhancers (Twarog *et al.*, 2019) to spring-loaded micro-needle pills (Abramson *et al.*, 2019) but some of the most promising results have come from targeting specialised regions of immune tissue, known as Peyer's Patches (Ochi *et al.*, 2006).

Intestinal immunity

Peyer's patches are lymphoid follicles in the distal small bowel (Heel *et al.*, 1997) that are crucial to the maintenance of intestinal immunity and tolerance (Fujihashi *et al.*, 2001). Their principle functions are immunosurveillance and response generation: luminal contents are continually sampled via M-cells — specialised epithelial cells — and translocated to resident macrophages and antigen-presenting-cells for the initiation of tolerogenic or immunogenic signalling (Mowat, 2003). Although M-cell independent, paracellular (Ménard, Cerf-Bensussan and Heyman, 2010) and direct (Lelouard *et al.*, 2012) antigen sampling pathways exist, M-cell uptake is the most important route (Jeurissen, Wagenaar and Janse, 1999) — and these cells are rightly regarded as 'portals' to the intestinal immune system (Cheroutre and Madakamutil, 2004). A number of adaptations contribute to their function: they have a reduced glycocalyx (Clark, Jepson and Hirst, 2001) and sparse microvilli (Neutra, Frey and Kraehenbuhl, 1996) to facilitate apical binding by luminal contents, and

they can uptake particles, macromolecules and microorganisms by several mechanisms[1] (Buda, Sands and Jepson, 2005). Particle uptake efficiency is primarily determined by size and surface. Awaad and co-workers reported optimal uptake (to murine Peyer's patches) for silica particles below 300 nm in diameter (Awaad, Nakamura and Ishimura, 2012) whilst Shakweh et al (2005) found that negative or neutral surface potentials best promoted uptake of poly(lactide-co-glycolide) nanoparticles. Unfortunately, even particles which meet this 'specification' often show limited bioavailability (Škalko-Basnet, 2014). Part of the problem may be compositional: reviewing the state of the art, the vast majority of materials that have been deliberately targeted to M-cells have been composed of organic polymers[2], whilst inorganic materials have been largely neglected.

Inorganic Particulates

Inorganic nanoparticles are taken up by the Peyer's patch in abundance (Powell, Thoree and Pele, 2007). Inert exogenous nanoparticles of silicate and titanium dioxide are a regular fixture of the western diet and accumulate in 'pigment' cells deep within the patch, becoming apparent in the tissue of children as young as eight years (Shepherd *et al.*, 1987; Lomer *et al.*, 2004). Interestingly, close examination of tissue and luminal contents also reveals endogenous nanoparticles of amorphous calcium phosphate (eACP) in large number, both within the intestinal lumen and inside Peyer's patches where they co-localise with luminal macromolecules in antigen presenting cells (Powell, Thoree and Pele, 2007; Powell *et al.*, 2015). Calcium phosphates such as ACP can be effective in vitro transfection materials (Welzel, Meyer-Zaika and Epple, 2004; Sokolova *et al.*, 2006; Olton *et al.*, 2007), and it has been hypothesised that the endogenous particles fulfil an equivalent role in the gut — acting as an innate antigen delivery system (Powell *et al.*, 2015). These findings raise the question of whether inorganic nanoparticles could be effective tools for delivering biotherapeutic cargo to Peyer's Patches.

A number of research groups have investigated clay minerals as general drug delivery vehicles, with some promising in vitro results (Viseras *et al.*, 2010; Jafarbeglou *et al.*, 2016). And, as mentioned previously, Awaad et al (2012) achieved good Peyer's patch uptake with fluorescently-labelled silica nanoparticles — that they propose as oral vaccine delivery vehicles. However, the compatibility of their synthetic process with biological cargo is questionable since synthesis takes place above pH 12, which is sufficiently high to induce denaturation and/or alkaline hydrolysis of many biomolecules (Ageno, Dore and Frontali, 1969; Whitaker, 1980; Ahmad, Kamal and Khan, 2005).

[1] For instance: adsorptive endocytosis, fluid phase endocytosis and phagocytosis.
[2] See, for example, Table 1. A des Rieux et al. Journal of Controlled Release 116 (2006) 1-27

Moreover, dietary silicate particles are persistent and resistant to degradation in Peyer's patches (Lomer *et al.*, 2004), and are implicated in Crohn's disease (Butler *et al.*, 2007).

Surprisingly, despite extensive use as an in vitro transfection agent, ACP has not been tested as an oral delivery vehicle. This is a significant omission in the literature; as a candidate material it offers a number of potential advantages. (i) ACP particles are readily synthesised by mild aqueous processes — ensuring biochemical cargo preservation (Combes and Rey, 2010). By way of contrast, the common microencapsulation method for preparing loaded polymeric particles uses dichloromethane to form an emulsion — and has a tendency to denature protein cargo (Raghuvanshi *et al.*, 1998). (ii) ACP prevents thermal denaturation of bound proteins, preserving structure and activity (Yang *et al.*, 2015). This stabilising effect may translate to protection against enzymatic digestion — which is inadequate with extant formulations (Škalko-Basnet, 2014). (iii) Endogenous ACP particles are found in abundance in the Peyer's patch (Powell *et al.*, 2015), reverse engineering them should allow the innate particle handling apparatus to be exploited efficiently. In addition to optimal size (the endogenous particles are under 300 nm) composition may facilitate uptake; ACP is known to interact well with membrane phospholipids (Wuthier and Eanes, 1975). (iv) Whilst largely insoluble under neutral conditions, at pH 5 ACP is highly soluble. As a result, after cellular uptake, ACP particles dissolve readily within the endosomal compartment — ensuring they do not persist. Furthermore, dissolution of ACP mineral generates soluble phosphate ions which buffer endosomal pH and increase osmotic pressure (Liu *et al.*, 2014), resulting in membrane leaks that allow free cargo to escape the endosome more rapidly (Hanifi, Fathi and Sadeghi, 2010). This phenomenon is known as the 'proton sponge effect' and contributes to increased transfection efficacy (Boussif *et al.*, 1995).

Amorphous calcium phosphate

Amorphous calcium phosphate (ACP) is a highly disordered mineral in the calcium orthophosphate family. In accordance with Ostwald's rule[3], ACP reliably forms as the initial daughter phase from spontaneously precipitating supersaturated (alkaline) calcium-phosphate solutions and acts as a precursor to more thermodynamically favourable minerals such as hydroxyapatite (van Kemenade and de Bruyn, 1987). These characteristics dictate the synthetic approaches to producing ACP materials and their subsequent use conditions.

[3] *During crystallisation the first phase formed is that closest in free energy to the starting state*; Ostwald, 1897)

Being fast forming and metastable, ACP is produced as a kinetic product — which carries both advantages and disadvantages. On one hand, synthesis of bulk material can be as trivial as mixing soluble calcium and phosphate solutions (of sufficient concentration and pH) and collecting the immediate precipitates (Termine and Eanes, 1972; Dorozhkin, 2010). Moreover, the rapid formation and resultant disordered structure of ACP undoubtedly facilitate the trapping and hosting of (biomolecular) cargo, which it does very well (Pele *et al.*, 2017) and is essential to delivery applications. On the other hand, ACP's drawbacks are two-fold: first, its tendency to undergo mineral phase transformation, which results in significant property changes, complicates both synthesis and use. Second, the particle size control required to prepare disperse nanomaterials is rendered more difficult by the pace of ACP's precipitation.

One corollary of the above is that, since ACP forms readily from supersaturated solution and yet also transforms phase readily, its yield and purity as a reaction product are best served by short processes at conditions of minimal solubility and high concentration. Being the conjugate salt of a weak acid, like all calcium orthophosphates, ACP exhibits pH dependent solubility which varies inversely with hydroxide concentration (Pan and Darvell, 2009). As such, it is commonly produced under alkaline conditions, ranging from pH 7-11 (Reynolds, 1997; Kim *et al.*, 2004). Alkaline conditions also retard mineral phase transformation (Boskey and Posner, 1973) and this conjunction of benefits (good yield and purity) makes extreme reaction conditions (>pH 11) attractive. However, as mentioned earlier, many biomolecules are vulnerable to alkaline hydrolysis and/or denaturation (Ageno, Dore and Frontali, 1969; Whitaker, 1980), thus for cargo delivery applications, compromise conditions are required — and these must be pin-pointed by experiment.

Whilst alkaline conditions are conducive to ACP mineral formation and protective of its amorphousness, the physiological environments in which materials are used for cargo delivery — and especially the gastrointestinal tract — are acidic to near neutral (Mikolajczyk *et al.*, 2015). At such pHs, ACP is prone to dissolution and phase transformation (Meyer and Eanes, 1978). Fortunately, both these issues are, in principle, tractable through formulation.

To forestall mineral dissolution, gastric conditions can (as mentioned earlier) be bypassed by coating capsules with enteric polymers. Although this is more difficult in small animal studies, where conventional capsules cannot be consumed, Basit and co-workers have developed a rodent equivalent. Their approach employs drug-loaded 'micro-capsules' of enteric polymer and was found to successfully deliver prednisolone to the rat small bowel without acid degradation (Kendall *et al.*, 2009). Conversely, intestinal dissolution, where in man the pH varies between 5.7 and 7.4

(Mikolajczyk *et al.*, 2015), ought to be resolvable by the mineral itself; if sufficient material were to be delivered to the lumen, intestinal juices would become saturated after only minor losses.

Unfortunately, reported solubility product constants (K_{sp}) for ACP vary by as much as three orders of magnitude (Combes and Rey, 2010), which complicates solubility predictions and loss estimates. Currently, much of the discrepancy in K_{sp} values is attributed to the existence of multiple isomorphs: ACP_1 which forms initially, comprising flocculated, spherical ~20 nm primary particles (Abbona and Baronnet, 1996); and ACP_2, a slower developing, lower solubility phase of distinct morphology, which has been identified as an intermediate between ACP_1 and hydroxyapatite by some authors (Christoffersen *et al.*, 1989; Christoffersen, Christoffersen and Kibalczyc, 1990; Abbona and Baronnet, 1996). However, ACP_2 has not been noted in a number of detailed recent studies (Dey *et al.*, 2010; Pan *et al.*, 2010) and the acicular spherulite morphology apparent in electron microscopy images from the work of Christoffersen and of Abbona is remarkably similar to that of hydroxyapatite (Pan *et al.*, 2010). As such, it is possible — perhaps likely — that ACP_2 does not exist as a discrete phase, but rather as an arbitrary composite of ACP and defective hydroxyapatite. This is pertinent to the practicalities of biomedical cargo delivery because in vitro studies with nano-crystalline hydroxyapatite have found it to be pro-inflammatory (Pele *et al.*, 2015) whilst ACP itself appears to be biologically silent (Pele *et al.*, 2017).

As already noted, amorphousness (of ACP) at point of synthesis can be ensured by using high pHs and short reaction times and these expedients are to no avail during in vivo or in vitro cell experiments. In vitro cell experiments might typically entail ~3 hours of particle exposure (Pele *et al.*, 2017) and small bowel transit times are similar (Yukioka *et al.*, 1987). ACP materials should ideally remain amorphous over that timescale. However, as shown by Boskey and Posner (1973) in a comprehensive X-ray diffraction and titrimetry study, in neutral solution, full conversion of ACP to hydroxyapatite takes place in less than 2 hours. Importantly, however, Boskey and Posner (along with other authors) have also shown that this transformation can be effectively delayed by doping ACP with other metal ions such as magnesium (Boskey and Posner, 1974; Root, 1990; Jin *et al.*, 2018). Indeed, Boskey and Posner reported that, in their system, doping ACP at magnesium-to-calcium (molar) ratios of 0.2 or higher precluded hydroxyapatite formation entirely (for at least 6 hours). Interestingly, a later study by Okamoto and Hidaka (1994), which examined 26 metal ions for their effects on hydroxyapatite mineralisation, found that of the inhibitory elements, magnesium was one of the least effective — raising the question of whether more potent metals such as zinc could provide ACP with long term phase stability.

In summary, ACP is a rapidly forming and somewhat ephemeral mineral, best formed under alkaline conditions. It readily and safely incorporates and delivers biological cargo to cells, innately in the gut, and during in vitro experiments. It is prone to dissolution and to mineral phase transformation, both of which can (in theory) be remediated by various formulation strategies.

Nanoparticles: stability and synthesis

As discussed previously, Peyer's patch entry mandates a nanoparticulate vehicle. Thus, beyond bulk mineral properties, crucial parameters for material development and performance in this thesis pertain to particle size and size stability in complex fluid. Akin to the challenges of working with ACP as a mineral, this entails stabilising a metastable state; thermodynamic preference for macroscopic speciation is the norm. Nanominerals, which are characterised by enormous specific surface areas, are almost always metastable with respect to bulk phases (Navrotsky, 2001) and are thus prone to both aggregation and dissolution under many solution conditions (Hsu and Liu, 1999; Mudunkotuwa and Grassian, 2011).

Chemically, the tendency for particles to flocculate is related to a balance between repulsive and attractive forces, traditionally modelled with Derjaguin–Landau–Verwey–Overbeek (DLVO) theory (Ninham, 1999). DLVO theory assumes that the total interaction energy of two particles consists of an (attractive) Van der Waals interaction energy and a (repulsive) electrostatic interaction energy (Hsu and Liu, 1999), with probability of aggregation determined by the relative magnitude of these terms (Mudunkotuwa and Grassian, 2011).

Electrostatic interaction energy is derived from particle surface charging, which occurs spontaneously at aqueous–solid interfaces due to differential ion adsorption (Delgado *et al.*, 2007). In the classical triple layer (TL) model, chemical (specific and permanent) adsorption at the solid surface forms the inner Helmholtz plane: a fixed layer of unbalanced charge (Kalinin and Radke, 1996). Columbic attractions draw co- and counter- ions toward the surface, but their hydration spheres prevent close approach and they form the outer Helmholtz plane: a second layer of semi-permanent inner-sphere ligands (Hiemstra and Van Riemsdijk, 1996). Beyond this plane, particles are enveloped by the Gouy-Chapman layer — a transient cloud of counter-valent ions (Attard, Antelmi and Larson, 2000). Electrostatic stabilisation is derived from the (magnitude of the) potential difference between the dispersion medium and the Gouy-Chapman layer (Lyklema, 1989), known as the zeta potential. These electrokinetic phenomena are commonly exploited in nanotechnology: neutral surfaces are functionalised with specifically adsorbing charged species to increase their surface potential and improve colloidal stability (Studart, Amstad and Gauckler,

2007). A weakness of this approach is that it is contingent upon both surface and solution chemistry; electrostatic stabilisation loses efficacy under circumstances where zeta potentials are diminished, for instance at high ionic strengths (Delgado *et al.*, 2007). Polyvalent counter-ions are particularly problematic in this regard, screening surface charge and inducing particle agglomeration at modest concentrations (Liu, Moreno and Neretnieks, 2008). As a consequence, electrostatically stabilised particles are often vulnerable to agglomeration in complex media such as body fluids (Treuel *et al.*, 2014).

Alternative strategies to stabilising colloids make use of osmotic and steric effects which, whilst neglected by DVLO theory (Ninham, 1999) and the TL model (Feiler, Jenkins and Ralston, 2000), can be pivotal (Napper, 1983). Polymer functionalised colloids are stabilised by both effects: (i) upon an initial approach between neighbouring particles, adsorbed macromolecules lose configurational entropy and increase free energy (Hesselink, Vrij and Overbeek, 1971). And (ii), upon closer approach, interpenetration of polymer layers adsorbed on the colliding particles causes a local spike in osmotic pressure, promoting separation (Israelachvili, 2011). These effects are robust to ionic strength: a significant advantage over electrostatic stabilisation (Kumar, 2007). On the other hand, steric-osmotic stabilised colloids are more vulnerable to temperature fluctuations (Caruso, 2003), which is also problematic from a biotechnology perspective. Happily, both strategies can be combined by functionalising particles with polyelectrolytes and this (electrosteric stabilisation) is touted to provide the benefits of both worlds (Schwarz, Contescu and Putyera, 2004).

Whilst preventing phase separation of disperse particles is a general challenge for nanotechnology, it is exacerbated for ACP due to the kinetics and mechanism of formation. Precipitation of ACP occurs not via ion-by-ion association as per classical nucleation theory but via the aggregation of pre-nucleation clusters ca. 1 nm in size (Dey *et al.*, 2010). These clusters are believed to be analogous, or perhaps identical to, Posner Clusters — the $Ca_9(PO_4)_6$ structural units which comprise short-range (0.9 nm) order domains in solid ACP and HAp (Mancardi *et al.*, 2017). Importantly, the pre-nucleation clusters have been postulated to have an excess free energy associated with their surface which lowers the free energy barrier of their subsequent aggregation, such that in strongly supersaturated solutions precipitation is a 'run–away' process (Habraken *et al.*, 2013). Whilst the thermodynamic stability of the clusters (relative to individual solution ions) is yet not settled (Gebauer *et al.*, 2014), ab initio potential energy surface calculations have also found that cluster aggregation of $Ca_3(PO_4)_2$ monomers is thermodynamically favourable and feasible without passing through any energy barriers (Treboux *et al.*, 2000; Kanzaki *et al.*, 2001). A caveat is that computational demands limited the calculations to small clusters (of three monomers) and in

vacuum (i.e. neither solvation nor entropy were accounted for). Nonetheless, these results and the cryo-TEM study by Habraken et al do accord with empirical observations on the speed of ACP formation (Eanes, 1998; Wang *et al.*, 2009).

One implication of these characteristics is that size control of ACP is difficult, and unsurprisingly many of the literature methods for 'nanomaterials' produce agglomerated products (Sun *et al.*, 2010; Chen *et al.*, 2011; Zhao *et al.*, 2014; Karimi *et al.*, 2016). One means of surmounting this is to employ a top down process: first precipitating bulk ACP and then 'nano-nising' it, via for example, attrition milling in the presence of a dispersant (Yang, Best and Cameron, 2009). Whilst this can be an effective and high concentration route for preparing nanoparticles, the comminution limit (a brittle/ductile transition which determines the smallest particle size achievable) for ACP is likely to be around 300 nm (calculated from: Saber-Samandari and Gross, 2011, in conjunction with: Field, Farhat and Walley, 2014), which is at the upper bound for Peyer's patch uptake. Furthermore, to get close to the comminution limit, high energy, long duration, stirred media milling would likely be required and this would almost certainly be deleterious to cargo, as seen in super-fine grinding of whey powders (Sun et al., 2016), and ball milling of lysozyme — which reduced lysozyme activity by 30% (Lee, Maia and Pokorski, 2017). Sol-gel methods also offer high concentration products but tend to use non-aqueous solvents (Layrolle, Ito and Tetsuya, 1998) which are disadvantageous from a cargo perspective. Indeed, from solution, aqueous methods to nano ACP are generally the simplest and most 'bio-friendly' approaches — but are often at very low working concentrations (< 6 mM Ca/PO_4). They typically fall into three categories, in ascending complexity:

1. Co-precipitation of calcium and phosphate salts in the presence of disperse scaffolds that direct growth (Pele *et al.*, 2015).

2. Brief mixing of calcium and phosphate solutions to initiate particle growth before application of a 'capping' agent once at appropriate size to prevent further growth/aggregation (Welzel, Meyer-Zaika and Epple, 2004; Kovtun *et al.*, 2012; Peetsch *et al.*, 2013).

3. Limiting particle size by constraining growth within defined barriers — e.g. within reverse microemulsions or liposomes — and then functionalising the disperse particles (Altinoğlu *et al.*, 2008; Morgan *et al.*, 2008).

Of these approaches, co-precipitation is the simplest but has limited evidence supporting it as a viable route. In contrast, the Epple group have developed numerous nanodisperse ACP materials

for in vitro transfection using the second kind of strategy, but only at low working concentrations. More impressively, materials produced via the third approach, as exemplified by Adair and colleagues, have been used intravenously to deliver near-IR fluorescent dye in a whole-body murine imaging study — one of the very few in vivo studies with ACP particles (Altinoğlu *et al.*, 2008). That success made option 3 a 'safer bet' in some respects, but the complexity and low throughput of the process also made it a last resort. As they were, none of the published processes met the requirements of this project; exploratory syntheses and chemical assays were crucial to bridging the gap.

1.2 Aim and objectives

This thesis aimed to develop and demonstrate a practical platform for in vitro and in vivo biomolecule delivery by repurposing amorphous calcium phosphate (ACP) — a widely used in vitro vehicle — and using it to transport, proof of principle, fluorescent cargo to Peyer's patches (small bowel lymphoid follicles) in oral studies with small animals. The specific objectives of this thesis are outlined below, in the sequence by which they are addressed in subsequent chapters.

I. **To parameterise the synthesis and composition of bulk ACP.** Chapter 2 establishes preferential conditions for producing bulk ACP mineral, implements a modified mineral composition with advantageous properties, and ascertains usage limitations with respect to solubility and phase transformation.

II. **To develop a practical route to ACP nanoparticles.** Chapter 3 develops a fluidic reactor for producing disperse ACP nanoparticles at suitable scale and concentration for in vivo studies. An array of surface functionalisation agents are explored and three found to best stabilise ACP particles.

III. **To optimise materials for solution stability and detection via confocal microscopy**. Chapter 4 characterises the lead materials via physicochemical techniques and in vitro cellular assays to ensure their suitability for in vivo study.

IV. **To formulate materials for oral delivery and test them in vivo.** Chapter 5 develops a formulation strategy to overcome gastric digestion and then iteratively tests formulated ACP nanomaterials in an oral murine model to demonstrate proof of principle biological cargo delivery to Peyer's patches.

Chapter 2 Amorphous calcium phosphate: bulk mineral studies

2.1 Introduction

Thorough understanding of mineral chemistry is crucial to the optimal production and use of inorganic nanoparticles in aqueous environments. Knowledge of the precipitation kinetics and solubility profiles of related (ie competing) phases is of particular importance in designing syntheses that achieve efficient conversion rates (yields) and selectivity (specificity of product). Downstream, the safe and effective use of mineral materials — particularly in biotechnology — requires (inter alia) context specific information of solubility and phase transformation.

Calcium phosphate minerals, being conjugate bases of weak acids, exhibit pH dependent solubility behaviour: becoming more soluble under acidic conditions, and less soluble under alkaline conditions. This behaviour is defined by solubility equilibria, for which thermodynamic constants (solubility product constants; K_{sp}) can be calculated. K_{sp} values are mineral phase dependent, being affected by both composition and structure (Cornell and Schwertmann, 2003). Whilst there are well established (albeit method dependent) values for crystalline calcium phosphate phases, this is not the case for amorphous calcium phosphate (ACP) — for which reported solubility product constants vary by three orders of magnitude (Gustafsson *et al.*, 2008).

This divergence may be driven by the putative existence of multiple isomorphs; a lower solubility isomorph (ACP_2) has been reported by some authors (Christoffersen *et al.*, 1989; Christoffersen, Christoffersen and Kibalczyc, 1990). Or, it may be driven by ACP's tendency to transform into crystalline phases of lower solubility (Abbona and Baronnet, 1996). In either case, uncertainty prevails — and hinders good judgement with respect to synthetic conditions and application limitations.

Thus, in this chapter, I sought to obtain an accurate grasp of ACP solubility for two reasons: (i) to design syntheses that effectively balanced yield (improved by greater alkalinity) and cargo considerations (strong bases promote biomolecule hydrolysis and/or denaturation; Whitaker, 1980). And (ii) to understand the likely limitations of later materials with regards to dissolution and phase transformation in physiologically representative conditions. In parallel, I would seek to optimise bulk mineral properties prior to commencing nanomaterial development.

2.2 Results and discussion[4]

2.2.1 Synthesis and solubility of amorphous calcium phosphate (ACP)

I began my studies by seeking to establish the solubility behaviour of ACP, preparing supersaturated solutions across an extended pH range (4 to 11) by mixing pH matched calcium chloride and sodium phosphate solutions at various concentrations and a fixed (total) Ca/P ratio of 1.6. In view of Ostwald's Rule (during crystallisation the first phase formed is that closest in free energy to the starting state; Ostwald, 1897), short reaction times (~2 minutes) were employed to favour the metastable mineral ACP as a kinetic product. Ultrafiltration was used to fractionate reactants and products — subsequently quantified by inductively coupled plasma optical emission spectroscopy (ICP-OES). It is apparent from the results (Table 2.1) that effective ACP syntheses require alkaline conditions (pH > 8) to obtain good yields (>80%; denoting efficient conversion of soluble reactants to insoluble mineral). To avoid perturbing the system with secondary effects[5], I opted not to use pH buffers. As a consequence, pH decreases of up to 3 units were observed concomitantly with mineral formation. For a pragmatic means of delivering cargo in vivo, I would hope to achieve synthesis concentrations of at least (10 to 50 mmol/L). Given the pH shifts observed here, maintaining stable alkaline conditions whilst precipitating mineral at those reactant concentrations would necessitate either: (i) highly alkaline (pH ≥11) initial conditions (likely to be deleterious to biological cargo), or (ii) a means – such as base addition or buffer use — of stabilising pH at a more moderate range (pH 8 to pH 9). A key limitation of this experiment was that product (mineral) yield was determined indirectly, by subtracting the soluble from the total concentration for each sample. The findings, however, should be reliable since (i) spin conditions were sufficient to eliminate (visible) retentate, and (ii) the membrane size (3 kDa) of the ultra-filters would be sufficient to block particles much above ~ 1 nm in size.

Although the methodology I have used here (co-precipitation of soluble reactants from supersaturated solution) is of principal relevance to mineral synthesis, it also allows a rough estimate of equilibrium solubility across a wide pH range – with implications for later use of ACP materials. Plotting post-precipitation pH against soluble (Mw < 3 kDa) analyte concentration (Figure 2.1) yields an inversely proportional relationship between pH and solubility for both elements (Ca

[4] Materials and methods for this chapter can be found from page 43.

[5] Many buffers, such as citrate, strongly complex Ca^{2+} ions. Even Good's buffers are prone to weak interactions (A. Azab and M. Anwar, 2012) and since they have narrow pH ranges, this experiment would have required a multitude of different buffering agents – complicating comparison of results collected in different pH regions.

and P). Assuming I can produce (and disperse) ACP particles at calcium concentrations in excess of 0.01 Mol/L, these data indicate that cargo delivery would be feasible in the near neutral pH range but challenging below ca. pH 6 — where solubility increases prohibitively.

Table 2.1. Calcium phosphate co-precipitation experiments and their outcomes. Total concentrations of calcium and phosphorus were determined via ICP-OES, with all phosphorus assumed to be phosphate. Stoichiometric yields were calculated by subtraction ((total–soluble)/total) relative to the limiting reactant — phosphate.

pH		Concentration/10^{-3}mol/L		Relative Yield %
Initial	Post-precipitation	Calcium	Phosphate	
4.0	4.0	10	5.8	1
4.0	4.0	20	12	2
4.0	4.0	49	29	2
6.2	5.5	19	12	38
6.2	5.5	20	12	32
6.2	5.3	24	15	38
6.2	5.4	25	16	35
6.2	5.1	40	22	17
6.2	5.0	49	30	34
7.1	6.4	4.9	3.0	6
7.1	6.0	9.5	5.8	32
7.1	5.9	10	6.1	29
7.1	5.7	14	8.7	35
7.1	5.6	15	9.1	31
8.0	7.5	2.3	1.4	2
8.0	7.4	2.4	1.5	6
8.0	6.8	4.7	2.9	40
8.0	6.5	4.9	3.0	24
10.6	10.5	0.2	0.1	38
10.6	10.2	0.5	0.3	64
10.6	9.6	1.0	0.6	82
10.9	9.3	1.6	0.9	91
10.9	8.8	3.4	2.1	96
10.9	8.0	10	5.9	98
10.9	7.8	20	12	99

Despite some methodological differences, these results are in reasonable agreement with solubility values previously published by Meyer and Eanes (1978). For instance, using an autotitrator to maintain the pH of a calcium phosphate solution at 7.4 (via KOH addition), Eanes and Meyer reported 2.4 mMol/L of soluble calcium at ~5 minutes — whilst I observed 2.2 mMol/L of soluble calcium at a post-precipitation pH of 7.54 at 2 minutes. Curiously, findings from Christoffersen et al (Christoffersen, Christoffersen and Kibalczyc, 1990) — obtained via an approach very similar to mine — diverged more greatly in outcome. With respect to my data, their results indicate 1.5-fold higher solubility for ACP_1 (the initial phase formed in their experiments) and 20% lower solubility for ACP_2 (which they report as a secondary phase), raising the question of which isomorph I produced here — if indeed either. However, since Christoffersen's work was conducted at elevated temperatures[6] (30 °C to 42 °C) and in narrow pH ranges (pH 6.3–6.6 and pH 5.6–5.8 for ACP_1 and ACP_2 respectively), point to point comparison is of limited value.

More usefully, Christoffersen's raw data enabled Gustafsson and co-workers to compute thermodynamic solubility product constants for ACP_1 and ACP_2 (Gustafsson *et al.*, 2008). I used these and other constants from the literature (Table 2.5, page 47) to run thermodynamic simulations with the geochemical modelling programme PHREEQC (version 3; Parkhurst & Apello, 2013), establishing non-competitive equilibrium solubility predictions for ACP_1, ACP_2 and crystalline calcium phosphate minerals (Appendix A; Figure A.1.1). Figure 2.2 comprises solubility data for my experimental results alongside the PHREEQC simulations for: both ACP isomorphs, dicalcium phosphate dihydrate (DCPD) and hydroxyapatite (HAp) — the latter two being the fastest nucleating and most stable crystalline calcium phosphate phases respectively (Lu and Leng, 2005; Pan and Darvell, 2009). Under alkaline conditions, there is good accordance between my experimental solubility values and the model predictions for ACP_1 solubility at room temperature. There is, however, a distinct inflection in the experimental solubility response curve around phosphate's second pK_a (7.21; Hunter, 2012), after which the experimental data appears to accord better with ACP_2. This is puzzling since in Christoffersen's work ACP_2 was exclusively found as a secondary product (subsequent to ACP_1 precipitation). Moreover, ACP_2 has not been observed in other studies at standard temperature (25 °C; Pan, Liu, Tang, & Xu, 2010).

[6] Retrograde solubility is noted for both hydroxyapatite and dicalcium phosphate dihydrate (Tenhuisen and Brown, 1997). Moreover, temperature dependence (of ACP solubility) is apparent in the Christoffersen study.

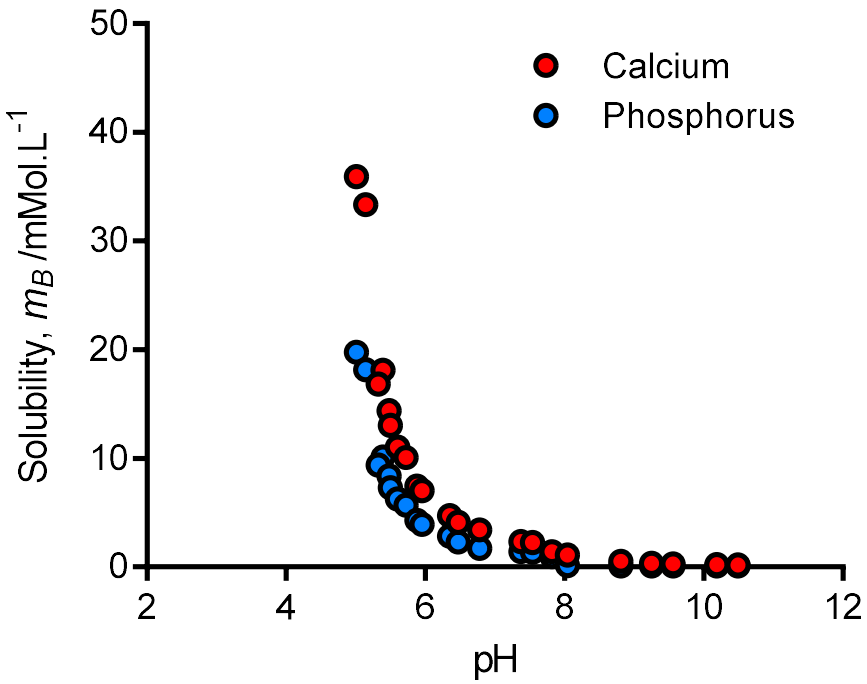

Figure 2.1. Soluble ion concentrations of precipitating calcium phosphate solutions in the pH interval 5–10.5 as determined by ultrafiltration (3 kDa) and ICP-OES. Each data point is the mean of analytical triplicates from a single sample, error bars are obscured by the markers.

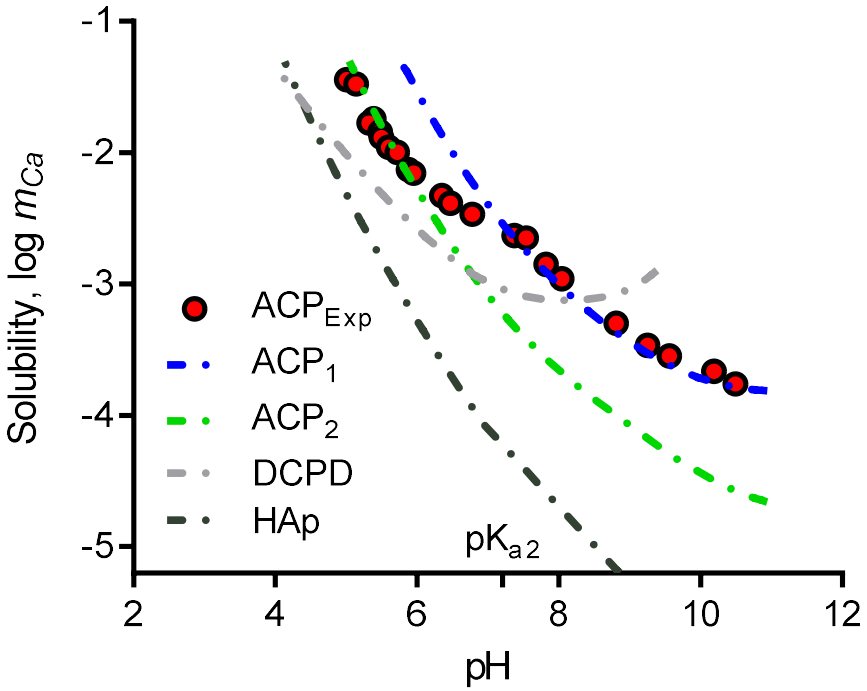

Figure 2.2. Calcium solubility: experimental data (replotted from Figure 2.1) and results from PHREEQC simulations for two ACP isomorphs, dicalcium phosphate dihydrate (DCPD) and hydroxyapatite (HAp). Modelling entailed an excess of each mineral (10 mol) being titrated down from pH 11 with 1 mol of HCl in 10000 steps at 25 °C.

Furthermore, (solubility curve) explanations relying on ACP isomorph differences are inconsistent with precipitate stoichiometries (mole ratio of calcium:phosphorus) from my initial solubility series (Figure 2.3). Under alkaline conditions, sample stoichiometries accorded with those of ACP. Conversely, samples collected at lower pHs had Ca/P ratios outwith the norm (for ACP). The apparent discontinuity in stoichiometry at ca. pH 7.2 is certainly not a function of ACP isomorph divergence — since ACP_1 and ACP_2 have identical Ca/P ratios (Christoffersen, Christoffersen, & Kibalczyc, 1990). Although other authors (Meyer and Eanes, 1978) noted some pH dependence in ACP Ca/P ratio (due to variable incorporation of acid phosphate — HPO_4^{2-}), their results nonetheless fell within a relatively narrow band (1.37 to 1.46). My results, rather, are suggestive of crystalline phase (DCPD and perhaps HAp) formation at lower pHs; precipitate stoichiometry being a good litmus test for calcium phosphate phases — which vary widely in Ca/P (Wang and Nancollas, 2001). Given the limited reaction times in these experiments, this tentative finding is somewhat surprising. And I would have liked to follow-up with direct mineral phase determination for these samples. Unfortunately, due to the low processing volumes, modest concentrations and variable yields, most of the syntheses of interest had product masses one to two orders of magnitude too low for analysis via the techniques available to me — Fourier Transform Infra-Red (FTIR) spectroscopy and powder X-ray diffraction (XRD).

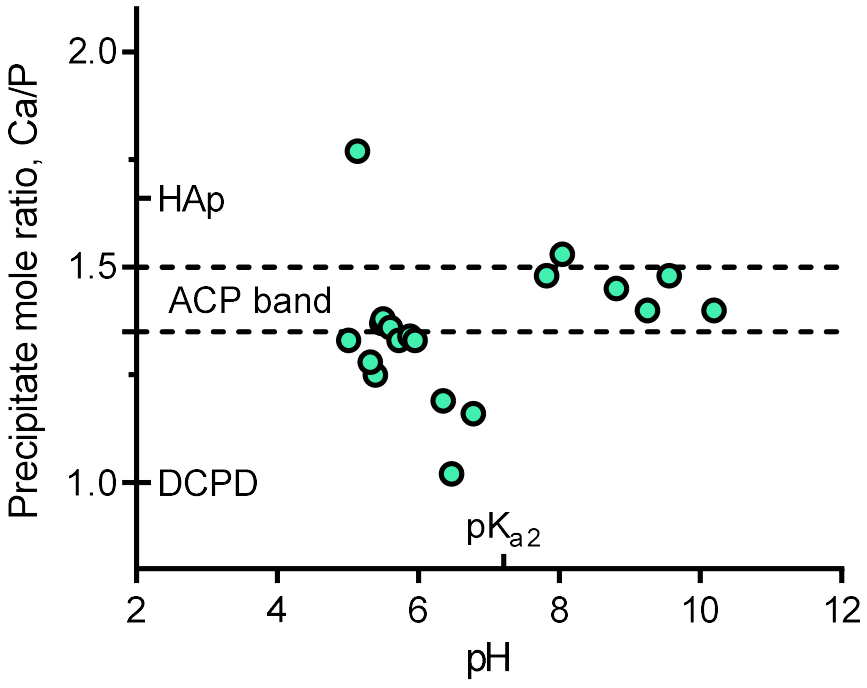

Figure 2.3. Calcium/phosphate ratios of precipitates collected from supersaturated solutions vs post-precipitation pH as per Table 2.1 (pg 24). ACP band values 1.35 – 1.5 (Dorozhkin, 2012. pg 169-170).

In an attempt to redress this evidence gap, I conducted higher scale syntheses at a few selected pHs (Table 2.2) and collected precipitates for phase characterisation via FTIR and XRD (Figure 2.4 and Figure 2.5a-b). From the FTIR spectra it was apparent that precipitates collected at pH 7.9 and pH 3.4 comprised ACP and DCPD respectively (Figure 2.4). Intermediate traces (pH 5.8 and pH 5.3) also showed DCPD fingerprint vibrations but these were less prominent (than in the spectra collected at pH 3.4). In FTIR, the vibrational frequencies of functional groups are dependent upon their immediate chemical environment (Gregorio *et al.*, 2018) and spectra comprise a weighted sum of the underlying vibrations. For these analyses I had controlled for sample mass and maintained consistent measurement parameters. Thus, reduced peak intensities for DCPD specific PO_4 vibrations (wavenumbers) in the pH ~5 samples were qualitatively indicative of a more heterogenous arrangement of phosphate groups in those samples. In turn, this suggested either: (i) a lower proportion of DCPD, or (ii) smaller and/or more defective DCPD crystals. Whilst FTIR could not differentiate between these two possibilities, XRD could. Indeed, beyond confirmation of the principal mineral phases (revealed by reflection position), profile fitting of DCPD patterns (eg Figure 2.5b) allowed separation of instrumental and sample contributions to peak shape (asymmetry and broadening). Thence, crystallite domain sizes could be calculated by the Scherrer equation (Holzwarth and Gibson, 2011). Notably, Scherrer sizes were similar (207 – 267 nm) for all three DCPD containing samples, suggesting that differential composition (ie dilution of DCPD with ACP) was the driver for the differences in the FTIR spectra.

In aggregate, solubility data, Ca/P ratios and mineral phase characterisation results from these initial syntheses (Table 2.1 and Table 2.2) attest to the predomination of ACP under alkaline conditions. Conversely, samples precipitated at near-neutral pHs, appear to be comprised from mixed phases (ACP and DCPD) — although the presence of ACP in these can only be inferred and has not been shown directly. A limitation of this work was the omission of bridging or overlapping experiments between the solubility results collected from low-scale syntheses (Table 2.1) and the mineral phase characterisation obtained on higher scale samples (Table 2.2). Ideally, a single, multi-point experiment would have been conducted at intermediate scale and correlative mineral phase and solubility data collected for each sample. Nevertheless, these results were sufficient for the intended goals of confirming suitable conditions for ACP formation and use, and identifying likely ‘problem phases’ — DCPD in this case.

Table 2.2. Conditions for 50 mL co-precipitation syntheses and their resultant mineral phases, as determined by XRD and FTIR.

pH		Concentration/10^{-3}mol/L		Mineral Phase
Initial	Post-precipitation	Calcium	Phosphate	
4.0	3.4	100	100	DCPD
6.0	5.3	20	12	DCPD/ACP[1]
8.0	5.8	20	12	DCPD/ACP[1]
11.0	7.9	20	12	ACP

1. Presence of ACP is inferred in these samples.
ACP = amorphous calcium phosphate; DCPD = dicalcium phosphate dihdyrate
FTIR = Fourier Transform Infrared Spectroscopy; XRD = X-ray diffraction

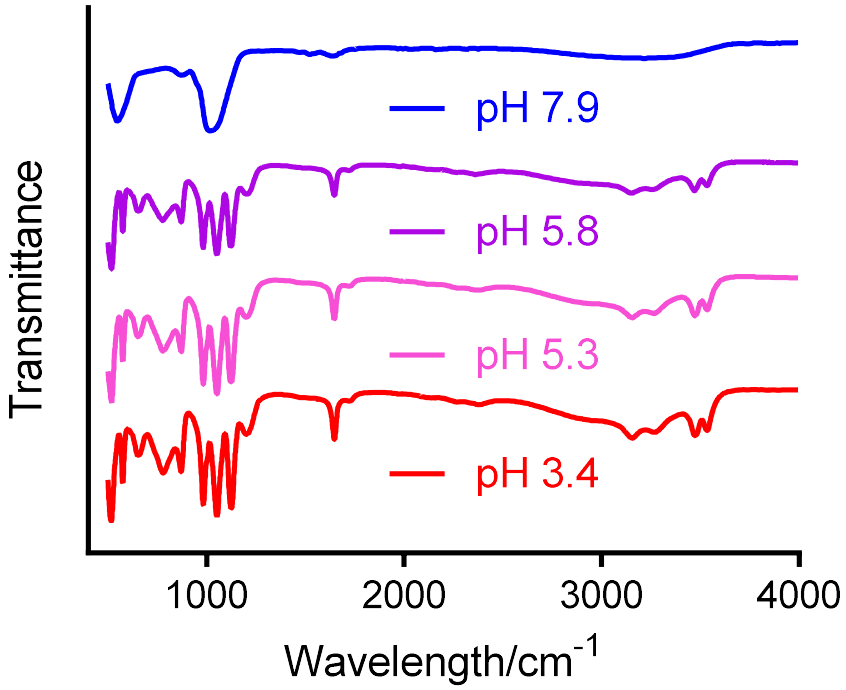

Figure 2.4. FTIR spectra for calcium phosphate precipitates produced from 50 mL co-precipitation experiments. Spectra were smoothed by Savitzky-Golay filtering, overlaid and off-set, without scale adjustment. Spectra are labelled by post-precipitation pH. Spectra for DCPD exhibit strong and distinct PO_4 vibrations at 987, 1058, and 1137 cm^{-1}, and moderately intense, distinct H_2O vibrations at 1650, 3470 and 3530 cm^{-1} (Hirsch *et al.*, 2014). Conversely, ACP spectra exhibit broad/diffuse absorbance bands, from ~800-1200 cm^{-1} for PO_4 vibrations, and from 2600-3600 cm^{-1} for H_2O vibrations (Combes and Rey, 2010).

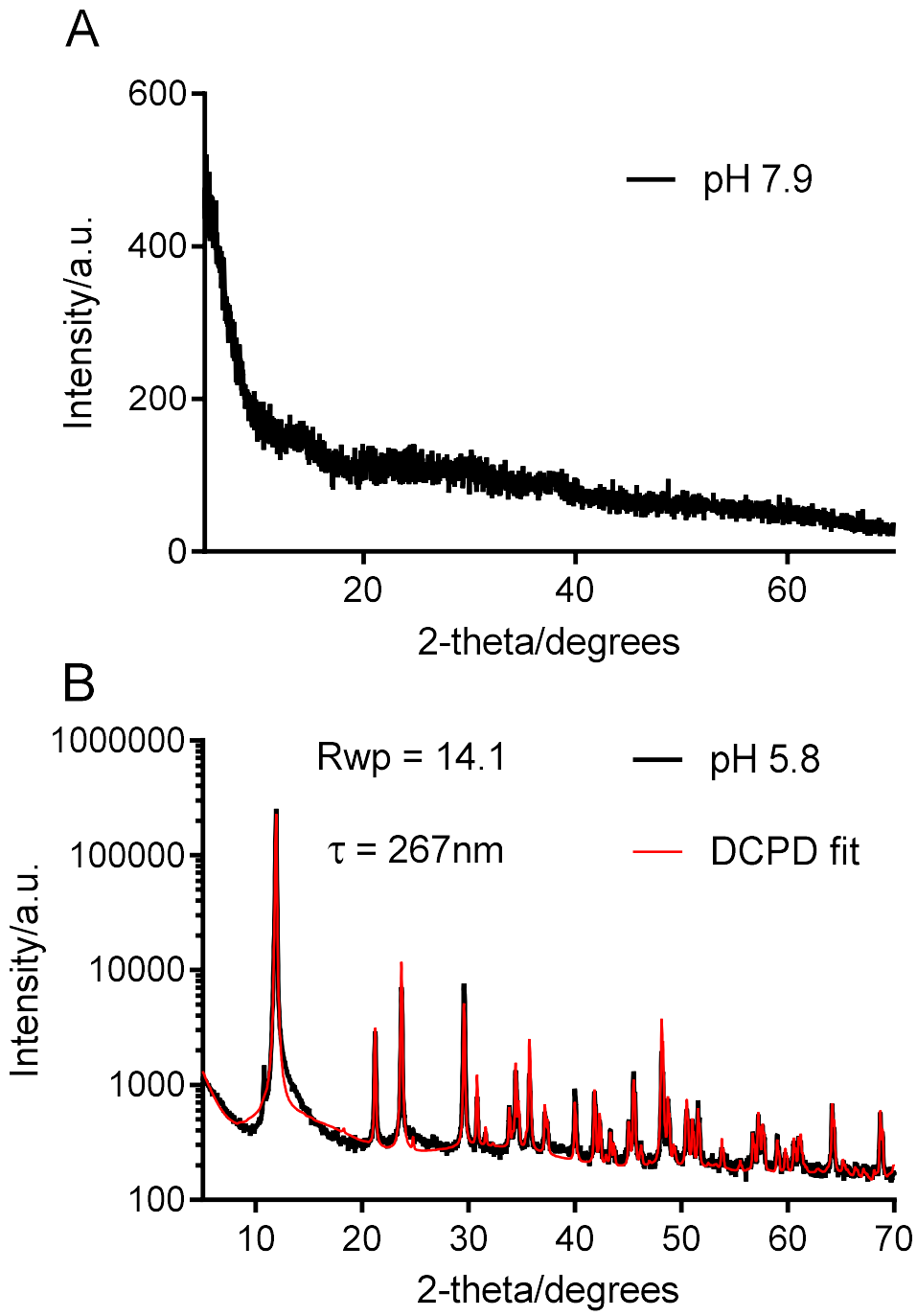

Figure 2.5. X-ray diffraction patterns for calcium phosphate precipitates. Amorphous calcium phosphate was precipitated from alkaline solution (**A**). Dicalcium phosphate dihydrate (**B**) was precipitated from neutral solution. Both patterns are labelled with the post-precipitation pHs. Deconvolution of sample and instrument contributions to peak shape via profile fitting (**B**; red) allowed the coherent crystalline domain size (τ) to be calculated via the Scherrer equation (page 45). The fit agreement was good except for the intense (020) DCPD reflection at ~12° 2-theta which had some unresolved distortion.

In the context of ACP synthesis, other mineral phases are undesirable side-products. Considering the results above, the most likely contaminant phase in rapid (synthetic) processes is DCPD. To better ascertain the conditions under which DCPD could be problematic, further simulations were carried out with PHREEQC. Saturation indices[7] (SIs) of ACP_1, DCPD and HAp[8] were calculated for solutions containing fixed concentrations of soluble calcium and phosphate (Ca/P ratio 1.67) from pH 4 to pH 11. It was found that at target (synthesis) concentrations, DCPD is — in principle — capable of precipitating (SI > 0) across a broad range of pHs (Figure 2.6a). In practice, however, ACP_1 has a greater thermodynamic drive toward precipitation (ie higher SI values) under alkaline conditions and is generally favoured kinetically. Consequently, I would expect ACP_1 to form exclusively above the cross-over point (ie where $SI_{ACP} > SI_{DCPD}$). On the other hand, cross-over points vary substantially with mineralising ion concentration: from pH 6.3 at 50 mmol/L [Ca^{2+}] to pH 8.3 at 0.5 mmol/L (Figure 2.6a-c). This suggests that if concentrations are sufficiently low, DCPD would be favoured over ACP_1 — even under mild alkaline conditions — raising the spectre of secondary DCPD precipitation occurring in ACP processes due to 'left-over' soluble ions in the mother liquor. However, saturation index also changes with concentration; at a [Ca^{2+}] of 5×10^{-4} mol/L, neither ACP_1 nor DCPD is capable of precipitating (SIs < 0) at the cross-over point (Figure 2.6c). As a consequence, DCPD is not likely to be an issue at this concentration.

To illustrate the complex interplay between concentration, pH, and speciation, Figure 2.7 combines cross-over point pHs (blue diamonds) and corresponding DCPD saturation indices (red circles) at those cross-over points for eight solutions (with [Ca^{2+}] from 5×10^{-2} mol/L to 5×10^{-4} mol/L and Ca/P ratios of 1.67), with composite equilibrium solubility minima (dashed line; data replotted from Figure 2.2) for ACP_1 and DCPD. It is apparent that to forestall DCPD formation, syntheses should be conducted at pH > 8.5 where calcium (and phosphate) are solely partitioned as ACP_1 and soluble ions. It is also apparent that applications for ACP based materials which entail dilution or acidification may result in dissolution and re-precipitation of DCPD. From the saturation index trend, this is less likely to result from dilution at neutral conditions, and more likely to occur from exposure to low pH in the absence of dilution. This dynamic is concerning since it exacerbates the issue of ACP's acid-solubility (by driving the equilibrium away from ACP), and increases the risk of cargo loss (during dissolution and reprecipitation).

[7] Saturation index (SI) is a useful measure of the tendency of mineral phases to precipitate (SI > 0), equilibrate (SI = 0) or dissolve (SI < 0) under a specific set of conditions. The SI of a solution is calculated from the log of the ratio of the ion activity product (IAP) of that solution to the solubility product constant (Ksp), thus: SI = log (IAP/Ksp).

[8] This discussion concerns the results for ACP and DCPD; HAp data are presented in Appendix A; Figure A.1.2.

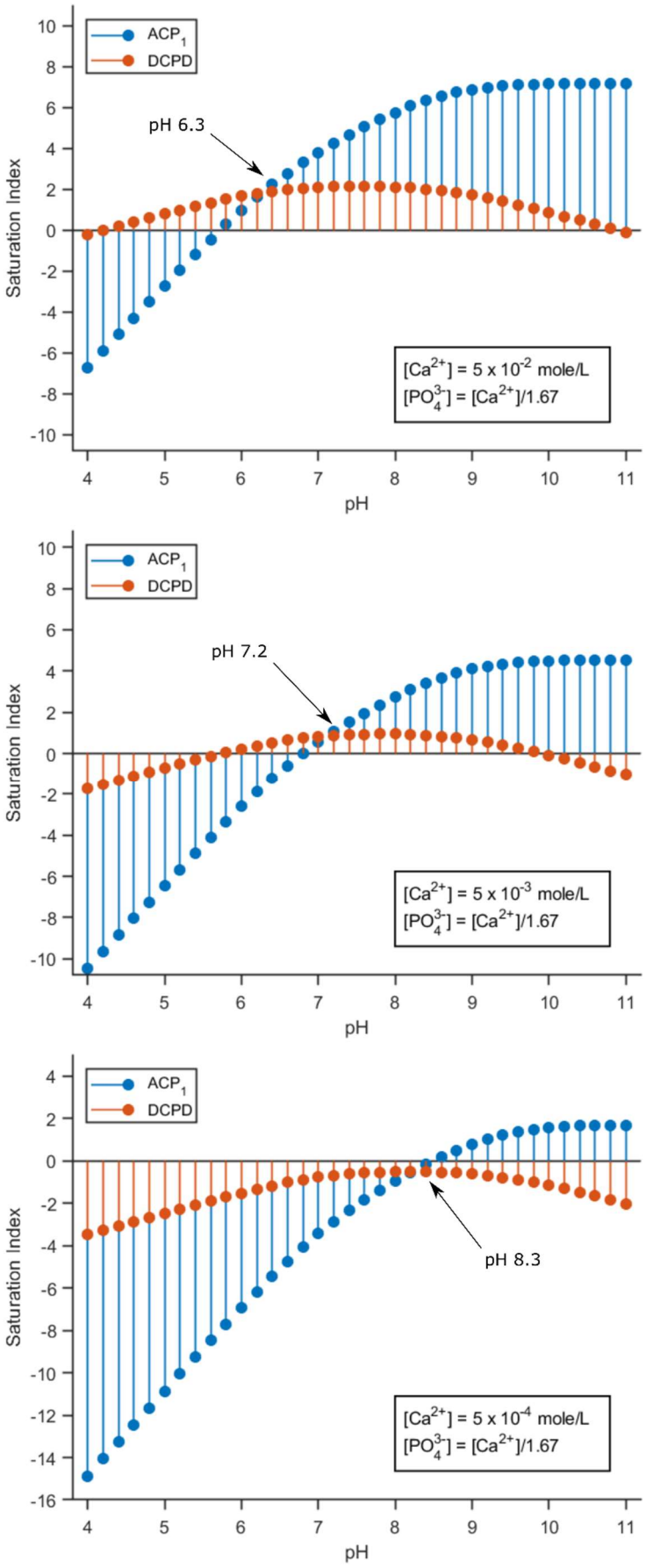

Figure 2.6 Calculated saturation indices (SI) of ACP_1 and DCPD in the $CaCl_2$–Na_2HPO_4–H_2O system.

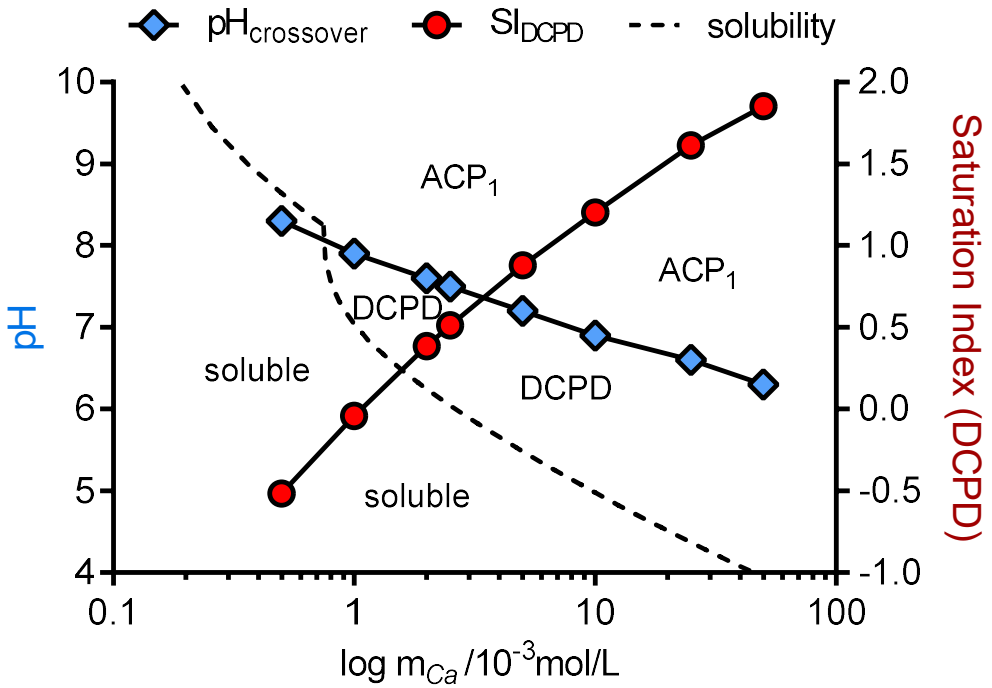

Figure 2.7 Speciation in the ACP-DCPD-$CaCl_2$-Na_2HPO_4-H_2O system. Cross-over point pHs (blue diamonds) delineate the ACP-DCPD potential phase boundary; corresponding DCPD saturation indices (red circles) depict thermodynamic trajectories and are complemented by composite solubility data (dashed line) for ACP_1-DCPD (minima; compiled from Figure 2.2). Series lines are present to guide the eye.

2.2.2 Mineral modification

Fortunately, although transformation of ACP into more thermodynamically favourable phases (esp. hydroxyapatite (HAp) and dicalcium phosphate dihydrate (DCPD)) over time is largely inevitable, various measures can be employed to delay and slow conversion. As discussed in the previous section, preparation of ACP particles from highly supersaturated alkaline solutions is a good strategy for preventing crystalline impurities at point of synthesis. This is essential since HAp crystallisation is autocatalytic (Boskey and Posner, 1974). Post-synthesis, samples could be maintained in alkaline conditions — however even at pH 9, Boskey and Posner reported full conversion of ACP to HAp within 3 hours. Since (room temperature) crystallisation is solution mediated (Boskey and Posner, 1973), stored samples might be freeze-dried or dispersed in non-aqueous solvents such as glycerol. But, in biomedical experiments, ACP materials will inevitably be subject to aqueous, neutral or acidic environments for several hours or more. And, since little modification to those environments is possible, the materials themselves must be modified to preserve their amorphousness during use.

One means of inhibiting mineral phase transformation of ACP is to dope its' structure with other metal ions. Magnesium and strontium are most well studied in this role (Boskey and Posner, 1974; Root, 1990; Gelli *et al.*, 2018; Jin *et al.*, 2018), but at least 12 other elements have been identified as inhibitory to HAp formation (Okamoto and Hidaka, 1994). Interestingly, dual substitution with Mg and Sr has been found to convey synergistic benefits with respect to mineralisation prophylaxis (Jin *et al.*, 2018). Other inhibitory elements have not been explored in this way — a potentially significant omission given that magnesium was one of the poorest performing inhibitors in the study reported by Okamoto and Hidaka. Were all 14 inhibitory elements to be considered as both single and dual dopants, there would be 105 combinations — too many for experimental screening in this project. However, many of the 14 (eg Cd, Sn) are toxic and undesirable additives for a biomedical research tool. Indeed, taking oral tolerance (and dietary presence) as a proxy for suitability, there was a shortlist of five bivalent metals which might reasonably be used to dope ACP, four of which (Mg, Sr, Zn, Cu) were confirmed inhibitors (Table 2.3).

Table 2.3. Oral exposure safety of constituent ACP ions and potentially advantageous dopants.

Element	Dietary Limit (mg/day)	Metric	Reference
Ca	2500	UL	EFSA, 2006
P	2000	NAE	EFSA, 2006
Mg	250	UL	EFSA, 2006
Sr	140	MRL	US Dept. of Health, 2004
Zn	25	UL	EFSA, 2006
Fe(II)	50	LOAEL	EFSA, 2006
Cu	5	UL	EFSA, 2006

LOAEL = Lowest Observed Adverse Effect Level, MDI = Mean Daily Intake, MRL = Minimum Risk Level, NAE = No Effect Limit, UL = Upper Limit

Further to tolerability, it was crucial that dopants be both efficacious crystallisation inhibitors and compatible with my preferred conditions for ACP synthesis. Specifically, it was imperative that dopants not precipitate as independent or separate phases during synthesis. Thus, prior to commencing laboratory studies, I used PHREEQC to conduct thermodynamic speciation calculations — considering each metal with respect to hydroxide (Figure 2.8a) and phosphate (Figure 2.8b). Unfortunately, under probable reaction conditions (pH 9 and 100 mMol/L phosphate), most of the metals were (thermodynamically) driven to form separate hydroxide (Figure 2.8a) and phosphate (Figure 2.8b) phases. Indeed, under reaction conditions, only three metals (Mg, Sr, Cu) had greater solubility than calcium with respect to their phosphate phases (Figure 2.8b). Of these, neither Mg nor Sr would be likely to form hydroxides at pH 9, whilst cupric ions might (Figure 2.8a).

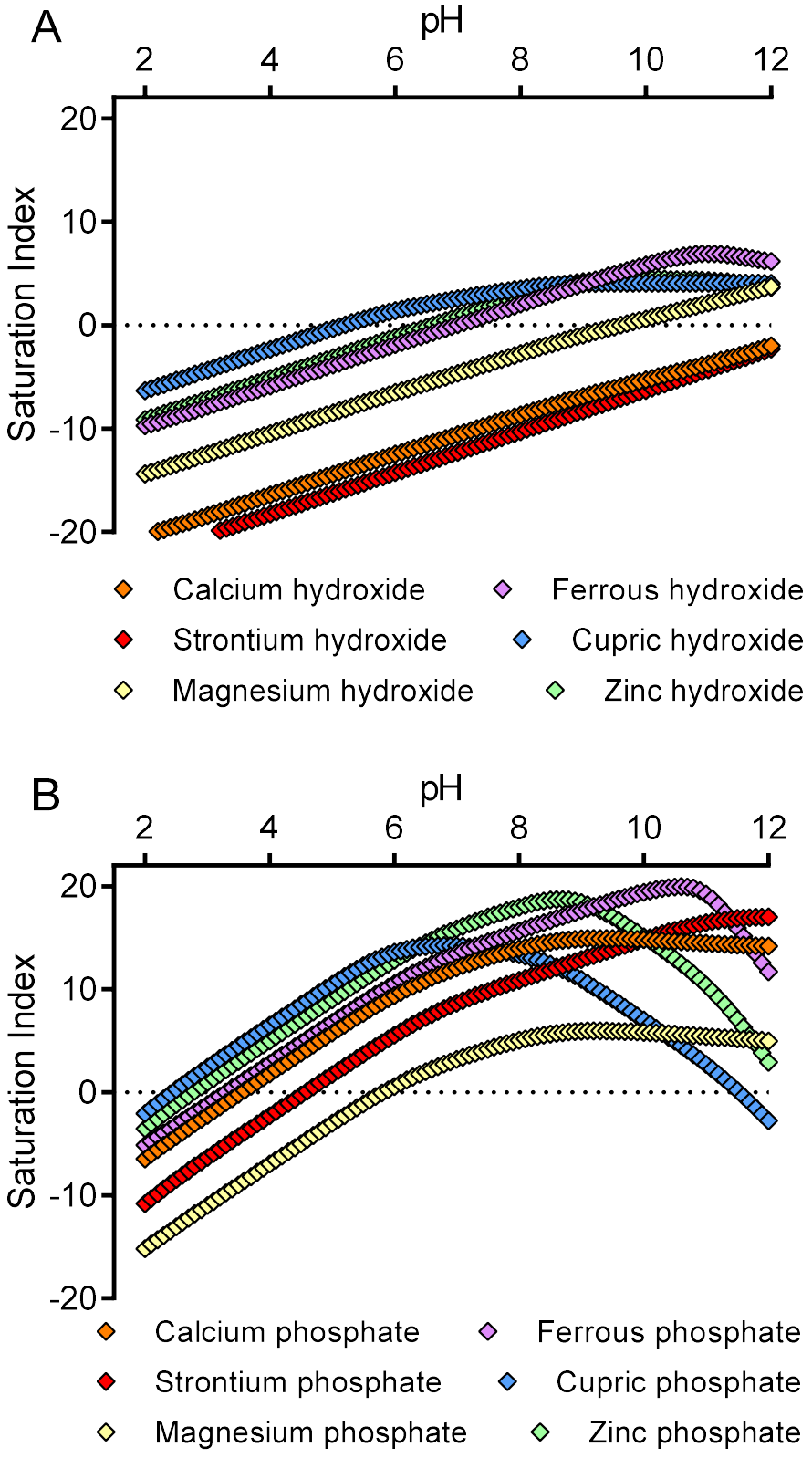

Figure 2.8. Calculated saturation indices (SI) for metal hydroxides (**A**) and phosphates (**B**) in the MCl_2–Na_2HPO_4–H_2O system, where M denotes a divalent metal. Calculations were carried out at 25°C in 0.1 pH unit increments, with metal and phosphate concentrations of 0.1 Mol/Litre.

Although not encouraging, the results above were not entirely damning for two reasons: (i) as noted previously, thermodynamically favourable phases do not necessarily eventuate when in kinetic competition, and (ii), aside from ACP, there was a dearth of equilibrium constants for amorphous phosphate phases — thus calculations were for tricalcium phosphate and its equivalents (which one would expect to be less soluble than their amorphous counterparts). However, unhappily, in subsequent observational experiments with magnesium, strontium, and copper, rapid precipitation was noted for the latter two elements under relevant conditions — leaving magnesium alone as a likely candidate.

Following these speciation simulations, simple co-precipitation experiments were conducted with calcium-phosphate-magnesium solutions to verify suitability of the latter element. Under mild alkaline conditions with modest supersaturation (calculated SI < 0.52 with respect to ACP_1), magnesium was found to have similar solubility to calcium (Figure 2.9) but was poorly incorporated (27% Mg yield at pH 8.2). Incorporation dropped further under neutral and mildly acidic conditions (to 11% at pH 6.4) due to greater solubility — notably higher for magnesium than calcium below pH 7 (Figure 2.9). In contrast, precipitation of highly supersaturated (calculated SI > 6.5 with respect to ACP_1) tris buffered calcium-magnesium-phosphate solutions at pH 9 resulted in higher yields for magnesium than for calcium at certain ratios — as reflected in the stoichiometry plot (Figure 2.10).

Magnesium's pH dependent solubility behaviour is a double-edged sword: on one hand, displacing calcium with magnesium ions would likely elevate mineral mass loss in dilute acid, exacerbating ACP dissolution. On the other hand, although magnesium inhibits HAp crystallisation as an incorporated ion, it does so more effectively when surface adsorbed (Ding *et al.*, 2014). Thus, selective losses of magnesium (eg between pH 6 and pH 7) would maximise HAp inhibition efficacy under precisely the conditions where that is most required. The corollary of this dynamic is that optimal doping levels for magnesium require a compromise between limiting mineral dissolution whilst ensuring mineralisation inhibition. Endogenous luminal ACP particles have a Ca:Mg ratio of ~1:5 (Powell *et al.*, 2015) and Boskey and Posner (1974) reported that this level of substitution was sufficient to entirely prevent HAp formation in their system (for at least 6 hours). Whilst other authors, working at much lower mineral concentrations, required ratios of 1:1 to achieve the same effect (Ding *et al.*, 2014), the former study was under more relevant conditions to my application. And perhaps tellingly, in the stoichiometry plot from my series of alkaline buffered precipitations (Figure 2.10), there was a subtle discontinuity between Mg:M (where M = Mg+Ca) ratios of 1:5 and 1:3 — suggesting that between these values, doping became less favourable. After weighing up this result and the literature evidence, I opted to employ a Mg:Ca ratio of 1:4 in further experiments.

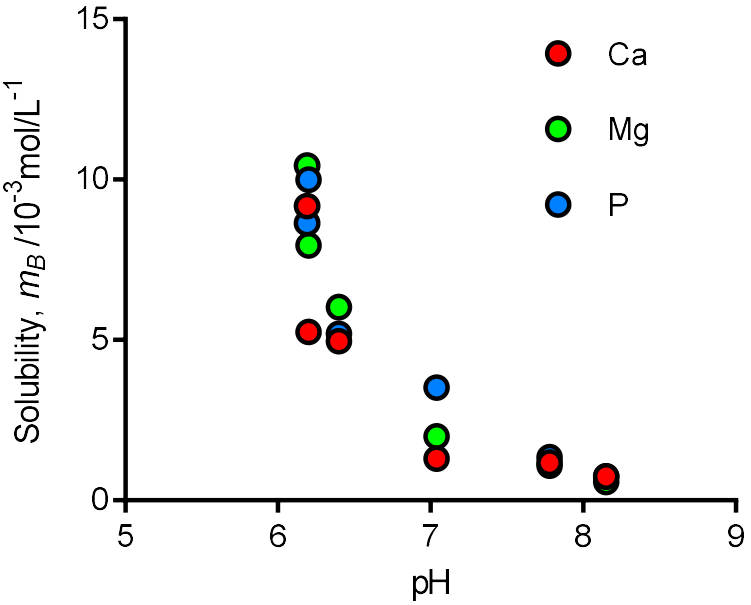

Figure 2.9 Soluble ion concentrations of precipitating calcium-magnesium-phosphate solutions in the pH interval 6–8, as determined by ultrafiltration (3 kDa) and ICP-OES. Means ± one standard deviation are presented for analytical duplicates. Error bars are obscured by the symbols.

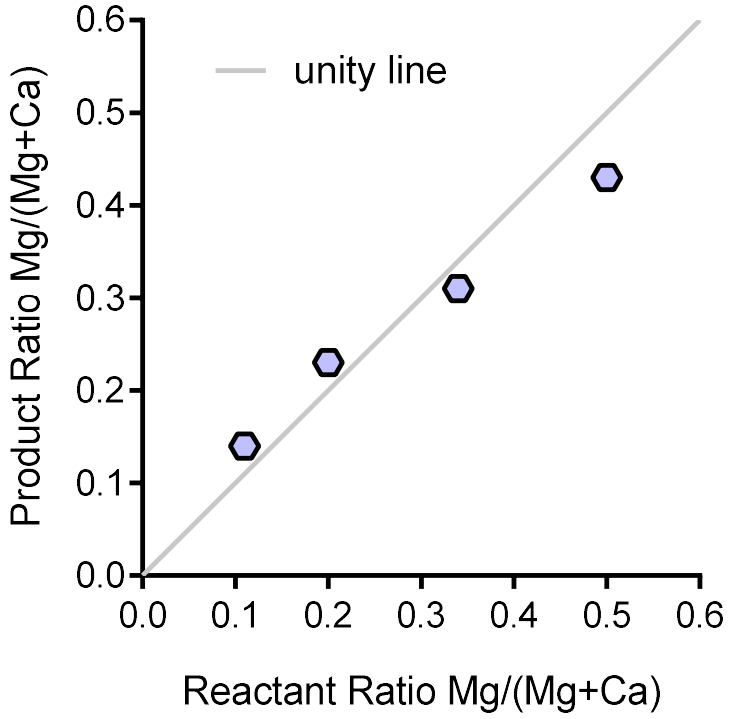

Figure 2.10 Stoichiometry of calcium-magnesium-phosphate materials produced at pH 9 from stocks of varying Ca/Mg ratios. Elemental determination was via ICP-OES. Means ± one standard deviation are presented, for analytical duplicates. Error bars are obscured by the symbols.

As an initial mineral phase transformation study, I precipitated unmodified ACP and magnesium substituted ACP (AMCP) and incubated the precipitates in tris buffered solution at pH 7. Extensive crystallinity was apparent in the FTIR spectra from ACP samples at the first time point (Figure 2.11) but, importantly, AMCP remained amorphous for at least three hours.

Unfortunately, this was not the case in a similar experiment under harsher conditions (pH 5.5, degassed ultra-pure water). Here, full conversion of AMCP to dicalcium phosphate dihydrate (DCPD) occurred within 30 minutes, as revealed by the precipitate stoichiometry — which dropped from ~1.6 (M/P; where M is the sum of Ca & Mg molarity) at point of synthesis, to 1 (M/P) by the earliest time-point (Figure 2.12a). Although undesirable, this result was not excessively alarming since the assay conditions (degassed ultra-pure water at 20°C) were not representative of physiological or cell culture environments.

Accordingly, a second series of assays were conducted at pH 5.5, but at 37°C and in simulated intestinal fluid rather than degassed water. In addition to AMCP, hydroxyapatite (HAp) and DCPD were assayed as reference materials. As before, AMCP precipitate stoichiometry indicated a rapid (sub 1 hour) mineral phase transformation to DCPD (Figure 2.12b). However, crucially, when AMCP was prepared in the presence of ovalbumin protein (as a model cargo), XRD showed it to remain amorphous for at least one hour (Figure 2.12c). Furthermore, the initial precipitate stoichiometry was preserved until after the second time-point (Figure 2.12b) from which one can impute a delay of at least 2 hours to phase transformation. The ACP stabilising effect of incorporated protein has previously been reported for HAp inhibition (Pele *et al.*, 2017), but not for DCPD — and is important given magnesium's apparent inability to inhibit the latter phase. X-ray diffraction on the eventual product indicated a phase mixture of DCPD and HAp, with DCPD as the major phase (Figure 2.12d), and this was also reflected in the endpoint stoichiometry of 1.2 (M/P).

Perhaps most significantly, in a similar subsequent experiment, after incubating AMCP-ovalbumin with simulated intestinal fluid for 3 hours, crude fractionation showed that ovalbumin remained almost entirely associated with insoluble mineral (Figure 2.13) with minimal losses to solution. This was in marked contrast to calcium and phosphate, which were solubilised by two thirds, and magnesium which suffered near total losses.

This series of experiments demonstrates that under physiologically representative conditions, mineral phase transformation of ACP can be delayed for 2-3 hours — sufficient for typical in vitro and in vivo experiments. Crucially, losses of protein were minimal in the face of significant mineral dissolution, allaying earlier concerns (page 31).

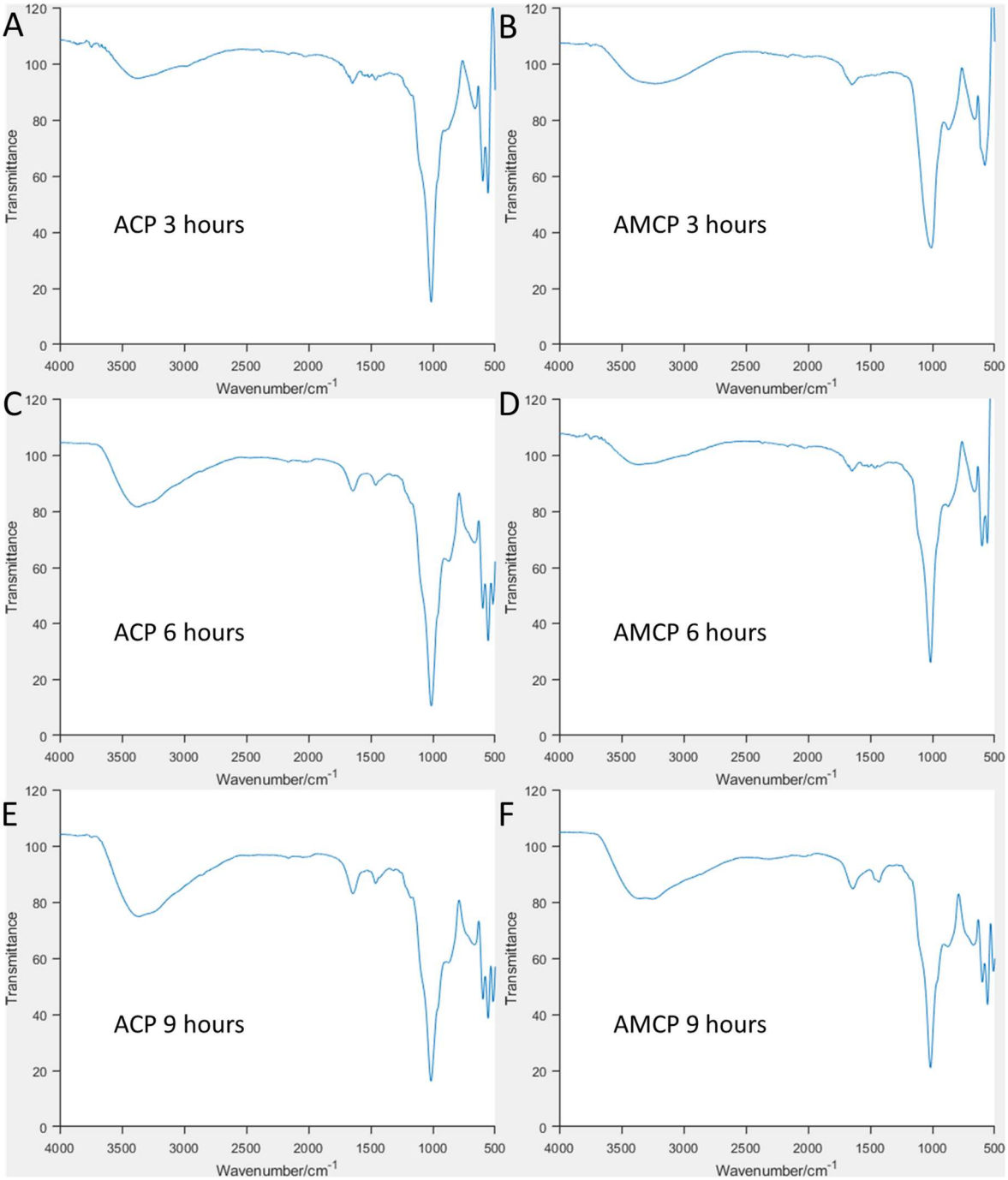

Figure 2.11 Mineral phase transformation of ACP and magnesium substituted ACP over time, in pH 7 tris buffer, as determined by FTIR. Presence of hydroxyapatite is indicated by sharpness of the $v_3(PO_4)$ peak at 1035 cm^{-1} and by the relative intensity of the $v_4(PO_4)$ peaks at 604 and 565 cm^{-1} vs the valley which separates them (Gregorio *et al.*, 2018).

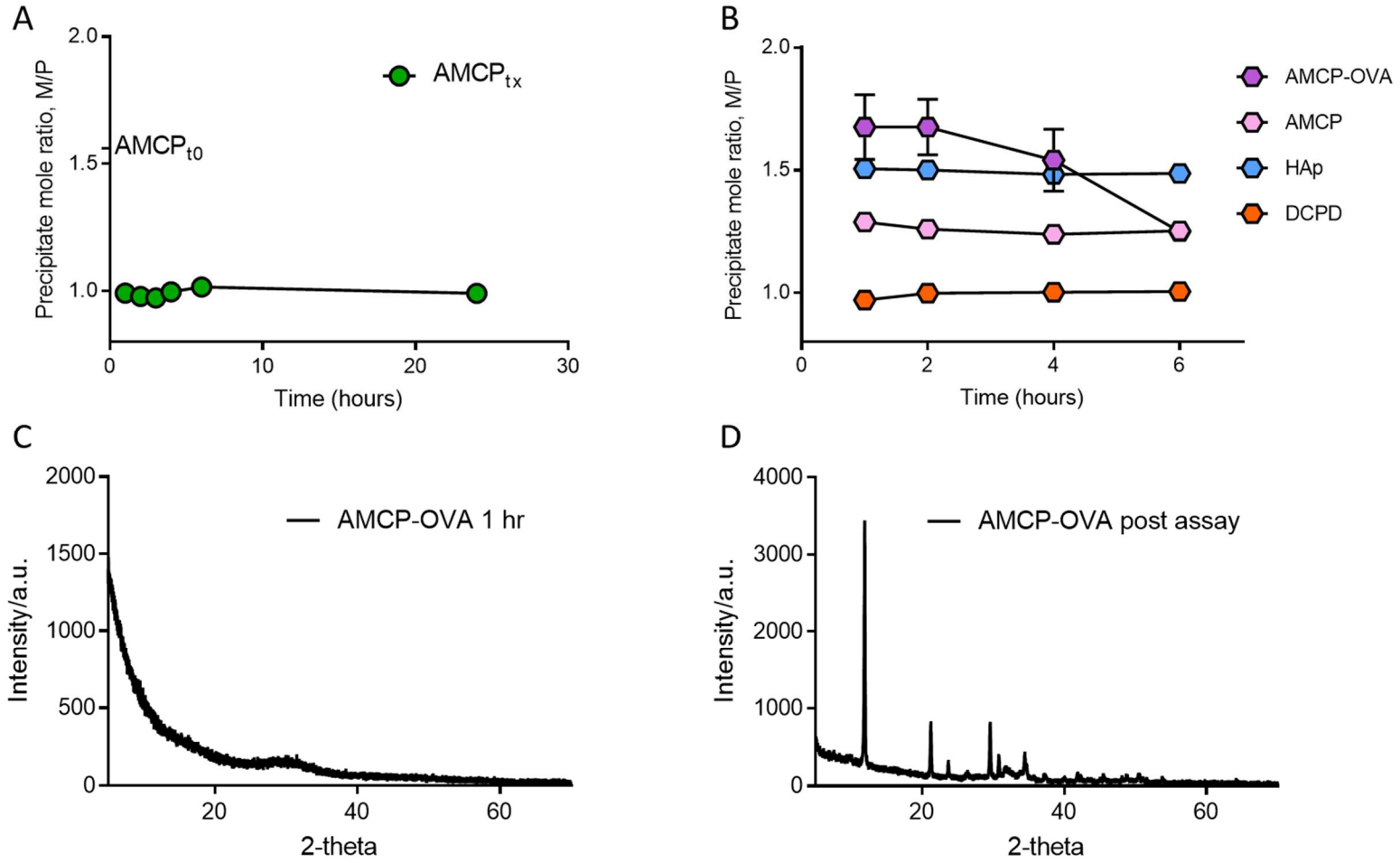

Figure 2.12 Mineral phase transformation of AMCP at pH 5.5, as determined by precipitate stoichiometry and X-ray diffraction. Exposure to degassed UHP water at pH 5.5 (**A**) resulted in a rapid drop in metal/phosphate ratio (from 1.55 to ~1), indicating phase transformation to DCPD. This also occurred to AMCP in contact with simulated intestinal fluid at pH 5.5 (**B**) whilst DCPD and HAp were unaffected. Importantly, formulated AMCP with protein (ovalbumin) cargo, delayed phase transformation (**C**) and slowed it (**B**), although the same crystalline end-point was reached eventually (**B** & **D**).

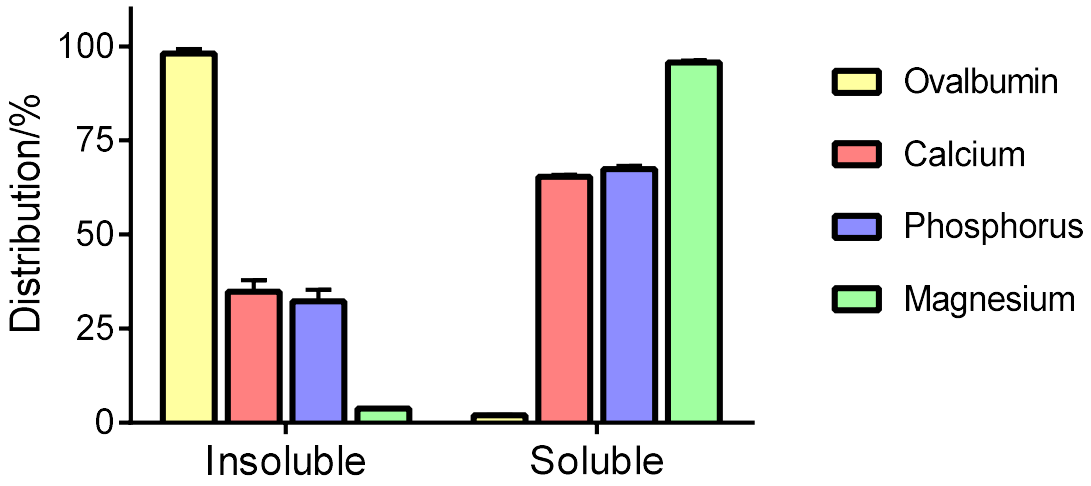

Figure 2.13 Fractionation of ovalbumin cargo and mineral ions after incubating AMCP-OVA with simulated intestinal fluid at pH 5.5 at 37°C for 3 hours. Fractionation was via centrifugation (16000 g for 10 minutes) and quantification via ICP-OES and Bradford assay for mineral ions and protein respectively. Means and single standard deviations are presented from analytical triplicates.

2.3 Conclusion

The aims of this chapter were to ascertain preferable synthetic conditions for bulk ACP mineral, and to determine the likely in-use limitations of the mineral — especially with regards to dissolution, phase transformation, and cargo loss.

Unsurprisingly, supersaturated alkaline conditions favoured amorphous calcium phosphate precipitation. Whilst ACP yield was best served by high alkalinity, such conditions would not be conducive to the stability of biomolecular cargo (Ageno, Dore and Frontali, 1969; Whitaker, 1980). Moreover, the practical benefits (of high pHs) to yield are modest; at reasonable process concentrations (eg 20-50 mMol/L [Ca]), conversion efficiency is likely to be greater than 90% at pHs as low as 7.4. On the other hand, at neutral conditions there is a risk of contamination with dicalcium phosphate dihydrate (DCPD) which precipitates competitively with ACP even in rapid syntheses. Above pH 8.2, ACP is thermodynamically more favourable than DCPD, thus conducting syntheses at pH ~9 would effectively preclude formation of the latter phase, whilst balancing yield and cargo stability considerations.

In man, intestinal pH varies between 5.7, immediately after gastric emptying, and 7.4, at the terminal ileum (Mikolajczyk *et al.*, 2015). In this work, those pHs corresponded to calcium solubilities of 10 and 2 mMol/L respectively. These values were depressed by co-formation of DCPD however — in isolation, ACP would have significantly higher solubility at pH 5.7. Consequently, to effect oral cargo delivery to Peyer's patches with ACP, materials would ideally be formulated to achieve calcium concentrations of 30 mMol/L in the ileal lumen. Importantly, in chemical assays at representative luminal conditions, a modified form of ACP (containing magnesium and ovalbumin) proved to retain its amorphousness and cargo for several hours — demonstrating feasibility of this approach for oral delivery.

By establishing preferable synthetic conditions for bulk ACP mineral and implementing a modified material (AMCP-ovalbumin) with distinct advantages over the unadulterated mineral, the work presented here facilitated subsequent development of ACP nanoparticles — as presented in the next chapter.

2.4 Materials and methods

Methodologies used in this chapter fall roughly into two groupings: fundamental analytical and characterisation techniques (for instance X-ray diffraction) and custom/complex methods (such as assays and simulations) that employ those analytical techniques to answer specific questions. For convenience, commonly applicable details for the fundamental techniques are presented first, in alphabetical (technique) order. Specific assay/synthesis methods are listed subsequently, in order of their appearance in the results and discussion. These make reference to and, where necessary, expand upon the earlier technique subsections. Except where otherwise noted all chemicals were obtained from Sigma Aldrich.

2.4.1 Fourier-transform infrared spectroscopy (FTIR)

FTIR spectra were collected with a Shimadzu IRPrestige-21 FTIR Spectrophotometer equipped with a Golden Gate single reflection diamond ATR accessory (Specac, Orpington, UK) from 500 to 5000 cm^{-1} at a resolution of 1 cm^{-1}. Spectra were subsequently smoothed in MATLAB by applying a second-order Savitsky Golay filter to data frames of length 35.

2.4.2 Inductively coupled plasma — optical emission spectrometry (ICP-OES)

Elemental analyses were carried by ICP-OES (Jobin Yvon Horiba Ultima 2C; Instrument SA, Longjumeau, France), equipped with a concentric nebulizer and cyclonic spray chamber. Plasma gas flow rate was 10 mL/min and sample flow rate was 1 mL/min. Triplicate measurements were made for each sample and means and standard deviations calculated from these. Window size was 0.08 nm (0.04 nm either side of the peak). There were 15 increments per profile and each increment had an integration time of 0.5 seconds. Prior to analysis, samples were diluted down to (analyte) concentrations below 10 mg/L in 5% HNO_3 (v/v). Multi-element calibration standards (50 µg/L to 10 mg/L calcium and phosphorus; 25 µg/L to 5 mg/L magnesium) were also prepared in 5% HNO_3. See Figure 2.14 for an example standard curve. Quantification was carried out using the lines tabulated below (Table 2.4). To convert measured phosphorus concentrations to phosphate ‘amounts’, for instance in mass balance calculations, the phosphorus mass was multiplied by the phosphorus:phosphate molar mass ratio.

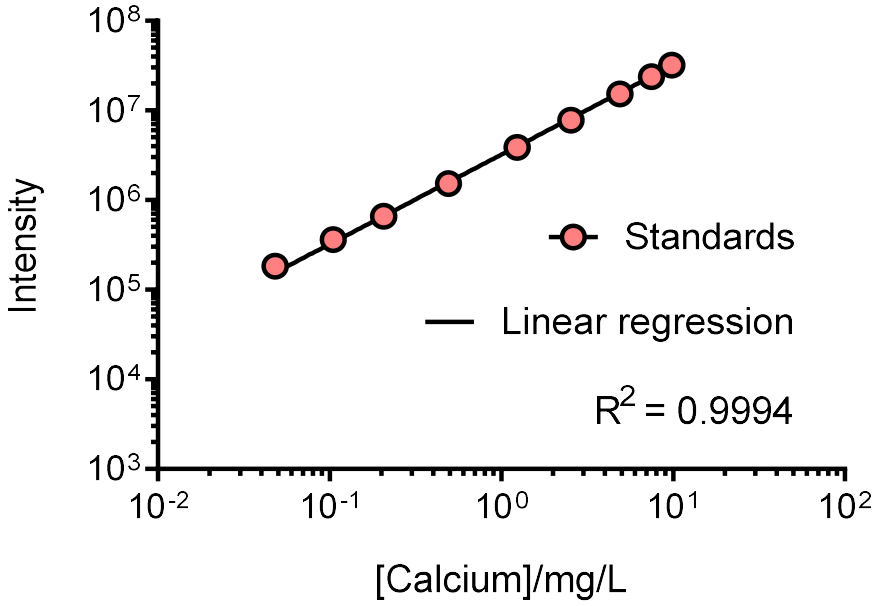

Figure 2.14 An example ICP-OES calibration curve with multielement standards in 5% HNO_3. Emission intensity at the 396.847 nm calcium line has a linear response to concentration in the 50 µg/L to 10 mg/L concentration range.

Table 2.4 ICP elemental emission lines and detection limits

Analyte	Line/nm	Detection limit/µg/L	Reference
Calcium	396.847	0.5	Winge, Peterson and Fassel, 1979
Phosphorus	177.49	200	Nollet and De Gelder, 2013
Magnesium	279.079	30	Winge, Peterson and Fassel, 1979

2.4.3 Powder X-ray diffraction (XRD)

All collected precipitates were washed with acetone three times and then stored in a vacuum desiccator. Powders were gently ground in an agate mortar and then drop cast onto a flat-plate sample holder using acetone. Diffraction data were collected with a D8 advance Bruker powder diffractometer equipped with a Goebel Mirror, VANTEC-1 fast detector and an incident beam monochromator with CuKα1 radiation (λ = 1.5406 Å). Data were collected at room temperature in the range of 5−70° 2θ, with step-scans of 0.15° 2θ and 5 seconds per step. Powder diffraction patterns were compared with simulated patterns from published structures in the international crystal structure database (ICSD) using TOPAS Academic 5 (Coelho Software, Brisbane).

Coherent crystal domain size was determined by applying iterative profile fitting to X-ray diffraction patterns in the 2θ range of 5-70°, using TOPAS Academic 5 and reported crystal structures for DCPD (Curry and Jones, 1971) and hydroxyapatite (Elliott, Mackie and Young, 1973). The background and peak shape were fitted by a shifted Chebyshev function with 11 parameters and a Pseudo-Voigt function (TCHZ type). Instrumental contributions to peak shape were obtained from a previous refinement, by Dr Giulio Lampronti, of diffraction data from a LaB_6 standard (collected with the same diffractometer geometry). The parameters describing instrumental contributions were fixed for subsequent profile fits on calcium phosphate samples. The March-Dollase model for preferred orientation was applied to DCPD diffraction data on the (0 1 0) crystallographic plane. Two isotropic parameters were used to account for Lorentzian and Gaussian sample contributions to peak broadening for crystalline domain size and microstrain respectively. The effect of crystalline domain size upon diffraction peak width is described by the Scherrer equation (Holzwarth and Gibson, 2011), as follows:

$$\tau_{hkl} = \frac{K\lambda}{B_{hkl}cos\theta} \quad (1)$$

Where, τ_{hkl} is the crystallite domain size in the dimension orthogonal to the lattice planes and hkl are the Miller indices of those planes. K is a crystallite shape factor, λ is the X-ray wavelength, B_{hkl} is the full-width at half-maximum of the diffraction peak in radians, and θ is the Bragg angle.

2.4.4 UV-Vis

Ovalbumin protein concentrations were determined by the Bradford protein assay (Bio-Rad, Hertfordshire) according to manufacturer's instructions. Briefly, after citrate (mineral) digestion and dilution, 150 µL aliquots of sample were pipetted, in triplicate, into separate wells in a 96 well plate and then mixed with equal volumes of 1x Brilliant Blue G-250 dye reagent and incubated for 20 minutes. Absorbances of samples, matrix matched ovalbumin standards, and blanks were then measured at 595 nm with a Fujitsu Fluostar Omega plate reader. Sample concentrations were determined by interpolating a standard curve (Figure 2.15) using Prism 6 (Graphpad Software).

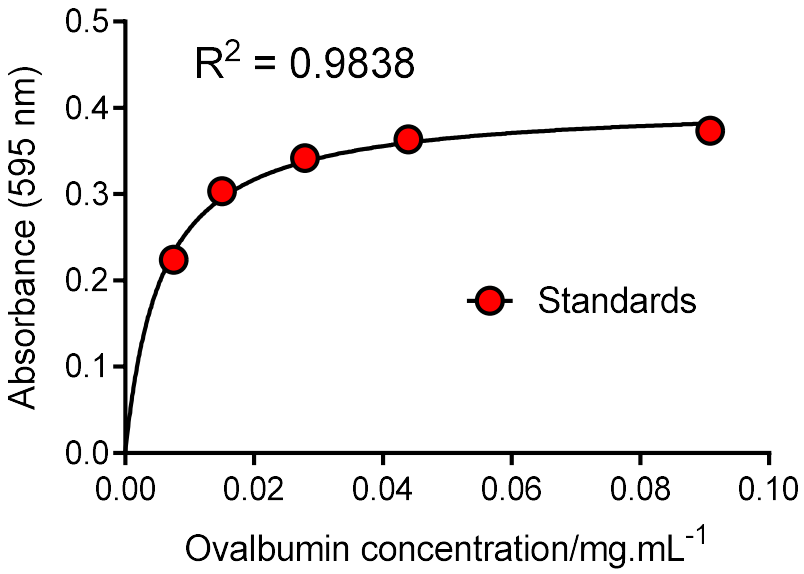

Figure 2.15 An example Bradford assay calibration curve with matrix-matched ovalbumin standards

2.4.5 Co-precipitation yield and solubility study

Calcium chloride and sodium phosphate stocks were prepared in UHP water at pHs of approximately 4, 6, 7, 8, 10 and 11, at concentrations of 100 mMol/L. Stock solutions were pH matched (ie phosphate stocks were adjusted with 1 Mol/L HCl or NaOH to match calcium stock pHs within 0.05 pH units). UHP stocks of pH modified (and matched) water were also prepared and used to dilute stock aliquots to desired reactant concentrations (detailed in Table 2.1). Calcium and phosphate solutions were then mixed vigorously in equal volumes (2.5 mL each) for 2 minutes. After this, the pH was recorded (Hanna Instruments) and aliquots were taken for fractionation. Soluble ions were separated by ultrafiltration through 3 kDa filters (Sartorius Vivaspin; 16,000 g, 5 minutes) to isolate soluble ions. Other aliquots were left unadulterated, as totals. All samples were diluted with 5% HNO_3 and analysed via ICP-OES.

2.4.6 Speciation simulations

An aqueous geochemistry simulation program (PHREEQC version 3, USGS) was used to carry out thermodynamic speciation calculations (Parkhurst and Apello, 2013). Mass-action expressions were constructed for relevant equilibria using carefully selected thermodynamic constants (Table 2.5, Table 2.6). Activity coefficients were calculated using extended Debye–Hückel theory. Two methods were used: (i) to generate solubility results, excess solid (10 moles) of mineral in pH 11

water was titrated with 1 mole of 1 mol/L HCl in 10000 increments, equilibrium phase distributions were calculated at each increment. (ii) A matrix of theoretical solution compositions (eg containing soluble calcium and phosphate ions) was evaluated for their tendency to precipitate (saturation index) in the absence of precipitation (ie equilibrium phases were not calculated). Example code can be found in Appendix A, for both methods.

Table 2.5. K_{sp} table for calcium phosphate simulations

Phase	Mass-action expression	Log K_{sp}	Reference
ACP_1	$Ca_3(PO_4)_2 = 3Ca^{+2} + 2PO_4^{-3}$	-25.50	Gustafsson et al., 2008
ACP_2	$Ca_3(PO_4)_2 = 3Ca^{+2} + 2PO_4^{-3}$	-28.25	Gustafsson et al., 2008
DCPD	$CaHPO_4{:}2H_2O = Ca^{+2} + H^+ + PO_4^{-3} + 2H_2O$	-18.99	Minteq database
HAp	$Ca_5(PO_4)_3OH + H^+ = 5Ca^{+2} + 3PO_4^{-3} + H_2O$	-44.33	Minteq database
OCP	$Ca_4H(PO_4)_33H2O = 4Ca^{+2} + H^+ + 3PO_4^{-3} + 3H_2O$	-47.08	Minteq database
β-TCP	$Ca_3(PO_4)_2 = 3Ca^{+2} + 2PO_4^{-3}$	-28.92	Minteq database

Table 2.6. K_{sp} table for metal phosphate and hydroxide simulations in Figure 2.8

Phase	Mass-action expression	Log K_{sp}	Reference
Calcium phosphate	$Ca_3(PO_4)_2 = 3Ca^{+2} + 2PO_4^{-3}$	-32.68	Haynes, 2010
Cupric phosphate	$Cu_3(PO_4)_2 = 3Cu^{+2} + 2PO_4^{-3}$	-36.85	Haynes, 2010
Ferrous phosphate	$Fe_3(PO_4)_28H_2O = 3Fe^{+2} + 2PO_4^{-3} + 8H_2O$	-36.00	Minteq database
Magnesium phosphate	$Mg_3(PO_4)_2 = 3Mg^{+2} + 2PO_4^{-3}$	-23.98	Haynes, 2010
Strontium phosphate	$Sr_3(PO_4)_2 = 3Sr^{+2} + 2PO_4^{-3}$	-27.80	Holt et al, 1954
Zinc phosphate	$Zn_3(PO_4)_24H_2O = 3Zn^{+2} + 2PO_4^{-3} + 4H_2O$	-35.42	Minteq database
Calcium hydroxide	$Ca(OH)_2 = Ca^{+2} + 2OH^-$	-5.299	Haynes, 2010
Cupric hydroxide	$Cu(OH)_2 = Cu^{+2} + 2OH^-$	-19.32	Dirkse, 1986
Ferrous hydroxide	$Fe(OH)_2 = Fe^{+2} + 2OH^-$	-16.31	Haynes, 2010
Magnesium hydroxide	$Mg(OH)_2 = Mg^{+2} + 2OH^-$	-11.25	Haynes, 2010
Strontium hydroxide	$Sr(OH)_2 = Sr^{+2} + 2OH^-$	-3.307	Lambert, 1992
Zinc hydroxide	$Zn(OH)_2 = Zn^{+2} + 2OH^-$	-16.52	Haynes, 2010

2.4.7 Co-precipitation syntheses for mineral phase determination

Syntheses for phase determination were carried out by mixing equal volumes (25 mL each) of pH matched calcium chloride and sodium phosphate solutions, with mechanical stirring (Stuart SS10, fitted with a four-blade propeller. After 2 minutes of mixing, 50 mL of ice cold acetone was added and the resultant fluid centrifuged for 5 minutes at 12000 g. Precipitates were washed three times in ice cold aqueous acetone (1:1) and then three times in ice cold acetone and then dried under vacuum. Solution compositions were as tabulated in Table 2.2.

2.4.8 Precipitation of potential dopant metal minerals

Metal chloride salts were dissolved in UHP at 50 mMol/L and diluted 10 fold in either: (a) 110 mMol/L sodium phosphate, buffered with 100 mMol/L tris, at pH 9, or (b) 100 mMol/L tris at pH 9. Precipitate formation was determined by visual observation.

2.4.9 Precipitation of magnesium substituted ACP

The pH dependent solubility response of amorphous magnesium substituted calcium phosphate (AMCP) was determined in similar fashion to that of unmodified ACP. pH matched calcium and phosphate solutions were mixed in equal volume (5 mL each) according to Table 2.7. Sample fractionation and analysis was exactly as described in Section 2.4.5.

Table 2.7 Synthetic parameters for AMCP syntheses corresponding to the pH dependent solubility results presented in Figure 2.9.

Synthesis concentration/mMol.L^{-1}			Ion ratios (total)		pH	
P	Mg	Ca	Ca+Mg/P	Ca/Mg	Initial	Final
27.48	12.09	31.43	1.58	2.60	9.9	6.2
28.50	9.54	25.93	1.24	2.72	10.2	6.2
16.74	6.81	16.33	1.38	2.40	10.3	6.4
7.77	2.58	5.84	1.09	2.26	10.1	7.0
3.24	1.41	3.41	1.49	2.43	10.4	7.8
1.68	0.79	1.92	1.61	2.44	10.4	8.2

Subsequently, a further set of materials of varying magnesium contents were produced from tris buffered solution. In these syntheses, 500 mL of 300 mMol/L tris buffer stock was made up and split in two: half was adjusted to pH 9.09 and half to pH 8.09. Phosphate (disodium salt) was dissolved at a concentration of 110 mMol/L in the pH 9.09 stock. The pH 8.09 stock was split into 50 mL portions and calcium chloride and magnesium chloride dissolved within them, at (Ca/Mg)

ratios of 8:1, 4:1, 2:1 and 1:1. Total metal ion concentrations were 1 Mol/L in all cases. To precipitate mineral, 5 mL portions of the metal solutions were added to 45 mL portions of phosphate solution under vigorous mixing. Precipitates were collected by centrifugation and washed three times in ice cold pH 9 water and then three times in ice cold acetone and then dried under vacuum.

Finally, AMCP for phase transformation kinetics was prepared as reported by Pele et al (2017), with minor modification. Briefly, ovalbumin (where used) was dissolved at 0.5g/L in a Ca/Mg solution containing 35 mMol/L $CaCl_2$ and 7.2 mMol/L $MgCl_2$ and 0.15 Mol/L tris buffer at pH 9. The resulting Ca/Mg/protein solution was then mixed with an equal volume of phosphate (PO_4) solution which contained 39 mMol/L Na_2HPO_4 in 0.15 Mol/L tris buffer, also at pH 9. Precipitates were collected and processed as described immediately above. ACP for the initial phase transformation experiment was prepared in the same fashion as AMCP but the metal stock contained 42 mMol/L calcium chloride and no magnesium.

2.4.10 AMCP assays

To ascertain phase transformation kinetics, materials prepared as above were assayed in three environments: (i) 50 mMol/L tris buffer in UHP water at pH 7.4 and room temperature. (ii) pH 5.5, nitrogen-degassed, UHP water at room temperature. And (iii) pH 5.5, simple simulated intestinal fluid, comprising 10 mMol/L $NaHCO_3$, 100 mMol/L KCl, and 0.5 mMol/L lecithin, at 37°C. The assays at pH 5.5 employed an integrated pH probe and autotitration system (Metrohm, Switzerland) to control pH. Autotitration solutions were 1 Mol/L HCl and 1 Mol/L NaOH. Mineral-calcium-concentrations were 25 mMol/L in the pH 7 assay and 40 mMol/L in the auto-titration assays.

In a subsequent assay, the auto-titrator-simulated-intestinal-fluid experiment was repeated, but at a mineral-calcium-concentration of 15 mMol/L. In this experiment, mineral ions and cargo were fractionated into soluble and insoluble components by centrifugation (16000 g for 10 minutes). Sample aliquots were then prepared for analysis in triplicate. For ICP-OES, this entailed dilution with 5% HNO_3 for protein free samples, or overnight digestion with conc. HNO_3 and then dilution with UHP water (to reach a final HNO_3 concentration of 5%) for protein containing samples. For cargo concentration determination by UV-Vis, aliquots were mixed 1:1 with 100 mMol/L pH 3 citrate buffer to dissolve any mineral present.

Chapter 3 Synthesis of ACP nanoparticles

3.1 Introduction

Due to the tendency of ACP to form micron — and larger — sized agglomerates in solution, synthetic routes to disperse ACP nanoparticles require some means of altering the mineral surface chemistry. Chapter 1 contains a discussion of the approaches by which this is commonly accomplished. In brief, the simplest strategies involve co-precipitation of soluble calcium and phosphate salts in the presence of a templating dispersant. More complex methods employ flow chemistry to sequentially grow and then 'cap' particles with a suitable ligand, whilst the most elaborate approaches constrain particle size by confining the reaction space to individual nano-droplets — typically using microemulsions or microfluidic devices. In accordance with parsimony, I began with the simplest approach.

Please note that in this and subsequent chapters I do not use ACP and AMCP to differentiate between materials on the basis of their magnesium content; the vast majority do contain magnesium and in the rare cases where they do not, it is noted.

3.2 Results and discussion[9]

3.2.1 Single step co-precipitation

As a starting point for producing ACP nanoparticles I adapted a co-precipitation method from Pele et al. (2015) and used dynamic light scattering (DLS) to monitor the reaction progress. This method entailed spiking replete tissue culture media (TCM) with calcium saline; TCM provided the phosphate substrate and a protein dispersant in the form of fetal calf serum (FCS). Prior to calcium addition, DLS measurements on aliquots of TCM showed a peak at ~6 nm (Figure 3.1a), broadly consistent with the albumin proteins which largely comprise FCS (Adel *et al.*, 2008). Upon calcium chloride addition, a population of ~200 nm (hydrodynamic diameter) particles emerged, initially as a minor volume fraction (Figure 3.1b), but subsequently predominating (from ca. 1 hour onwards; Figure 3.1a). Intermediate time-point measurements (eg 30 mins) evinced a bimodal distribution pattern (Figure 3.1b-c), indicating distinct populations; encouragingly, once formed, the larger particles remained size-stable in solution for at least 24 hours (Figure 3.1d-f) despite gradual conversion to hydroxyapatite (Appendix B; Figure B.1.1).

Interestingly, mineralisation progression was also apparent in the DLS signal kinetics. Whilst all of the available particle size measures followed broadly similar trends, intensity-weighted metrics (Figure 3.1d&f) exhibited steeper and better conditioned size-time responses than their volume-weighted counterparts (Figure 3.1e). This is unsurprising since, by definition, intensity distributions are highly sensitive to scattering power — which increases considerably (~5000 fold under measurement conditions[10]) between 6 nm and 200 nm (Figure 3.1g). What does surprise, however, is the comparative trend in overall signal intensity (Figure 3.1h), which continues to increase long after the particle size distributions have stabilised. The scale of this discrepancy is well illustrated by the rate constants obtained from single-phase association (SPA) fits (Figure 3.1i). Changing optical properties almost certainly underly this behaviour; scattering power is highly sensitive to refractive index (RI). Indeed, according to Mie theory, (under measurement conditions) hydroxyapatite particles should reflect approximately 200 fold more light to the detector than bovine serum albumin (BSA) particles of equivalent size (Figure 3.1g). ACP lacks an established RI (Past, 1974) but a value in the range of 1.45 – 1.55 is likely, giving it a scattering efficiency ~2 – 6 fold lower than HAp and ~30 – 100 fold greater than BSA (Appendix B; Figure B.1.2). With this in mind, it seems probable that RI variations are responsible for a proportion of the intensity-volume

[9] Materials and methods for this chapter can be found from page 72
[10] λ = 633nm, θ = 175°

metric mismatch seen at early to intermediate time-points and entirely causative of the late-stage count-rate increases.

To my knowledge, use of dynamic light scattering to monitor mineral phase transformation by imputing optical property variation has not been discussed previously. These findings raise the prospect of simultaneous particle size and phase measurement, in-situ, and merit further work.

Unfortunately, as a practical method for producing disperse ACP particles, this experiment left much to be desired; process concentration was low ($[H_xPO_4^{x-3}]$ = 6.7 mMol/L; $[Ca^{2+}]$ = 4 mMol/L), conversion was slow, and — although it could not be seen by FTIR — by the time (~2 hours) all the particles had formed, defective HAp was likely present. Moreover, after collecting the particles by centrifugation, I was unable to resuspend them despite extended ultrasonication — stymying the possibility of washing or concentrating the particles down-stream.

Simplified single-step co-precipitation

To ascertain whether this re-dispersion failure was a general feature of single-step ACP co-precipitations or a fault of these specific conditions, I conducted a series of syntheses in a simplified system. In lieu of TCM and FCS, I mixed tris-buffered calcium chloride and sodium phosphate solutions in the presence of polyelectrolytes (bovine serum albumin (BSA), ovalbumin (OVA), or carboxymethycellulose (CMC)) and assessed the dispersion and redispersion of the resulting particles. To do this efficiently, I employed visual observation (aided by a laser pen) as a pass-fail adjunct to DLS. I found that matching mineralising-ion (MI; calcium, magnesium and phosphate) and polyelectrolyte concentrations to those in the Pele method yielded similar results (disperse colloids of ~ 200 nm; Figure 3.2a, Table 3.1). Increasing the pH to 9 improved yield without affecting dispersion behaviour — which also proved insensitive to variation in MI ratio (Ca:Mg:P) at low concentration. Conversely, doubling total MI concentration resulted in polydisperse products; in the case of BSA or OVA, particle agglomeration was slowed but not prevented by increasing polyelectrolyte levels. Higher loadings of CMC — reportedly an effective stabiliser for ACP particles (Peetsch *et al.*, 2013)— were more effective at maintaining dispersion but still could not resuspend centrifuged particles (Figure 3.2b), a major sticking point. Cargo incorporation was also poor; when synthesised in the presence of a soluble fluorescent dye (calcein), less than 5% of the cargo was trapped by the particles.

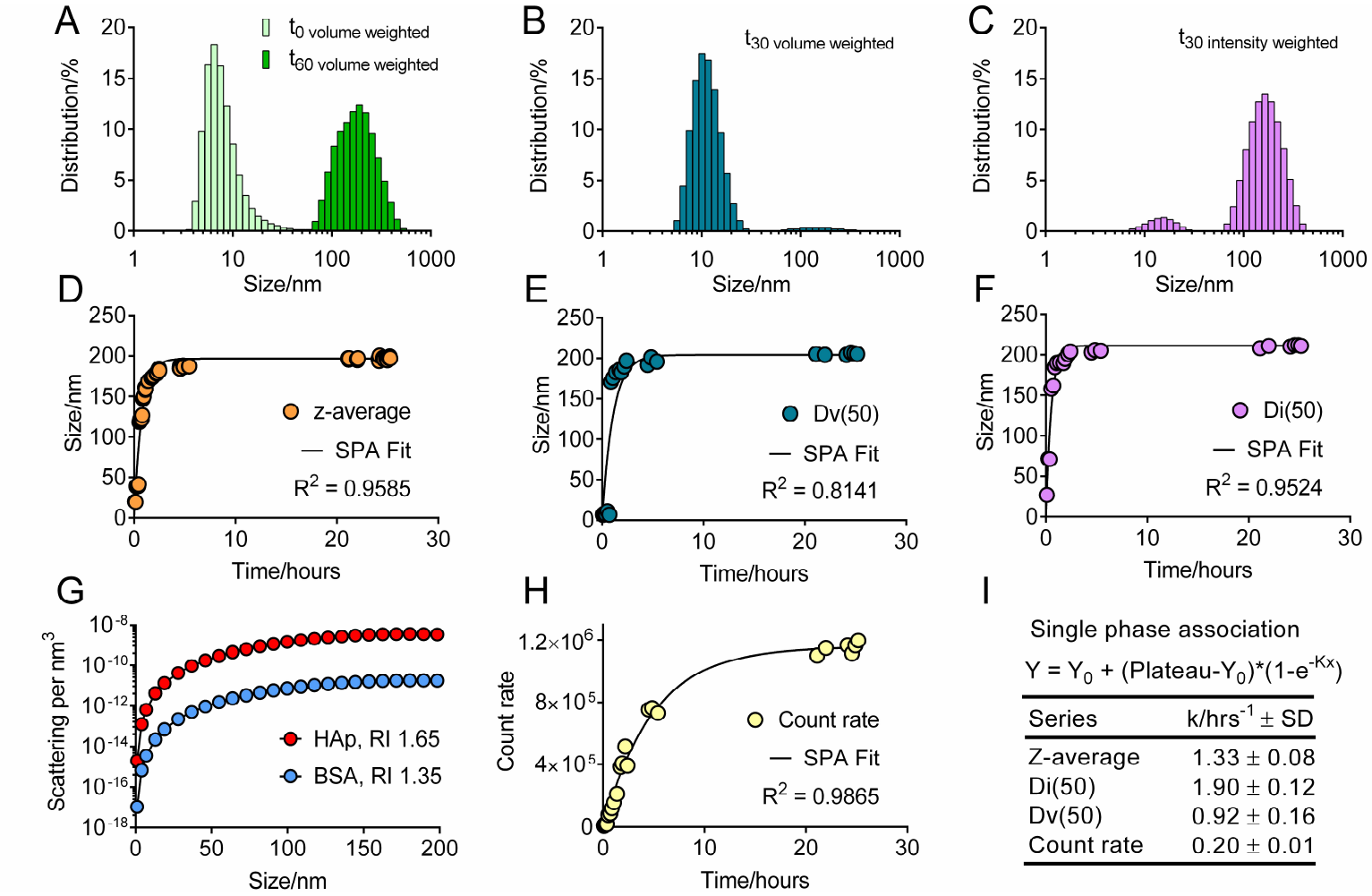

Series	k/hrs^{-1} ± SD
Z-average	1.33 ± 0.08
Di(50)	1.90 ± 0.12
Dv(50)	0.92 ± 0.16
Count rate	0.20 ± 0.01

Figure 3.1 Single-step co-precipitation of calcium phosphate particles in tissue culture media. Addition of $CaCl_2$ led to mineralisation of bovine serum proteins, yielding calcium phosphate colloids (**A-C**). Particles were size stable from ~2 to 26 hours (**D-F**) despite transformation to hydroxyapatite (Appendix B; Figure B.1.1). Mie theory calculations (**G**) suggest mineralisation associated refractive index changes led to a progressive elevation in scattering efficiency, explaining sluggish count-rate kinetics **(H** and **I**). All data are shown without error bars, for single runs of 12 measurements.

Given that calcein has a reasonable affinity for mineralised calcium (O'Brien, Taylor and Lee, 2002), I suspect that poor incorporation was a result of competition from the polyelectrolytes for mineral interaction — which is likely to be a general process flaw (since cargo loading and particle coating occur simultaneously, and at a disadvantageous mass ratio for the cargo). The single step nature of this process is probably also responsible for the re-dispersion and concentration limitations I encountered; engendering concomitant mineral formation and dispersant binding would inevitably have led to mineralisation of the dispersant molecules themselves. If this resulted in exposed surface regions of ACP, neighbouring composites (of mineral and protein) would have been prone to sticking together via electrostatic interactions whenever they made contact (eg during centrifugation).

Table 3.1 Simplified single-step coprecipitation syntheses of polyelectrolyte functionalised ACP. Materials were prepared by mixing pH matched metal (calcium and magnesium) and phosphate salt solutions in the presence of dispersant. Dispersion status was assessed by eye and then followed up by dynamic light scattering for materials that were apparently disperse or could not be judged. The first row summarises the tissue culture media experiments presented earlier.

Code	Dispersant (w/w)	pH	Calcium	Magnesium	Phosphate	Disperse	Redispersable
M1	10% FCS	7.4	4	0.4	6.7	Yes	No
M2	0.5% BSA	7.4	4	0.4	6.7	Yes	No
M3	0.5% BSA	7.4	4	1	5	Yes	No
M4	1% BSA	7.4	4	1	5	Yes	No
M5	1% OVA	7.4	4	1	5	Yes	No
M6	1% BSA	9.0	4	1	5	Yes	No
M7	2% BSA	9.0	4	1	5	Yes	No
M8	1% OVA	8.9	4	1	5	Yes	No
M9	1% BSA	8.9	8	2	10	No	No
M10	1% OVA	8.9	8	2	10	No	No
M11	1% BSA	9.0	8	2	6	No	No
M12	2% BSA	9.0	8	2	6	No	No
M13	4% BSA	9.0	8	2	6	No	No
M14	1% OVA	8.9	8	2	6	No	No
M15	2% OVA	8.9	8	2	6	No	No
M16	4% OVA	8.9	8	2	6	No	No
M17	1% CMC	9.0	4	1	3	Yes	No
M18	2% CMC	9.0	6	1.5	4.5	Yes	No
M19	4% CMC	9.0	8	2	6	Yes	No

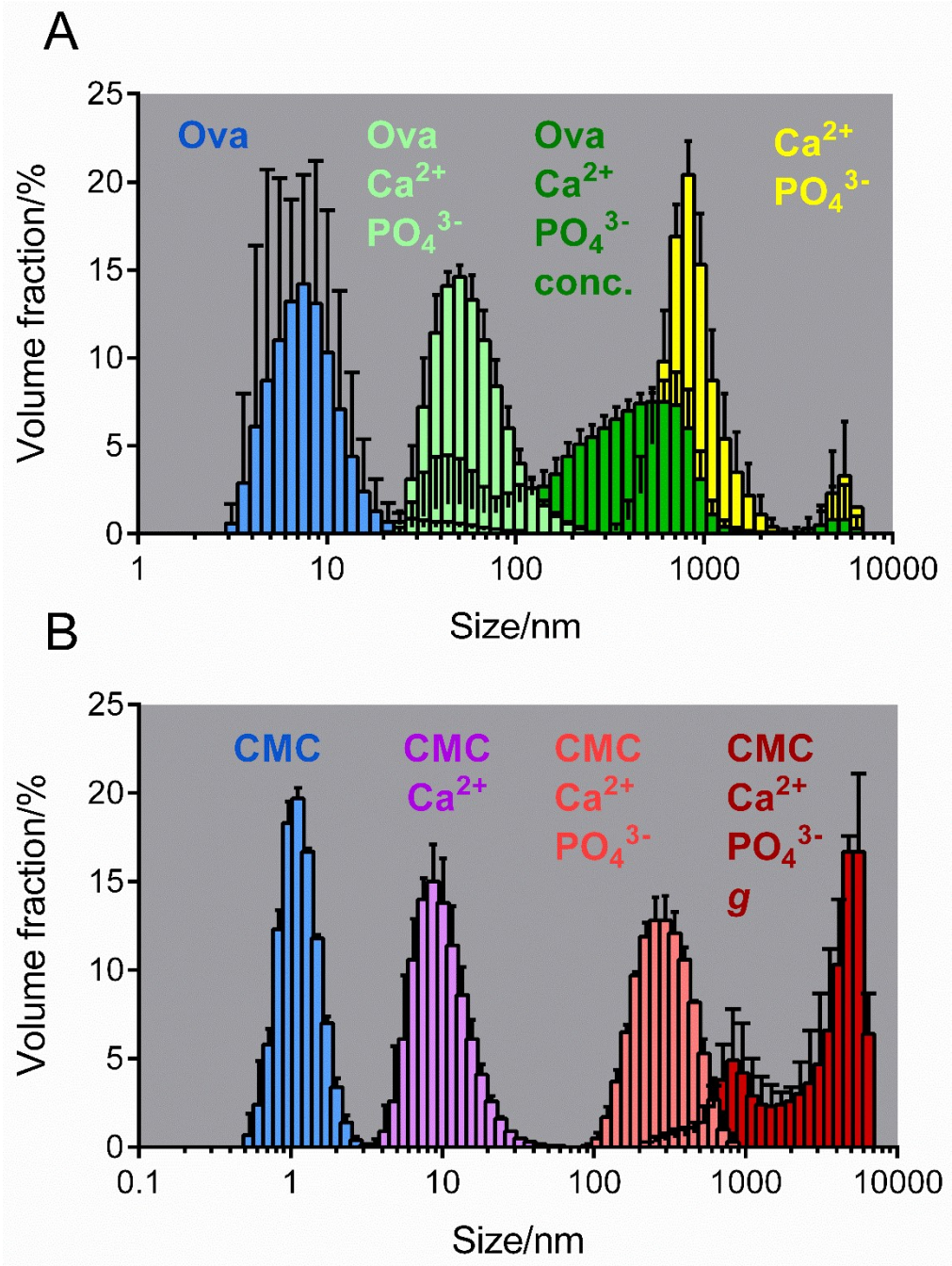

Figure 3.2 Example particle sizing results for single step coprecipitation syntheses. Data are shown for polyelectrolyte alone (blue, **A** & **B**) and for polyelectrolytes combined with various mineralising ions (green, **A**; purple & terracotta, **B**). A polyelectrolyte free precipitation (yellow, **A**) is also shown for reference, as is a post-centrifugation CMC material (crimson, **B**). Volume weighted distributions were obtained via dynamic light scattering. Mean ± standard deviations are presented for 6 measurements of 12 runs.

3.2.2 Stepwise co-precipitation

In an attempt to obviate the limitations of single-step methods without sacrificing the simplicity of 'bucket chemistry', I decided to employ a separation heuristic[11]; segregating particle formation into two discrete steps: (1) mineral precipitation, and (2) surface coating (eg with polyelectrolye). ACP's exuberant precipitation behaviour was a complication to this approach; in the absence of dispersant, co-precipitation of calcium and phosphate solutions rapidly leads to large (>µm) agglomerate formation (Figure 3.2a). As a quick feasibility study I investigated these aggregation dynamics in a dispersant-free system and found that by quickly (≤ 1 second) diluting a pristine supersaturated calcium-magnesium-phosphate solution, I was able to detect a progression from ~1 nm Posner Cluster equivalents through to medium sized (ca. 30 nm) nanoparticles over a period of 30 seconds or so (Figure 3.3a). These DLS measurements were obtained close to the instrument's detection limit and as single runs, so their values are indicative only. Nonetheless they constituted sufficient proof-of-principle to merit further multi-step work.

I subsequently found that at low mineralising ion concentrations (5-to-10 mMol/L $H_xPO_4^{x-3}$ and M^{2+} — Ca:Mg 4:1), quickly diluting precipitating calcium-magnesium-phosphate solutions with a dispersant such as carboxymethylcellulose would quench particle growth in the sub-micron range. Moreover, these particles were re-dispersible after centrifugation, facilitating washing and further formulation (Figure 3.3b). On the other hand, the particles were generally larger than desirable (50-300 nm being optimal) and the process was rather erratic due to my difficulty reproducing timings. At higher loadings (> 20 mMol/L) the method failed (Figure 3.3c), likely due to concentration dependent enhancement of particle coagulation kinetics (Heine and Pratsinis, 2007).

At this juncture I had, in principal, a means of producing disperse ACP particles but required more sophisticated reaction control — in particular, I needed to shorten the initial precipitation step in a reproducible manner. To this end I turned my attentions to flow chemistry methods, which although more complex and time-consuming to establish than batch approaches, can offer greater reproducibility and finer control of synthetic parameters (Pastre, Browne and Ley, 2013).

[11] "*…place each part of an object in conditions that are most favourable for its operation*." (Tessari and De Carvalho, 2015)

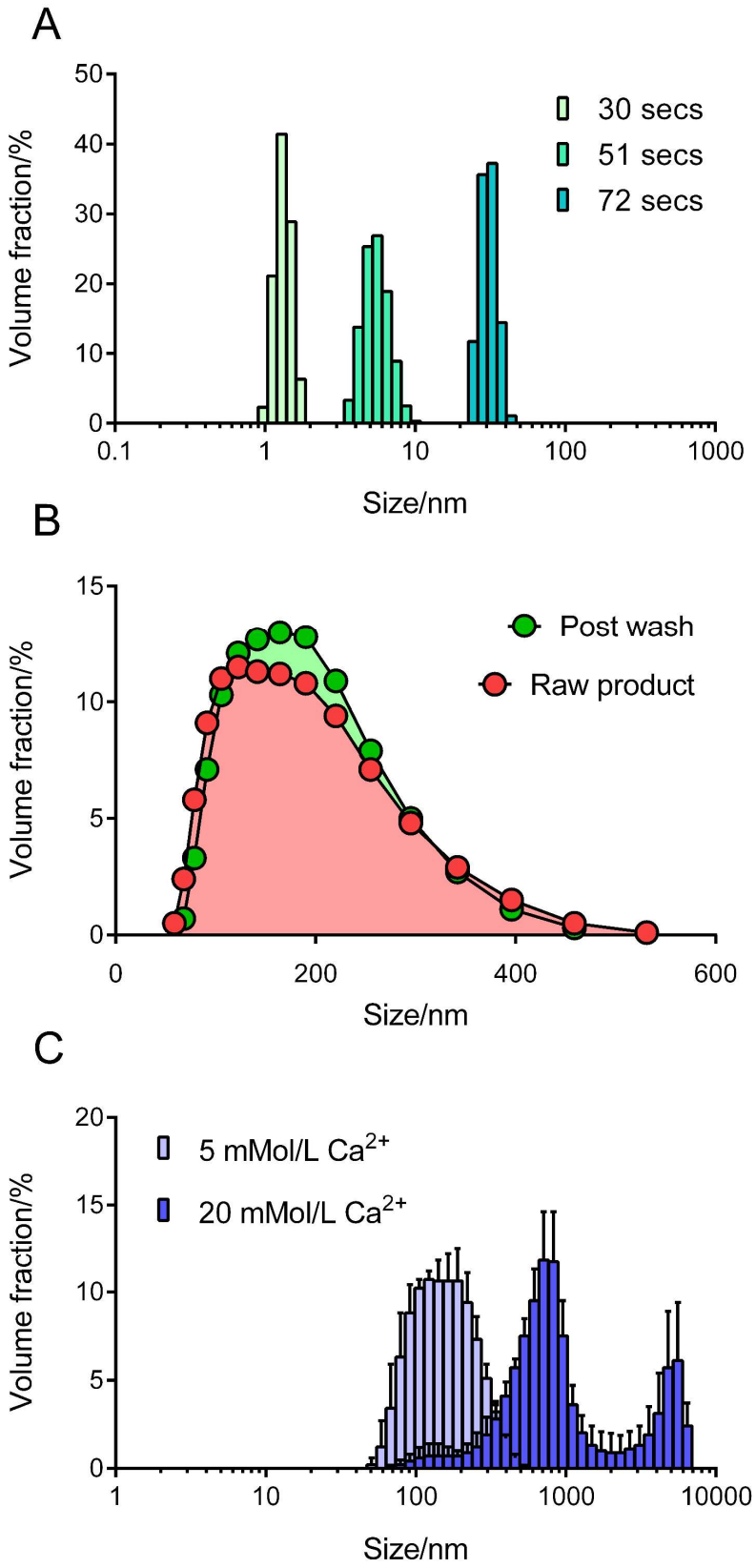

Figure 3.3 Dynamic light scattering particle sizing results from sequential coprecipitation experiments. In the absence of dispersant, ACP agglomerates rapidly (**A**). Quickly adding carboxymethcellulose to precipitating calcium-phosphate solutions can quench particle growth, resulting in disperse and redispersible colloids (**B**) but, using 'bucket chemistry', this only worked at low concentration (**C**).

3.2.3 Flow chemistry

My first foray into the realm of flow chemistry was to reproduce a continuous flow reactor and method (for producing ACP nanoparticles) previously described by Matthias Epple and colleagues (Peetsch *et al.*, 2013). Operating this reactor under the reported conditions consistently yielded disperse and re-dispersible carboxymethylcellulose-functionalised ACP nanoparticles of comparable size (Figure 3.4) to the products of my earlier labours and to the published results (see figure 1 of that manuscript). Unfortunately, operating the reactor at useful concentrations[12] (eg ion feeds ≥ 30 mMol/L) rapidly led to accumulation of precipitate within the tubing, ultimately clogging the reactor and preventing syntheses at scale.

This kind of channel fouling is the bane of single phase flow chemistry and various strategies are employed to avoid it (Nightingale *et al.*, 2014). I adopted one of the simplest measures to side-step problematic reaction–wall interactions: forgoing the walls. I accomplished this by developing a free impinging jet reactor (IJR) in which substrate streams are pumped through a pair of nozzles aligned such that the resultant fluid jets collide in mid-air (Figure 3.5; Demyanovich & Bourne, 1989). This style of reactor is capable of inducing efficient micromixing at µs time scales (Erni and Elabbadi, 2013) and therefore lends itself well to fast reactions, but surprisingly (to the best of my knowledge, and in contrast to confined impinging jet reactors) has not previously been applied to producing calcium phosphates or even disperse nanoparticles in general.

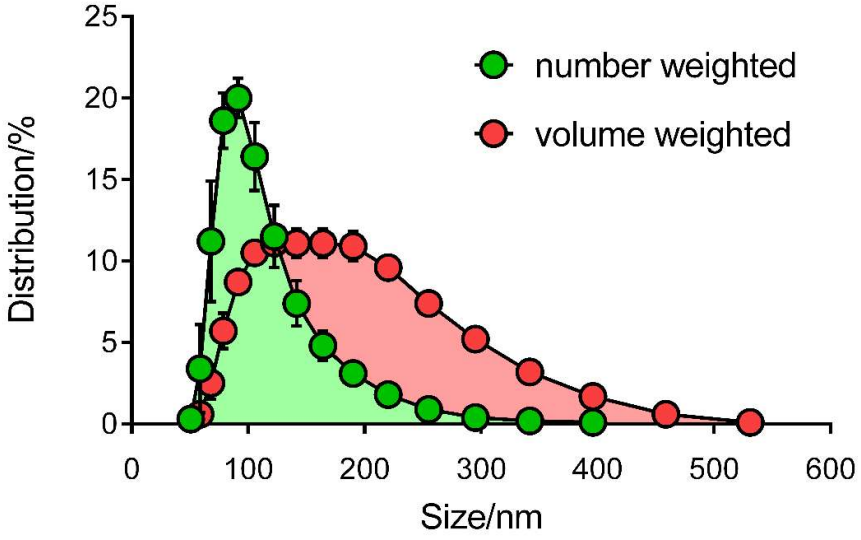

Figure 3.4 Volume and number weighted size distributions for washed and resuspended ACP-CMC particles produced via the method of Peetsch et al and determined via DLS. Mean ± standard deviations are presented for 6 measurements of 12 runs.

[12] Cf outlet concentrations in the original paper of 2.4 mMol/L (Ca^{2+}) and 1.44 mMol/L ($H_xPO_4^{x-3}$).

This gap may, in part, be because much of the literature[13] describing IJRs is concerned with their fluid dynamics and consequently involves specialist equipment and finely-calibrated nozzle configurations. Moreover, peak (IJR) performance requires maximising jet impact energy without inducing atomisation of the resulting merged stream and this sweet-spot is dependent on solution composition via variables such as viscosity and surface tension (Kumar, Prasad and Kulkarni, 2013) — as a consequence, significant optimisation is needed for every synthesis. These factors are all barriers to practical synthetic chemistry. Thankfully, in my system, acceptable synthetic results were possible with primitive equipment (Figure 3.6). My first reactor (Figure 3.6a) was extremely basic and only effective at low concentrations: both the metal (calcium and magnesium, 4:1) and phosphate feeds were ≤ 10 mMol/L. The next device (Figure 3.6b) employed rigid nozzles (crimped stainless-steel needles) on adjustable arms. This allowed me to establish a maximum (fission-free) impingement angle (θ) of ~ 120° (similar to the results of Kumar et al) and allowed access to higher concentrations. The rigid needles required frequent, and laborious, alignment however, so I returned to a soft-nozzle arrangement (Figure 3.6c). That device, whilst crude, was utilitarian and facile to fabricate – being comprised from a minimum of off the shelf components – and sufficed for most of my subsequent PhD work. Much later, Adrian Ison (Department of Veterinary Medicine, University of Cambridge) kindly machined me a sophisticated manifold (Figure 3.6d-e) but this was primarily in aid of convenience and aesthetics rather than performance.

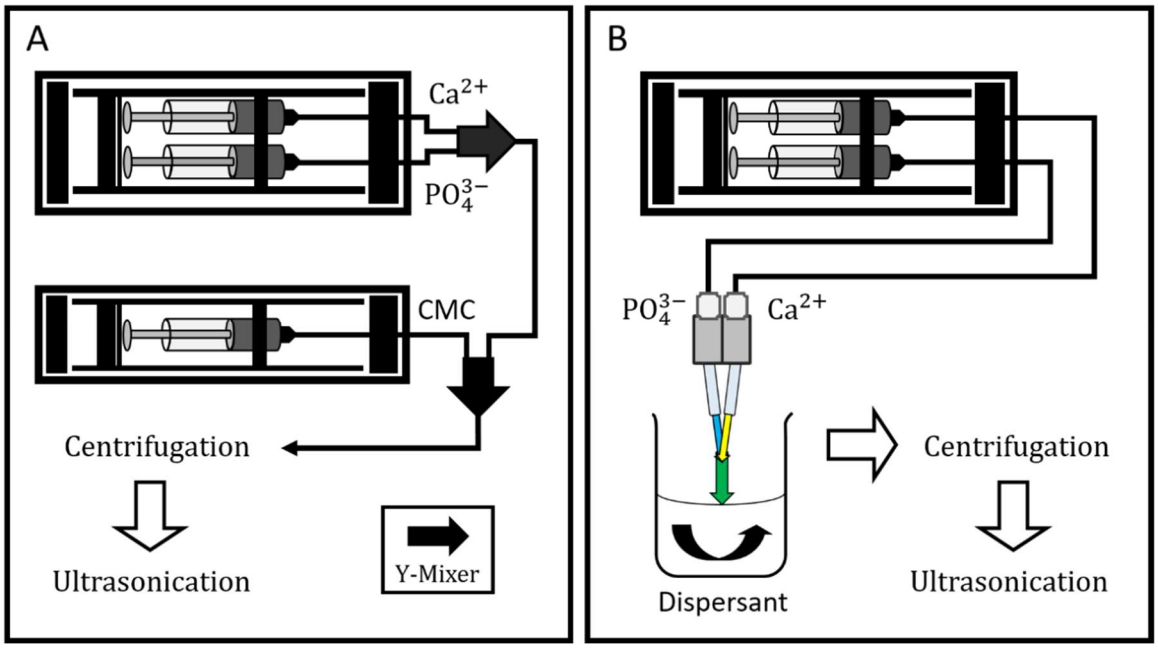

Figure 3.5. Schematic comparing ACP nanoparticle synthesis via: (**A**) conventional confined flow processes (Peetsch et al., 2013), and (**B**) a free impinging jet reactor. See page 77-78 for methods.

[13] For instance: Demyanovich & Bourne, 1989; Li & Ashgriz, 2006; Jung, Hoath, Martin, & Hutchings, 2010; Erni & Elabbadi, 2013; Zhang, Liu, Qi, Jiao, & Yuan, 2016

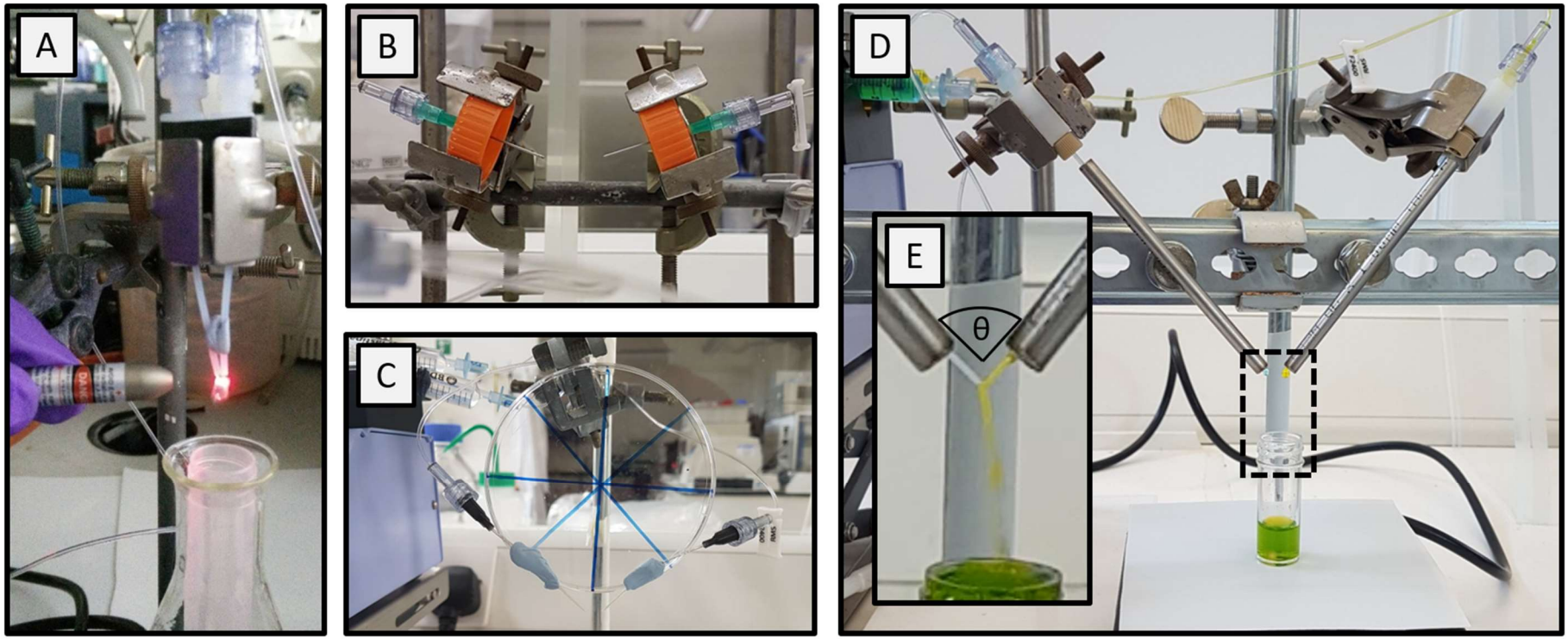

Figure 3.6 Iterative development of an impinging jet reactor. The first, basic mixing device (**A**) used PTFE tubing and blue-tac to induce mixing. Subsequent devices employed crimped steel (**B**) or PTFE needles (**C**) at greater, and adjustable impingement angles (θ). The most sophisticated manifold (**D** & inset **E**) used PTFE tubing sheathed in stainless steel tubes affixed to flat-head screws for convenient and accurate adjustment.

Synthetic parameters

As alluded to above, in the course of refining my impinging jet reactor I naturally explored a variety of variables to ascertain critical synthetic parameters and establish process limits and tolerances. Of the parameters I investigated, ultimately four proved significant: reactant concentration, flow-rate, impingement angle and dispersant choice.

At low concentration (metal[14] and phosphate feeds ≤12.5 mMol/L) and low flow rates (ea 1 mL/min), almost all (≥ 95 %) of the particles produced by the reactor fell within the target size range of 50–300 nm. At elevated (feed) concentrations, product particle sizes increased — shifting away from the optimum distribution (Figure 3.7). Due to the difficulty of isolating and analysing the size and dispersion of unadulterated ACP particles at point of precipitation, these data are by necessity collected for a given dispersant (in this case carboxymethylcellulose; CMC) and after a degree of processing (centrifugation and resuspension via ultrasonication). Consequently, it was difficult to determine whether the observed trends in product size were driven by the immediate precipitation conditions within the impinging jets (degree of supersaturation, available reaction mass, micromixing time etc) or by some down-stream factor such as a limitation in dispersant effectiveness (ie the CMC failing to quench secondary particle growth above a given mineral concentration or ionic strength).

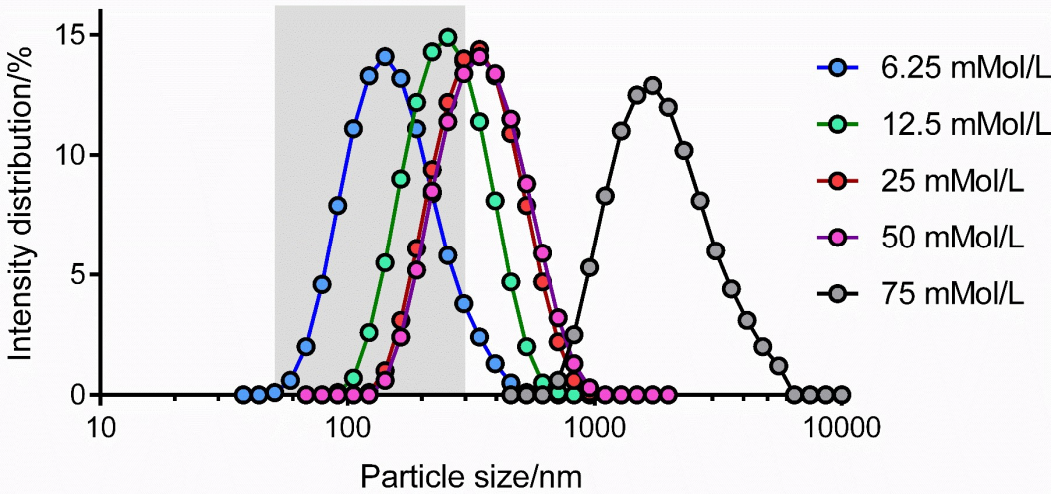

Figure 3.7 Particle size dependence upon reactant feed concentrations. Intensity weighted dynamic light scattering size distributions were obtained for ACP-CMC materials produced with reactant feeds (total metal = phosphate) ranging from 6.25 mMol/L to 75 mMol/L at flow rates of 1 mL/minute. Means of 3 measurements are presented without error bars for clarity.

[14] Calcium chloride and magnesium chloride, at a ratio of 4:1.

Identifying and resolving which aspects of the synthesis were acting as a bottleneck was critical to my goal of producing ACP colloids of suitable particle size and concentration for in vivo work. Accordingly, I attacked both stages of the process: investigating primary precipitation and secondary dispersion[15] conditions. I did this in concert — since either strand could inform or stymie the other — but for clarity I will present the work here in turn: starting with secondary parameters before returning to reactor conditions.

Secondary parameters

Although I experimented briefly with alternative collection (filtration) and redispersion (pipetting and manual percussion) methods, the principal focus of my secondary parameter studies was testing an array of potential dispersant species with the aim of determining which substance would most effectively stabilise ACP colloids under synthetic conditions.

Overall, I tested more than 30 candidate substances for dispersion efficacy, including molecules previously reported as ACP-stabilisers (such as casein phosphopeptides; Reynolds, 1997), others used generally to coat nanoparticles (eg tannic acid; Lin & Xing, 2008), and a few wild-cards with amenable chemistry (eg sodium tripolyphosphate; STPP). Given my previous partial successes with anionic polyelectrolytes[16], such as carboxymethylcellulose (CMC), these featured heavily. But I also considered cationic polymers (eg poly-l-lysine) and small charged species (eg citrate). The molecules tested, their outcomes and the rationale behind their testing are summarised in Table 3.2. Chemical structures of key dispersants are presented in Figure 3.8, and representative size distributions are displayed in Figure 3.9. Most candidates failed to produce disperse ACP particles, even at low reactor (calcium, magnesium and phosphate) concentrations, instead resulting in macroscopic or polydisperse products. A handful of substances were partial successes in that they either (i) produced disperse particles at low (feed) concentrations but failed at scale (50 mMol/L ion feeds being the benchmark), or (ii) yielded well sized colloids at scale but suffered significant size changes in simple alkaline solution within 2-3 hours, or (iii) were effective so far as they were tested but would be impractically expensive to use at scale (eg poly-l-glutamate, casein phosphopeptides). Ultimately, only three dispersants proved effective and appropriate for syntheses at higher scale: carboxymethylcellulose, quillaja saponin, and sodium tripolyphosphate.

[15] In this context, I refer to dispersion and secondary conditions in the sense of everything that happens to particles following their formation in the IJR: thus, their quenching by dispersant, isolation by centrifugation, and resuspension via ultrasonication.

[16] *"Macromolecules in which a substantial portion of the constitutional units contain ionic or ionizable groups"* (McNaught, Wilkinson and others, 1997).

As discussed previously (Chapter 1), colloidal stabilisation is usually accomplished via electrostatic or steric means. The latter is typically superior at engendering redispersion since the repulsive forces which mediate electrostatic stabilisation are prone to being overwhelmed by Van der Waals interaction energies if particles are forced into contact, whilst the entropic effects responsible for steric stabilisation are thermodynamic in nature (Morgan, Goff and Adair, 2011). In that context, the predominance of high molecular weight compounds amongst efficacious (and somewhat efficacious) dispersant species in my system was unsurprising. There were, however, a few unexpected results: (i) the failure of both polycationic compounds — poly-L-lysine (PLL) in particular. And (ii), the success of quillaja saponin (QS) and sodium tripolyphosphate (STPP) — two low molecular weight entities.

With regards to (i), PLL is widely used as an electrosteric dispersant (for instance, Hartono et al., 2012) and, below its' pKa (ca. pH 10; Hermans, 1966), it is essentially a cationic analogue of poly-L-glutamate (PLG). PLG was, at least partially, effective in my system. Effective steric stabilisation requires strong particle-polymer interactions — either in the form of covalent bonds or via specific adsorption (Caruso, 2003). I had previously determined that unadulterated ACP has a near neutral zeta potential (Appendix B; Figure B.1.4) and so expected similar outcomes with PLL and PLG. However, calculations by other workers indicate that ACP inner surface potentials are in fact highly negative but are well screened by counter ions (Habraken et al., 2013). If that is the case, it is feasible that polycations such as PLL would induce flocculation by effecting charge neutralisation and bridging between neighbouring ACP particles.

On the subject of (ii), the surprising effectiveness of QS and STPP; QS is a heterogenous mixture of glycosides comprised from the triterpene quillaic acid and various sugars, the major component has a reported molecular weight of only 1650 Da (Oakenfull and Sidhu, 1989; Mitra and Dungan, 1997). However, having both hydrophobic and hydrophilic moieties, in aqueous solution, QS molecules arrange into anionic micelles ~ 3.7 nm in size (Mitra and Dungan, 1997) and possibly form similar, larger, structures around ACP particles. STPP, on the other hand, is truly a small molecule — with no capacity for self-assembly. Comprising three phosphate groups, however, STPP must have (a) good affinity for calcium and (b) a significant negative potential under alkaline conditions, perhaps allowing it to stabilise ACP via surface potential alone.

Having, in this screening study, identified three effective dispersants (CMC, QS and STPP) of diverse chemistry, I thus proceeded with my primary parameter enquiries.

Table 3.2 A tabulated list of the dispersants tested in the impinging jet reactor, their outcomes, and the rationale for testing them. Checkmarks indicate effective dispersants likely to be of practical use whilst tildes indicate partial success or good performance but limited usefulness (ie due to reagent cost). Crosses denote failure.

Dispersant	Outcome	Rationale	Reference
LMW species			
Citric Acid	✗	GRAS ligand used to stabilise NPs	Bastús, Merkoçi, Piella, & Puntes, 2014
CTAB	✗	Artificial surfactant; used to stabilise ACP NPs	Welzel, Meyer-Zaika, & Epple, 2004
Gluconic Acid	✗	GRAS ligand used to stabilise NPs	Sun et al., 2009
Polysorbate 20	✗	Artificial surfactant; used in FBPI	FDA, 2019
Tripolyphosphate	✓	Inhibits mineral phase transformation of ACP	Root, 1990
TTAB	✗	Similar molecule to CTAB	N/A
Other natural products			
Arabic Gum	✗	PE stabiliser; used in FBPI	FDA, 2019
Locust Bean Gum	✗	As above	FDA, 2019
Quillaja Saponin	✓	Powerful natural surfactant	Mitra & Dungan, 1997
Tannic Acid	~	GRAS food ingredient, used to stabilise NPs	Lin & Xing, 2008
Peptides, polypeptides and proteins			
Poly-**a**spartic acid	~	PE; interacts with calcium phosphates	Krogstad, Wang, & Lin-Gibson, 2017
Bovine Serum Albumin	~	Stabilised ACP particles in section 3.2.1	N/A
Casein	✗	Contains peptides used to stabilise ACP NPs	Reynolds, 1997
beta-Casein	✗	As above	Reynolds, 1997
Casein phosphopeptides	~	Used to stabilise ACP NPs	Reynolds, 1997
L-Glutamic Acid	✗	To compare monomer/polymer efficacy	N/A
Poly-L-**G**lutamic Acid	~	PE; L-glu is the most abundant residue of OVA	Nisbet et al, 1981
L-Lysine	✗	To compare monomer/polymer efficacy	N/A
Poly-L-**L**ysine	✗	PE, used to stabilise NPs	Babič et al, 2008

Table 3.2 (continued)

Ovalbumin	~	Stabilised ACP in section 3.2.1	N/A
Zein	✗	Used to prepare nano-vehicles	Zhong & Jin, 2009
*Poly**s**accharides*			
Alginic Acid	✗	PE; used in FBPI and to prepare NPs	Kim & Lee, 2010
Carrageenan (κ, ι, λ)	✗	As above	Kim & Lee, 2010; Tye, 1989
Carboxymethylcellulose	✓	PE; stabilises ACP NPs	Peetsch et al., 2013
Chitosan	✗	PE stabiliser; used to prepare NPs	Twu, Chen, & Shih, 2008
Pectin	✗	PE stabiliser; used in FBPI	FDA, 2019
Synthetic polymers			
Poly**a**crylic acid	✗	PE used to stabilise $CaCO_3$ NPs	Cai, Zhao, Wang, & Yu, 2010
Poly**e**thyleneglycol	✗	GRAS polymer, used to stabilise NPs	Jokerst, Lobovkina, Zare, & Gambhir, 2011

ACP = Amorphous calcium phosphate, CTAB = Cetrimonium bromide, FBPI = Food, beverage and pharmaceutical industries, GRAS = Generally recognised as safe, LMW = Low molecular weight, NPs = Nanoparticles, OVA = Ovalbumin, PE = Polyelectrolyte, TTAB = Tetradecyltrimethylammonium bromide

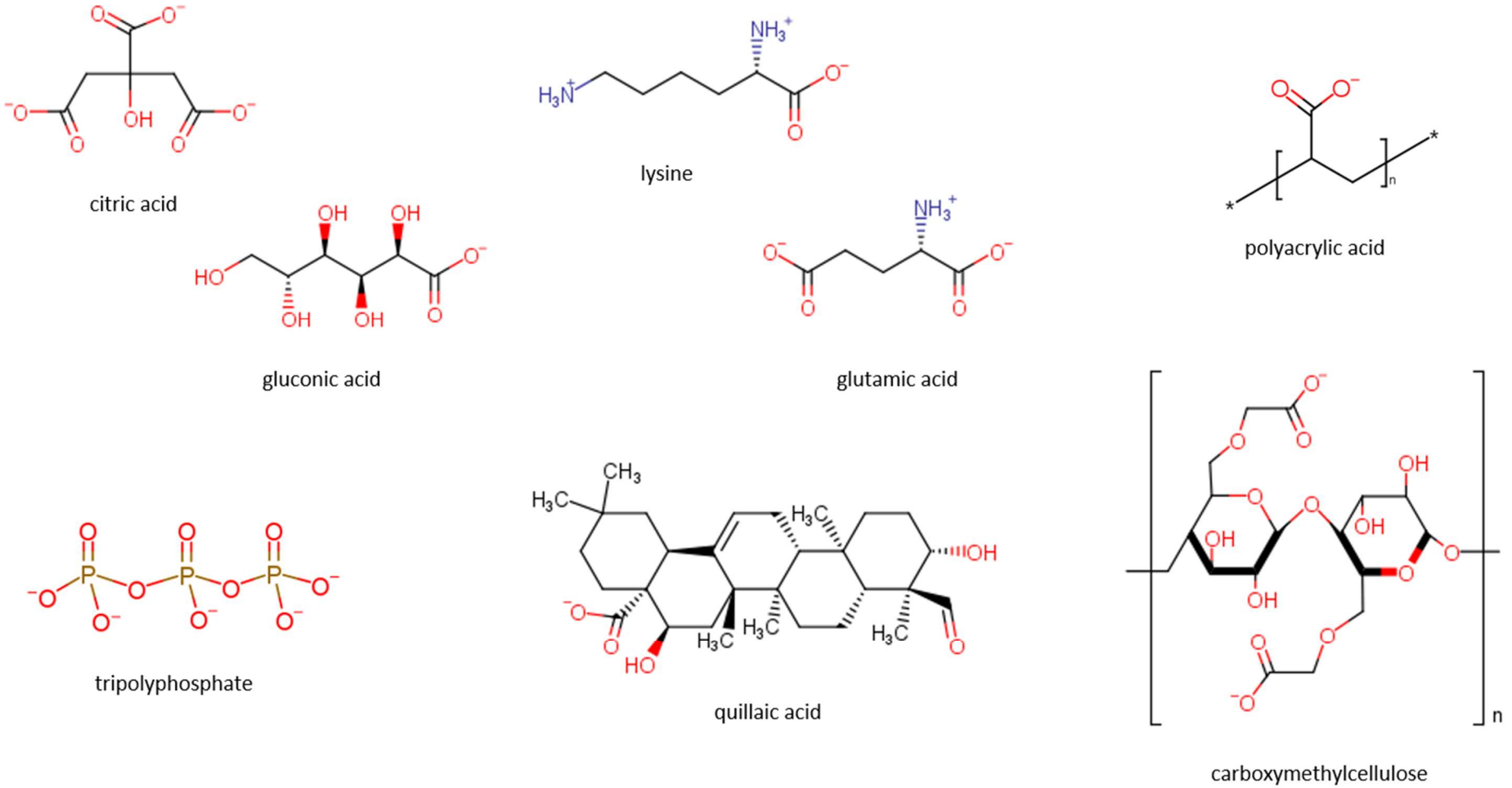

Figure 3.8 Skeletal structural formulae for selected dispersants from the list in Table 3.2, including representations of the three effective dispersants: (sodium) tripolyphosphate, quillaic acid (a key component of quillaja saponin), and carboxymethylcellulose. Carboxylate and amino groups are shown in their deprotonated and protonated forms respectively.

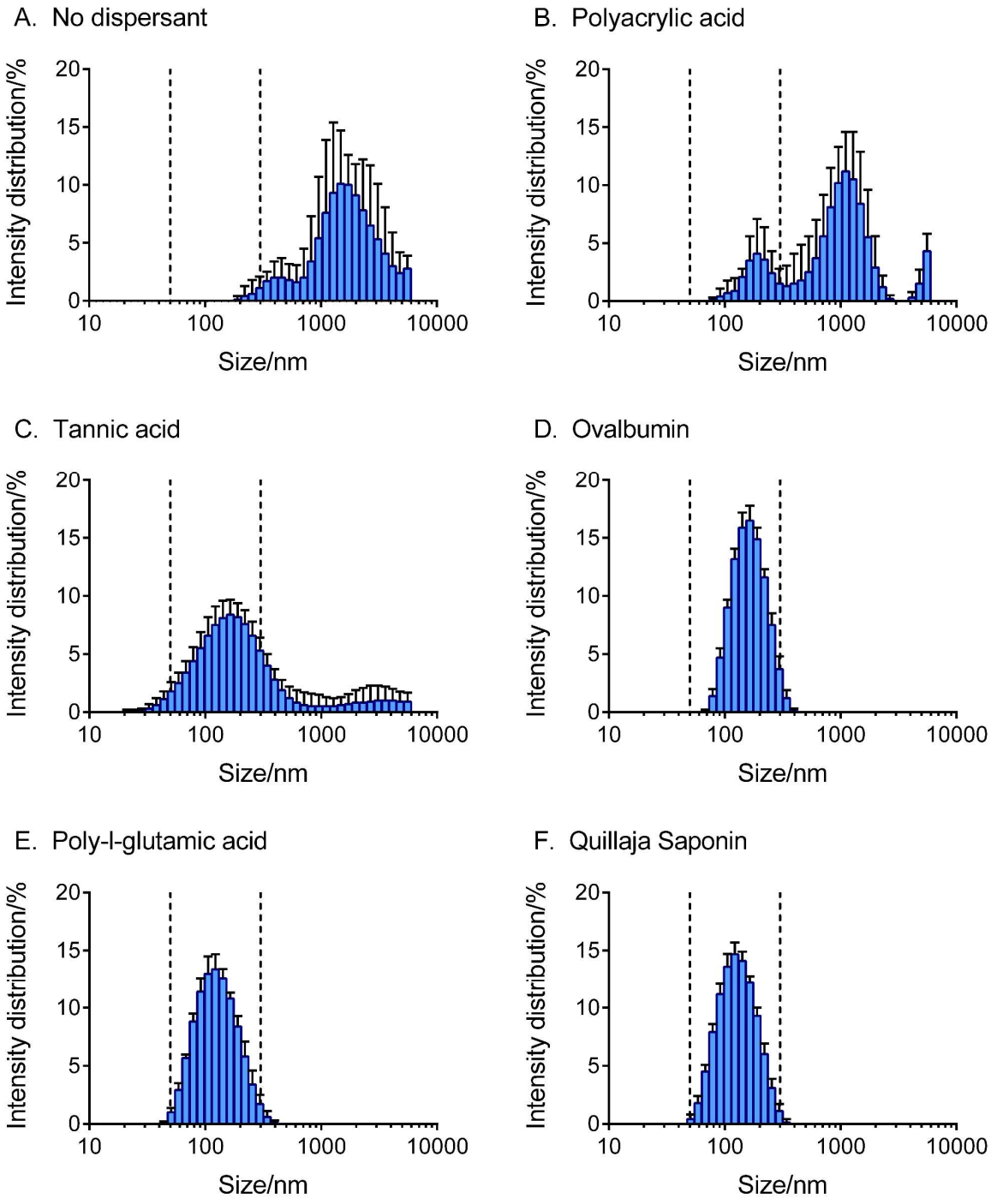

Figure 3.9 Example size distributions for ACP materials produced by impinging jet reactor. Unfunctionalised particles (**A**) in comparison with the target size bracket (50-300 nm, dashed lines) and colloids modified with ineffective (**B** & **C**), semi-effective (**D**) and effective dispersants (**E** & **F**). Dynamic light scattering (DLS) size results are presented as intensity distribution means and single standard deviations from 6 runs of 12 measurements on each material — after centrifugation and attempted resuspension in pH 9 water at original concentration.

Primary precipitation parameters

Previous studies employing confined impinging jet reactors to produce polymeric nanoparticles found that, within bounds, particle size was highly dependent upon the characteristic mixing time (τ) — which varied inversely to the three halves power of jet velocity (Johnson and Prud'homme, 2003). For a fixed nozzle width, jet velocity is approximately proportional to volumetric flow rate, thus I began my precipitation parameter studies by conducting syntheses at incrementally increased reactant fluid-stream flow rates in the hope that this would lead to smaller products. Usefully, this proved so. Increasing flow rates led to smaller products and narrower distributions (Figure 3.10), compensating somewhat for the effect of concentration; although even at 20 mL/min, materials made with 50 mMol/L reactant feeds were still larger than their slow-flow low concentration counterparts.

I carried out these experiments with both carboxymethylcellulose (CMC; Figure 3.10a-b) and quillaja saponin (QS; Figure 3.10c-d) as dispersants. In both cases log-log plots of flow rate vs size evinced a power-law relationship. Interestingly the best-fit exponents were quite different, with quillaja saponin stabilised materials appearing to exhibit greater size-sensitivity. This may have resulted from a disparity in dispersant properties since 90 kDa CMC is almost 200-fold larger and much more viscous than quillaic acid, or it could be a consequence of methodological differences. In the first set of experiments, with CMC, my DLS method utilised automatic instrument optimisation of measurement parameters such as position, attenuation and duration. In general this approach is preferable, since for any given material it provides the best chance of the instrument obtaining a viable measurement. However, variation in these settings can also skew results. Thus, for a set of closely related materials, fixed parameter methods can offer better trend sensitivity. Accordingly, I employed a method of this sort in the second set of experiments, with quillaja saponin, and the resultant data did show lower variability — noticeable in the log-log plots (Figure 3.10b&d). In either case (regarding the origin of the exponent difference between the two data-sets) my suspicion is that the flow-rate size-response captured in Figure 3.10b is a closer approximation of the true reactor/reaction dynamics. Importantly, synthetic yield (conversion to ACP) was equivalent at flow rates of 1 mL/minute and 20 mL/minute, being in all cases above 95% for calcium and magnesium and above 60% for phosphate.

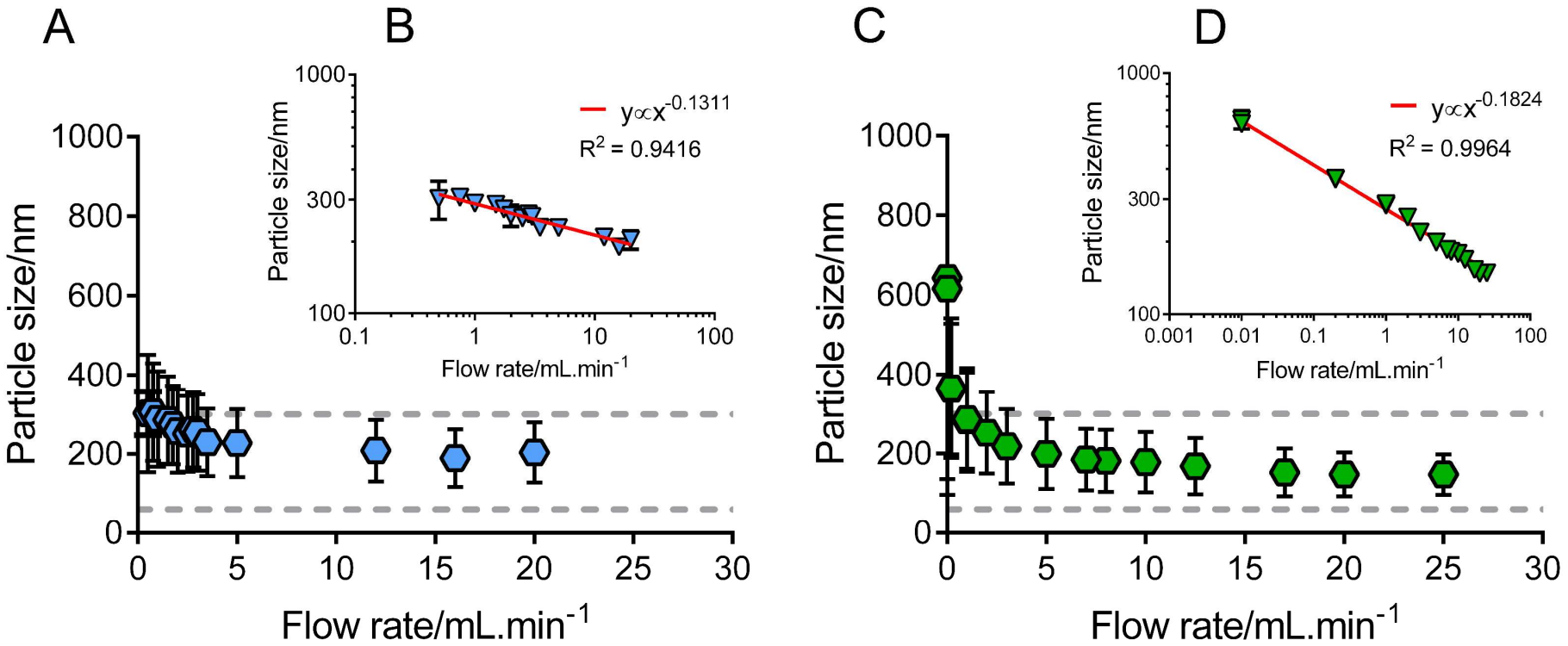

Figure 3.10 Particle size vs reactant flow rates for CMC and QS stabilised ACP nanoparticles. Z-average means from three measurements are presented for 14 and 17 independent syntheses using CMC (**A** & **B**) and quillaja saponin respectively (**C** & **D**). Each point represents a single synthesis. Both data sets (CMC and quillaja saponin) are displayed on linear-linear (**A** & **C**) axis plots and duplicated in the log-log (**B** & **D**) insets. Grey dashed lines in the linear plots indicate the target size range (50 – 300 nm). Log-log best fit lines are displayed in red. Linear plot (**A** & **C**) error bars indicate estimated distribution widths calculated from z-average and cumulant PdI values according to (σ = PdI^2/z-average^2). In contrast, error bars in the log-log insets (**B** & **D**) give z-average error as 1 SD of mean (z-average) values. The two data-sets were collected with different DLS methods. Each CMC material z-average measurement comprised 11 runs with automatically instrument adjusted duration, attenuator, and measurement position. Quillaja saponin material data was obtained with a customised DLS method utilising 9 runs of 7 seconds per measurement, a position of 4.65 mm and an attenuator of 4. Syntheses were carried out with 50 mMol/L reagent feeds ($CaCl_2$, Na_2HPO_4) and 1% (w/w) dispersant, all at pH 9 with 100 mMol/L tris buffer. Impingement angle was ~ 110°.

Further to jet velocity, impinging jet reactor micromixing is greatly influenced by (jet) impingement angle (θ). As intimated earlier, optimal results are attained by minimising mixing zone width without compromising jet coalescence and this break point is contingent upon system-specific variables such as, ia, fluid viscosity, and jet velocity (Erni and Elabbadi, 2013). Nonetheless, several authors have reported good results with θ of ca. 120° (Li and Ashgriz, 2006; Kumar, Prasad and Kulkarni, 2013). My first reactor (Figure 3.6a) had a fixed impingement angle of ~ 10° so upon producing an adjustable device (Figure 3.6b) I immediately explored larger values. Impingement angles were estimated with a standard protractor and, due to the limited accuracy, substantial steps (ca. 50°) were used. My findings accorded with the literature results, with product particle size distributions minimised for θ ~ 110° (Figure 3.11), where efficient (and rapid) micromixing would be expected. Indeed, operating the reactor at that theta value, with 20 mL/min flow rates and sodium tripolyphosphate (STPP) as a dispersant, yielded perfectly sized products at reactor (feed) concentrations of 100 mMol/L (with respect to metal and phosphate), which is a roughly 10 fold increase relative to the process reported by Peetsch et al (2013). Moreover, upon isolation via centrifugation these materials could be re-dispersed in a quarter of their original volume to yield dispersions at concentrations greater than 1% (w/v).

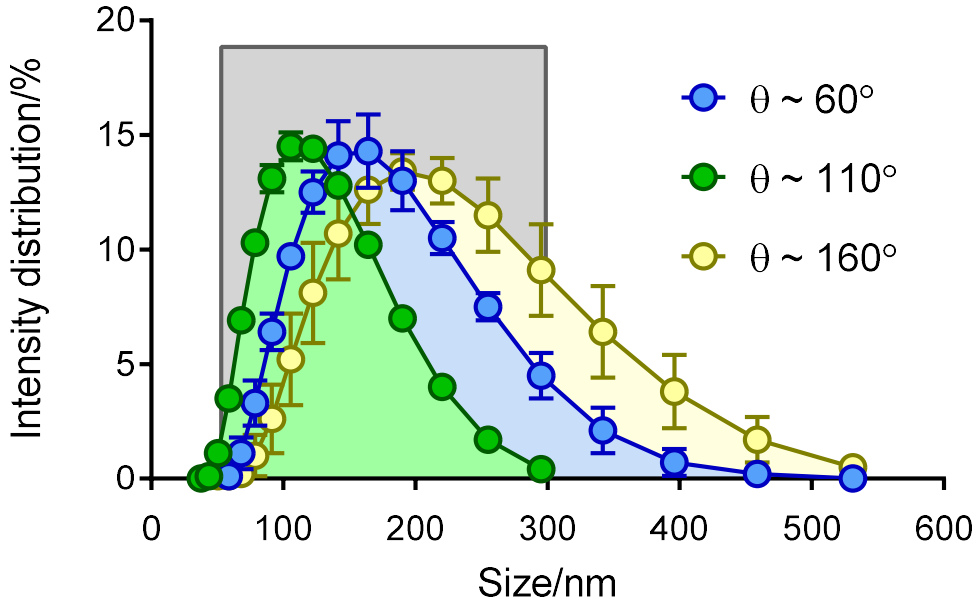

Figure 3.11 The impact of jet impingement angle upon particle size distribution for tripolyphosphate stabilised ACP particles. DLS intensity statistics: mean and standard deviation are presented for 6 measurements of 12 runs for each material with automatic instrument optimisation of attenuator and measurement position. Syntheses were carried out with 20 mL/min flow rates using 100 mMol/L reagent feeds ($CaCl_2$, Na_2HPO_4) and 1% (w/w) dispersant. All solutions were maintained at pH 9 with 150 mMol/L tris buffer.

3.3 Conclusion

In this chapter, a variety of simple 'bucket chemistry' approaches to co-precipitating ACP particles were explored. One-step dispersant-templated syntheses yielded disperse nanoparticles at low concentration, but the raw products could not be isolated and then resuspended afterwards. This was partially resolved by adopting a sequential co-precipitation method from which the products were re-suspendable. However, this approach was also constrained to low process concentrations, and ultimately, batch methods proved inadequate to the task.

Eventually, an impinging jet reactor was developed and found to be an effective route to ACP nanoparticles. Indeed, the above process represents a significant improvement in practicality with respect to the art on ACP colloid synthesis. Moreover, as a case study, it demonstrates proof of principle suitability of unconfined impinging jet reactors for disperse nano/micro-particle production in general. Further work is warranted; numerous improvements suggest themselves, for instance: (i) micromixing would likely be improved with better jet alignment (reducing asymmetry), and (ii) pumping dispersant solution into the lower reservoir simultaneously with the reactants (rather than using a fixed volume of dispersant) would ensure a constant particle:dispersant ratio throughout the synthesis — improving product homogeneity, reducing the risk of late-stage aggregation and potentially allowing higher reactant concentrations and/or lower dispersant volumes to be used. Finally, (iii) undoubtedly, there exist more effective dispersants than those I have tested and — given the critical importance of surface chemistry in mediating particle behaviour — these are worth seeking.

Nonetheless, within the context and resource of my project, products from the partially optimised IJR process outlined above appeared fit-for-purpose when combined with carboxymethylcellulose, quillaja saponin or sodium tripolyphosphate (STPP). Accordingly, I attempted to confirm and compare suitability of these three dispersants via in vitro studies and physicochemical characterisation, as described in the next chapter.

3.4 Materials and methods

Methodologies used in this chapter fall roughly into two groupings: fundamental analytical techniques (for instance dynamic light scattering) and syntheses. For convenience, commonly applicable details for the fundamental techniques are presented first, in alphabetical (technique) order. Synthesis methods are listed subsequently, in order of their appearance in the results and discussion.

Except where otherwise noted all chemicals were obtained from Sigma Aldrich. Adapters and connectors for the fluidics apparatus were obtained from Thames Restek. Freedom Tubing was obtained from RMS Medical Products, PTFE needles were obtained from Adhesive Dispensing, all other tubing and the syringes were obtained from VWR. Ultrasonication was carried out with a Microson XL2000 (Misonix Ltd, Farmingdale, New York).

3.4.1 Dynamic Light Scattering (DLS)

DLS measurements were performed with a Zetasizer Nano ZSP (Malvern Instruments Limited). using Dispersion Technology Software 7.11. 400 µL sample volumes were analysed in disposable polystyrene cuvettes (VWR). In the absence of reliable optical property data for ACP, literature values for hydroxapatite were used: refractive index 1.65, absorbance 0.01. The medium was water, with a refractive index of 1.33 and a viscosity of 1.0031 cP. Measurements were carried out at 20°C, with a brief period of thermal equilibrium (1-2 minutes) prior to measurement, and at a scattering angle of 173°. Measurement position and attenuation factor were automatically optimised by the instrument to minimise secondary scattering and maintain photon counts within the linear range of the detector (100 – 500 kcps). Three to six measurements of at least 10 runs (each of at least 10 seconds) were performed on each sample, with the number of runs and the run duration automatically chosen by the instrument software. The in-build general purpose model was used for data processing. Results were then reported as means ± one standard deviation from measurement replicates .

There were a number of occassions where the method deviated from the above. **Firstly**, in the tissue culture media co-precipitation experiment in which particle size was changing over time, measurements were made as usual but the data are presented as individual measurements rather than average values. **Secondly**, in the study of unmodified ACP's growth and aggregation kinetics, which required rapid measurements, there was no thermal equilibration and each measurement consisted of two runs of 10 seconds at a measurement position of 4.65 mm and with an attenuator factor of 10. Parameters were otherwise as above. Data are presented as single measurements.

Thirdly, in the flow-rate vs particle size experiments carried out with quillaja saponin stabilised ACP nanoparticles, measurement position was manually fixed at 4.65 mm and the attenuation factor was set to four. Parameters were otherwise as above, data are presented as means ± one standard deviation from measurement replicates .

3.4.2 Fourier-transform infrared spectroscopy (FTIR)

FTIR spectra were collected with a Shimadzu IRPrestige-21 FTIR Spectrophotometer equipped with a Golden Gate single reflection diamond ATR accessory (Specac, Orpington, UK) from 500 to 5000 cm^{-1} at a resolution of 1 cm^{-1}. Spectra were subsequently smoothed in MATLAB by applying a second-order Savitsky Golay filter to data frames of length 35.

3.4.3 Inductively coupled plasma — optical emission spectrometry (ICP-OES)

Elemental analyses were carried by ICP-OES (Jobin Yvon Horiba Ultima 2C; Instrument SA, Longjumeau, France), equipped with a concentric nebulizer and cyclonic spray chamber. Plasma gas flow rate was 10 mL/min and sample flow rate was 1 mL/min. Triplicate measurements were made for each sample and means and standard deviations calculated from these. Window size was 0.08 nm (0.04 nm either side of the peak). There were 15 increments per profile and each increment had an integration time of 0.5 seconds. Prior to analysis, samples were diluted down to (analyte) concentrations below 10 mg/L in 5% HNO_3 (v/v). Multi-element calibration standards (50 µg/L to 10 mg/L calcium and phosphorus; 25 µg/L to 5 mg/L magnesium) were also prepared in 5% HNO_3. See Figure 3.12 for an example standard curve. Quantification was carried out using the lines tabulated below (Table 3.3). To convert measured phosphorus concentrations to phosphate 'amounts', for instance in mass balance calculations, the phosphorus mass was multiplied by the phosphorus:phosphate molar mass ratio.

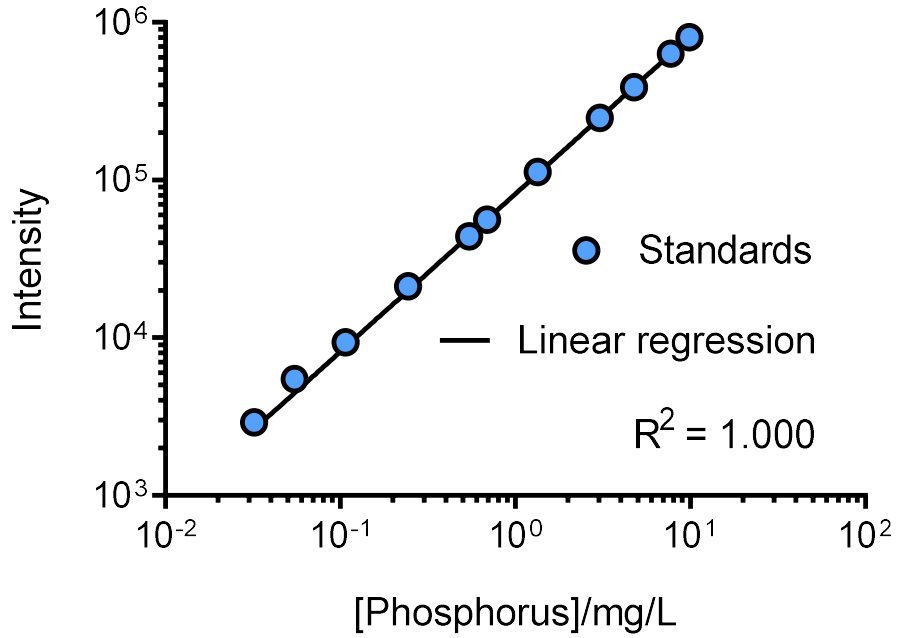

Figure 3.12 An example ICP-OES calibration curve with multielement standards in 5% HNO_3. Emission intensity at the 177.49 nm phosphorus line has a linear response to concentration in the 50 µg/L to 10 mg/L concentration range.

Table 3.3 ICP elemental emission lines and estimated detection limits from the literature. Reproduced from chapter 2.

Analyte	Line/nm	Detection limit/µg/L	Reference
Calcium	396.847	0.5	Winge, Peterson and Fassel, 1979
Phosphorus	177.49	200	Nollet and De Gelder, 2013
Magnesium	279.079	30	Winge, Peterson and Fassel, 1979

3.4.4 Mie scattering calculations

Mie theory calculated scattering profiles for 1-200 nm particles were produced with Malvern's scattering function utility, embedded within the freely available Zetasizer family software (v 7.13). Zetasizer measurement conditions were used in the calculations to ensure applicability of the results. Thus, the scattering angle was set to 175°, the radiation wavelength (λ) to 633 nm, the medium refractive index to that of water at that wavelength (1.33). Particle refractive indexes were varied between 1.35 and 1.65 as described in the text; the imaginary quotient was kept as 0.01 throughout.

3.4.5 UV-Vis

Calcein incorporation was assayed using a Fujitsu Fluostar Omega plate reader. Particles containing calcein were measured for fluorescence intensity with an excitation wavelength of 485 nm and an

emission wavelength of 520 nm. Calcein incorporation yields were determined by interpolating a linear regression between matrix matched standards prepared by dilution of the same calcein-phosphate stock used to prepare the particles (Figure 3.13). Each sample and standard was analysed in duplicate wells and the mean values were used.

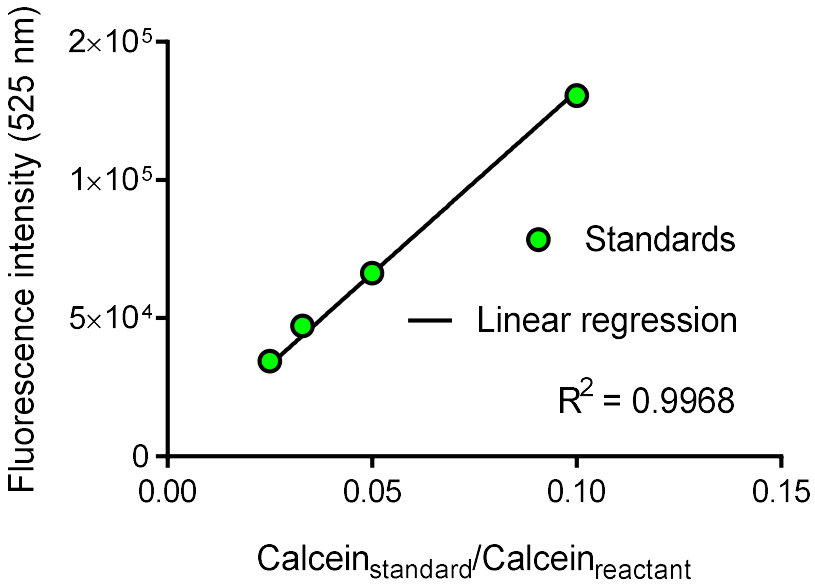

Figure 3.13 An example UV-vis calibration curve with matrix-matched calcein standards

3.4.6 Pele co-precipitation

A previously reported (Pele *et al.*, 2015) method of calcium phosphate co-precipitation in tissue culture media was carried out with several modifications: the 20 x 10^{-3} mol/L calcium stock was prepared directly in sterile saline and 0.2 µm filtered once, and the reaction was carried out at room temperature in air rather than at 37 °C. Thus, the method in brief: a 20 x 10^{-3} mol/L calcium (chloride, dihydrate) solution was prepared in sterile saline and then 0.2 µm filtered. Replete tissue culture medium was prepared by adding 10% heat inactivated fetal calf serum [PAA], 2 x 10^{-3} mol/L L-glutamine, 100 µ/ml penicillin and 100 µg/mL streptomycin to RPMI 1640 media (contains 6.7 x 10^{-3} mol/L $H_xPO_4^{x-3-}$ as purchased) and then 0.45 µm sterile filtering. 2.5 mL portions of calcium saline were then added to polypropylene tubes, each containing 10 mL of replete TCM, resulting in final concentrations of 4 x 10^{-3} mol/L Ca^{2+} and 5.4 x 10^{-3} mol/L $H_xPO_4^{x-3-}$. Solutions were then incubated at room temperature. One aliquot was transferred to the NanoZSP for in situ sizing measurements over time. To collect particles for mineral phase determination, samples were ultracentrifuged at 17 000 g for 30 minutes, washed with acetone twice, dried under vacuum and then kept at -80°C.

DLS data (size metrics and derived count rates) from the tissue culture media co-precipitation experiment were plotted against reaction time in Prism 6 (Graphpad Software) and fitted with a single phase association function of the form

$$y = y_0 + (Plateau - y_0)(1 - e^{-Kx})$$

Where y_0 was constrained to 0 and plateau values were set to the mean of the final six values in each series. K was unconstrained.

3.4.7 Single-step co-precipitation

Simplified single-step co-precipitations were carried out by mixing tris-buffered, pH matched, metal (calcium and magnesium chloride) and phosphate (sodium phosphate) solutions at room temperature in the presence of polyelectrolyte dispersants. Tris-HCl was dissolved in UHP water and pH adjusted with 5 Mol/L NaOH such that the final Tris concentration was 50 mMol/L. These buffer stocks were subsequently used to prepare all other solutions. Metal stocks were prepared by dissolving calcium chloride and magnesium chloride in tris buffer at Ca:Mg molar ratios of 10:1 or 4:1 and at total (metal ion) concentrations of 8.8 mMol/L to 20 mMol/L. Phosphate stocks were prepared by dissolving monosodium phosphate and disodium phosphate in tris buffer at a ratio of 1:4 (pH 7.4 stocks) or using disodium phosphate alone (pH 9 stocks). Phosphate stocks were made up at concentrations of 6 mMol/L to 20 mMol/L. The dispersants were always added to the phosphate stocks — to avoid calcium chelation. The protein dispersants (bovine serum albumin and ovalbumin) were simply added to the phosphate stocks in small portions with gentle mixing via a magnetic stirrer. Carboxymethylcellulose was more challenging to add to solution — to avoid clumping, small portions had to be added with mixing from an overhead stirrer (Stuart SS10, fitted with four blade propeller). When cargo was used it was also always added to the phosphate solution: calcein was used at a 1:100 calcein:calcium molar ratio. Reactions were carried out by adding metal stock solution (5 mL) to phosphate-dispersant stock solution (5 mL) with mixing. 1 mL aliquots were centrifuged at 16000 g for 5 minutes and re-dispersed at original volume in UHP or pH 9 water using ultrasonication (Microson XL2000; Misonix Inc., Farmingdale, New York). Particle sizing measurements were carried out directly and upon re-dispersed materials. ICP was carried out on re-dispersed materials for yield calculations. UV-vis was used to quantify calcein incorporation.

3.4.8 Stepwise co-precipitation

To probe the aggregation dynamics of dispersant-free ACP, I mixed 5 mL of 12 mMol/L phosphate stock with 5 mL of 20 mMol/L calcium-magnesium (4:1) chloride stock and immediately diluted the resulting solution 10-fold. An aliquot was analysed via dynamic light scattering with a custom method as described above. All solutions were at pH 9 and tris-buffered (50 mMol/L) and were prepared as per the single-step co-precipitation solutions.

3.4.9 Confined flow syntheses

A previously reported continuous flow device (Peetsch *et al.*, 2013) for preparing nanodisperse ACP particles was reproduced (Figure 3.5a, page 59) with minor modification: equipment limitations meant that flow rates had to be reduced by 48%. To compensate for this (and ensure flow velocity remained high, narrower tubing was used (1.6 mm internal diameter instead of 2.54). However, due to the exponential relationship between diameter and area, the narrower bore tubing resulted in a 33% higher flow speed (relative to the published synthesis) and so tubing lengths had to be extended by 33% to maintain equal hydrodynamic residence times. Thus, the method was as follows: 6 mMol/L calcium nitrate and 3.6 mMol/L ammonium phosphate solutions were made up in UHP, adjusted to pH 9 with concentrated ammonium hydroxide and loaded (separately) into two 20 mL syringes. 2 g L^{-1} CMC solution was also made up in UHP and adjusted to pH 9 and loaded into a second pair of 20 mL syringes. The calcium and phosphate syringes were placed side-by-side on a Harvard Apparatus Elite 11 syringe pump and connected to Y-mixer A by two 50 mm lengths of 1.6 mm internal diameter PTFE tubing. The two CMC syringes were loaded onto two separate Grady syringe pumps and connected to Y mixer B by another two 50 mm lengths of tubing. The outflows of Y mixers A and B were then connected by Y mixer C, with tubing intervals of 65 mm between A and C and 20 mm between B and C. From the outflow of Y mixer C, a final section of 400 mm of tubing fed into a plastic beaker where product was collected. The calcium and phosphate solutions were pumped at flow speeds of 13 mL.min^{-1} each, giving a hydrodynamic residence time of 0.3 seconds between Y mixers A and C. The CMC solutions were each pumped at 3.33 mL.min^{-1} giving a combined outflow (from Y mixer B) of 6.5 mL.min^{-1}. Pumping two CMC solutions in tandem was necessary because the maximum flow rate for the Grady syringe pumps was 200 mL/hour, and 390 mL/hour was required. Collected product was centrifuged at 16000 g for 5 minutes and then re-suspended by ultrasonication (Microson XL2000; Misonix Ltd, Farmingdale, New York). Note that, for clarity, Y-mixer B is not represented in Figure 3.5a, rather the CMC source is depicted as a single syringe. Thus, in the schematic, only Y mixers A and C are shown.

3.4.10 Unconfined jet reactor syntheses

The general form for the unconfined jet reactor was as depicted in Figure 3.5b (page 59). The first iteration of this reactor was fabricated as follows. Freedom 2400 medical grade tubing (RMS Medical Products) was used to connect BD plastipak luer-lok syringes with female luer 1/4-28 male Tefzel adapters. These were embedded into two parallel Tefzel 1/4-28 x 1/4-28 unions. Each union fed a 50 mm length of 1/16 inch PTFE tubing oriented vertically downwards. The union-tubing joints were simply flangeless 1/8 PEEK nuts with flangeless 1/16 ferrules. PTFE tubing was cut with scalpel blades to avoid deforming it and the ends were carefully aligned such that they were never in contact but emerging fluid streams would merge before plunging into a vessel containing dispersant solution to quench particle growth. The second iteration of the unconfined jet reactor used Freedom 2400 medical grade tubing to connect BD plastipak luer-lok syringes directly to crimped stainless steel needles (22 gauge). In the third iteration of the unconfined jet reactor, PTFE needles (Adhesive Dispensing; 22 gauge) were used. Nozzles were oriented 10 cm (vertically) above dispersant reservoirs. A Harvard Apparatus Elite 11 syringe pump was used throughout. Metal and phosphate solutions were prepared as outlined in the single step co-precipitation methods, but at concentrations of up to 100 mMol/L. Reactant stoichiometry was kept at 8Ca:2Mg:10P. Solutions were buffered with tris at twice their phosphate or metal concentration (ie for a 50 mMol/L synthesis, 100 mMol tris was used) except for syntheses carried out with 100 mMol/L reactant feeds where the concentration of tris was 150 mMol/L. Dispersant solutions were buffered to the same extent. The volume ratio between metal, phosphate and dispersant solutions was always 1:1:2. To remove excess polymer and cargo, initial products were centrifuged at 17000 g for 10 minutes and resuspended via ultrasonication (Microson XL2000; Misonix Ltd, Farmingdale, New York).

Chapter 4 Physicochemical and *in vitro* characterisation

4.1 Introduction

The previous chapter details the development of a method for producing functionalised ACP colloids at useful concentrations. During process development, three lead dispersants had emerged as apparently potent stabilisers — namely quillaja saponin, carboxymethylcellulose, and sodium tripolyphosphate. In this chapter I describe the physiochemical and *in vitro* characterisation of materials produced using those promising dispersants. There were two aspects to this characterisation. (i) I needed to confirm that the general synthetic method (employing the impinging jet reactor) resulted in products of suitable particle size and mineral phase, and further, was amenable to cargo incorporation. (ii) I also needed to establish the dispersion stability of the variously functionalised materials in physiological and complex media and to assess their relative effectiveness at in vitro cargo delivery. The overall aim was to generate results that would enable a good judgement of which, if any, of the materials would be suitable for further work with regards to formulation and in vivo testing. Note that the electron microscopy analyses presented in this chapter were performed by Dr Andy Brown and the plunge-freezing of samples by Dr Nicole Hondow, both at the Leeds Electron Microscopy and Spectroscopy Centre. The python script to calculate the resolvent kernel used in centrifugal size analysis was written by Mr Stephen Farr of the Theoretical Condensed Matter group at the Cavendish Laboratory. Cell culture was performed by Dr Rachel Hewitt, and immunohistochemistry and confocal microscopy by Dr Jack Robertson.

4.2 Results and discussion[17]

4.2.1 Size stability and surface charge in simple solutions

Particle size results presented in the previous chapter were carried out under conditions of synthetic rather than physiological relevance — ie they were made in pH 9 water. Thus, prior to undertaking detailed characterisation via time consuming methods, I began by quickly testing particle size and size stability under neutral conditions. Carboxymethylcellulose (CMC) and quillaja saponin (QS) stabilised materials remained disperse, and in the nano to sub-micron size range for at least a day in water (Figure 4.1a-b) and at least 2 hours in high ionic strength solutions (Figure 4.1c). Unfortunately, however, sodium tripolyphosphate (STPP) functionalised materials aggregated instantly upon exposure to a simple pH 7 tris-buffered solution (Appendix C; Figure C.1.1). Although I was unable to obtain confirmatory zeta-potential data for STPP materials in neutral solution, I believe this collapse in dispersibility was driven by a loss of negative surface potential due to polyphosphate protonation. Two of tripolyphosphate's hydroxyl groups (one on either terminal phosphate group) have pKa's between pH 7 and 8, leading to lower charge microspecies predominating under neutral conditions (Figure 4.2). In contrast, zeta-potential measurements with carboxymethylcellulose and quillaja saponin were stable from pH 5 to pH 9 (Figure 4.3), allowing them to consistently impart stability via electrostatic repulsion, in addition to other (previously discussed) effects.

Whilst polyelectrolytes have numerous advantages as dispersants, they can complicate analysis. Dynamic light scattering determines particle size based upon Brownian motion and conveys little structural or compositional information. As such, it struggles to discriminate between particles and agglomerates of polymer. To ensure my particle sizing data for CMC and QS materials corresponded to 'actual' ACP particle populations and not dispersant-based-artefacts, work with complementary techniques was necessary. Transmission electron microscopy (TEM) was the obvious starting point, since, in combination with its integrated techniques, it is uniquely well suited to detailed nanoparticle characterisation — offering near simultaneous information on particle size, shape, structure, and composition.

[17] Materials and methods for this chapter can be found from page 102

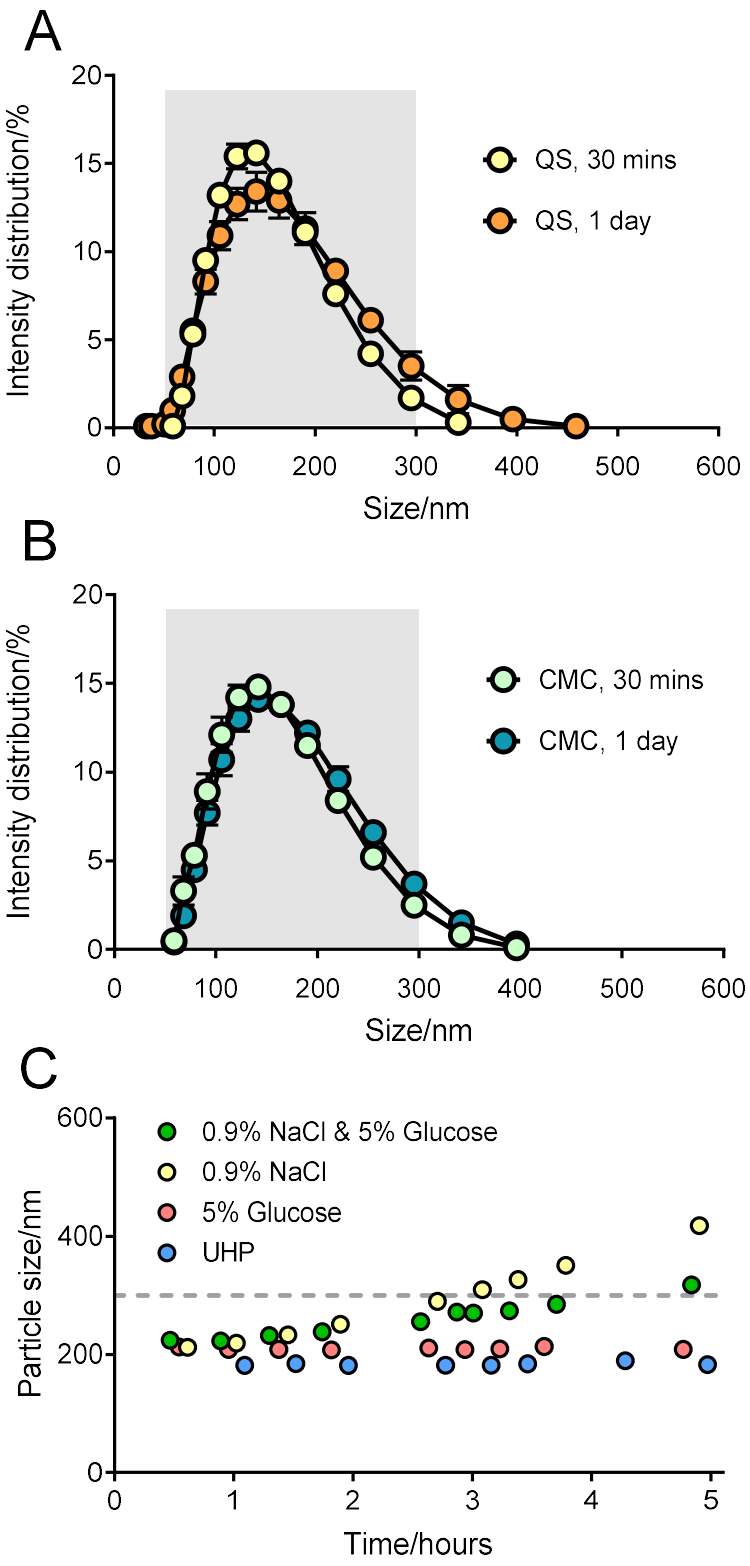

Figure 4.1 Particle size stability of ACP colloids in simple, pH neutral solutions as determined by dynamic light scattering: (**A**) quillaja saponin and (**B**) carboxymethylcellulose (CMC) functionalised particles in UHP water, and (**C**) CMC-ACP particles in high ionic strength solutions. Means and standard deviations from three measurements are shown for intenstity weighted statistics (**A**-**B**) and z-averages (**C**).

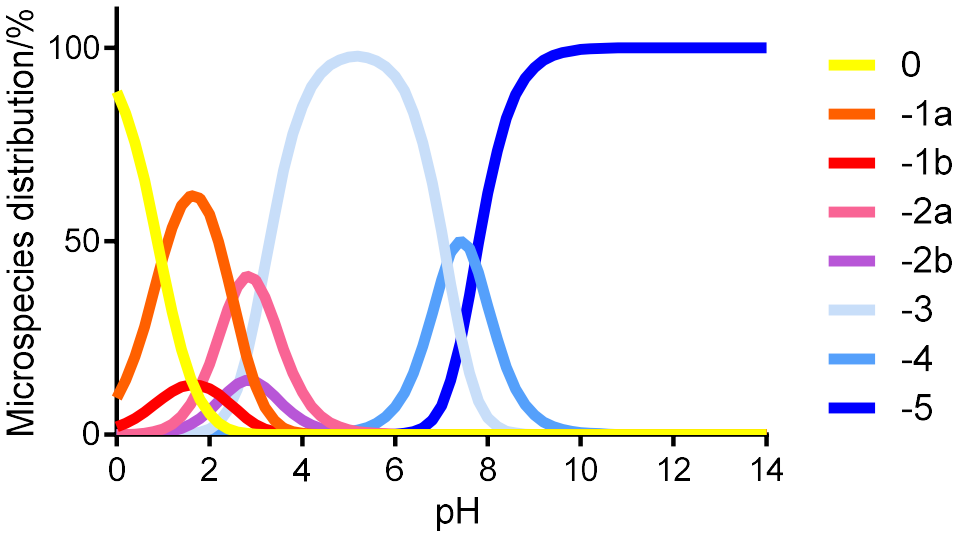

Figure 4.2 Calculated microspecies charge distributions for tripolyphosphate $[P_3O_{10}]^{-5}$ as a function of pH. Charge differences result from varying deprotonation; tautomers are denoted with letters (a or b) in the legend, see Figure 4.16 for structural representations of the microspecies. Calculations were done at 298 K in 0.2 pH unit increments.

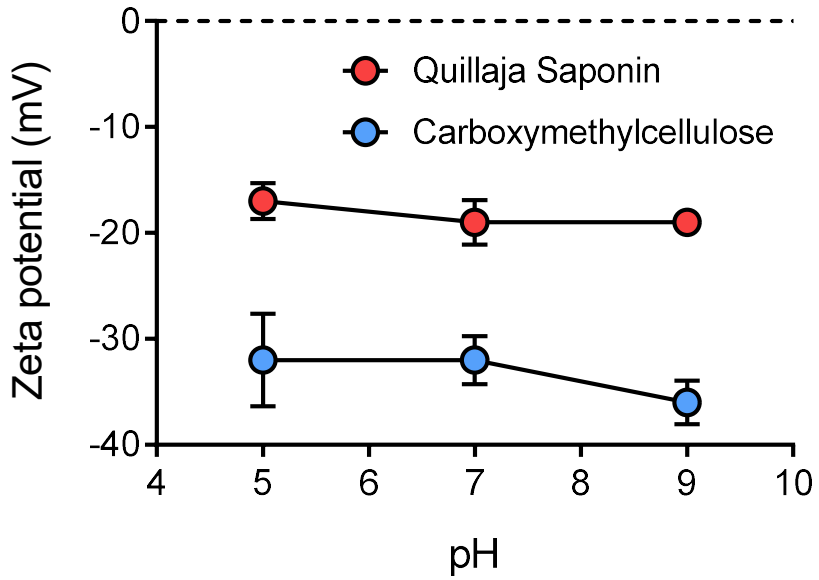

Figure 4.3 Laser doppler velocimetry derived zeta-potentials for 1% (w/w) aqueous dispersant solutions in the absence of ACP. Mean ± standard deviations are presented for three measurements, each comprising 10-100 runs.

4.2.2 Transmission electron microscopy

Transmission electron microscopy (TEM) images obtained on drop cast samples of freshly synthesised quillaja saponin (QS) stabilised ACP revealed a pearl-chain fractal-like structure of agglomerated ~20 nm spheroids, enveloped in a low contrast layer (Figure 4.4). This pearl-chain configuration matches the reported structure of ACP_1 (Abbona and Baronnet, 1996) and, importantly, electron diffraction (Figure 4.4, upper inset) confirmed amorphousness. Porosity, apparent in the dark field images (Figure 4.4, lower inset), was artefactual — induced by beam damage during imaging. Energy dispersive X-ray spectroscopy (EDX) confirmed that the core structures were comprised of calcium phosphate, whilst the outer layer (presumably the organic dispersant) was carbon rich (Figure 4.5).

Size analysis was carried out by converting the individual ACP particles into masks that DigitalMicrograph could assign dimensions to (Figure 4.17, page 105). From a modest dataset of 59 particles, mean length and breadth were 139 ± 78 nm and 72 ± 39 nm. Dynamic light scattering (DLS) on an aliquot of the same material sample yielded a Dn(10)[18] of 57 ± 8 nm and Dn(90) of 117 ± 13 nm. Within the limitations of comparing an in-solution hydrodynamic diameter averaging technique with a 2-dimensional vacuum-based per-particle technique, I consider these data to accord well. And although image analysis in electron microscopy is notoriously sensitive to user judgement, for these images it was generally easy to determine independent particles by spatial separation. As a result, I was confident that the DLS datasets for quillaja saponin stabilised materials corresponded to coated mineral particle populations and not clumps of dispersant.

Electron microscopy of carboxymethylcellulose (CMC) stabilised ACP materials was more awkward. Few particles could be discerned in drop-cast samples, despite glow-discharge treating the holey carbon grids (necessary for retention of hydrophilic particles). The particles that could be seen were too few in number for sensible quantitative analysis but appeared to be of approximately the right size — if perhaps more polydisperse than their QS counterparts (Figure 4.6). The apparent polydispersity may, however, have been an artefact of preparation (ie drop-casting and drying) so we conducted an adjunct experiment using an alternative preparation method: plunge-freezing. In this approach, a small volume (3.5 µL) of aqueous sample is pipetted onto a glow-discharged grid, blotted and rapidly immersed in liquid ethane. Freezing is sufficiently rapid that water vitrifies —

[18] Particle size data by number distribution, which is the closest comparator to electron microscopy data (since it is also number based). Dn(10) and Dn(90) denote, respectively, the diameters corresponding to 10% and 90% of the cumulative undersize particle size distribution (by number) — thus 80% of the distribution fall between the Dn(10) and Dn(90) values.

arresting molecular motion and preserving the dispersion state of any particles in solution (White, Walker and Trinick, 1998; Hondow *et al.*, 2012). Glassy water is subsequently removed by vacuum, leaving — in theory — pristine colloids on dry grids. Two samples of each QS-ACP and CMC-ACP were processed by plunge-freezing and subsequently imaged by TEM. In these image sets, both materials appeared to be disperse and of similar particle size and morphology (Figure 4.7) which was encouraging and sufficient confirmation that my previous datasets obtained via DLS did indeed correspond to populations of disperse ACP_1 particles (and not macromolecule agglomerations). Furthermore, examination of aged CMC-ACP dispersions revealed a surprising resilience to mineral phase transformation: after 1 week in solution (pH 9 water) the particles retained their amorphousness (Appendix C; Figure C.2.1), which was indicative of surface passivation — a phenomenon that has previously been reported for ACP when functionalised with other polyelectrolytes (Bar-Yosef Ofir *et al.*, 2004).

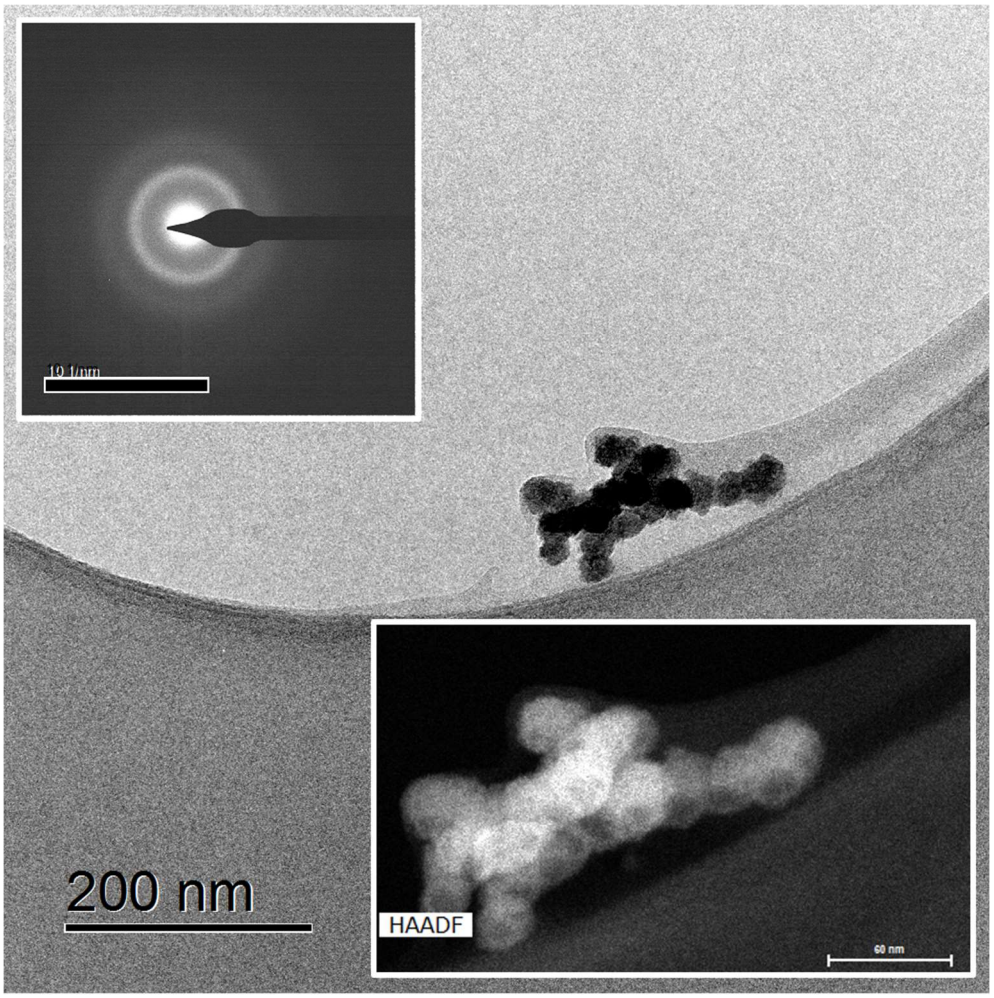

Figure 4.4 Characterisation of quillaja saponin stabilised ACP via transmission electron microscopy and electron diffraction. Bright field (main; scale bar 200 nm) and dark-field STEM (lower inset; scale bar 60 nm) images and an electron diffraction pattern (upper inset; scale bar 10 nm^{-1}) are shown for the same particle from a drop-cast sample.

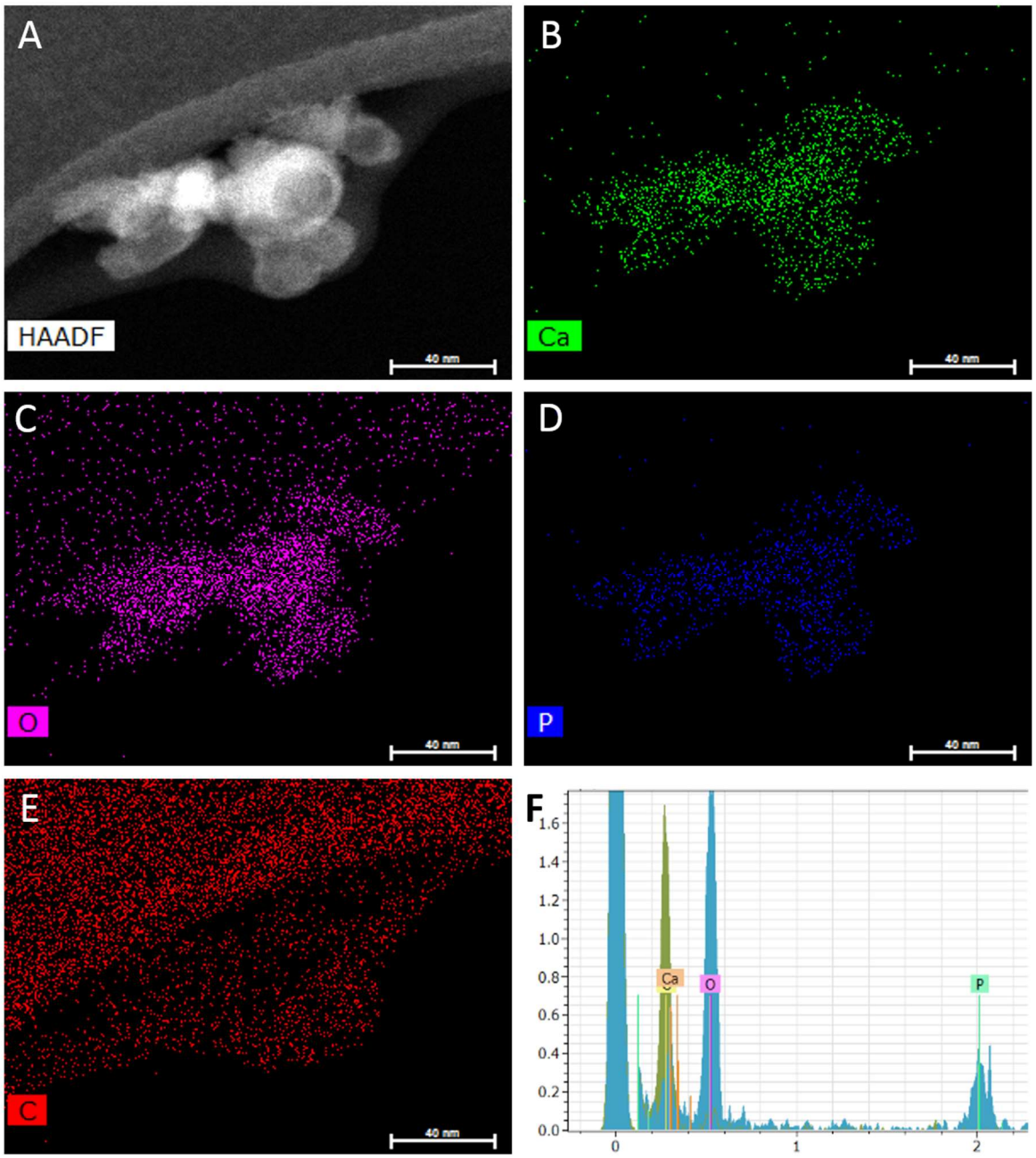

Figure 4.5 Characterisation of quillaja saponin stabilised ACP via scanning transmission electron microscopy and energy dispersive X-ray spectroscopy. A single particle is shown in dark field (**A**) alongside accompanying EDX maps (**B-E**), and spectra (**F**), detailing chemical composition for the same area. The spatial distributions of calcium (**B**), oxygen (**C**) and phosphate (**D**) are concordant with the high contrast regions of the dark field image (**A**), which are certainly ACP mineral. Carbon (**E**) is more widely spread (the holey film is unsurprisingly rich) but, upon inspection, aligns very well with the low-contrast layer in the dark field image.

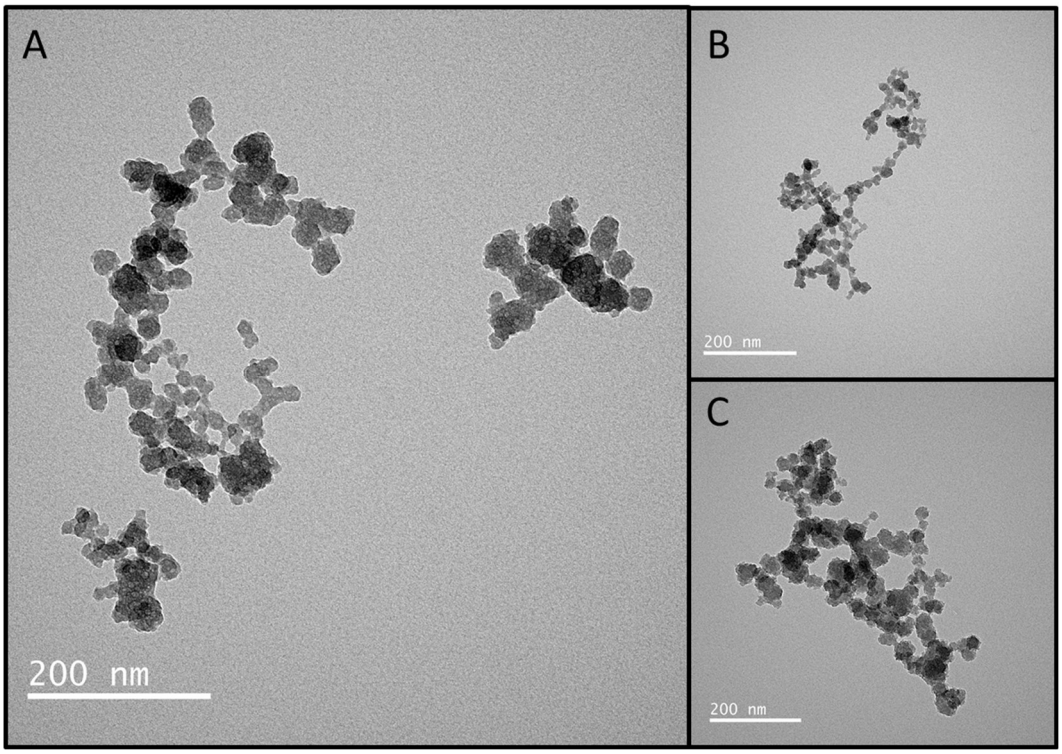

Figure 4.6 Transmission electron microscopy images of drop cast CMC-ACP particles. All scale bars are 200 nm.

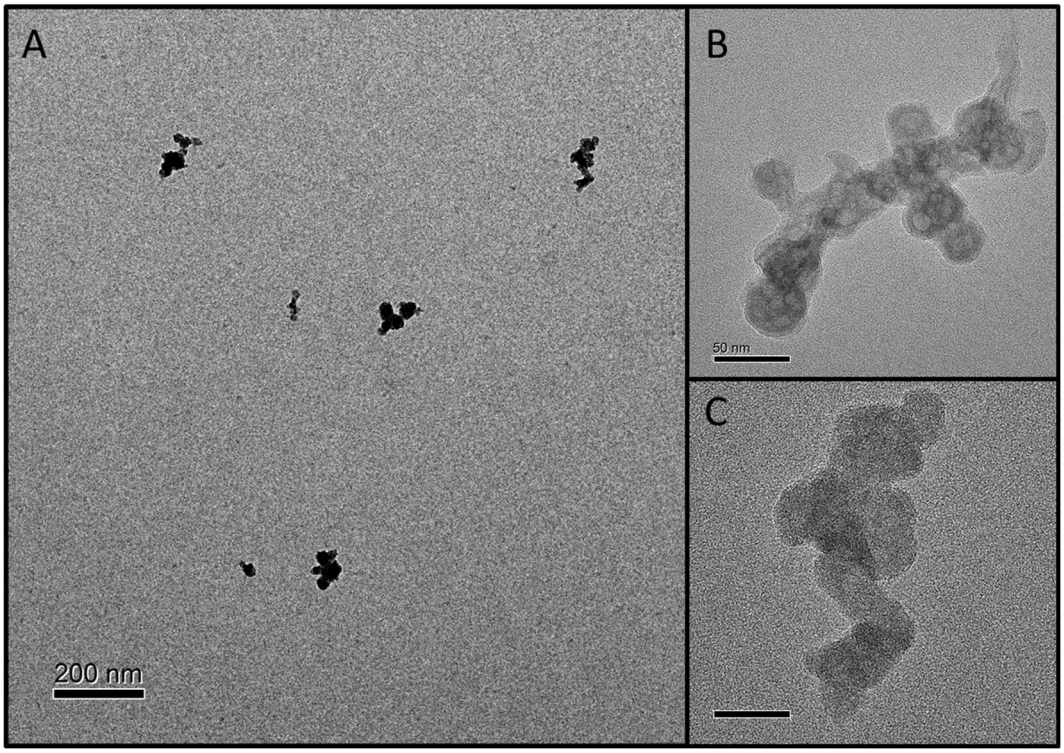

Figure 4.7 Transmission electron microscopy images of plunge frozen ACP particles functionalised with carboxymethycellulose (**A** & **B**) and quillaja saponin (**C**). The scale bar for **A** is 200 nm; the bars in **B** and **C** are 50 nm.

4.2.3 Particle sizing in complex media

Having confirmed that the putative ACP colloids produced in the previous chapter were indeed amorphous calcium phosphate particles, my next task was to ascertain the dispersion state of the materials in complex solutions, namely tissue culture media (TCM) and simulated intestinal fluid (SIF). Neither transmission electron microscopy nor dynamic light scattering were especially well suited to this work — the former due to its high skill threshold and expense and low throughput, the latter due to muddling of analyte signal by contributions from other insoluble components (eg proteins). Indeed, *in situ* particle size analyses in complex fluids are notoriously challenging. For simplicity's sake I resolved to employ a separation technique (to fractionate samples based on particle size) in conjunction with inductively coupled plasma optical emission spectroscopy (ICP-OES) to quantify the mineral concentration in each fraction.

Of all the particle size separation techniques that exist, three types are used most widely: filtration, chromatography, and sedimentation. I ruled out chromatography as too finickity and experimented briefly with filtration, having poor results (Appendix C; Figure C.3.1), before turning to sedimentation. Sedimentation methods are themselves a broad and varied group of techniques, but all operate on the general principal that — ceteris paribus — the settling velocity of a particle in a fluid of different density is approximately proportional to the square of the radius, as described by Stokes' Law (2).

$$V = \frac{(p - \sigma)gD^2}{\eta} \tag{2}$$

Where V is the particle velocity, p is the density of the particle, σ the density of the fluid, η the viscosity of the fluid, g the acceleration of gravity and D the diameter of the particle. Density, viscosity, and gravitation are typically fixed parameters for a given experiment, thus if the settling speed of a particle is known, the equation can simply be rearranged to yield the Stokes' diameter. Although Stokes' Law has largely been superseded in modern techniques by more sophisticated expressions such as the Lamm equation, under certain conditions it has predictive power for micron and sub-micron particle sedimentation (Slater and Cohen, 1962; Allen, 1997) and its calculations are not computationally expensive. Moreover, high performance methods such as analytical ultracentrifugation and analytical differential centrifugal sedimentation require specialised and expensive equipment and typically employ density gradients and/or line-start sample introduction (Laue, 1996; Bernhardt, 2000). I wanted a means of assaying homogenous fluids with minimal

perturbation (to best capture the *in-situ* dispersion state) and my method needed to work with a desktop centrifuge.

For method development and validation, I used a simple particle standard: commercial tricalcium phosphate powder, nominally of 100 to 200 nm in size. Dispersion of the powder in UHP water and removal of agglomerates yielded a stable dispersion whose particles were of comparable size to the ACP colloids produced earlier (Figure 4.8a). Centrifuging small (1 mL) aliquots of this dispersion at different speeds and analysing supernatants via ICP-OES resulted in a recovery curve (Figure 4.8b). From this curve, the limits of the particle size distribution could be approximated simply by solving Stokes' Law at two points: one near the origin and another at the start of the plateau. Determining the shape of the particle size distribution was more complex; fortunately Kamack (1972) has reported an integral equation (Equation 4, page 109) that relates sediment weight recovery curves to underlying particle size distributions and I used this to calculate the cumulative undersize distribution (Figure 4.8c). Differentiation of the cumulative distribution yielded the discrete particle distribution (Figure 4.8d). Despite the simple (physical) basis for my approach, DLS and sedimentation derived size distributions for tricalcium phosphate accorded fairly well — although there was some divergence in the upper tails of the peaks. Broadening of the upper range of the sedimentation distribution indicates that experimental settling was faster than predicted by the model for some particles. This mismatch was likely a result of either (i) settling enhancement via hydrodynamic interactions between neighbouring particles (Allen, 1997), (ii) agglomeration of colliding particles during centrifugation (Bernhardt, 2000), or (iii) deviation from the spherical morphology assumed by Stokes' Law — since fractal bodies settle more rapidly than their equivalent spheres (P. Johnson, Li and E. Logan, 1996). Other factors, such as (a) neglecting Brownian motion (most relevant to the settling of small particles) and (b) my use of cylindrical rather than sector shaped vessels, would have acted in opposition — inducing overestimation of settling velocities (Bernhardt, 2000) and thus shifting the sedimentation distribution to smaller sizes. Clearly these competing distortions balanced out well for tricalcium phosphate particles in the lower half of the size distribution but did so less well in the upper range. Nevertheless, concordance between the datasets was, on the whole, good.

Accordingly, I sought to apply the same methodology to ACP colloids in various media. Unfortunately, whilst doing so I encountered issues with quillaja saponin: despite a consistent supplier and specification, batch to batch performance variability became significant. Some batches failed to produce disperse ACP particles at all, whilst others gave only temporary stabilisation (Appendix C; Figure C.3.2). Differences appeared to be somewhat related to saponin content but

were not predictable. Given the importance of reliability to my future in vivo work and to the project goal of producing useful research tools, I discontinued work with quillaja saponin and proceeded solely with carboxymethylcellulose (CMC).

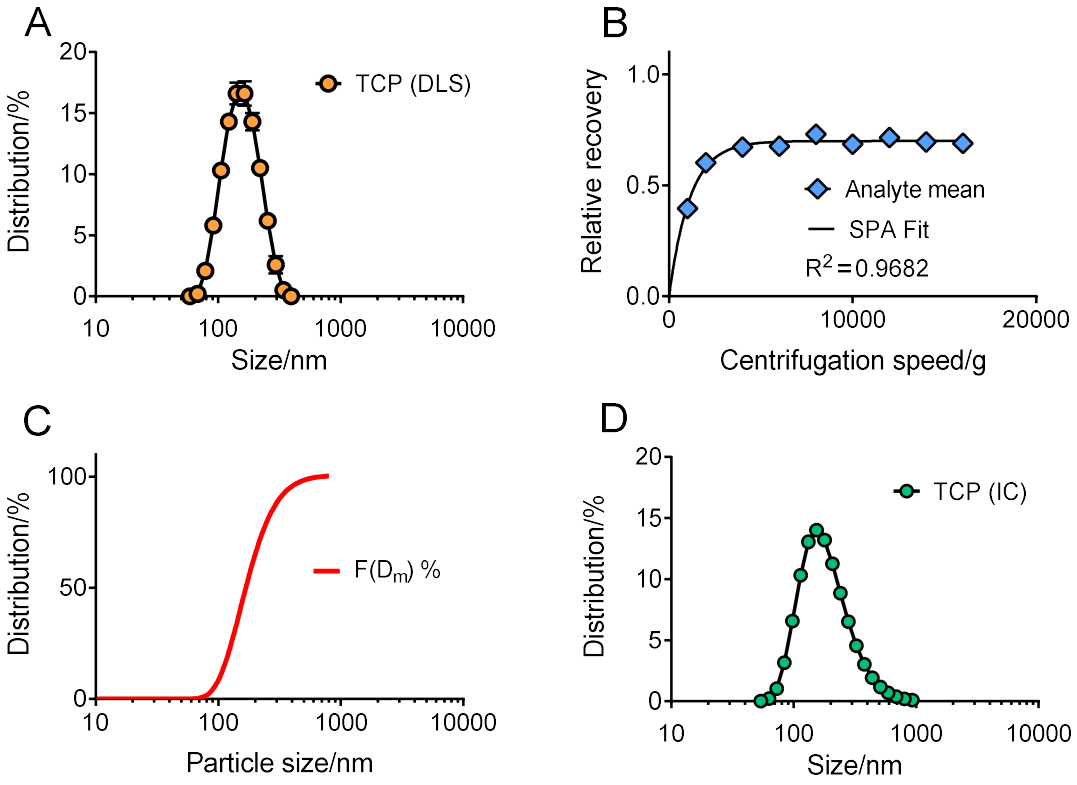

Figure 4.8 Particle sizing of a tricalcium phosphate dispersion via dynamic light scattering (**A**) and cumulative integral centrifugation(**B**-**D**). Centrifugal particle recovery was quantified by ICP-OES (**B**) and processed into a cumulative undersize distribution (**C**) via Kamack's solution. From this, the discrete distribution (**D**) was obtained via differentiation.

I used a range of suspension media for the CMC-ACP colloid centrifugation assays (Figure 4.9), beginning simply with a suspension in pH 9 water (Figure 4.9a-c). This ensured particle stability and allowed me to validate the sedimentation size data via DLS (Figure 4.9a). As in the tricalcium phosphate assays, the sedimentation size distribution exhibited more skewness than its analogous DLS data set. However, curiously, relative broadening was lower here (than for tricalcium phosphate) and agreement (between the DLS and sedimentation distributions) was better. Considering the probable, previously enumerated, sources of distribution broadening, these ACP particles were (a) fractal-like in morphology and (b) assayed at an equivalent solid suspension loading (w/w) to the tricalcium phosphate. Inter-particle hydrodynamic settling enhancement is concentration dependent (Allen, 1997) so if it were occurring in these assays one would expect its

effects to be of a similar magnitude in both the TCP and ACP systems. Consequently, the improved error balancing seen in with the latter materials is suggestive of carboxymethylcellulose playing a role. This might be by (i) preventing mid-assay particle agglomeration (were that the primary driver of velocity underestimation in the tricalcium phosphate assays), or, more speculatively, (ii) increasing the drag coefficient of settling particles.

In any event, accordance between the initial DLS and sedimentation data was good, so I proceeded to assay ACP colloids in complex media — namely tissue culture media (Figure 4.9d-f) and simulated intestinal fluid (Figure 4.9g-i). For reasons given earlier, I could not obtain corroborative *in situ* DLS data for these assays but did so on parallel samples (ie from the same syntheses) to at least ensure that the initial products were suitable. Relative to pH 9 (Figure 4.9b), ACP recovery curves in tissue culture media (Figure 4.9e) and simulated intestinal fluid (Figure 4.9h) had shallower gradients, and neither reached a stable plateau. This translated into a broadening of the particle size distributions at their lower limits (Figure 4.9f&i) which was probably driven by dissolution and reprecipitation of (protein and CMC stabilised) ACP due to the lower pH — which was 7.4 in both tissue culture media (TCM) and simulated intestinal fluid (SIF). Encouragingly, there was no discernible agglomeration in either medium despite the relatively high ionic strength of the assay solutions.

It might be noted here that, thus far, all the suspensions assayed by this method have comprised (or seemed to comprise) disperse nano to sub-micron sized particles — agglomerated particles have not been purposely measured during method validation nor detected in 'live' assays. As a corollary, at this stage, it has not been demonstrated that the assay actually discriminates between suspensions of disperse nanoparticles on one hand, and suspensions of large agglomerates on the other hand. This was addressed naturally by assays I carried out whilst developing formulations for in vivo ACP delivery and, for narrative reasons, is presented in the next chapter (see Figure 5.9, page 126).

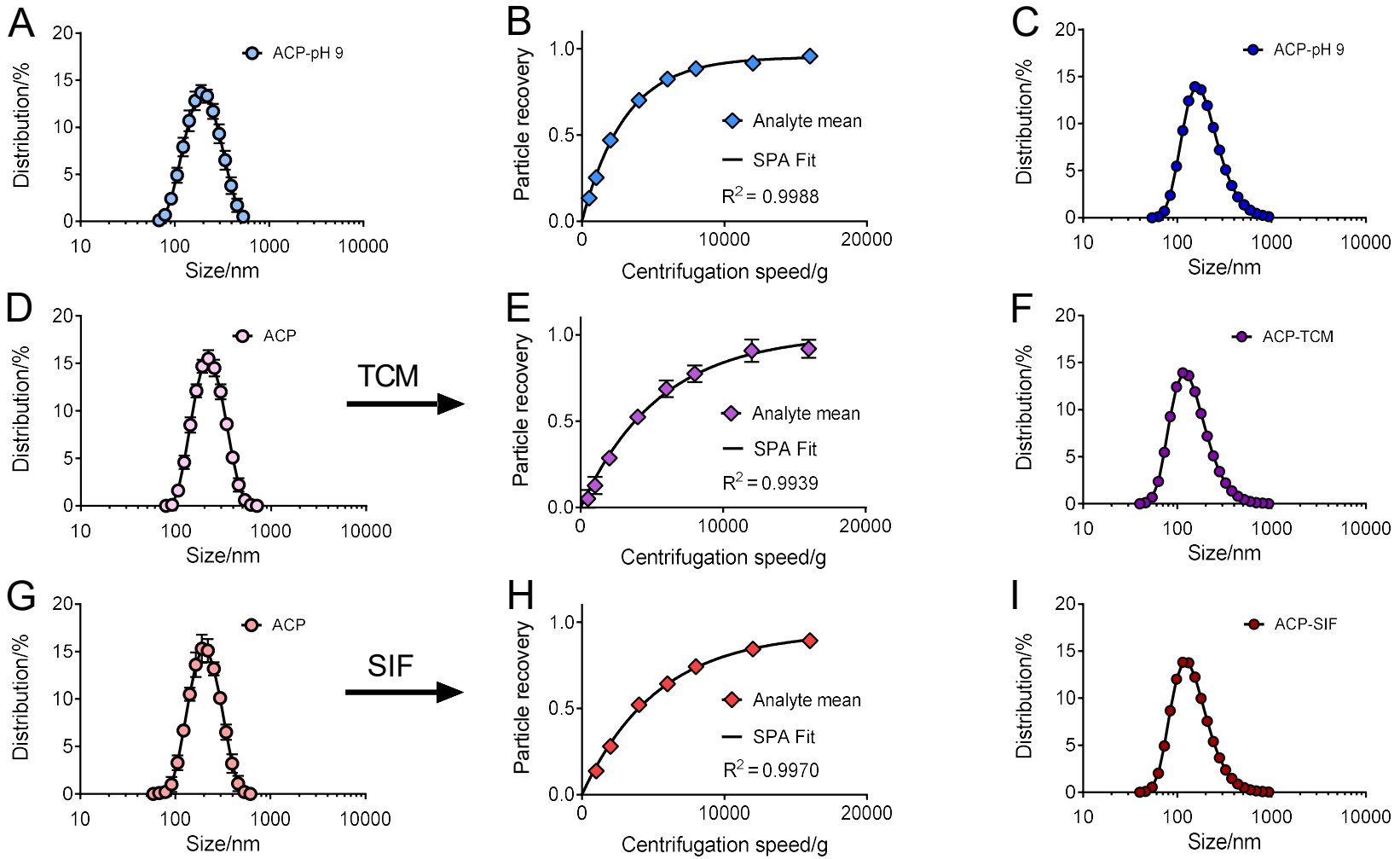

Figure 4.9 Particle sizing of CMC-ACP colloids by dynamic light scattering and integral centrifugation. Reference DLS size data (**A**) was obtained for particles in pH 9 water, upon centrifugation their recovery curve (**B**) was processed into size results (**C**). Subsequent stability assays employed tissue culture media (**D-F**) and simulated intestinal fluid (**G-I**). DLS data shown in **D** & **G** were obtained in pH 9 water — rather than assay buffer.

After finding that the dispersion stability of CMC-ACP particles was robust to physiological solution compositions at neutral and alkaline conditions, I next considered particle behaviour at a greater variety of pHs. I did this by suspending ACP colloids in an alkaline (pH ~9) version of simulated intestinal fluid and titrating with dilute HCl down to pH ~5, generating a supraphysiological (intestinal) pH range. I took aliquots at regular intervals and, to speciate them efficiently, used a simplified centrifugation method. In this basic method, only two sedimentation conditions were employed: (i) a low speed run (5 minutes at 300 g) to sediment large agglomerates whilst minimising nanoparticle recovery, and (ii) an aggressive regime (10 minutes at 16000 g) to recover all the particulate material present. Fractionation was then estimated by difference. As expected, under alkaline and neutral conditions the nanoparticulate fraction predominated (Figure 4.10a). At lower pHs, progressive solubilisation ensued (Figure 4.10b) but, importantly, there was never any appreciable macroscopic (> 1 μm) material (Figure 4.10c).

As discussed in previous chapters, pH sensitive dissolution is a largely unavoidable characteristic of ACP as a mineral; as a feature it is a double-edged sword: it ensures non-persistence and thus tolerance in biological settings, but simultaneously constrains material utility and suitability for certain applications. For the particular application of oral delivery of biomolecular cargo, ACP's acid solubility is a liability in two respects: (i) the harsh gastric environment, and (ii) the small bowel lumen — where, in man, the pH varies between 5.7 and 7.4 (Mikolajczyk *et al.*, 2015). The former challenge was necessarily addressed by formulation with gastro-protective polymers, as described in the next chapter. But the latter could, in principal, be overcome by simply swarming the ileum with a sufficient number of particles — so long as they remained disperse. Should particles be prone to agglomeration in luminal conditions, there would be simultaneous partitioning of nanoparticulate material into both soluble and 'solid' phases — and the enterprise would be doomed. Happily, in the assays above, CMC-ACP particles evinced excellent dispersion stability in both tissue culture and simulated physiological contexts, and were therefore worthy of further study in vitro and in vivo.

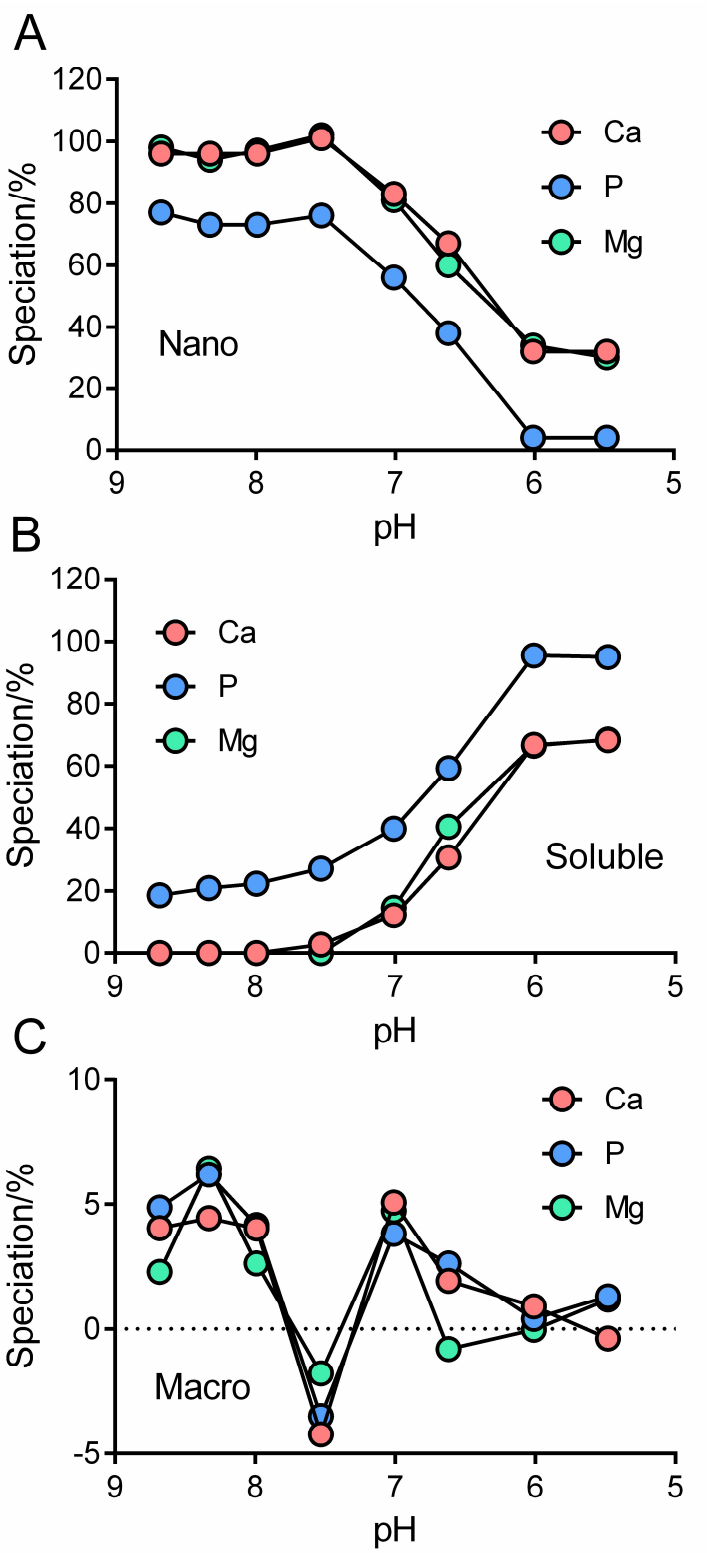

Figure 4.10 pH dependent speciation of CMC-ACP in simulated intestinal fluid. Data are presented for a single assay, showing the relative abundance of ACP mineral ions with respect to (**A**) nanoparticulate, (**B**) soluble and (**C**) macroscopic fractions. pH was adjusted via titration with dilute HCl, whilst phase separation was accomplished via centrifugation and elemental quantification by ICP-OES.

4.2.4 In vitro cargo incorporation, delivery and imaging

Following characterisation of CMC-ACP with respect to particle size, mineral phase and size stability, but prior to embarking upon animal studies, in vitro assays were required to: (i) demonstrate effective incorporation of various cargo within the CMC-ACP particles, (ii) ensure that the colloids were up-taken avidly by relevant cells in vitro, and (iii) optimise the particulate payload for analytical advantage — chiefly with respect to confocal microscopy, since that would be the primary technique for tissue analysis. With regards to (iii) there were two key factors to consider. First, robustness and intensity of signal. Second, provenance of signal. Since it might be expected that a proportion of CMC-ACP particles would dissolve in the intestinal lumen, some cargo release would also be anticipated. We would, ideally, want our imaging to discriminate between uptake of free vs particulate held cargo.

Using the impinging jet reactor, cargo loading proved to be facile; the synthetic method required no adjustment beyond adding the desired cargo to one of the ion feed solutions — usually phosphate. As summarised in Table 4.1, a range of cargo were incorporated: from inorganic nanoparticles such as quantum dots to soluble dyes and protein-dye conjugates — exemplifying the versatility of ACP as a carrier. Although the principal focus was on imaging cargo (which naturally included protein conjugates), in line with the wider project objective of developing a material that could effect 'general' in vivo delivery of biomolecular cargo, immunomodulatory polynucleotides were also incorporated as a proof of principal.

Cargo loading had minimal or no impact on particle size (Appendix C; Figure C.4.1). Incorporation efficiency, determined by fluorescence measurements on washed particles, was typically 15–30%, and, in the concentration ranges tested, was independent of the number of components added. Although the loading levels in these materials were not high (≤ 5% w/w), simultaneous incorporation of multiple cargo components is an important advantage for particulate delivery tools in biomedical research — since it facilitates combination therapy as well as tracking of actives. Dual loading was also a desirable feature for my work for two reasons. First, it would allow evaluation of signal co-localisation in cellular and in vivo experiments and thereby discriminate between ACP-based delivery vs independent uptake of a single cargo moiety. Second, and depending on the nature of the cargo, dual loading could facilitate analytical triangulation, wherein confocal imaging would be augmented (and de-risked) by complementary techniques such as *in situ* electron microscopy (EM).

Table 4.1 Examples of molecular and particulate cargo investigated in this project.

Cargo category	Examples	Purpose
Inorganic particles	CdSeS/ZnS core-shell quantum dots	Confocal and EM imaging
Polynucleotides	Polyinosinic:polycytidylic acid	Immunostimulant
Protein conjugates	TRITC-BSA, DQ-BSA, Alexa-647-OVA	Confocal imaging
Soluble fluorophores	Calcein, IAEDANS, Xylenol Orange	Confocal imaging

EM = Electron microscopy, TRITC = Tetramethylrhodamine, BSA = Bovine serum albumin, OVA = ovalbumin, IAEDANS = 5-({2-[(iodoacetyl)amino]ethyl}amino)naphthalene-1-sulfonic acid

One implementation of a dual loading approach was to label CMC-ACP particles with calcein and ~6 nm cadmium-based quantum dots. Calcein, although a small, organic fluorophore, is cell membrane impermeable and has a good affinity for calcium mineral (Lee *et al.*, 2003; Hu *et al.*, 2007), thus it could be expected to give a reliable fluorescent proxy for the ACP nanoparticles. The quantum dots would provide a unique elemental signature for electron microscopy and a robust (non-bleaching) fluorescent signal that could then be correlated against calcein. Thus, dual-labelled-calcein-quantum-dot materials were prepared and, in the first instance, characterised by transmission electron microscopy and energy dispersive X-ray (Appendix C; Figure C.4.2, Figure C.4.3, Figure C.4.4) which indeed confirmed that (i) the quantum dots could be detected, and (ii) that the recovered quantum dots were associated with the ACP particles and hadn't sedimented in independent flocs.

Unfortunately, in vitro cell experiments with this cargo pairing (Figure 4.11a-e) found that upon particle-delivery, cellular calcein-quantum-dot signal correlation was unreliable. Whilst a proportion of cells showed good signal co-localisation (Figure 4.11c) many others only had signal from calcein (Figure 4.11d), or from quantum dots (Figure 4.11e). ACP-free quantum dots were used as a positive control (Figure 4.11b) and demonstrated that the quantum dots were capable of independent cell entry, so it was not surprising that some cells were both quantum-dot-positive and calcein-negative (a degree of dissolution and cargo loss is inevitable under pH neutral conditions). However, the finding of calcein-positive quantum-dot-negative cells was surprising, since it indicated either: selective labelling of ACP particles (such that, at point of synthesis, many ACP particles contained calcein but not quantum dots) or that selective dissolution and reprecipitation had effectively expelled the quantum dots into the tissue culture media. Most concerning, imaging flow cytometry results from the same experiment indicated that cellular uptake of calcein-labelled ACP was lower when co-formulated with quantum dots (Appendix C; Figure C.4.5).

Following poor initial in vitro results with quantum dots, further work focused on protein-dye conjugates, in combination with calcein and other soluble dyes with good calcium affinity. One incarnation of this strategy employed the bovine serum albumin (BSA) derivative DQ-BSA. The albumin molecules which comprise DQ-BSA are heavily labelled with boron-dipyrromethane (BODIPY) fluorophores — which self-quench in close proximity to each other. Proteolytic degradation of albumin into singly labelled peptide fragments results in dye de-quenching and thus evolution of fluorescent signal. Given the prevalence of hydrolytic enzymes within the gastrointestinal tract, it seemed likely that DQ-BSA would give good indication of whether luminal cargo spilling had occurred. Unfortunately, in vitro studies with DQ-BSA labelled particles showed them to be toxic and disruptive to cell membranes (Figure 4.12a). Furthermore, the BODIPY emission peak was extremely broad and interfered with other channels (Figure 4.12b).

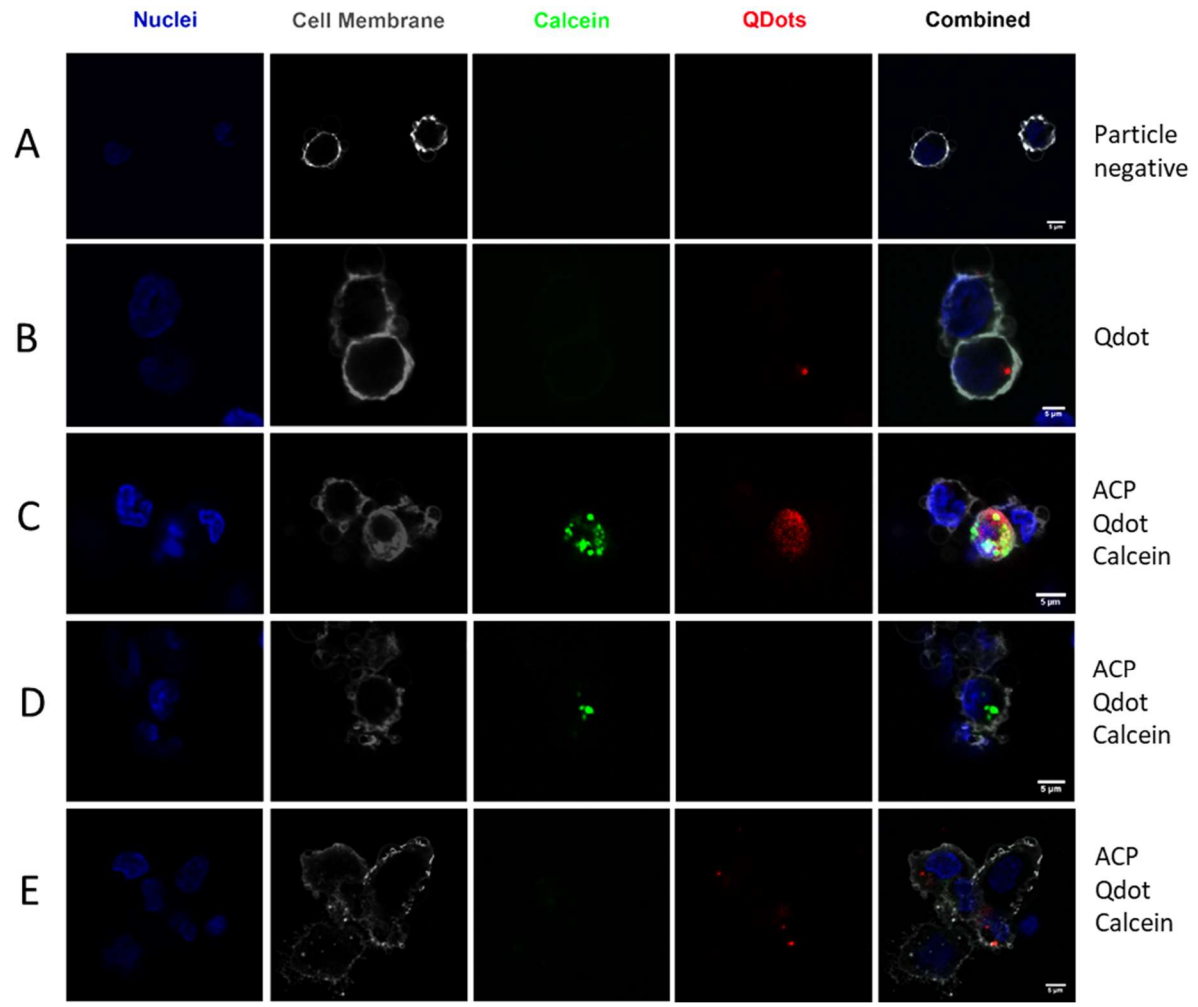

Figure 4.11 In vitro uptake of calcein and quantum dots by peripheral blood mononuclear cells after incubation with particle free media (**A**), quantum dots (**B**), or dual, calcein and quantum dot, labelled ACP particles (**C-E**). Cargo co-localisation was good in some cells (**C**) but many only showed calcein (**D**) or quantum dot signal (**E**). Images were obtained by confocal microscopy. Scale bars equate to 5 µm.

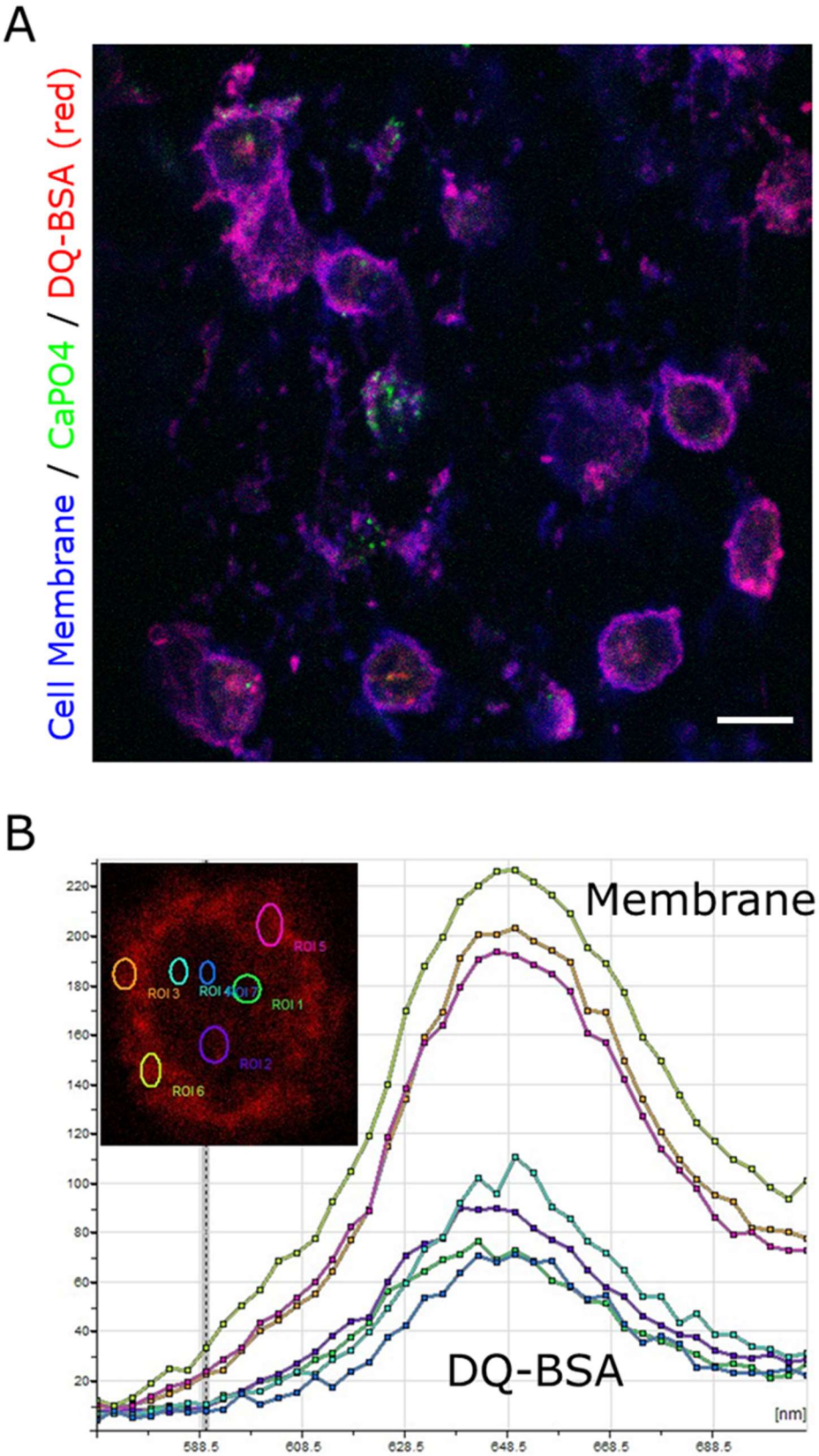

Figure 4.12 Impact of DQ-BSA loaded CMC-ACP particles on peripheral blood mononuclear cells. Pervasive membrane rupture is evident in the multi-channel composite (**A**) whilst lambda scans of bright regions (**B**) revealed a diffuse emission peak that interfered with other channels. Images were obtained by confocal microscopy. Scale bar equates to 20 µm.

DQ-BSA being manifestly unsuitable, alternative strategies were considered. One of these entailed loading particles with a Förster resonance energy transfer (FRET) fluorophore pair, wherein dipole coupling would mediate non-radiative energy transfer between neighbouring cargo molecules — causing laser excitation of one cargo entity (the donor) to induce emission of the other (the acceptor). FRET is contingent upon both spectral overlap and spatial proximity; transfer efficiency declines in proportion to the sixth power of the distance between donor and acceptor moieties (Latt, Cheung and Blout, 1965). Consequently, FRET signal would require cargo pairings to remain within in-tact ACP nanoparticles and allow discrimination between independent and particle held cargo.

Calcein, as described earlier, was an advantageous cargo element — and was therefore retained. Being a fluorescein derivative, it seemed likely to display similar FRET activity. Accordingly, in an initial pilot study, several pairings of calcein with reported fluorescein partners were screened for FRET activity (Table 4.2). To do this efficiently, the screening was acellular: cargo loaded particles were centrifuged and the resultant pellets imaged after being embedded in gelatine. Of the combinations tested, tetramethylrhodamine (TRITC) proved the best partner, giving a reasonable amount of FRET signal (Figure 4.13). However, with the concentrations used, there remained significant signal in the calcein channel, indicating incomplete quenching and thus sub-optimal stoichiometry. Subsequent, cellular, experiments with the calcein-TRITC pair iterated through several cargo concentration combinations, eventuating at an optimal BSA-TRITC:calcein label ratio (40:1 by mass, 2.6:1 by fluorophore stoichiometry —accounting for molecular weight differences and the degree of BSA labelling) that gave good, specific, FRET signal without bleed through. Although the total cargo content for this material was less than 5% (w/w), it proved successful in both primary human and murine macrophage cells (Figure 4.14a and Figure4.14b respectively) and thus was subsequently used in oral feeding studies, as described in the next chapter.

Table 4.2 Spectral characteristics of the fluorophores and FRET pairings tested in screening assays

FRET pair *a* (donor)	FRET pair *b* (acceptor)	Excitation max/nm	Emission max/nm
Calcein		488	525
Tetramethylrhodamine		544	570
Sulforhodamine B		559	577
IAEDANS		336	490
Calcein	Tetramethylrhodamine	488	570
Calcein	Sulforhodamine B	488	577
IAEDANS	Calcein	336	525

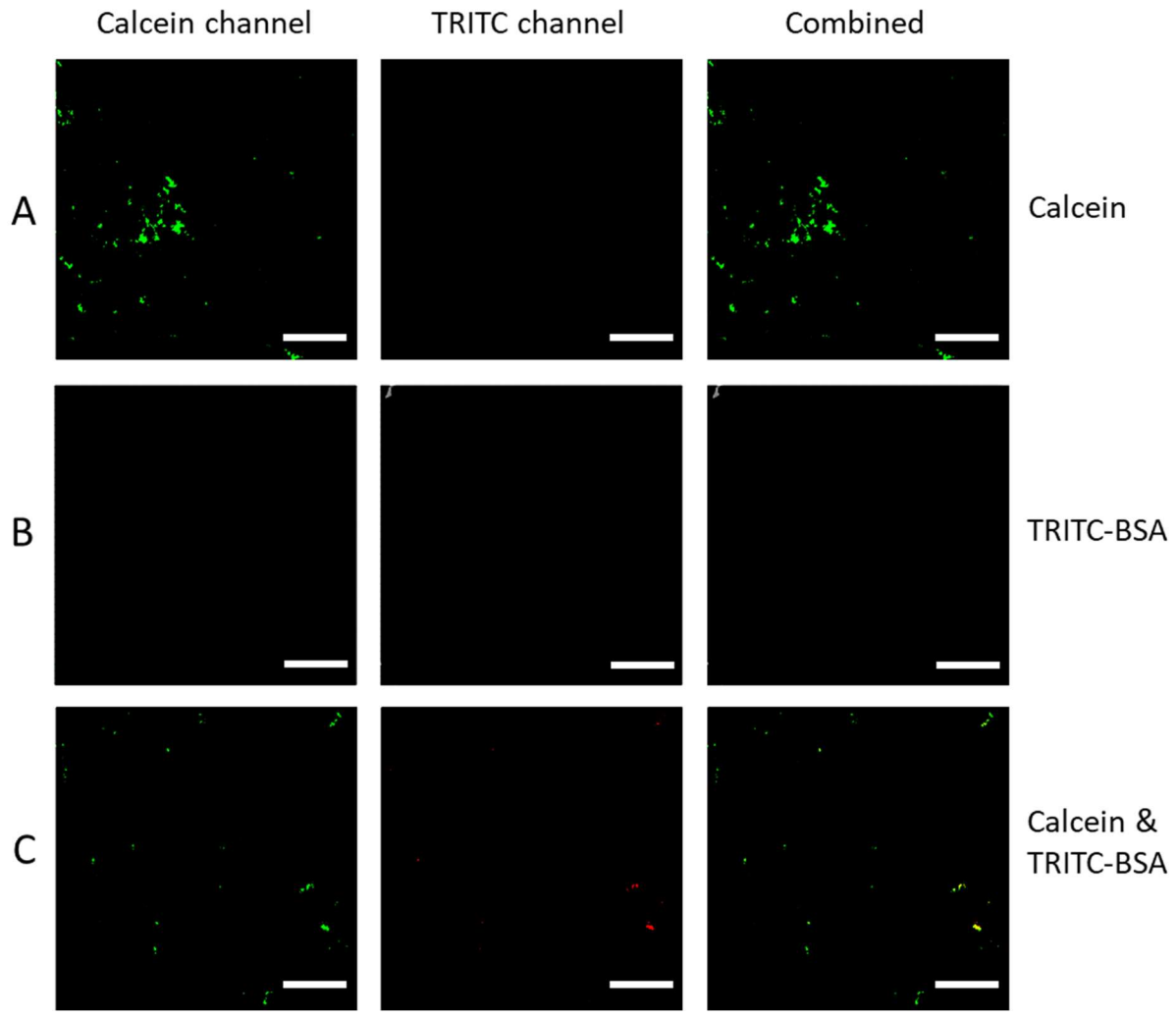

Figure 4.13 Confocal images of cargo loaded gelatine embedded ACP pellets during FRET screening. Images show particles loaded with calcein (**A**), bovine serum albumin-tetramethylrhodamine conjugate (TRITC-BSA) (**B**), or calcein and TRITC-BSA (**C**). A 488 nm laser was used throughout; in the FRET pair (**C**) this led to emission in both the calcein (left) and TRITC (middle) channels, indicating incomplete quenching of calcein. To produce the materials imaged here, cargo loading was achieved by dispersing the fluorescent labels in phosphate reactant solutions prior to synthesis at concentrations of 0.01 mg/mL and 0.2 mg/mL for calcein and TRITC-BSA respectively. Images are binaries with scale bars equating to 50 µm.

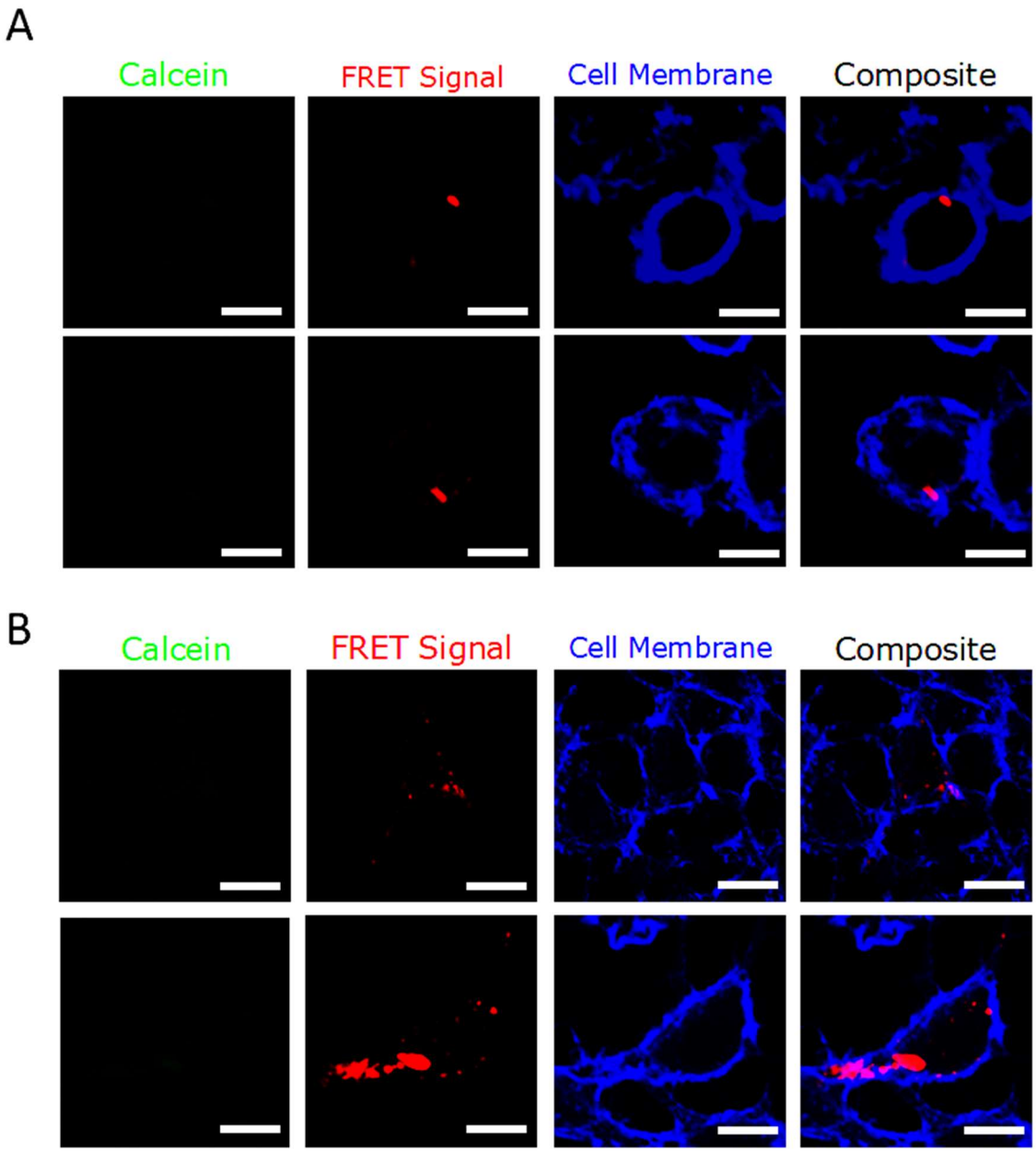

Figure 4.14 Confocal images of FRET active CMC-ACP particle uptake by peripheral blood mononuclear cells (A) and murine RAW macrophages (B). Particles were loaded with calcein and bovine serum albumin-tetramethylrhodamine conjugate (TRITC-BSA) by dispersing the labels in the phosphate reactant solution at concentrations of 0.01 mg/mL and 0.4 mg/mL respectively. There was little to no signal in the calcein channel, indicating effective quenching. Scale bars equate to 10 µm.

4.3 Conclusion

Work in this chapter demonstrated the stability and suitability of carboxymethlcellulose (CMC) ACP colloids for in vitro cargo delivery and as superior candidates to either quillaja saponin (QS) or sodium tripolyphosphate (STPP) materials for in vivo studies. Electron microscopy confirmed that the colloids produced by the previously described impinging jet reactor were indeed comprised from amorphous calcium phosphate (isomorph 1). QS-ACP and STPP-ACP were found to suffer from batch variability and pH driven agglomeration respectively. In contrast, CMC-ACP proved reliable and robust to agglomeration in a range of complex media. In cellular experiments, CMC-ACP particles were uptaken avidly and when loaded with a suitable FRET pair of fluorophores, yielded a bright and spectrally specific signal in confocal microscopy images. These outcomes paved the way for the animal studies described in the next chapter.

4.4 Materials and methods

Methodologies used in this chapter fall roughly into two groupings: fundamental analytical techniques (for instance dynamic light scattering) and more complex assays. For convenience, commonly applicable details for the fundamental techniques are presented first, in alphabetical (technique) order. Methods for the more involved assays are listed subsequently, in order of their appearance in the results and discussion.

Except where otherwise noted all chemicals were obtained from Sigma Aldrich. Freedom Tubing was obtained from RMS Medical Products, PTFE needles were obtained from Adhesive Dispensing Ltd. Syringes were obtained from VWR. Ultrasonication was carried out with a Microson XL2000 (Misonix Ltd, Farmingdale, New York).

4.4.1 Dynamic light scattering

DLS measurements were performed with a Zetasizer Nano ZSP (Malvern Instruments Limited). using Dispersion Technology Software 7.11. 400 µL sample volumes were analysed in disposable polystyrene cuvettes (VWR). In the absence of reliable optical property data for ACP, literature values for hydroxapatite were used: refractive index 1.65, absorbance 0.01. The medium was water, with a refractive index of 1.33 and, with the exception of Figure 4.1b, a viscosity of 1.0031 cP. For Figure 4.1b, the viscosity — determined at 20°C via a SV-10 Vibro Viscometer (A&D Ltd, Japan) — was set to 1.35 cP. Particle sizing results for Figure4.1b assuming a viscosity of 1.0031 cP are shown in Appendix C; Figure C.1.2. All measurements were carried out at 20°C, with a brief period of thermal equilibrium (1-2 minutes) prior to measurement, and at a scattering angle of 173°. Measurement position and attenuation factor were automatically optimised by the instrument to minimise secondary scattering and maintain photon counts within the linear range of the detector (100 – 500 kcps). Three to six measurements of at least 10 runs (each of at least 10 seconds) were performed on each sample, with the number of runs and the run duration automatically chosen by the instrument software. The in-build general purpose model was used for data processing. Results were then reported as means ± one standard deviation from measurement replicates .

4.4.2 Inductively coupled plasma — optical emission spectrometry (ICP-OES)

Elemental analyses were carried by ICP-OES (Jobin Yvon Horiba Ultima 2C; Instrument SA, Longjumeau, France), equipped with a concentric nebulizer and cyclonic spray chamber. Plasma gas flow rate was 10 mL/min and sample flow rate was 1 mL/min. Triplicate measurements were made for each sample and means and standard deviations calculated from these. Window size was 0.08 nm (0.04 nm either side of the peak). There were 15 increments per profile and each increment had an integration time of 0.5 seconds. Prior to analysis, samples were diluted down to (analyte) concentrations below 10 mg/L in 5% HNO_3 (v/v). Multi-element calibration standards (50 µg/L to 10 mg/L calcium and phosphorus; 25 µg/L to 5 mg/L magnesium) were also prepared in 5% HNO_3. See Figure 4.15 for an example standard curve. Quantification was carried out using the lines tabulated below (Table 4.3). To convert measured phosphorus concentrations to phosphate 'amounts', for instance in mass balance calculations, the phosphorus mass was multiplied by the phosphorus:phosphate molar mass ratio.

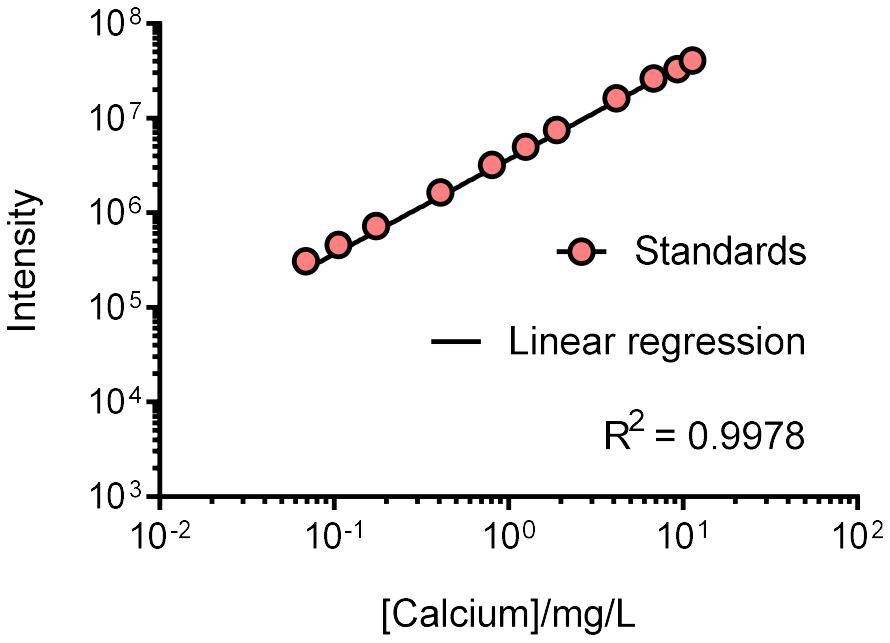

Figure 4.15 An example ICP-OES calibration curve with multielement standards in 5% HNO_3. Emission intensity at the 396.847 nm calcium line has a linear response to concentration in the 50 µg/L to 10 mg/L concentration range.

Table 4.3 ICP elemental emission lines and estimated detection limits from the literature. Reproduced from chapter 2.

Analyte	Line/nm	Detection limit/µg/L	Reference
Calcium	396.847	0.5	Winge, Peterson and Fassel, 1979
Phosphorus	177.49	200	Nollet and De Gelder, 2013
Magnesium	279.079	30	Winge, Peterson and Fassel, 1979

4.4.3 Microspecies calculations

MarvinSketch (ChemAxon) was used to calculate microspecies charge (deprotonation) distribution as a function of pH for tripolyphosphate $[P_3O_{10}]^{-5}$. Calculations were done at 298 K in 0.2 pH unit increments. The 8 structures, including two pairs of tautomers, are depicted below.

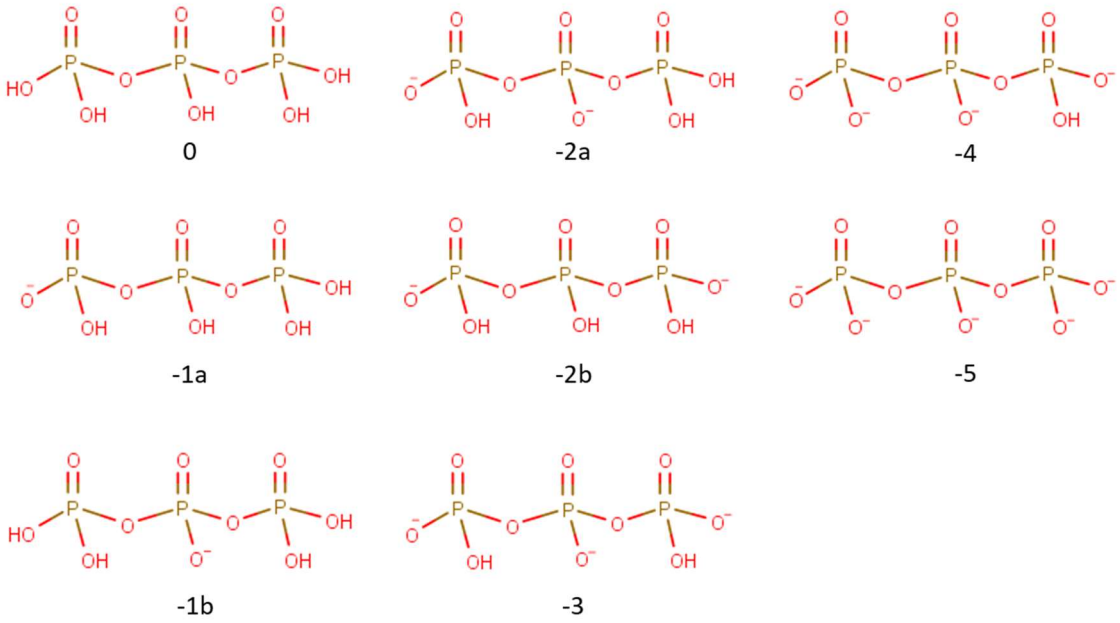

Figure 4.16 Skeletal structural representations of tripolyphosphate microspecies. Microspecies charge is indicated by number and tautomer pairs are labelled with 'a' and 'b'. Structures 1b and 2a are the dominant forms of their respective tautomer pairs.

4.4.4 Pycnometry

Density determinations were made with 5 mL calibrated Gay-Lussac type BLAUBRAND density bottles (Brand GMBH, Wertheim, Germany) in accordance with the SOP (Blaubrand, 2015), excepting use of ethanol rather than water as the displacement medium — to avert mineral dissolution. Three assays were conducted on each material with a minimum of 100 mg of sample used per measurement and the means used for density calculations.

4.4.5 Transmission Electron Microscopy

TEM images were obtained with a FEI Titan Cubed Themis 300 G2 S/TEM equipped with FEI SuperX EDX spectrometer, Gatan Quantum ER imaging filter and Gatan OneView CCD. For the initial analyses, freshly prepared disperse materials were drop cast onto plasma-treated holey carbon grids (Agar Scientific Ltd.) and air-dried. Plunge frozen samples were prepared with a FEI Vitrobot© mark IV plunge freezer. Particle size analysis (Figure 4.17) was done on images at 145k magnification, at 1 nano amp of screen current and with 2 second capture times.

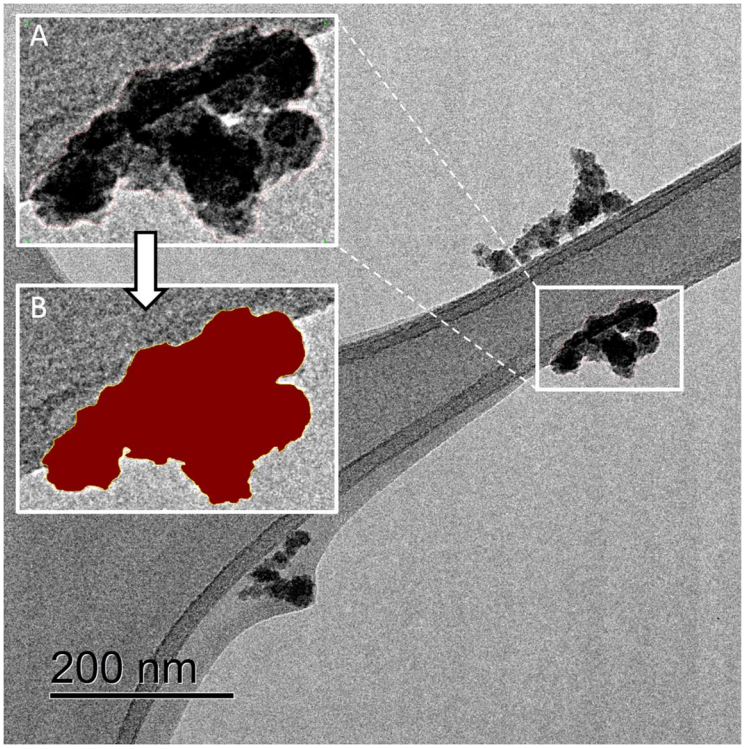

Figure 4.17 Workflow for particle size analysis by transmission electron microscopy. Discrete particles were manually outlined in Digital Micrograph (**A**) and then converted to masks (**B**) to obtain size statistics.

4.4.6 UV-Vis

Cargo incorporation was assayed using a Fujitsu Fluostar Omega plate reader. Excitation and emission wavelengths were 485/520 nm for calcein, 544/590 for TRITC-BSA, 485/590 for Sulforhodamine B, 584/620-10 for DQ-BSA. Concentrations were determined by interpolating a linear regression between matrix matched standards of known concentration. Each sample and standard was analysed in duplicate wells and the mean values were used.

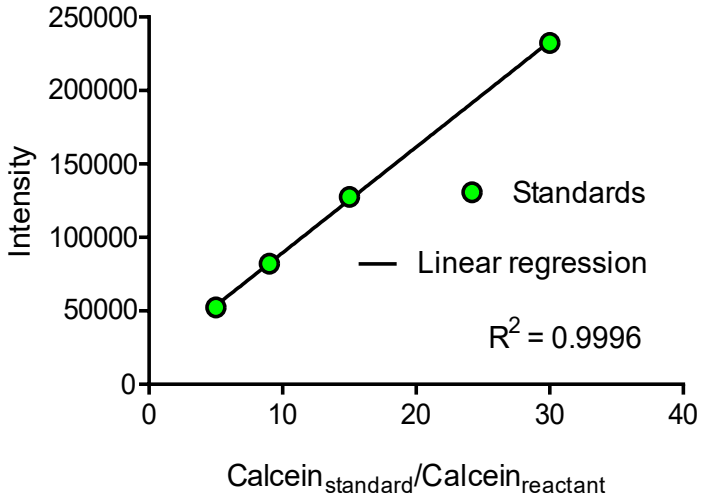

Figure 4.18 An example UV-vis calibration curve with matrix-matched calcein standards

4.4.7 Zeta-potential

Data were collected at 20°C with a Zetasizer Nano ZSP (Malvern Instruments Limited) and disposable folded capillary cells (Malvern Instruments Limited) after a 60 second thermal equilibration period. For each sample three measurements were taken, each of which comprised a minimum of 10 and a maximum of 100 runs. Attenuation and voltage were automatically selected by the instrument. The Smolochowski approximation was used. The dispersant was water, with a dielectric constant of 80.4. Optical parameters for the dispersant and the calcium phosphate particles were as detailed in the Dynamic Light Scattering general method.

4.4.8 Particle synthesis

Materials and solutions were prepared as described in the previous chapter. In brief, reactant solutions were (i) phosphate: 50 mMol/L PO_4, 100 mMol/L tris, pH 9 and (ii) metal: 40 mMol/L Ca^{2+}, 10 mMol/L Mg^{2+}, 100 mMol/L tris, also pH 9. Cargo was dissolved/dispersed in phosphate reactant solution. Particle dispersant solutions (ie carboxymethylcellulose, quillaja saponin or sodium tripolyphosphate) were also at pH 9, contained 100 mMol/L tris buffer, and had dispersant concentrations of 1% w/w.

Particles were prepared as follows. Two 10 mL plastic luer-lok syringes (Becton Dickinson) were loaded with the reactant solutions and connected to PTFE needles (Adhesive dispensing Ltd.) via Freedom 2400 medical grade tubing (RMS Medical Supplies). PTFE needle nozzles were orientated at a θ of approximately 110°, above a 10 mL volume of dispersant solution. Reactants were simultaneously pumped (5 mL each) from the syringes using an Elite 11 Syringe pump (Harvard Apparatus) at flow rates of 20 mL/min. The resultant impinging jets collided and cascaded into the dispersant solution under vigorous (magnetic stirrer-bar) agitation and were immediately centrifuged at 16 000 g for 10 minutes to recover the particles and remove unbound cargo and excess dispersant in the supernatant. Particles were resuspended by ultrasonication. Calcein, IAEDANS and the quantum dots were obtained from Sigma Aldrich, all other cargo (Tetramethylrhodamine-BSA, Sulforhodamine B, DQ-BSA) were obtained from Thermofisher Scientific. Within phosphate reactant solutions, quantum dots were dispersed at 0.1 mg/mL, and DQ-BSA at 0.4 mg/mL. Other cargo were incorporated at a range of concentrations, as tabulated below (Table 4.4 and Table 4.5). The best performing combination in the initial acellular screening was 0.01 mg/mL calcein & 0.2 mg/mL TRITC-BSA, whilst the optimised combination in the cellular experiments was 0.01 mg/mL calcein and 0.4 mg/mL TRITC-BSA.

Table 4.4 FRET pair combinations tested during acellular screening experiments.

PO_4 Solution Dye Conc. (mg/mL)			
Calcein	TRITC-BSA	IAEDANS	Sulforhodamine B
0.1	0.1	-	-
0.1	0.2	-	-
0.1	0.4	-	-
0.1	0.8	-	-
0.1	-	0.1	-
0.1	-	0.2	-
0.1	-	0.4	-
0.1	-	0.8	-
0.1	-	-	-
0.1	-	-	-
0.1	-	-	0.2
0.1	-	-	0.4
0.05	0.1	-	-
0.05	0.2	-	-
0.05	-	0.1	-
0.05	-	0.2	-
0.05	-	-	0.1
0.05	-	-	0.2
0.01	0.1	-	-
0.01	0.2	-	-
0.01	-	0.1	-
0.01	-	0.2	-

TRITC = Tetramethylrhodamine, BSA = Bovine serum albumin, IAEDANS = 5-({2-[(iodoacetyl)amino]ethyl}amino)naphthalene-1-sulfonic acid

Table 4.5 In vitro cell assay FRET cargo combinations.

PO_4 Solution Dye Conc. (mg/mL)	
Calcein	TRITC-BSA
0.01	0
0.01	0.2
0.01	0.4
0.005	0
0.005	0.2
0.005	0.4
0	0.2
0	0.4

4.4.9 Centrifugal size analysis

Cumulative homogenous centrifugal sedimentation was used to obtain particle size distributions according to the general methods described by Slater & Cohen (1962), E. Robison and W. Martin (1948) and H.J Kamack (1951, 1972) but with some alterations. In particular, I employed variable speed rather than time, as a more practical means of collecting distributions which contained small-ish (< 0.1 µm) particles. I also employed ICP-OES (rather than gravimetry) to determine concentration, which allowed me to use much smaller sample volumes.

For method development and validation, tricalcium phosphate particles (Sigma Aldrich), nominally 200 nm in diameter were dispersed in UHP at 1 mg/mL via ultrasonication. Aliquots (1 mL) of the resultant polydisperse suspensions were placed in 2 mL cylindrical centrifuge tubes (ThermoFisher Scientific), centrifuged at 1000 g for 5 minutes with a Micro Star 17 or Micro Star 17R desktop centrifuge (VWR), and the agglomerate-free supernatants recovered. These supernatants were pooled, particle sized via dynamic light scattering and allowed to stand overnight. Dynamic light scattering was then used the following day to confirm colloidal stability (of the pooled supernatant). The pooled supernatant was then assayed as outlined below.

For ACP assays, particles were prepared as outlined in Chapter 3 and placed in assay solution (eg pH 9 water) at original concentration. Assay solutions other than pH 9 water were (a) replete tissue culture media: RPMI 1640 supplemented with 10% heat inactivated fetal bovine serum (PAA), and (b) phosphate-free simulated intestinal fluid comprising 10 mMol/L $NaHCO_3$, 30 mMol/L tris, 100 mMol/L KCl, 2.5 g/L bovine serum albumin, 4 mMol/L sodium taurocholate and 0.5 mMol/L lecithin, pH adjusted to 7.4. Suspensions were incubated in media for 2 hours at 37°C with mixing, and then assayed as follows.

From homogenous colloidal suspensions, aliquots were taken as above. Each aliquot was then centrifuged (with the same centrifuge(s) as above) for 5 minutes (tricalcium phosphate) or 10 minutes (ACP particles) at defined speeds, removed carefully from the centrifuge and 850 µL of supernatant removed. Both supernatant and precipitate (the latter also containing 150 µL of supernatant) were acidified with 5% HNO_3 and — along with total samples obtained from the original colloidal stock — analysed via ICP-OES for calcium and phosphorus content in duplicate.

The means of these values were plotted against centrifugation speed and fitted, in Prism 6 (GraphPad Software), with a single phase association model of the form

$$y = y_0 + (Plateau - y_0)(1 - e^{-Kx})$$

Where y_0 and K were constrained to values > 0. With this function and the resulting best fit values (y_0, K, and plateau), recovery efficiency could be interpolated for any given centrifugal condition.

Solving Stokes' Law for the centrifugation conditions at the plateau gave the lower limit of the particle size distribution (of those particles that could be sedimented under experimental conditions). Equally, by considering particle recovery near the origin, an effective upper limit to the particle size distribution could be calculated: solving Stokes' Law at a low speed and then interpolating recovery efficiency at that speed gave an upper bound to the concentration of particles of or greater to that size.

Parameters used in these Stokes' Law calculations were as follows: sedimentation distance (maximum) 2.35 cm, viscosity 0.01 g/cm.second^{-1}, fluid density 1 g/cm^3, centrifugation time 300 seconds (TCP) or 600 seconds (ACP), ACP particle density 1.73 g/cm^3, TCP particle density 3.14 g/cm^3. Particle densities were determined by pycnometry, as described in section 4.4.4.

Calculating the full particle size distribution was more involved (than determining the limits). From Kamack (1972), the integral equation relating recovery efficiency to particle size distribution is

$$p(D_m) = \frac{1}{1-\exp(-a)} \int_0^{D_m} \left\{ exp\left(\frac{-aD^2}{{D_m}^2}\right) - \exp(-a) \right\} f(D) dD \qquad (3)$$

in which p is the weight fraction of suspended particles, f(D) = dF/dD is the differential particle size distribution, $a = 2\ln(r/r_0)$ is an apparatus constant, r is the distance between the axis of the centrifuge and the bottom of the Eppendorf, whilst r_0 is the distance between the axis of the centrifuge and the free surface of the suspension in the eppendorf, D_m is the smallest particle which will settle from r_0 to r under the centrifugation conditions (ie the largest particle remaining in suspension). D_m is calculated by Stokes' Law, given earlier. An exact solution to this equation is also given by Kamack (1972):

$$F(D_m) = \frac{\exp a - 1}{a} \left(q(D_m) \int_0^{\infty} h_1(x) q\{D_m \exp(-x)\} \right) \qquad (4)$$

Where $F(D_m)$ is the weight fraction of particles smaller than diameter D_m, and where

$$q(D) = p(D) + \frac{1}{2} D \frac{dp}{dD}$$

and

$$h_1(x) = h(x)\exp(-2x)$$

Where the resolvent kernel, h(x) is given by

$$h(x) = k(x) - \int_0^\infty k(x - x')h(x')dx \qquad (5)$$

where

$$k(x) = 2a \exp a \exp\{(-2x)\} \quad for\ x \geq 0$$

$$k(x) = 0 \qquad for\ x \leq 0$$

The integrals in (4) and (5) were evaluated numerically, the former via a combination of MATLAB (Appendix D) and Excel calculations, the latter via a Python script (Appendix D kindly written for me by Mr Stephen Farr (Theoretical Condensed Matter group, Cavendish Laboratory, University of Cambridge).

For the titration speciation assay, simulated intestinal fluid was prepared as before: comprising 10 mMol/L $NaHCO_3$, 30 mMol/L tris, 100 mMol/L KCl, 2.5 g/L bovine serum albumin, 4 mMol/L sodium taurocholate and 0.5 mMol/L lecithin. However, the pH was adjusted to 9 ± 0.1 rather than 7.4. ACP particles were resuspended at original volume in assay buffer and then titrated with 0.1 Mol/L HCl. A reduced centrifugal method (Figure 4.19) was implemented to crudely fractionate particles into three phases: macroscopic (> 1 µm), nanoparticulate, and soluble. Fractionation entailed removing three parallel 1 mL aliquots from assay solutions at each measurement point. One would be diluted with 5% HNO_3 and analysed for elemental concentrations of calcium, magnesium and phosphorus by ICP-OES without further processing. This sample was the total. A second aliquot would be centrifuged at 300 g for 5 minutes to sediment all large (> 1 µm) particles whilst minimising collection of nanoparticulate ACP. The supernatant from this sample was then analysed (after undergoing acidification and dilution). Subtraction of that supernatant from the total sample gave the ionic concentrations of macroscopic material in the assay. The third aliquot would be centrifuged at 16 000 g for 10 minutes to collect all the nanoparticles in solution and the supernatant treated in the same fashion as that of the first (slow-speed) supernatant. The second supernatant gave the soluble fraction directly, whilst subtraction of the soluble fraction from the first supernatant gave the nanoparticulate fraction. Centrifugation parameters for the restricted assay were determined based on Stokes' Law calculations and confirmed by experiment (Appendix C; Figure C.3.4 and Figure C.3.5).

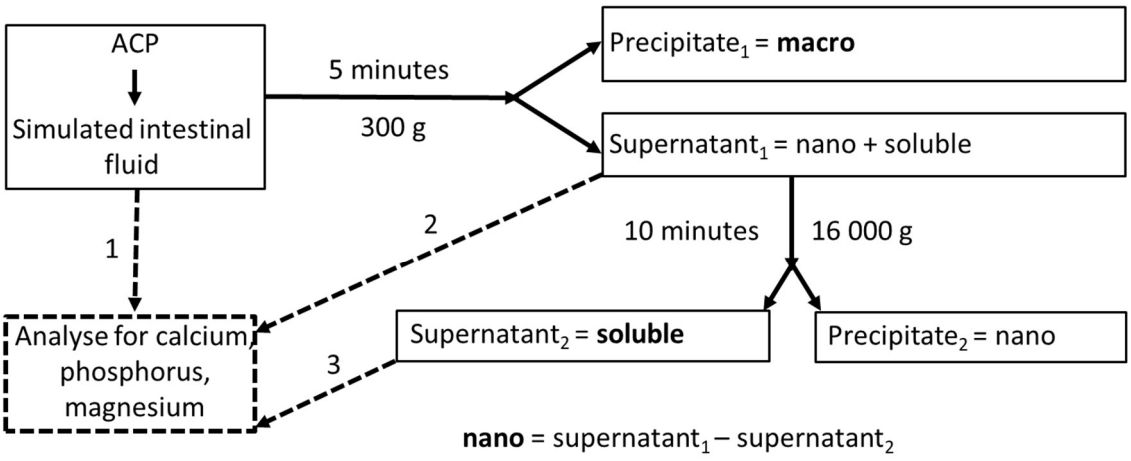

Figure 4.19 Schematic of the reduced centrifugal sedimentation assay.

4.4.10 In vitro cell studies

RAW 264.7 monocyte/macrophage cells purchased from the American Type Culture Collection (ATCC) were grown on coverslips according to ATCC suggested culture methods. Cells were pre-stimulated with peptidoglycan from Staphylococcus aureus [Invivogen tlrl-pgns2] by adding 1 microgram per mL to the cell culture media the evening prior to the experiment in order to induce differentiation to a macrophage phenotype prior to particle incubations. Particles in replete tissue culture media were then added to the RAW macrophages at 3 to 4 mMol/L [calcium] with coverslips in and incubated for 3 hours.

Fresh leukocyte cones were purchased from the National Blood Service (Cambridge, UK) and peripheral blood mononuclear cells (PBMC) were isolated by density gradient centrifugation with Lymphoprep (Axis-Shield, Norway). Separated mononuclear cell layers were washed twice, re-suspended in freezing medium, and stored frozen until use. Prior to experimentation, PBMCs were thawed, washed, and rested in tissue culture medium overnight before a 3-hour particle exposure at 3 to 4 mMol/L [calcium].

After incubation, cells were processed either for confocal microscopy or imaging flow cytometry.

For confocal microscopy, sample staining, incubations and washes all took place with gentle rotation on an orbital shaker. Media was removed from chambers/wells and 4% paraformaldehyde (PFA) was added for 10 minutes at room temperature. PFA was then removed and cells were washed three times, 3 minutes per wash, with phosphate buffered saline (PBS). After the last wash, PBS was

removed and the cells were incubated with Wheat Germ Agglutinin, Alexa Fluor 555 Conjugate (Thermofisher Scientific) 20µg/ml for 10 minutes. After this, cells were washed again, 3 times with PBS, for 3 minutes each. 1 drop of antifade (Prolong diamond; Thermofisher Scientific) was then added to each sample and they were then mounted. Imaging was carried out using an SP8 confocal microscope (Leica) with images collected using Leica Application Suite software.

Imaging flow cytometry and cell processing for it were carried out as previously reported (Hewitt *et al.*, 2017). Following particle exposure, cells were washed with PBS and then re-suspended in approximately 200 µL of chilled PBS which also contained 1% bovine serum albumin (BSA). Cells were stained with Alexa 488-conjugated CD14 (BD Biosciences, Reading, UK) for 20 minutes on ice, at the manufacturer's recommended concentration. Following staining, cells were washed with BSA-PBS and then resuspended in a minimal volume of PFA containing PBS to fix the cells. Imaging flow cytometry was carried out with the ImageStreamX Mark I platform (Amnis-Merck-millipore). INSPIRE software (Amnis) was used for acquisition and IDEAS software (Amnis Seattle, WA, USA) for analysis. A single stain compensation tube was prepared for ALEXA-488-CD14, as well as control (particle free) tubes and singly-labelled ACP particles. Immediately before acquisition, cells were filtered through 35 µm nylon cell strainer mesh tubes (BD Biosciences). A minimum of 30,000 events per sample were acquired. Compensation matrices were generated by running single stained particles or cells and analysed using IDEAS software.

Chapter 5 Formulation and in vivo studies

5.1 Introduction

The aim of the work reported in this chapter was to determine whether ACP colloids, developed according to prior chapters, could deliver incorporated cargo to cells in vivo, specifically cells of intestinal lymphoid aggregates, namely Peyer's patches.

The approach for this was to (i) identify a strategy for oral delivery, (ii) demonstrate gastric protection in vitro, (iii) demonstrate intestinal release of ACP particles in vitro, and (iv) investigate in vivo murine dosing with iterative test-and-analysis approaches. This chapter describes the studies and their outcomes, to demonstrate in-principle effectiveness of Peyer's Patch targeting by ACP colloids upon ingestion.

Recently I was part of a team considering how nanoparticles can be best administered to animals with physiological relevance (da Silva *et al.*, 2020). Several aspects were highlighted. Firstly, gavage (ie bolus dosing) is non-physiological and it induces stress which alters intestinal function. Secondly, prior to gavage a long (overnight) fast is generally required to ensure that the upper gut is entirely 'empty'. Small rodents have rapid metabolisms (Brody, 1934) and require regular food intake; in mice, overnight deprivation can induce starvation signs — such as hepatic steatosis — and body weight losses in excess of 10% (Heijboer *et al.*, 2005; van Ginneken *et al.*, 2007), confounding findings. Thirdly, abnormally concentrating particles risks their agglomeration at point of delivery. Conversely, laboratory rodents (e.g. mice) graze when feeding, so strategies to incorporate particles into their diets offer excellent opportunity for physiological oral delivery.

In the case of amorphous calcium phosphate however, exposure to gastric acid (murine stomach pH ~3–4; McConnell, Basit and Murdan, 2008) would inevitably lead to complete dissolution. Furthermore, the mineral may have undesirable interactions with other dietary components if directly incorporated into a rodent diet. In man, acid sensitive compositions are protected through the stomach by coating capsules or tablets with pH sensitive enteric polymers that remain insoluble under gastric conditions but solubilise in the intestine (Tarcha, 1990). Although rodent anatomy precludes conventional capsules, analogous strategies have been developed using ~100 µm microsomes comprised from enteric polymer as mini-capsules to achieve intestinal delivery (Kendall *et al.*, 2009). For the purposes of this project, a Russian doll strategy could be envisaged wherein microsomes would be loaded with ACP particles that would themselves be loaded with imaging cargo.

5.2 Results and discussion[19]

5.2.1 Initial formulation

Unfortunately, following some efforts towards microsomal formulations, my progress was thwarted by technical challenges (in particular relating to poor loading of mineral within the microsomes) and intellectual property barriers. Brief data for this work are shown in Appendix D. Since an alternative approach was necessitated, I subsequently adapted a reported method for voluntary oral administration via sweetened gels (Zhang, 2011) by incorporating gastro-protective polymers in the recipe to impart the gels with this property. The hope was for the gels to be consumed as a temporary substitute for normal laboratory chow, remain as solid 'chewosomes' upon ingestion, and then to unfurl in the small bowel where the polymer is soluble— allowing delivery of disperse and undigested ACP particles without physiological perturbation. To this end I experimented with two commercially available enteric polymers, HP-55 and Eudragit L100-55. The former is a grade of the cellulose derivative hypromellose phthalate whilst the latter is a copolymer of methacrylic acid and methyl methacrylate (Terao, Matsuda and Shouji, 2001). Both polymers begin to solubilise above pH 5.5 (Liu *et al.*, 2011) and for compatibility with ACP, the gels needed to be prepared using alkaline water (pH 9). Consequently, to achieve solid formulations, a gel forming agent was also needed. The Zhang protocol employs gelatine for this purpose and thus requires formulation to take place at ~60 °C, which is suboptimal so far as ACP is concerned — due to the risk of accelerating mineral phase transformation. Accordingly, in addition to producing gelatine-based materials, I also considered alternative gel-formers, such as hydroxyethylcellulose (HEC) — which can be formulated at room temperature.

The capacity of the gels to protect ACP particles from gastric conditions was assessed in a simple in vitro assay. Formulated materials containing ACP colloids (nanoparticles prepared as outlined in chapter 3) were exposed to a simulated gastric stage wherein they were 'diluted' ten-fold in pH 2, 100 mMol/L citrate buffer, and mixed vigorously for thirty minutes at 37 °C, before being centrifuged at 16000 g for 100 minutes and then having their the supernatants diluted and analysed via ICP-OES for calcium and phosphorus and via fluorescence for cargo (calcein). In addition to four gel materials comprising HP-55 or Eudragit L100-55 **and** gelatine or HEC, a fluid formulation (free from gelatine or HEC) was produced for each enteric polymer and tested as a control.

[19] Materials and methods for this chapter can be found on page 134

There were distinct differences between the enteric polymers (Figure 5.1). Measurable losses of calcium and phosphorus from the gels into the solution were much higher for Eudragit-L100-55 materials than the other materials. This trend was attenuated for cargo losses, perhaps due to size driven differences in diffusion coefficient; calcein being more than 10-fold heavier than calcium. Surprisingly, losses for the HP-55-based liquid formulation (yellow bars) were minimal and equivalent to those from the HP-55 gels, raising the question of whether co-formulants (ie HEC or gelatine) were indeed needed. However, viscous liquid formulations of this sort face significant challenges with regards to oral administration, being too viscous for gavage, more awkward to introduce as a food than gels and likely inferior at taste masking.

Whilst this assay was simplistic, neglecting physical aspects of digestion such as mastication, it sufficed as a proof-of-principle measure of protection and as a selection tool — the failure of Eudragit-L100-55 materials to confer gastro-protection led to HP-55 being adopted for subsequent studies.

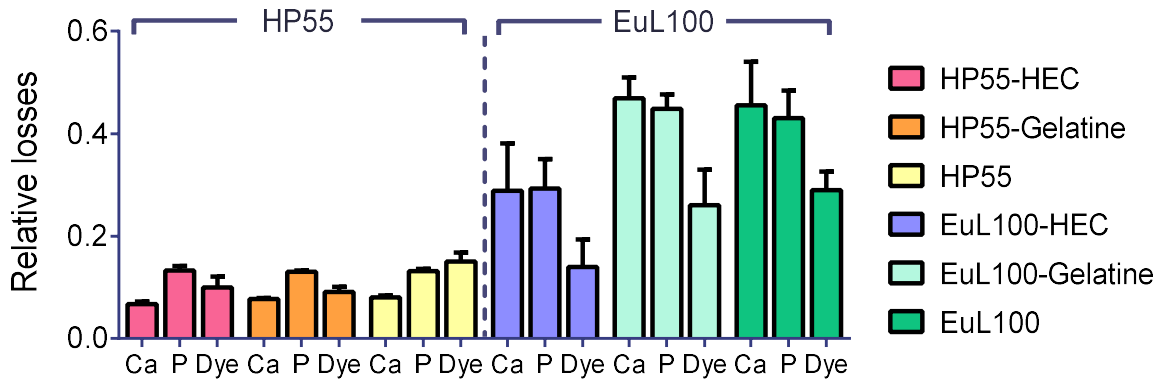

Figure 5.1 In vitro gastro-protection of ACP nanoparticles by enteric polymer formulations at pH 2. Ca denotes calcium, P denotes phosphorus, in solution by ICP-OES. Dye denotes calcein, in solution by UV-Vis.

After demonstrating proof-of-principle in vitro gastric protection I sought to determine whether HP-55 formulations would subsequently release their ACP cargo in simulated intestinal conditions. Unlike the gastric assay, which merely required separation of soluble (calcium and phosphate species) from insoluble, to ascertain the effectiveness of particle release I needed to discriminate between three fractions: (i) soluble, (ii) nano (in the form of free ACP particles), and (iii) macroscopic (agglomerated or unreleased ACP particles). Following my previous success with sedimentation-based analyses (chapter 3), I opted to employ similar methods here — beginning with the most basic approach possible, before increasing complexity.

Thus, in the first instance, after subjecting materials to simulated gastric conditions as outlined above, I centrifuged them gently (5 minutes at 100 g), removed the acidic supernatant and then resuspended the loose precipitates in pH 7.2 citrate buffer to engender particle release and dissolution. After a 90 minute incubation, I centrifuged the materials at 16000 g for 100 minutes and analysed the supernatants for calcium and phosphate. The three previously described HP-55 formulations were tested thus, and — in this assay — all were found to release at least half of their mineral payloads (Figure 5.2). Given that both gelatine and HEC formulations performed equivalently here and in the earlier gastro-protective assay, whilst HEC had practical advantages as a co-formulant (not requiring heating), at this stage I down-selected HP-55-HEC as the main formulation.

Although these results were encouraging, this assay was binary, only differentiating between unreleased ACP on one hand, and citrate buffer released fractions on the other hand. Accordingly, to achieve better partitioning, I replaced the citrate buffer with simulated intestinal fluid (SIF) and introduced an additional separation step to the assay — namely, a slow centrifugation to remove macroscopic material, prior to the fast spin. This approach closely resembled the reduced centrifugal sedimentation method described in the previous chapter, adapted for the greater viscosity of these formulations. A schematic of the modified procedure is outlined below (Figure 5.3). Results from this protocol were broadly concordant with those from the citrate assay; roughly half of the payload was released as colloidal ACP (Figure 5.4). Although this level of performance left room for improvement, we judged it sufficient to proceed with in vivo testing.

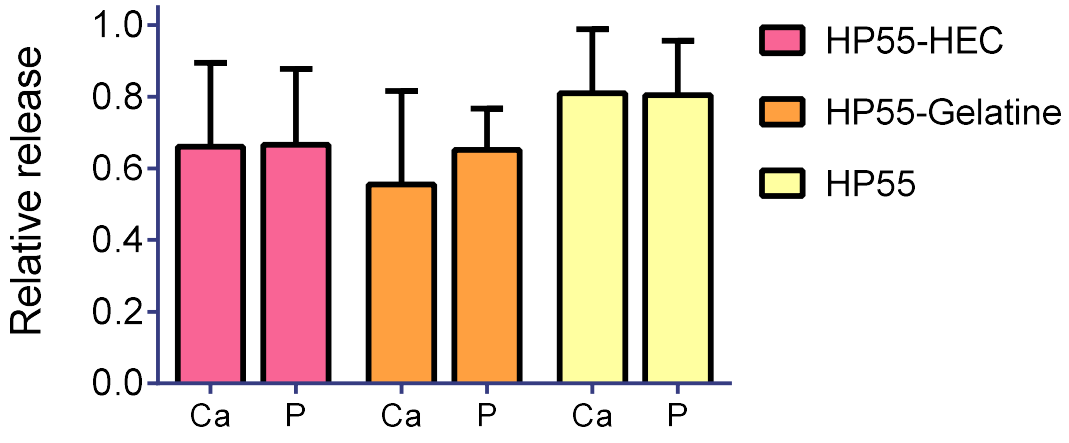

Figure 5.2. Simulated release of ACP colloids by HP-55 formulations at pH 7.2 in a simple citrate-buffer release assay. Ca denotes calcium, P denotes phosphorus, in solution by ICP-OES.

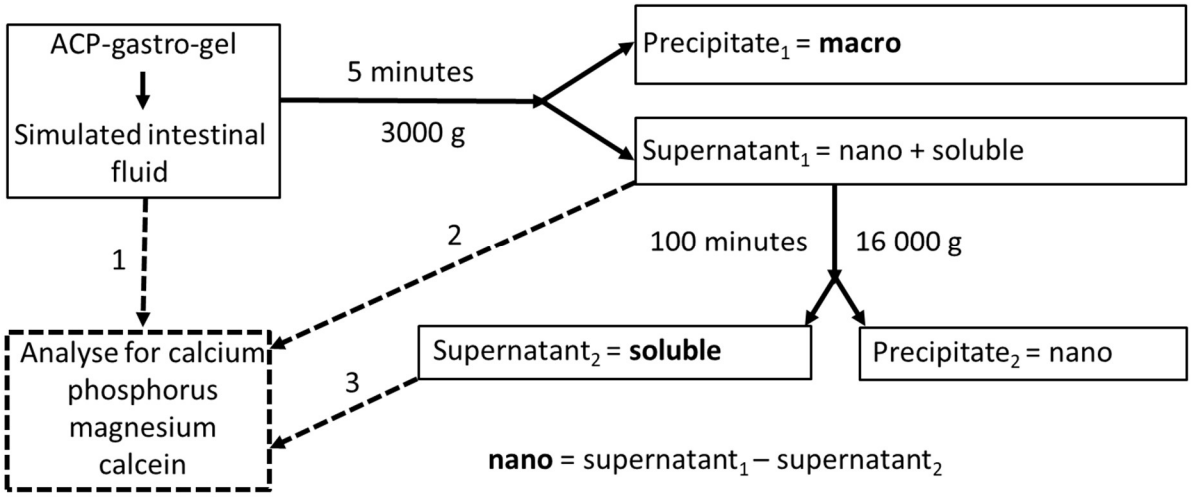

Figure 5.3. Schematic of the sedimentation-based simulated intestinal release assay. Sample 1 gives the total concentration, sample 2 the sum of the nanoparticulate and soluble fractions, and sample 3 gives the soluble concentration.

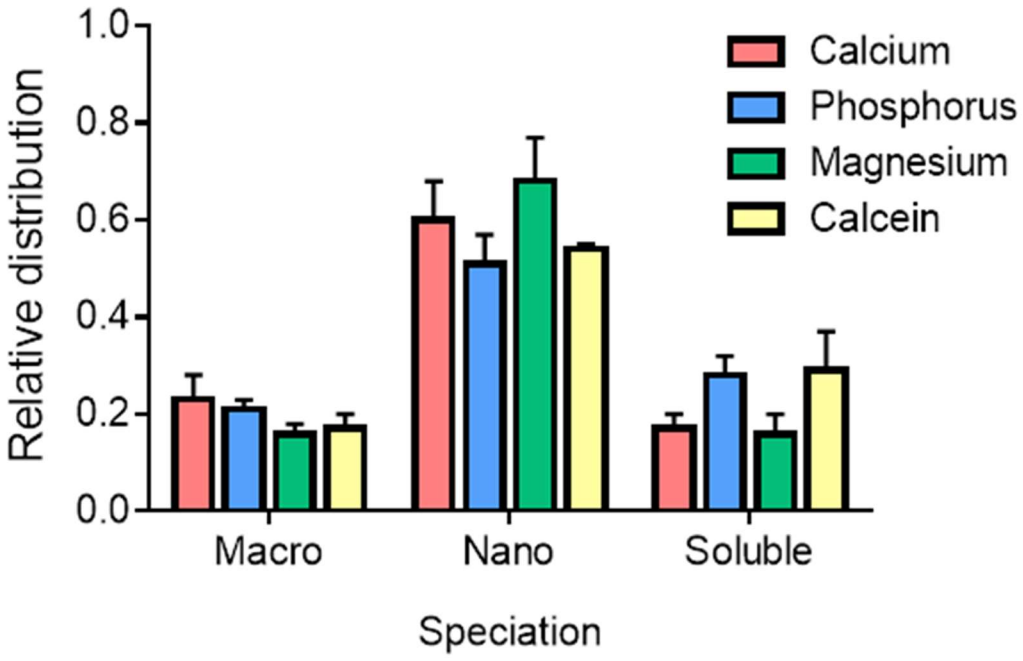

Figure 5.4. Speciation of formulated mineral and cargo in the simulated intestinal release assay. Materials were placed in simulated intestinal fluid and fractionated as outlined in Figure 5.3. ICP-OES was used to quantify calcium, magnesium and phosphorus. UV-Vis was used to quantify calcein.

5.2.2 In vivo iteration 1

Being a voluntary administration method, the effectiveness of drug-gel feeding is, *ipso facto*, dependent upon mice wishing to eat the material. In the original protocol (Zhang, 2011), reliable consumption was achieved by: (a) formulating the gels with sucralose and other artificial flavourings to impart a desirable taste for mice (and mask any drug taste) and (b) putting the mice through a 4 day training period, in which they were given empty (non-drug bearing) gels on a daily basis, to overcome their 'neophobia' and to accustom them to the new dietary material. In this method habituation is facilitated by an initial overnight fast to induce hunger although, as noted above, this is not an ideal scenario for a physiological experiment.

Moreover, sucralose is a gastric irritant, and ACP is not expected to have any unpleasant taste, so as simple a system as possible was sought for this work. I prepared ACP-free (but HP-55 containing) gels containing either (i) sucrose, (ii) sucrose and sucralose, or (iii) sucrose, sucralose and vanilla essence. These gels were shipped to our collaborator Prof Dana Philpott at the Department of Immunology, University of Toronto and fed to three mice, per sweetener formulation, daily, for four days, after a single initial overnight fast.

In all cases the gels were readily eaten so the simplest recipe (ie sucrose alone) was pursued for my further work. In the first experimental run, samples were prepared with or without ACP in sucrose-flavoured gels with the gastro-protectant polymer, HP-55. As imaging cargo the ACP was loaded with a Förster resonance energy transfer (FRET) pair of fluorophores, namely calcein and TRITC-conjugated bovine serum albumin, incorporated into the ACP as per chapter 3.

As per the Zhang protocol, for four days all mice received 200 mg of gel per day, either formulated with ACP particles (~4 mg ACP mineral per portion; group A, n=7) or as non-ACP-containing (empty) gels (control group B, n=6), and they ate willingly. On the last day, two hours after feeding, mice were euthanised and target organs recovered (large lymphoid patches of the intestine and mesenteric lymph nodes notably) and snap frozen and embedded in OCT for sectioning and confocal microscopy.

As in the previous chapter, sectioning, immunohistochemistry, and confocal microscopy throughout this chapter were done by Dr Jack Robertson. When sections were viewed by confocal microscopy, tissue from the control mice appeared to have similar fluorescence levels to those of the ACP-fed mice, for both FRET signal and calcein alone. In order to provide a rigorous comparison between control group and gel-fed tissue, a thresholding (signal-subtraction procedure) was carried out wherein fluorescence intensities were rescaled such that, in each channel, control tissue maxima were reduced

to ‘zero’ brightness and thus only signal of greater intensity (than control) would be apparent in the gel-fed tissue. Unfortunately, upon thresholding, neither the Peyer’s Patches (Figure 5.5), caecal patches, nor mesenteric lymph nodes (Figure 5.6) of gel-fed mice exhibited positive signal. On further investigation, it became apparent that within the tissues there was a strong and broad autofluorescent signal peak which was especially high around the FRET signal emission maximum (~560 nm; Figure 5.7). This would effectively preclude detection of the FRET pair (by raising the signal positivity threshold) under the experimental conditions used. Although broad, the autofluorescence peak faded noticeably at shorter and longer wavelengths (Figure 5.7). Accordingly, materials were reformulated with a non-FRET cargo pair that avoided the autofluorescence peak maxima. TRITC-BSA was replaced with a long-wavelength alternative, namely Alexa Fluor 647-conjugated BSA. Calcein was retained in the formulation since, in the absence of a FRET acceptor (ie TRITC), it would be expected to fluoresce much more strongly at its emission maxima (515 nm). As expected, this new cargo pairing was readily incorporated by ACP and well visualised in in vitro testing with murine macrophages (Figure 5.8). As in the previous chapter, the cell culture work for these results was carried out by Dr Rachel Hewitt.

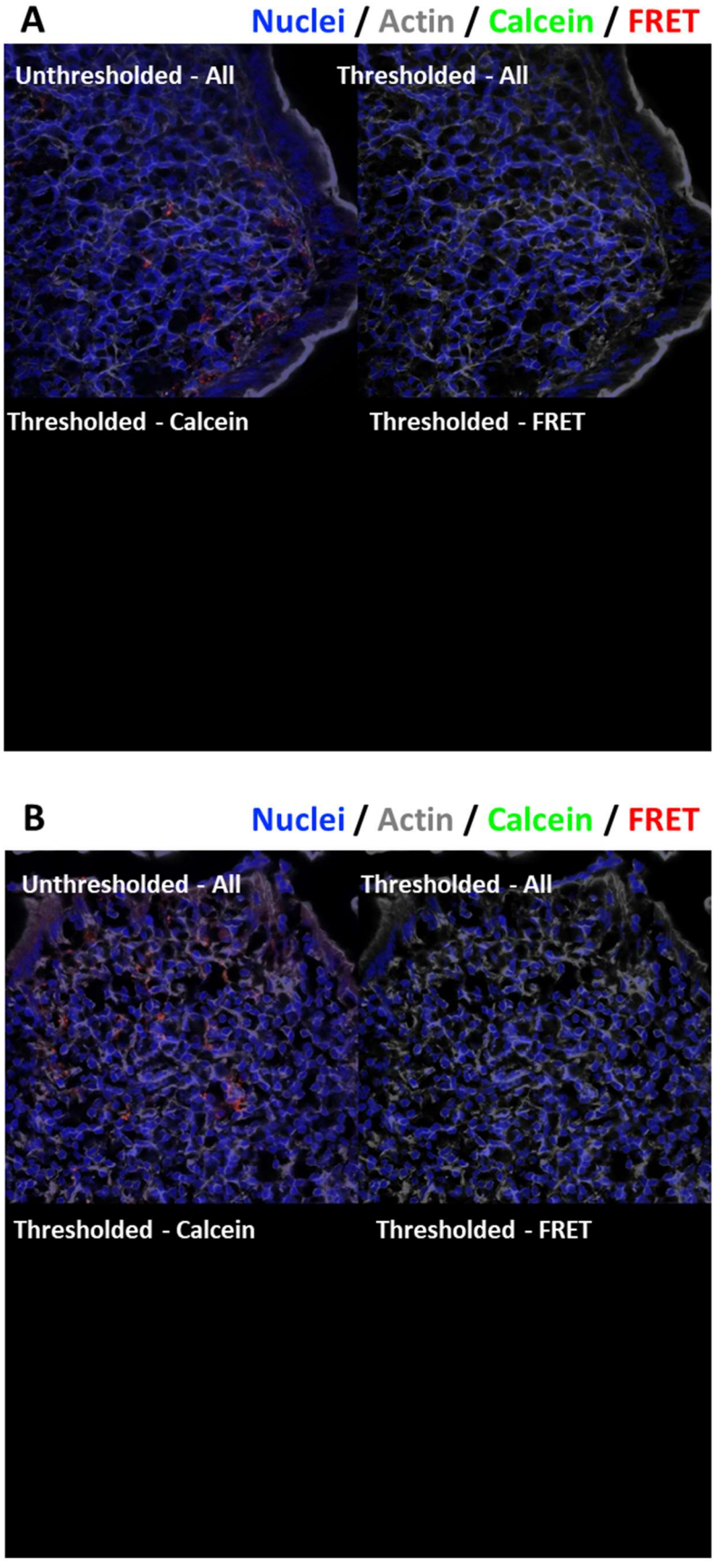

Figure 5.5. Peyer's Patch images of a control (**A**) and a gel fed (**B**) mouse, with and without thresholding, as visualised by confocal microscopy.

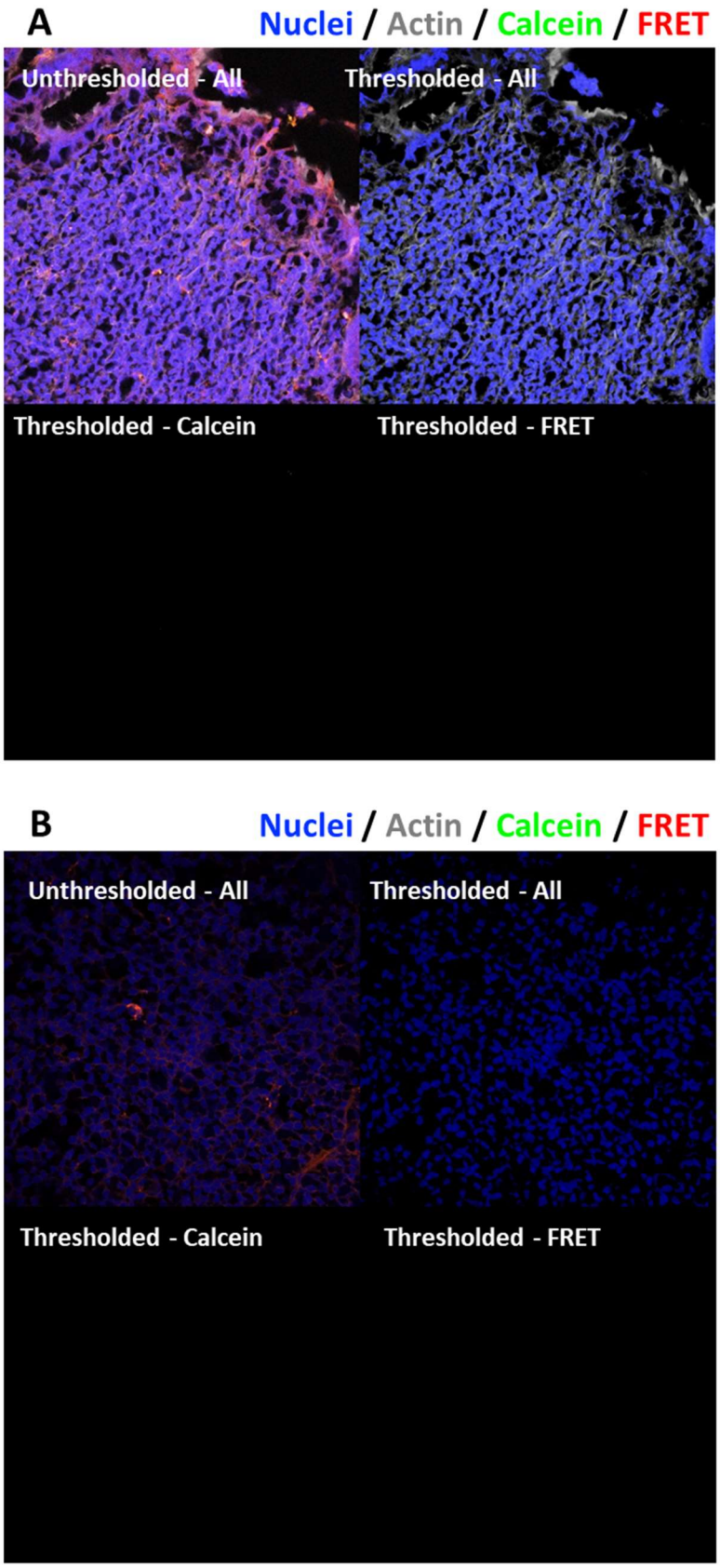

Figure 5.6. Caecal patch (**A**) and mesenteric lymph node (**B**) images from a gel-fed mouse before and after thresholding, as visualised by confocal microscopy.

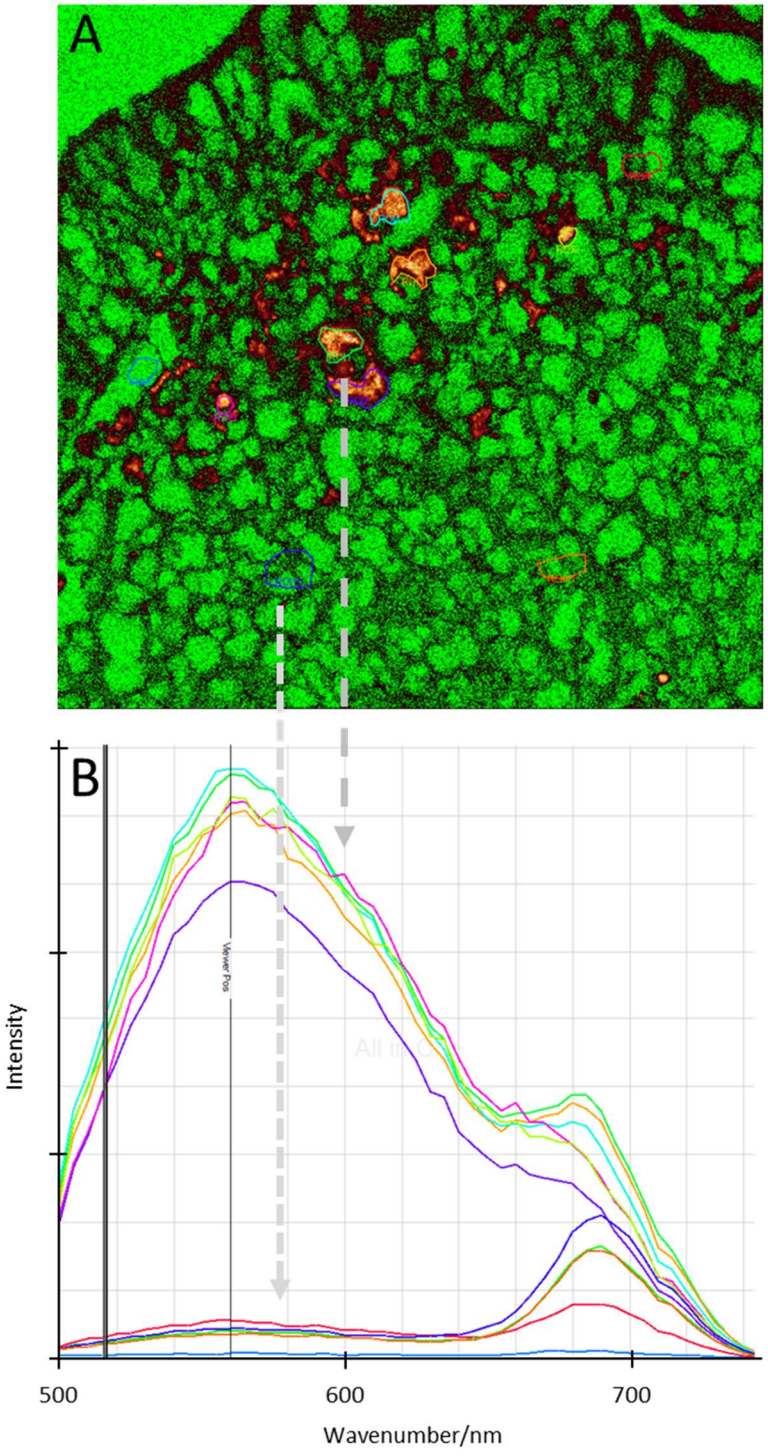

Figure 5.7. Autofluorescence in control group mouse Peyer's patch tissue. Highly fluorescent tissue is red, and normal tissue green, in the confocal image (**A**). Wavelength scans for selected regions (**B**) reveal the scale of the difference in emission intensity and the broad shape of the strong peak, with a maxima at ca. 560 nm

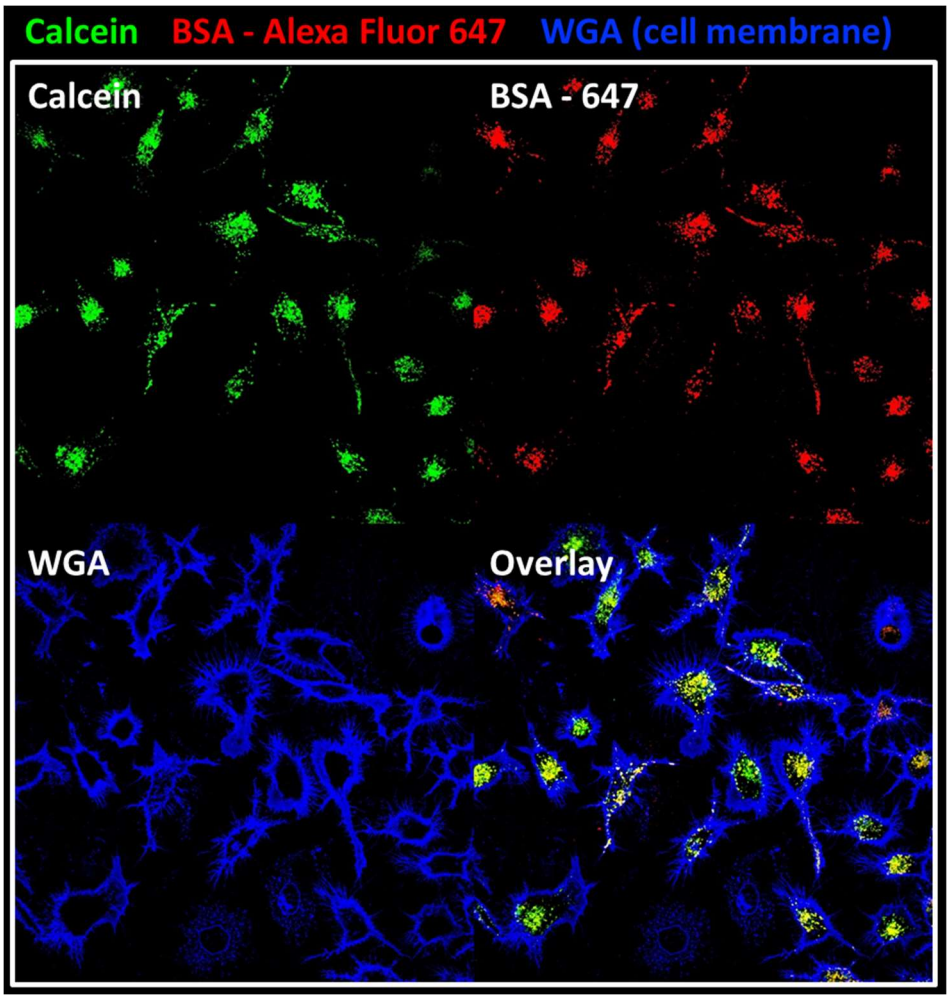

Figure 5.8. Murine RAW cells after in vitro exposure to dual labelled (calcein, Alexa-647-BSA) ACP particles, as visualised by confocal microscopy.

Notwithstanding the issue of elevated autofluorescence in the target tissue, other (hidden) factors could also have contributed to the failure of the first iteration. In particular, the gastro-gels had not previously been tested in vivo and it was possible that they were failing to protect or release their particulate payload, despite the encouraging in vitro data. Consequently, I set out to develop ACP suspensions (liquid formulations) that could be added to the second iteration of in vivo work as a third arm (ie to be tested in parallel with the gel and control groups). Ideally, the suspensions would be administered much like the gels — voluntarily, as sweetened soups — but as a last resort they might be gavaged, despite the aforementioned concerns with that form of administration.

5.2.3 Further formulation

In order for suspensions to successfully deliver ACP particles to the Peyer's Patches of study mice, there were three key prerequisites: First, the suspensions needed to preserve the dispersion and amorphousness of the ACP colloids during transit and study (up to one week). Second, the suspensions needed to be attractive to the mice (for ingestion) and/or suitable for gavage. Third, once administered, the suspensions needed to safely convey the ACP particles through the stomach without dissolution.

As described earlier (Chapter 4, page 84), carboxymethylcellulose-stabilised ACP particles, dispersed in pH 9 water, remain amorphous for at least 7 days. Thus, to ensure amorphousness during transit and testing, I needed only to prepare my suspensions at pH 9 or above. On the other hand, maintaining dispersion over this period of time was likely to be challenging due to the high particle concentrations required in the study. To combat both aggregation and phase transformation, I experimented with non-aqueous biocompatible solvents (glycerol and PEG-400) for my suspensions, finding glycerol to be more effective at maintaining dispersion than water or PEG-400 (Table 5.1). Indeed, suspensions of CMC-ACP in glycerol were largely size stable over 10 days — their z-average increased only to 192 ± 1.6 nm. Glycerol was also attractive as an ingredient since its sweetness would improve gustation and its humectant properties would minimise water activity. Unfortunately, formulating the glycerol suspensions with useful concentrations of bicarbonate or phosphate pH buffer — needed to neutralise stomach acid — led to significant ACP aggregation within 24 hours (Table 5.1) making such formulations unsuitable for transport. However, glycerol suspensions did prove to be compatible with bicarbonate buffer over the short term (Figure 5.9). This finding suggested that a double administration strategy might prove feasible — ie mice sequentially dosed with bicarbonate followed by the ACP-glycerol suspension.

Table 5.1. Dispersion stability of ACP-CMC suspension formulations as determined by dynamic light scattering. Z-average and polydispersity index means from 3 replicate measurements are shown.

Phase A	Phase B	Time/hours	Particle Size/nm	± SD	Polydispersity	± SD
pH 9 water	pH 9 water	0.25	298	5.5	0.33	0.05
pH 9 water	pH 9 water	~16	4306	1522	0.7	0.29
PEG-400	pH 9 water	0.25	312	9.5	0.30	0.06
PEG-400	pH 9 water	~16	2185	1428	0.59	0.28
Glycerol	pH 9 water	0.25	149	1.9	0.12	0.01
Glycerol	pH 9 water	~16	173	5.0	0.21	0.02
Glycerol	H_2CO_3 0.5 mol/L	~16	Could not be measured			
Glycerol	H_2CO_3 0.1 mol/L	~16	3936	1156	0.71	0.26
Glycerol	H_2CO_3 0.01 mol/L	~16	185	1.67	0.18	0.04
Glycerol	H_xPO_4 0.2 mol/L	~16	6011	641	0.16	0.19
Glycerol	H_xPO_4 0.1 mol/L	~16	1115	210	0.59	0.06
Glycerol	H_xPO_4 0.01 mol/L	~16	180	3.72	0.15	0.02

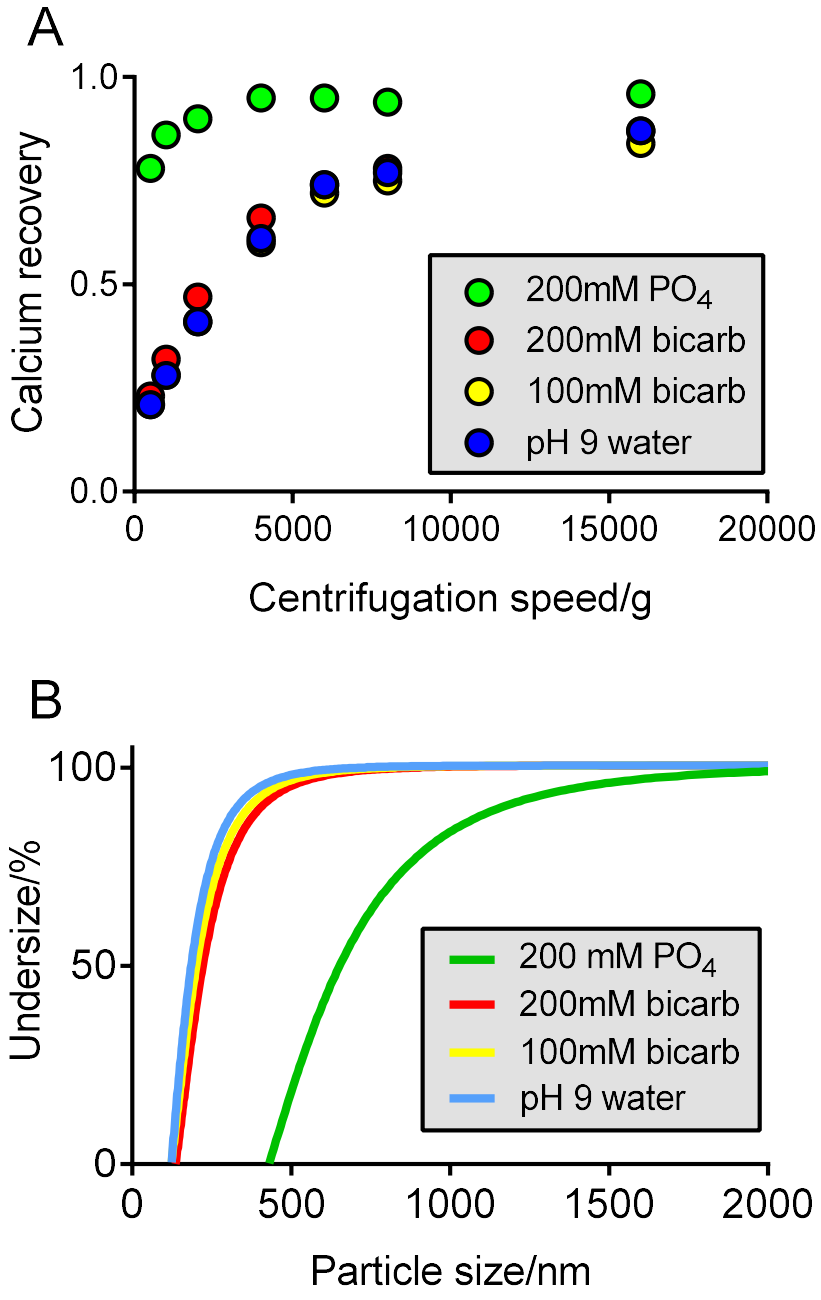

Figure 5.9. Centrifugal sedimentation analysis of ACP glycerol suspensions. After ten days in glycerol, particles were mixed 1:1 with buffer solutions, incubated for two hours then diluted and assayed. Recovery curves for calcium (**A**) were processed into cumulative size distributions (**B**) as described in the previous chapter.

5.2.4 In vivo iteration 2

As previously, prior to the particle feeding study, a training period was required. For this iteration, empty (ACP-free) gels and suspensions and a bicarbonate buffer solution were sent to Toronto. After an overnight fast, the mice consumed both gels and suspensions avidly. However, this was not the case when mice were gavaged with bicarbonate, which understandably interfered with their appetite. This presented a significant problem for the suspensions, since they required concomitant bicarbonate administration to have a chance of surviving the stomach. With the mice reluctant to voluntarily ingest suspensions after receiving bicarbonate, the only practical recourse would have been to sequentially gavage them with bicarbonate and then the particle suspensions. We could not countenance that level of physiological insult so, ultimately, the suspension strategy was abandoned.

During this training period we also experimented with a reduced fasting period of four hours to curtail starvation effects. Unfortunately, short fasts proved insufficient to motivate gel consumption. After a week of unsuccessful training in which the mice underwent multiple fasts, short and long, there was a two-week hiatus to allow them to recover. Following this, the mice were placed on the standard training protocol, as per iteration 1, and ate fairly reliably (Table 5.2).

The second iteration feeding study tested whether Alexa-647 cargo, again with calcein and incorporated into ACP, could be fed to the mice and detected in the key tissue regions (Peyer's patch, caecal patch and MLN). Unfortunately, on this occasion, the mice did not eat well: on the final day, whilst two mice in the control group ate some food, only two (G3 and G4) in the Alexa-647 group 'nibbled' at the gels (Table 5.3).

Table 5.2. Feeding results from the second iteration's second training period.

Mouse	Overnight fast	1 hour fast	1 hour fast	1 hour fast	1 hour fast
C1	All eaten	No interest	Nibbled	No interest	No interest
C2	All eaten	Nibbled	All eaten	Mostly eaten	Mostly eaten
C3	All eaten	All eaten	All eaten	Nibbled	Mostly eaten
C4	All eaten	No interest	Mostly eaten	Mostly eaten	Mostly eaten
G1	All eaten	Mostly eaten	Mostly eaten	Mostly eaten	Nibbled
G2	All eaten	Nibbled	Mostly eaten	Nibbled	Mostly eaten
G3	All eaten	Nibbled	Nibbled	Nibbled	Mostly eaten
G4	All eaten	Mostly eaten	Mostly eaten	Nibbled	Mostly eaten

Table 5.3. Feeding results from the second iteration study

Mouse	Day 1	Day 2	Day 3	Day 4	Sac. time/mins
C1	No interest	All eaten	No interest	No interest	390
C2	Mostly eaten	Mostly eaten	Nibbled	Mostly eaten	375
C3	Mostly eaten	Mostly eaten	Nibbled	Mostly eaten	360
C4	Nibbled	Nibbled	Mostly eaten	No interest	345
G1	Mostly eaten	Mostly eaten	Mostly eaten	No interest	330
G2	Mostly eaten	Nibbled	Nibbled	No interest	315
G3	Nibbled	Mostly eaten	Nibbled	Nibbled	300
G4	Nibbled	Nibbled	Nibbled	Nibbled	285

Sac. time denotes the time between gel feeding and sacrifice on the last day

Immediately after euthanizing the mice, the intestines were removed and sections (7.5 cm in length) were flushed with saline from three areas, namely the lower, mid and proximal small bowel (i.e ileum, mid-lower jejunum, and duodenum/upper jejunum). Additionally, the target tissues were taken and snap frozen for microscopy (ie ileal and caecal lymphoid patches and mesenteric lymph nodes).

Initially, I undertook fluorescence analysis of the luminal flushings, showing that one of the particle fed mice (G3), that had nibbled on the food, circa 5 hours prior to culling, had readily detectable signal for both calcein (fluorescence at 525 nm) and Alexa-647-BSA (absorption at 647 nm) in material from the distal small bowel lumen (Figure 5.10). Subsequent tissue imaging, by confocal microscopy, confirmed marked fluorescence in the Alexa-647 channel in Peyer's patches of the same individual (G3). Other mice showed little indication of Alexa-647 in either their luminal washings or their Peyer's patches. None of the mice had Alexa-647 channel signal in non-Peyer's patch tissue (Figure 5.12) and none of the mice showed signal in the calcein channel anywhere (Figures 5.11 and 5.12).

Several aspects stood out from these analyses. First, and importantly, the study aim to achieve targeted oral delivery of biomolecular cargo to Peyer's patch was successfully met.

Second, of the two individuals (G3 and G4) who consumed ACP-gel on the final study day, one (G3) showed both luminal and tissue signal whilst the other (G4) showed neither. This suggests that some inter-individual difference (in for instance, the amount of material ingested, or transit time) led to little or no cargo reaching the small intestine of G4 on the final day.

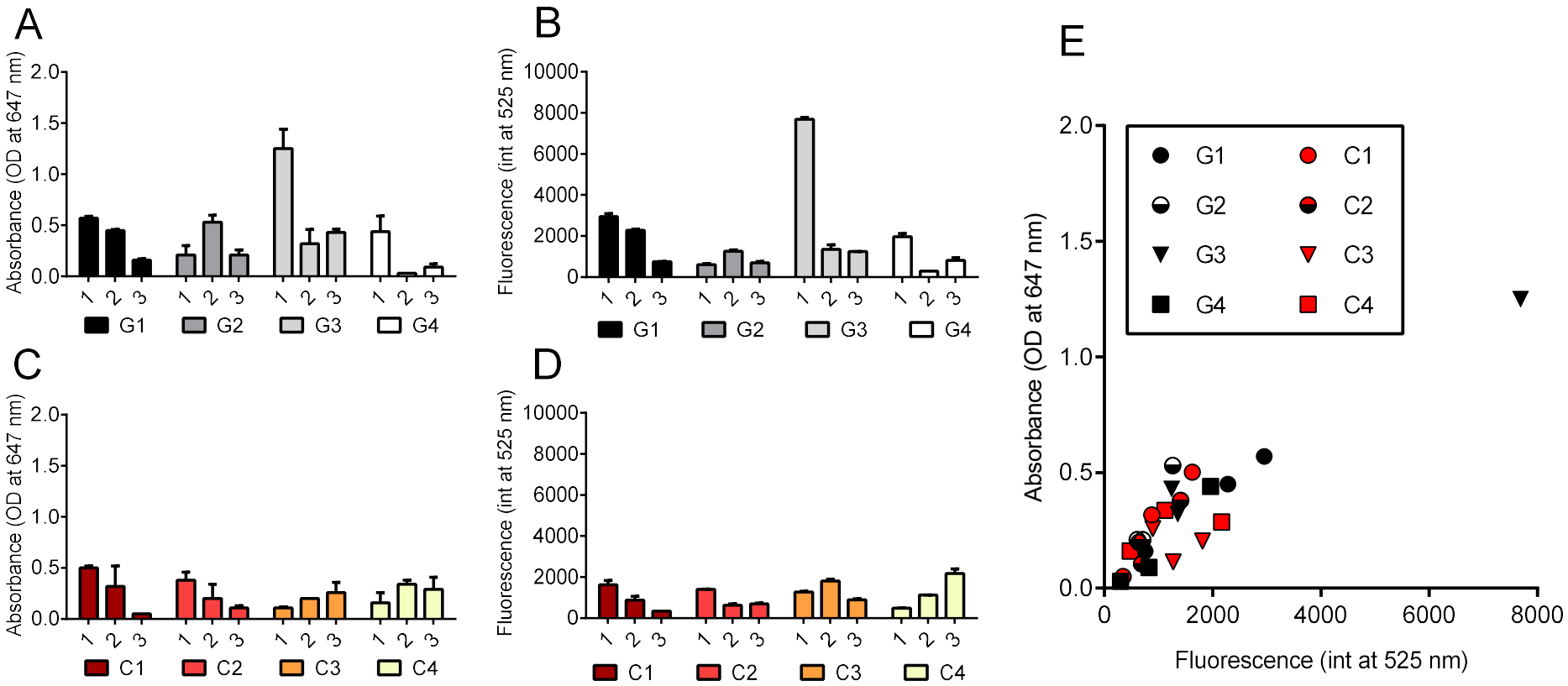

Figure 5.10. Optical spectroscopy of luminal contents from iteration two mice. Data are presented for the four gel-fed mice (G1-4) and the four control-group mice (C1-4). Separate flushings from the ileal, jejunal and duodenal tissue (1, 2 and 3 respectively) of ACP-gel fed (**A** & **B**) and control (**C** & **D**) mice were analysed via absorbance (**A** & **C**) and fluorescence (**B** & **D**) to detect Alexa-647 and calcein respectively. One individual (ACP-gel mouse 3) had clear ileal (1) signal above background in both channels, as seen in the summary correlation plot (**E**).

Third, all four of the ACP fed mice had partaken of gel during the study but as noted, only G3 had detectable tissue labelling. Thus, either G3 was an outlier due to some quirk of physiology (such as abnormally efficient particle uptake), or, more parsimoniously, was an outlier due to being the only animal to receive an effective dose of label on the final day. The other mice may well have had equivalent fluorescent signal in their patches earlier in the study — and it been cleared or quenched prior to sacrifice. The clearance kinetics of Peyer's patches are not well understood. In man, nano and micro-particles of dietary titania and silica are known to accumulate semi-permanently in distinct 'tattoo' cells at the basal aspect of Peyer's patches (Riedle *et al.*, 2020). However, the persistence of such inert materials is of little relevance to the retention of in-tact antigen or labile particles, let alone the quenching of fluorophores.

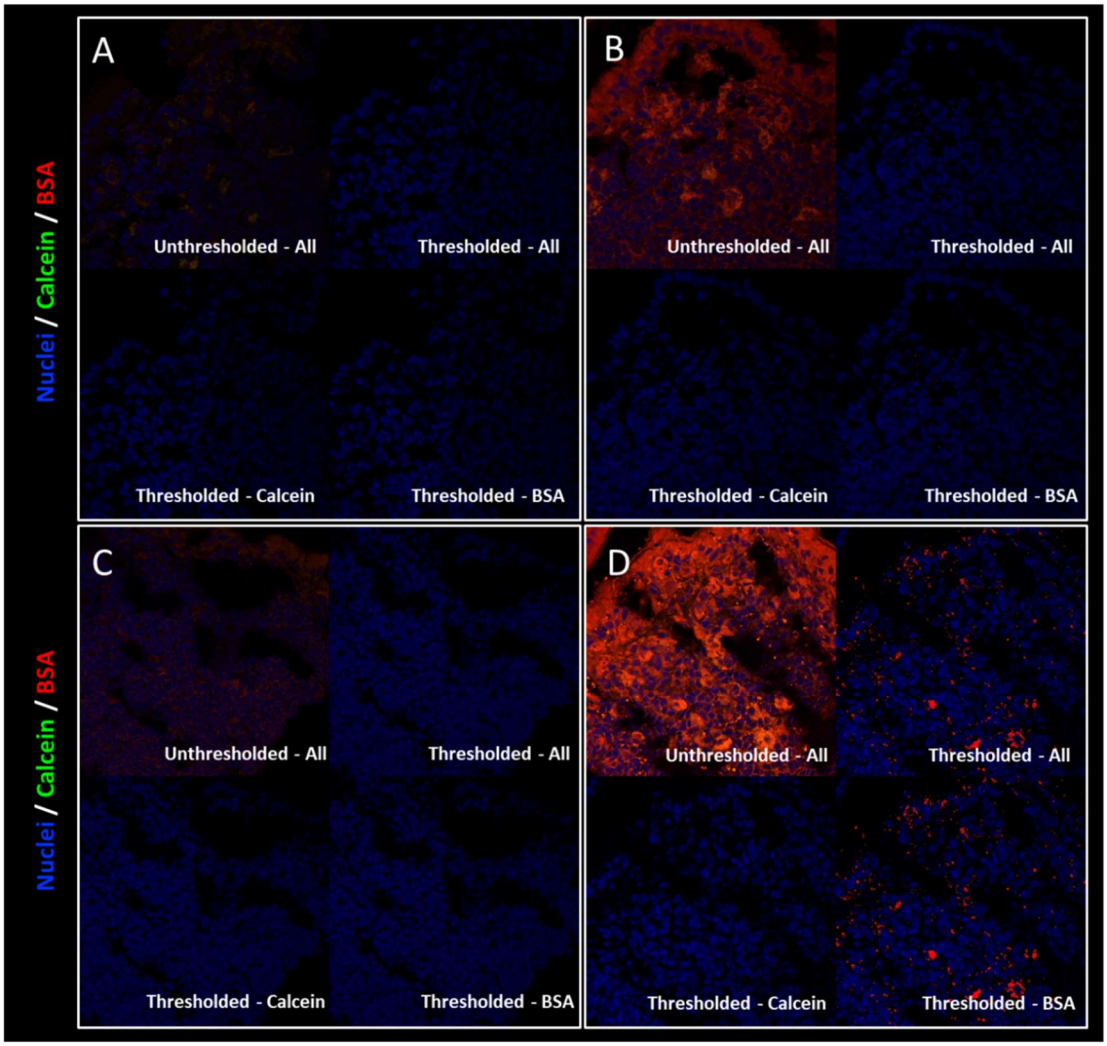

Figure 5.11. Peyer's Patches of control (**A** & **B**) and ACP-gel-fed (**C** & **D**) mouse tissue imaged via confocal microscopy. Raw signal of the highest control mouse (**B**; top left) was used to set thresholds. After thresholding, one individual (mouse G3) exhibited clear signal above background (**D**).

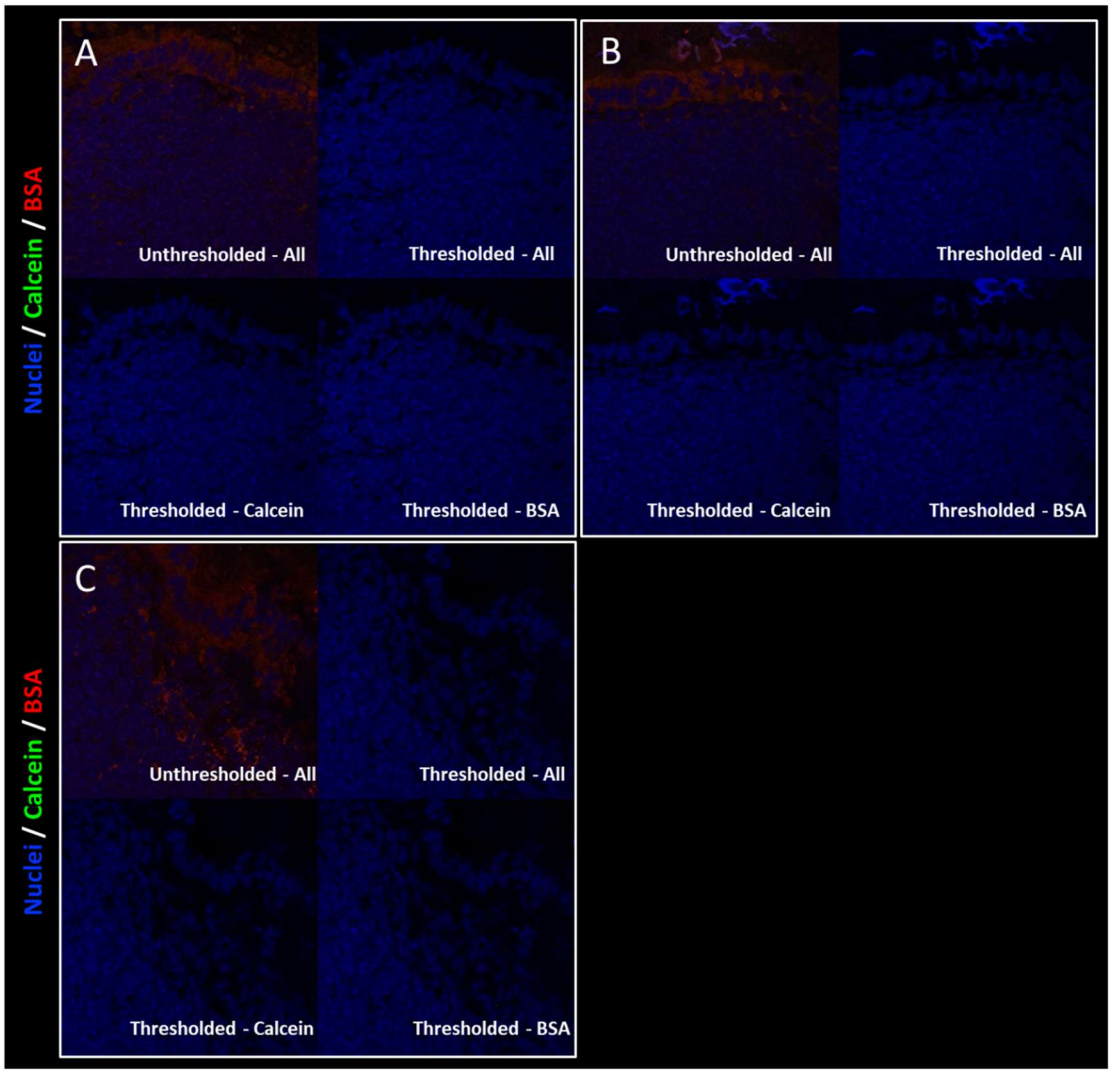

Figure 5.12. Caecal patches of control (**A** & **B**) and ACP-gel-fed (**C**) mouse tissue imaged via confocal microscopy. After thresholding, none of the mice exhibited positive signal.

Fourth, and following from the previous point, calcein signal (above background) was not detected in any tissue from the ACP-gel fed mice. During in vitro cell experiments, calcein fluorescence shows almost total attenuation within 24 hours (Miles *et al.*, 2015). Thus, in this study, a dearth of calcein tissue signal in animals who did not receive an effective final-day dose is unsurprising. However, the lack (of calcein signal) in Alexa-647 positive tissue from G3 — who had received a dose ca. 5 hours prior to sacrifice — is curious. There are several possible explanations for this: (i) attenuation may be more pronounced or rapid in vivo than in vitro; calcein fluorescence is, for instance, particularly vulnerable to quenching by iron (Hirayama and Nagasawa, 2017). (ii) There may be a reasonable amount of calcein signal present but masked by the high background. And/or (iii) the Alexa-647-BSA conjugate may have been uptaken independently (ie after ACP particle dissolution).

Determining which, if any, of these explanations holds water is one avenue for future work to consider, particularly with respect to (iii). Answering whether uptake seen here was due to free protein or due to particle held cargo — and whether that uptake is reproducible with alternative cargo — is germane to the utility of CMC-ACP as a broad-brush delivery tool. However, investigations of that sort will need to be preceded by experimental refinement in several other domains, namely: reliability of administration, sensitivity and reliability of signal detection, and elucidation of patch clearance kinetics.

The second in vivo iteration of this study was hampered by inconsistent dosing due to variable gel consumption, perhaps due to aversive conditioning from the abortive first training period — in which mice were gavaged with bicarbonate prior to training gel exposure. The viability of voluntary gel administration for future work could be easily addressed with prior observational studies in routine animal housing. Although physiologically perturbing, intravenous administration of omeprazole (a proton pump inhibitor) could obviate the need for protective gels entirely.

Analytical challenges surrounding label detection in the ileal environment are likely to prove more intransigent. One approach to mitigate the impact of autofluorescence on thresholding would be to use spectral unmixing, wherein lambda stack (x, y, λ) microscopy data are deconvoluted into underlying emission peaks, pixel by pixel. This would hopefully increase the prominence of distinct cargo signal vs background — which is likely to comprise a multitude of smaller but overlapping components. Collection of such data requires a confocal microscope equipped with a sensitive multispectral detector, such as the 32-channel gallium arsenide phosphide photomultiplier tube recently obtained for our Zeiss LSM 780 platform by my colleagues. Retrospective analyses with this instrument will hopefully prove fruitful here.

Once reliable administration and robust, sensitive, detection have been accomplished, kinetic studies of Peyer's patch particle and antigen processing will be possible. In view of the results presented above, a short time course of up to 24 hours would seem to be a sensible first step.

5.3 Conclusion

In summary, ACP can be loaded with cargo and incorporated into sweetened gels, with a gastro protecting polymer, which mice will eat but in a somewhat picky manner. Heavy fasting forces the mice to eat but that then is not physiological. However, by sifting out the exposed from non-exposed animals, through observations on feeding habits and measurements of 'what's in the gut lumen', it was possible to demonstrate clear Peyer's patch uptake of the cargo. Further work will now be required to understand whether this uptake is reliable and whether it is indeed mediated by the ACP particles or driven by 'free' protein.

5.4 Materials and methods

Methodologies used in this chapter fall roughly into two groupings: fundamental analytical techniques (for instance dynamic light scattering) and more complex assays and experiments. For convenience, commonly applicable details for the fundamental techniques are presented first, in alphabetical (technique) order. Methods for the more involved studies are listed subsequently, in order of their appearance in the results and discussion.

Except where otherwise noted all chemicals were obtained from Sigma Aldrich. Freedom Tubing was obtained from RMS Medical Products, PTFE needles were obtained from Adhesive Dispensing Ltd. Syringes were obtained from VWR. Centrifuge tubes (15 mL and 50 mL) were obtained from ThermoFisher Scientific. Ultrasonication was carried out with a Microson XL2000 (Misonix Ltd, Farmingdale, New York). The enteric polymers HP-55 and Eudragit-L100 were generous gifts from Shin-Etsu PFMD GmbH (Wiesbaden, Germany) and Evonik Industries AG (Darmstadt, Germany) respectively.

5.4.1 Dynamic light scattering

DLS measurements were performed with a Zetasizer Nano ZSP (Malvern Instruments Limited). using Dispersion Technology Software 7.11. 400 µL sample volumes were analysed in disposable polystyrene cuvettes (VWR). In the absence of reliable optical property data for ACP, literature values for hydroxapatite were used: refractive index 1.65, absorbance 0.01. The medium was water, with a refractive index of 1.33 and a viscosity of 1.0031 cP. Measurements were carried out at 20°C, with a brief period of thermal equilibrium (1-2 minutes) prior to measurement, and at a scattering angle of 173°. Measurement position and attenuation factor were automatically optimised by the instrument to minimise secondary scattering and maintain photon counts within the linear range of the detector (100 – 500 kcps). Three to six measurements of at least 10 runs (each of at least 10 seconds) were performed on each sample, with the number of runs and the run duration automatically chosen by the instrument software. The in-build general purpose model was used for data processing. Results were then reported as means ± one standard deviation from measurement replicates .

5.4.2 Inductively coupled plasma — optical emission spectrometry (ICP-OES)

Elemental analyses were carried by ICP-OES (Jobin Yvon Horiba Ultima 2C; Instrument SA, Longjumeau, France), equipped with a concentric nebulizer and cyclonic spray chamber. Plasma gas flow rate was 10 mL/min and sample flow rate was 1 mL/min. Triplicate measurements were made for each sample and means and standard deviations calculated from these. Window size was 0.08 nm (0.04 nm either side of the peak). There were 15 increments per profile and each increment had an integration time of 0.5 seconds. Prior to analysis, samples were diluted down to (analyte) concentrations below 10 mg/L in 5% HNO_3 (v/v). Multi-element calibration standards (50 µg/L to 10 mg/L calcium and phosphorus; 25 µg/L to 5 mg/L magnesium) were also prepared in 5% HNO_3. See Figure 5.13 for an example standard curve. Quantification was carried out using the lines tabulated below (Table 5.4).

To convert measured phosphorus concentrations to phosphate 'amounts', for instance in mass balance calculations, the phosphorus mass was multiplied by the phosphorus:phosphate molar mass ratio.

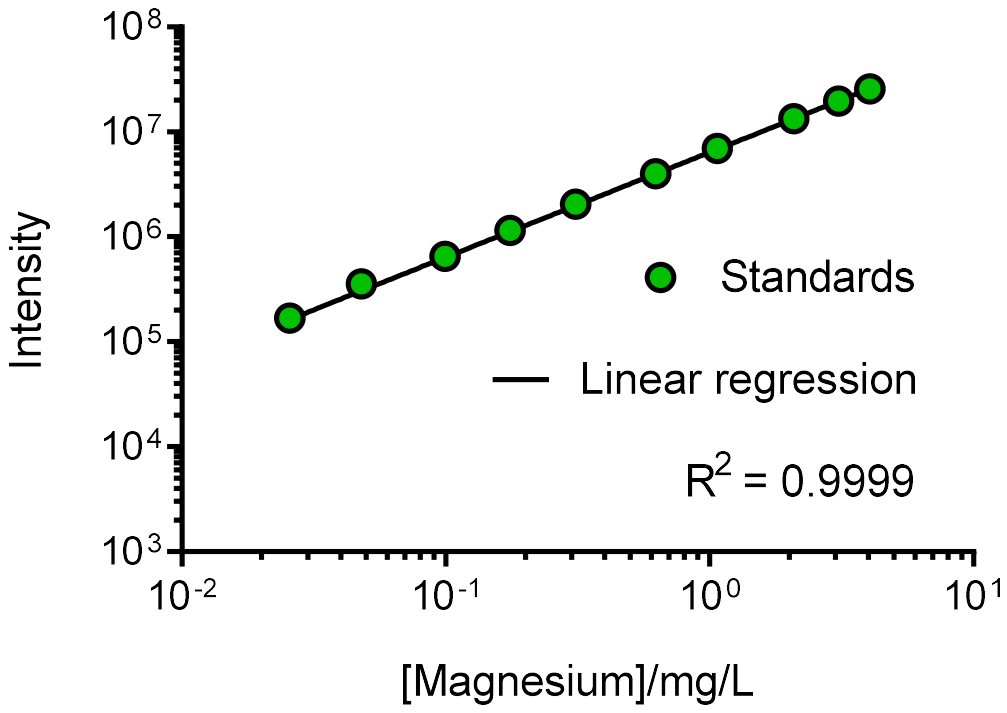

Figure 5.13 An example ICP-OES calibration curve with multielement standards in 5% HNO_3. Emission intensity at the 279.079 nm magnesium line has a linear response to concentration in the 25 µg/L to 5 mg/L concentration range.

Table 5.4 ICP elemental emission lines and estimated detection limits from the literature. Reproduced from chapter 2.

Analyte	Line/nm	Detection limit/µg/L	Reference
Calcium	396.847	0.5	Winge, Peterson and Fassel, 1979
Phosphorus	177.49	200	Nollet and De Gelder, 2013
Magnesium	279.079	30	Winge, Peterson and Fassel, 1979

5.4.3 UV-Vis

Cargo concentrations were determined with a Fujitsu Fluostar Omega plate reader. Calcein concentrations were determined as described in previous chapters. The plate-reader did not have a suitable laser/emission filter set to measure Alexa-647-BSA concentration by fluorescence so optical density (at 647 nm) was used instead (Figure 5.14). Concentrations were determined by interpolating a linear regression between matrix matched standards of known concentration. Each sample and standard was analysed in duplicate wells and the mean values were used.

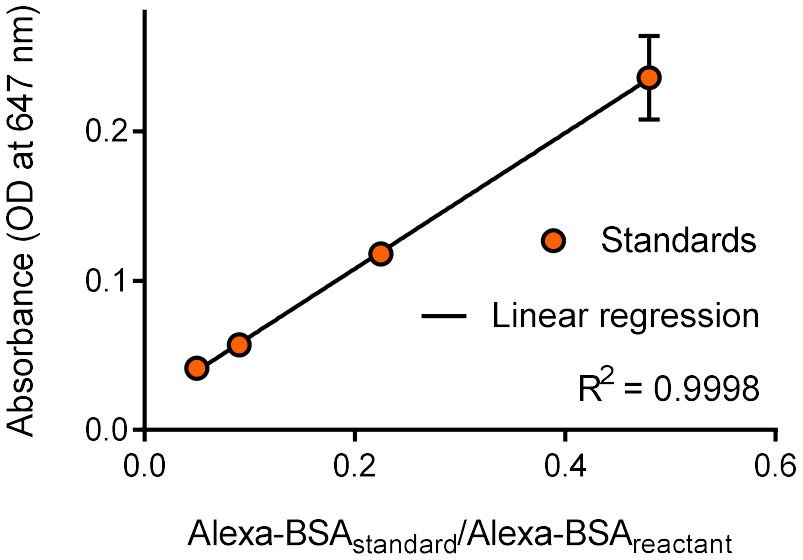

Figure 5.14 An example UV-vis calibration curve with matrix-matched Alexa-647-BSA standards

5.4.4 Particle synthesis

A higher scale implementation of the previously described synthesis was used to prepare CMC-ACP colloids. Thus, two 20 mL plastic luer-lok syringes (Becton Dickinson) were loaded with the reactant solutions and connected to PTFE needles (Adhesive dispensing Ltd.) via Freedom 2400 medical grade tubing (RMS Medical Supplies). PTFE needle nozzles were orientated at a θ of approximately

110°, above a 40 mL volume of 1% CMC solution. Reactants were simultaneously pumped (20 mL each) from the syringes using an Elite 11 Syringe pump (Harvard Apparatus) at flow rates of 20 mL/min. The resultant impinging jets collided and cascaded into the dispersant solution under vigorous (magnetic stirrer-bar) agitation. This initial product was decanted, in equal parts, into two 50 mL centrifuge tubes and these were immediately centrifuged at 20 000 g for 40 minutes to recover the particles and remove unbound cargo and excess dispersant in the supernatant. Particles were then resuspended by ultrasonication in formulation matrix as described elsewhere.

As in previous chapters, reactant solutions were (i) phosphate: 50 mMol/L PO_4, 100 mMol/L tris, pH 9 and (ii) metal: 40 mMol/L Ca^{2+}, 10 mMol/L Mg^{2+}, 100 mMol/L tris, also pH 9. The dispersant solution of carboxymethylcellulose (1% w/w) was also at pH 9 and buffered with 100 mMol/L tris. Cargo was diluted into phosphate solution. For in vitro formulation testing, calcein alone was used, at 0.4 mg/mL. For the first in vivo iteration, calcein was used at 0.01 mg/mL and TRITC-BSA at 0.4 mg/mL. For the second in vivo study, calcein was used at 0.1 mg/mL and Alexa-647-BSA at 0.4 mg/mL.

5.4.5 Formulation

Gel formulations for in vitro studies were prepared by resuspending CMC-ACP particle pellets (from synthesis) in alkaline aqueous solutions of enteric polymer and glycerol and adding either gelatine or hydroxyethylcellulose (HEC). Enteric polymers were solubilised in aqueous alkali as follows: 50 mL centrifuge tubes were partially filled with 22 mL of UHP water and 2 mL of 5 M NaOH. Portions of polymer were then added, with mixing, until a mass of 5.0 g ± 0.05 g had been added. Tubes were then mixed overnight on a rotary mixer. Gelatin stock was prepared by placing 5 g of gelatin in 25 g of cold water and heating until the solution cleared. ACP particles were prepared as described above, and following centrifugation, pellets were resuspended in pH 9 water at one fiftieth of their original volume, the resultant suspension was then mixed with enteric polymer solution and glycerol at mass ratios of 2:2:1. To this, HEC was added at 1% w/w ,or in the case of gelatine formulations, the suspension was heated to 50 °C in a thermostatic waterbath and 2 parts of hot gelatine stock added to 8 parts of ACP-glycerol-enteric-polymer suspension. The in vivo study gels were prepared as above, except that flavourings were added to the suspensions prior to HEC, at a mass ratio of 1:5. Where sucralose and sucrose were both used it was at a ratio of 1:1. Where vanilla essence was used it was used at 1 (ca. 20 µL) drop per 2 grams of gel formulation. The final gels used for in vivo testing had calcium, magnesium and phosphorus concentrations of 161 ± 5 mMol/kg, 44 ± 4 mMol/kg, and 132 ± 4 mMol/kg. Thus, each mouse consuming a 200 mg portion of gel would receive ~ 4 mg of ACP.

Suspension formulations developed in section 5.5.3 were prepared similarly to the gels; after standard ACP syntheses, centrifugation pellets were resuspended at one tenth their original volume in glycerol. Particle-glycerol suspensions were then incubated thus for varying periods of time (up to one week) before being mixed 1:1 with pH 9 buffer solutions. After a further incubation of up to 24 hours, these buffered suspensions were diluted 50 fold in UHP water and analysed via dynamic light scattering and/or centrifugal sedimentation. The latter was carried out exactly as described in the previous chapter, except that single phase association fitting was to calcium recovery data (rather than mean analyte data).

5.4.6 Gastro-protection assay

Assay buffer was prepared by pH adjusting a 100 mMol/L sodium citrate buffer to pH 2 ± 0.1 with 12 Mol/L HCl. Portions of ACP containing enteric gel (0.5 g) were placed in 4.5 g of assay buffer in 15 mL centrifuge tubes (ThermoFisher Scientific), shaken vigorously for 10 seconds and then mixed in a hybridisation oven (Boekel Scientific) for 30 minutes at 37°C. Tubes were then centrifuged at 16000 g for 10 minutes, following which, samples from their supernatants were diluted in: (i) UHP water or (ii) 5% HNO_3 (w/w), for analysis by UV-vis (calcein cargo) and ICP-OES (calcium and phosphorus) respectively.

5.4.7 Release assays

Citrate buffer

Gastric buffer was prepared as above. For the intestinal stage, trisodium citrate was dissolved in UHP water at 100 mMol/L and pH adjusted to 7.2. Portions of ACP containing enteric gel (0.5 g) were placed in 4.5 g of assay buffer in 15 mL centrifuge tubes, shaken vigorously for 10 seconds and then mixed in a hybridisation oven (Boekel Scientific) for 30 minutes at 37°C. Tubes were then centrifuged at 100 g for 5 minutes and the supernatants removed carefully. Subsequently, loose precipitates were resuspended in 4.5 mL of pH 7.2 citrate buffer and incubated for 90 minutes in a hybridisation oven at 37°C before being centrifuged at 16000 g for 100 minutes. Supernatant aliquots were then diluted in 5% HNO_3 and analysed for calcium and phosphate.

Simulated intestinal fluid

Gastric buffer and exposure were as per the citrate buffer assay. Following gentle centrifugation (100 g for 5 minutes), loose precipitates were resuspended in 4.5 mL of pH 7.4 intestinal release buffer comprising 10 mMol/L $NaHCO_3$, 150 mMol/L tris, 100 mMol/L KCl, 2.5 g/L bovine serum albumin, 4 mMol/L sodium taurocholate and 0.5 mMol/L lecithin. Samples were then incubated for 90 minutes in a hybridisation oven at 37°C before being processed as follows. Three 1 mL aliquots were withdrawn from each tube into cylindrical 2 mL centrifuge tubes (ThermoFisher Scientific). One was diluted for analysis without further processing. A second aliquot was centrifuged at 3000 g for 5 minutes to sediment all large particles whilst minimising collection of nanoparticulate ACP. The third aliquot was centrifuged at 16 000 g for 100 minutes to collect all the nanoparticles in solution. Supernatants from the centrifuged tubes were diluted for analysis. Dilution was in UHP water for UV-Vis and in 5% HNO_3 for ICP-OES. Centrifugation parameters for this version of the reduced assay were adjusted from the values used in the previous chapter to account for the greater viscosity of the assay solutions here (14 cP vs 0.89 cP for water). Viscosity measurements were made with a SV-10 Vibro Viscometer (A&D Ltd, Japan) at 25°C.

5.4.8 In vivo studies

C57BL/6 mice were maintained under specific pathogen free conditions in individual housing. For both training and experiments, each mouse received a single 200 mg portion of gel per day. All mouse experiments were conducted as approved by the University of Toronto animal care committee in accordance with the regulations of the Canadian Council on animal care.

5.4.9 Tissue Imaging

Snap frozen tissue was embedded in OCT and sectioned at 12 µm with a cryo ultramicrotome. Samples were then fixed with 4% paraformaldehyde (PFA) for 10 minutes at room temperature and following this, washed three times, 3 minutes per wash, with phosphate buffered saline (PBS). After the last sample wash, PBS was removed and the cells were incubated with Hoescht 33342 (ThermoFisher Scientific) for 20 minutes at room temperature. After this, cells were washed again, 3 times with PBS, for 3 minutes each. 1 drop of antifade (Prolong diamond; Thermofisher Scientific) was then added to each sample and they were then mounted. Imaging was carried out using an SP8 confocal microscope (Leica) using using Ar/ArKr and He/Ne Lasers. Images were collected with Leica Application Suite software.

5.4.10 In vitro cell studies

Raw 264.7 monocyte/macrophage cells purchased from the American Type Culture Collection (ATCC) were grown on coverslips according to ATCC suggested culture methods. Cells were pre-stimulated with peptidoglycan from Staphylococcus aureus [Invivogen tlrl-pgns2] by adding 1 microgram per mL to the cell culture media the evening prior to the experiment in order to induce differentiation to a macrophage phenotype prior to particle incubations. Particles in replete tissue culture media were then added to the RAW macrophages at 3 to 4 mMol/L [calcium] with coverslips in and incubated for 3 hours.

After incubation, cells were processed for confocal microscopy as follows. Sample staining, incubations and washes all took place with gentle rotation on an orbital shaker. Media was removed from chambers/wells and 4% paraformaldehyde (PFA) was added for 10 minutes at room temperature. PFA was then removed and cells were washed three times, 3 minutes were wash, with phosphate buffered saline (PBS). After the last wash, PBS was removed and the cells were incubated with Wheat Germ Agglutinin, Alexa Fluor 555 Conjugate (Thermofisher Scientific) 20μg/ml for 10 minutes. After this, cells were washed again, 3 times with PBS, for 3 minutes each. 1 drop of antifade (Prolong diamond; Thermofisher Scientific) was then added to each sample and they were then mounted. Imaging was carried out using an SP8 confocal microscope (Leica) with images collected using Leica Application Suite software.

Chapter 6 General Conclusion

Oral administration platforms for biological actives are highly sought after, yet remain elusive. Peyer's patches are one important delivery target, and due to their size-specific uptake requirements, have seen significant attention from nanoparticulate vehicles. To date, efforts have been largely confined to polymeric particles; few studies have been conducted with inorganic materials. In this thesis, amorphous calcium phosphate, a widely used in vitro transfection agent, was trialled as an in vivo delivery material.

6.1 Summary of results

Firstly, this thesis ascertained preferable synthetic conditions for cargo-carrying ACP as a bulk material, ensuring good yield and purity of mineral product whilst minimising the risk of cargo-degradation. Further, it established the limitations of ACP in simulated physiological conditions and demonstrated how these could be remediated by modifying the mineral with magnesium and protein.

Secondly, it developed an impinging jet reactor and applied it to producing disperse ACP nanoparticles at suitable scale and concentration for in vivo formulation, which was an advance on the current state of the art. Materials from this process were then characterised extensively and optimised for stability in simulated physiological conditions and for visualisation by confocal microscopy.

Thirdly, a novel formulation method, employing gastro-protective polymers in edible gels, was used to deliver formulated ACP nanoparticles to mice orally. Through iterative testing, targeted, proof of principle delivery to Peyer's patches was demonstrated with fluorescent protein cargo.

6.2 Conclusion

Inorganic nanoparticles are a promising and underexplored means of effecting oral delivery of biological cargo. Amorphous calcium phosphate (ACP) is a capable in vitro cargo vehicle and as shown in this work, this is also the case, within certain limitations, in vivo.

As a material, production and use of ACP is complicated by its rapid precipitation and pH sensitive solubility. Yet these shortcomings are entwined with significant advantages, such as trapping cargo effectively and being non-persistent — and thus well tolerated. In this thesis, speed and safety were prioritised; intestinal particle dissolution was worked around simply by formulating materials at greater concentrations, accepting some degree of losses. A more elegant solution would be to coat particles with a dispersant that reduced their lability, as has been done with iron oxide nanoparticles for intravenous injection (Bhandari *et al.*, 2018). Such a strategy would undoubtedly require fine-tuning to balance luminal loss prevention against the need to avoid particle persistence in tissue, but it should be possible to strike a compromise between these demands.

Further in vivo studies must ensure reliable administration and signal detection, both of which were found wanting in this work, and then proceed to evaluate Peyer's patch processing kinetics. Currently, the clearance rates of digestible cargo from Peyer's patches are poorly understood and moderately labile particles loaded with fluorescent and (rare) elemental labels would be well-suited to address this.

Appendix A Mineral Studies

A.1 PHREEQC Calculations

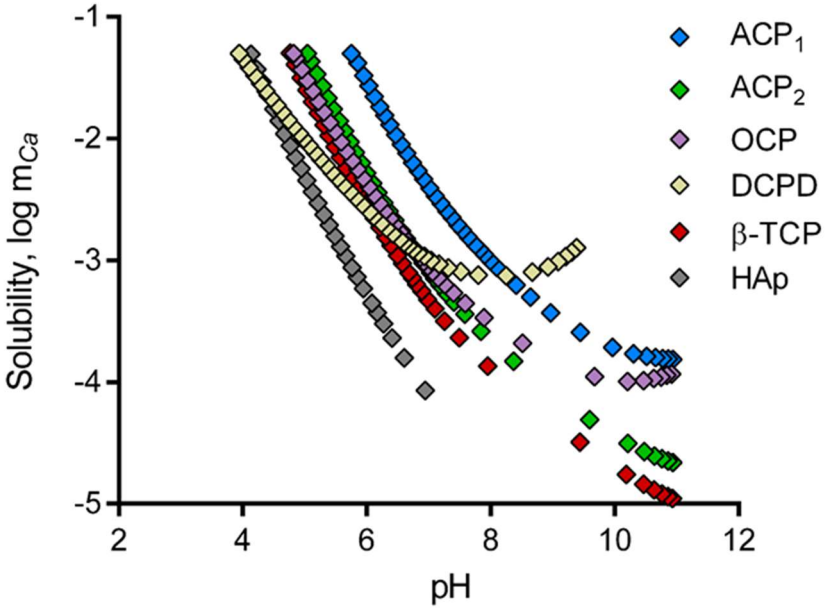

Figure A.1.1 PHREEQC solubility simulations for calcium phosphate minerals. Modelling entailed an excess of each mineral (10 mol) being titrated down from pH 11 with 1 mol of HCl in 10000 steps at 25 °C. Both ACP isomorphs were considered, along with octacalcium phosphate (OCP), dicalcium phosphate dihydrate (DCPD), beta-tri-calcium phosphate (TCP) and hydroxyapatite (HAp). Modelling entailed an excess of each mineral (10 mol) being titrated down from pH 11 with 1 mol of HCl in 10000 steps at 25°C.

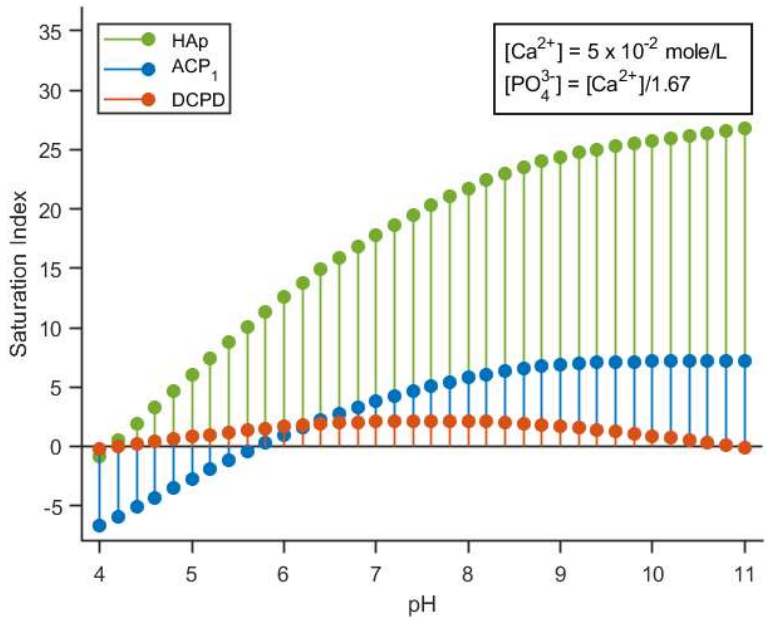

Figure A.1.2 Calculated saturation indices (SI) of ACP_1, DCPD and HAp in the $CaCl_2$–Na_2HPO_4–H_2O system.

General PHREEQC Code (applies to both methods):

# denotes comment (not passed to the interpreter)

PHASES

```
#-----------------------------------------------------
# Expressions of the form MnAb(s) = nM+ + bA-
# Values at 25C
# Where possible, values taken from IUPAC critical evaluations or cross-referenced from multiple authors.

#-------------------------------------------------------------
# Sources
# CRC Handbook of Chemistry and Physics 91st Edition
# IUPAC Solubility Data Series, Volume 52: Alkaline Earth Hydroxides
# IUPAC Solubility Data Series Volume 23: COPPER, SILVER, GOLD AND ZINC, CADMIUM, MERCURY OXIDES AND HYDROXIDES
# Cornell, R. M., & Schwertmann, U. (2003). The iron oxides: structure, properties, reactions, occurrences and uses. John Wiley & Sons. (page 216)
# Swain, H. A., Lee, C., & Rozelle, R. B. (1975). Determination of the solubility of manganese hydroxide and manganese dioxide at 25. deg. by atomic absorption spectrometry. Analytical Chemistry, 47(7), 1135-1137.
# Holt Jr, L. E., Pierce, J. A., & Kajdi, C. N. (1954). The solubility of the phosphates of strontium, barium, and magnesium and their relation to the problem of calcification. Journal of Colloid Science, 9(5), 409-426.
# minteq v4 database
#-------------------------------------------------------------
Aluminium_phosphate # CRC Handbook of Chemistry and Physics 91st Edition
AlPO4 = Al+3 + PO4-3
log_k -20.007

Calcium_hydroxide # CRC Handbook of Chemistry and Physics 91st Edition
Ca(OH)2 = Ca+2 + 2OH-
log_k   -5.299

#Calcium_hydroxide # IUPAC Solubility Data Series, Volume 52
#Ca(OH)2 = Ca+2 + 2OH-
#log_k -5.078
#delta_h  -12.75   #kJ/mol

Calcium_phosphate # CRC Handbook of Chemistry and Physics 91st Edition
Ca3(PO4)2 = 3Ca+2 + 2PO4-3
log_k   -32.684

#Calcium_phosphate # Holt 1954 Journal of Colloid Science
#Ca3(PO4)2 = 3Ca+2 + 2PO4-3
#log_k roughly 31
```

Cupric_hydroxide # IUPAC Solubility Data Series Volume 23
Cu(OH)2 = Cu+2 + 2OH-
log_k -19.32

Cupric_phosphate # CRC Handbook of Chemistry and Physics 91st Edition
Cu3(PO4)2 = 3Cu+2 + 2PO4-3
log_k -36.854

Ferrous_hydroxide # CRC Handbook of Chemistry and Physics 91st Edition
Fe(OH)2 = Fe+2 + 2OH-
log_k -16.31

#Ferrous_hydroxide # The Iron Oxides Cornell and & Schwertmann, reference: Feitknecht & Schindler 1963
#Fe(OH)2 = Fe+2 + 2OH-
#log_k -15.15

Ferrous_phosphate # Vivianite. Minteq v4 database
Fe3(PO4)2:8H2O = 3Fe+2 + 2PO4-3 + 8H2O
log_k -36
delta_h -0 kJ

Ferric_hydroxide # CRC Handbook of Chemistry and Physics 91st Edition
Fe(OH)3 = Fe+3 + 3OH-
log_k -38.554

#Ferric_hydroxide # Ferrihydrite. The Iron Oxides Cornell and & Schwertmann, reference: Langmuir & Whittemore, 1971
#Fe(OH)3 = Fe+3 + 3OH-
#log_k = -39.5

#Ferric_phosphate # CRC Handbook of Chemistry and Physics 91st Edition
#FePO4:2H2O = Fe+3 + PO4-3 + 2H2O
#log_k -15.004

Ferric_phosphate # Strengite. Minteq v4 database
FePO4:2H2O = Fe+3 + PO4-3 + 2H2O
log_k -26.4
delta_h -9.3601 kJ

Magnesium_hydroxide # CRC Handbook of Chemistry and Physics 91st Edition
Mg(OH)2 = Mg+2 + 2OH-
log_k -11.251

#Magnesium_hydroxide # IUPAC Solubility Data Series, Volume 52
#Mg(OH)2 = Mg+2 + 2OH-
#log_k -11.86 # or 9.38 (both tentative values)

```
Magnesium_phosphate # CRC Handbook of Chemistry and Physics 91st Edition
Mg3(PO4)2 = 3Mg+2 + 2PO4-3
log_k   -23.983

#Magnesium_phosphate # Holt 1954 Journal of Colloid Science
#Mg3(PO4)2 = 3Mg+2 + 2PO4-3
#log_k -27.2

#Magnesium_phosphate # Minteq v4 database
#Mg3(PO4)2 = 3Mg+2 + 2PO4-3
#log_k -23.28
#delta_h -0 kJ

Manganese_hydroxide # Swain 1975 Analytical Chemistry
Mn(OH)2 = Mn+2 + 2OH-
log_k = -13.046

Manganese_phosphate # Minteq v4 database
Mn3(PO4)2 = 3Mn+2 + 2PO4-3
log_k   -23.827
delta_h         8.8701kJ

Strontium_hydroxide # IUPAC Solubility Data Series, Volume 52
Sr(OH)2 = Sr+2 + 2OH-
log_k   -3.307

Strontium_phosphate # Holt 1954 Journal of Colloid Science
Sr3(PO4)2 = 3Sr+2 + 2PO4-3
log_k   -27.8

Zinc_hydroxide # CRC Handbook of Chemistry and Physics 91st Edition
Zn(OH)2 = Zn+2 + 2OH-
log_k   -16.523

#Zinc_hydroxide # IUPAC Solubility Data Series Volume 23, reference: Reichle et al
#Zn(OH)2 = Zn+2 + 2OH-
#log_k -16.759

Zinc_phosphate
Zn3(PO4)2:4H2O = 3Zn+2 + 2PO4-3 + 4H2O
log_k   -35.42
delta_h         -0      kJ

END
```

Example excess solid titration specific code as follows:

```
SOLUTION  1  alkaline water
        -units   mmol/L
        -temp   25
        -pH     11

EQUILIBRIUM_PHASES
        ACP1                    0       1

INCREMENTAL_REACTIONS true
REACTION 1
        HCl 1.0
        1 in 10000 steps

SELECTED_OUTPUT
        -file ACP_Dissolution_Curve.sel
        -pH true
        -totals Ca P
        -equilibrium_phases ACP1

END
```

Example Saturation Index method specific code as follows:

```
SELECTED_OUTPUT
        -file SS_metal_phosphates_2019_11_26.sel
        -pH true
        -totals P Ca Cu Fe Mg Mn Sr Zn Cl Na
        -SI Calcium_hydroxide Calcium_phosphate Cupric_hydroxide Cupric_phosphate
Ferrous_hydroxide Ferrous_phosphate Ferric_hydroxide Ferric_phosphate Magnesium_hydroxide
Magnesium_phosphate Manganese_hydroxide Manganese_phosphate Strontium_hydroxide
Strontium_phosphate Zinc_hydroxide Zinc_phosphate

SOLUTION_SPREAD
        -units   mmol/L
        -temp   25
```

Number	pH	P	Ca	Cl	Na
1	2	100	100	210	43
2	2.1	100	100	208	49
3	2.2	100	100	206	55
4	2.3	100	100	205	60
5	2.4	100	100	204	66
6	2.5	100	100	203	71
7	2.6	100	100	203	75
8	2.7	100	100	202	79
9	2.8	100	100	202	83
10	2.9	100	100	201	86
11	3	100	100	201	88
12	3.1	100	100	201	91
13	3.2	100	100	201	92
14	3.3	100	100	201	94
15	3.4	100	100	200	95
16	3.5	100	100	200	96
17	3.6	100	100	200	97
18	3.7	100	100	200	97
19	3.8	100	100	200	98
20	3.9	100	100	200	98
21	4	100	100	200	99
22	4.1	100	100	200	99
23	4.2	100	100	200	99
24	4.3	100	100	200	99
25	4.4	100	100	200	99
26	4.5	100	100	200	100
27	4.6	100	100	200	100
28	4.7	100	100	200	100
29	4.8	100	100	200	100
30	4.9	100	100	200	100
31	5	100	100	200	101
32	5.1	100	100	200	101

33	5.2	100	100	200	101
34	5.3	100	100	200	101
35	5.4	100	100	200	102
36	5.5	100	100	200	102
37	5.6	100	100	200	102
38	5.7	100	100	200	103
39	5.8	100	100	200	104
40	5.9	100	100	200	105
41	6	100	100	200	106
42	6.1	100	100	200	107
43	6.2	100	100	200	109
44	6.3	100	100	200	111
45	6.4	100	100	200	113
46	6.5	100	100	200	116
47	6.6	100	100	200	120
48	6.7	100	100	200	124
49	6.8	100	100	200	128
50	6.9	100	100	200	133
51	7	100	100	200	138
52	7.1	100	100	200	144
53	7.2	100	100	200	149
54	7.3	100	100	200	155
55	7.4	100	100	200	161
56	7.5	100	100	200	166
57	7.6	100	100	200	171
58	7.7	100	100	200	176
59	7.8	100	100	200	180
60	7.9	100	100	200	183
61	8	100	100	200	186
62	8.1	100	100	200	189
63	8.2	100	100	200	191
64	8.3	100	100	200	192
65	8.4	100	100	200	194
66	8.5	100	100	200	195
67	8.6	100	100	200	196
68	8.7	100	100	200	197
69	8.8	100	100	200	198
70	8.9	100	100	200	198
71	9	100	100	200	198
72	9.1	100	100	200	199
73	9.2	100	100	200	199
74	9.3	100	100	200	199
75	9.4	100	100	200	199
76	9.5	100	100	200	200
77	9.6	100	100	200	200
78	9.7	100	100	200	200
79	9.8	100	100	200	200
80	9.9	100	100	200	200

81	10	100	100	200	200
82	10.1	100	100	200	200
83	10.2	100	100	200	200
84	10.3	100	100	200	200
85	10.4	100	100	200	200
86	10.5	100	100	200	200
87	10.6	100	100	200	200
88	10.7	100	100	200	200
89	10.8	100	100	200	201
90	10.9	100	100	200	201
91	11	100	100	200	201
92	11.1	100	100	200	201
93	11.2	100	100	200	202
94	11.3	100	100	200	202
95	11.4	100	100	200	203
96	11.5	100	100	200	203
97	11.6	100	100	200	204
98	11.7	100	100	200	205
99	11.8	100	100	200	206
100	11.9	100	100	200	208
101	12	100	100	200	210
102	12.1	100	100	200	213
103	12.2	100	100	200	216
104	12.3	100	100	200	220
105	12.4	100	100	200	225
106	12.5	100	100	200	232
107	12.6	100	100	200	240
108	12.7	100	100	200	250
109	12.8	100	100	200	263
110	12.9	100	100	200	279
111	13	100	100	200	300
112	13.1	100	100	200	326
113	13.2	100	100	200	358
114	13.3	100	100	200	400
115	13.4	100	100	200	451
116	13.5	100	100	200	516
117	13.6	100	100	200	598
118	13.7	100	100	200	701
119	13.8	100	100	200	831
120	13.9	100	100	200	994
121	14	100	100	200	1200

Appendix B Synthesis of ACP nanoparticles

B.1 Single step co-precipitation

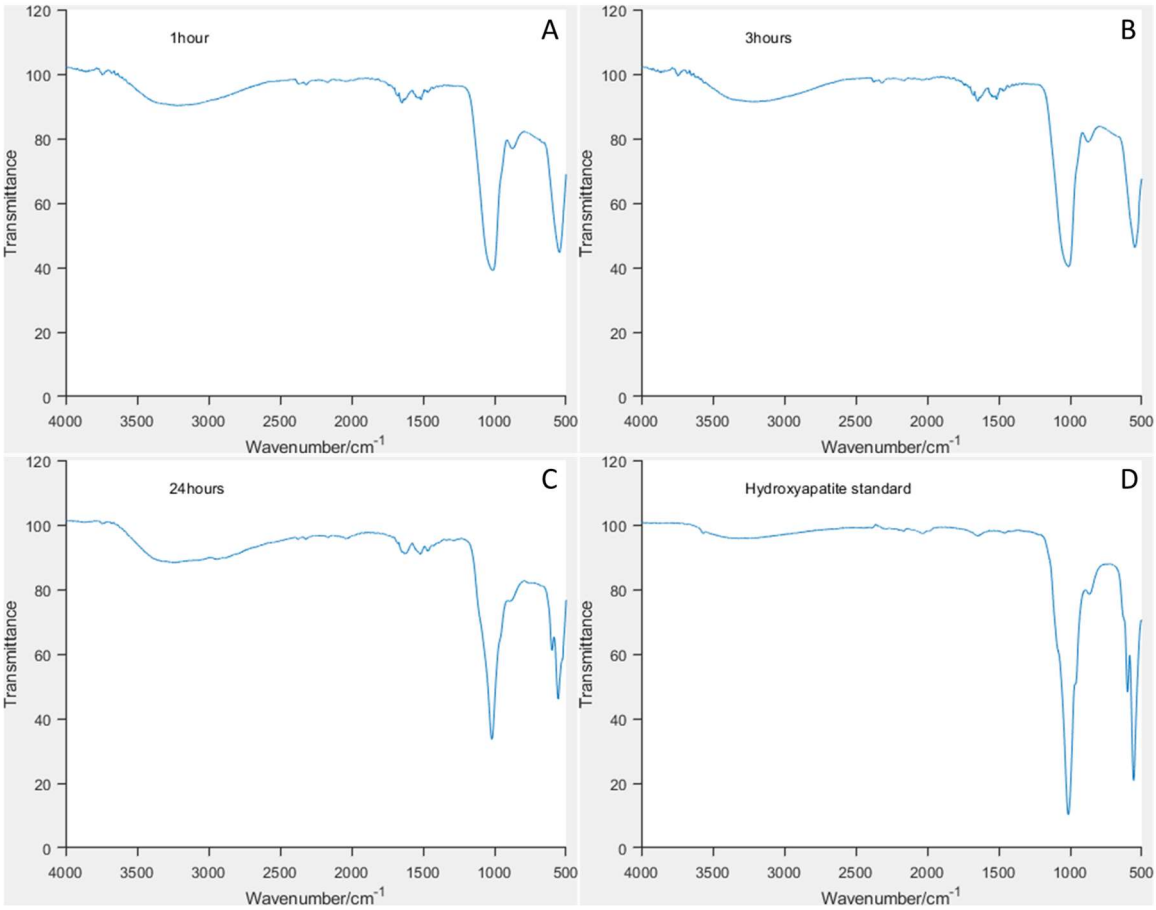

Figure B.1.1 FTIR spectra showing crystallisation of hydroxyapatite from amorphous calcium phosphate in tissue culture media over time (**A**-**C**) in comparison with a hydroxyapatite standard (**D**).

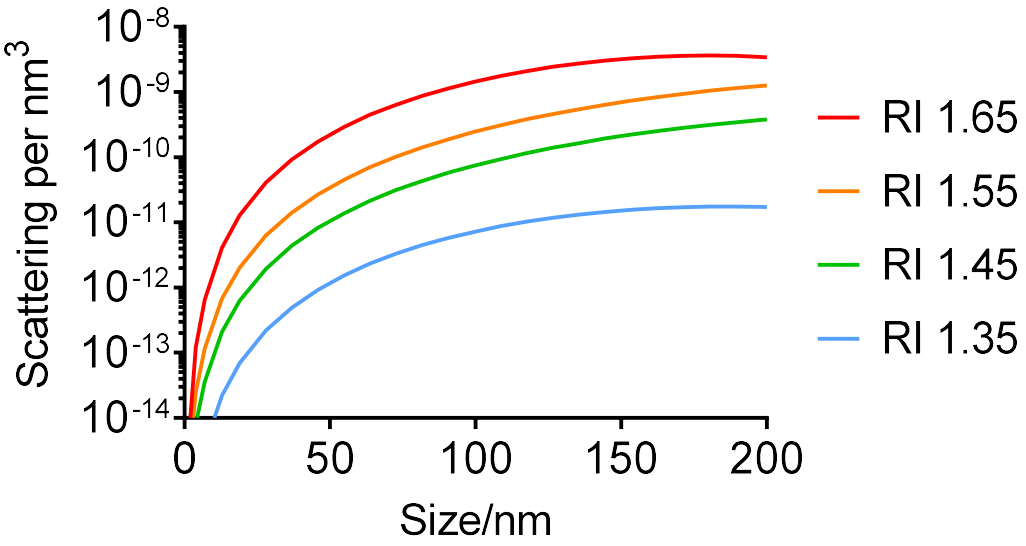

Figure B.1.2 Calculated scattering efficiencies for particles during DLS measurements as a function of refractive index (RI) and size in the 0 –200 nm interval

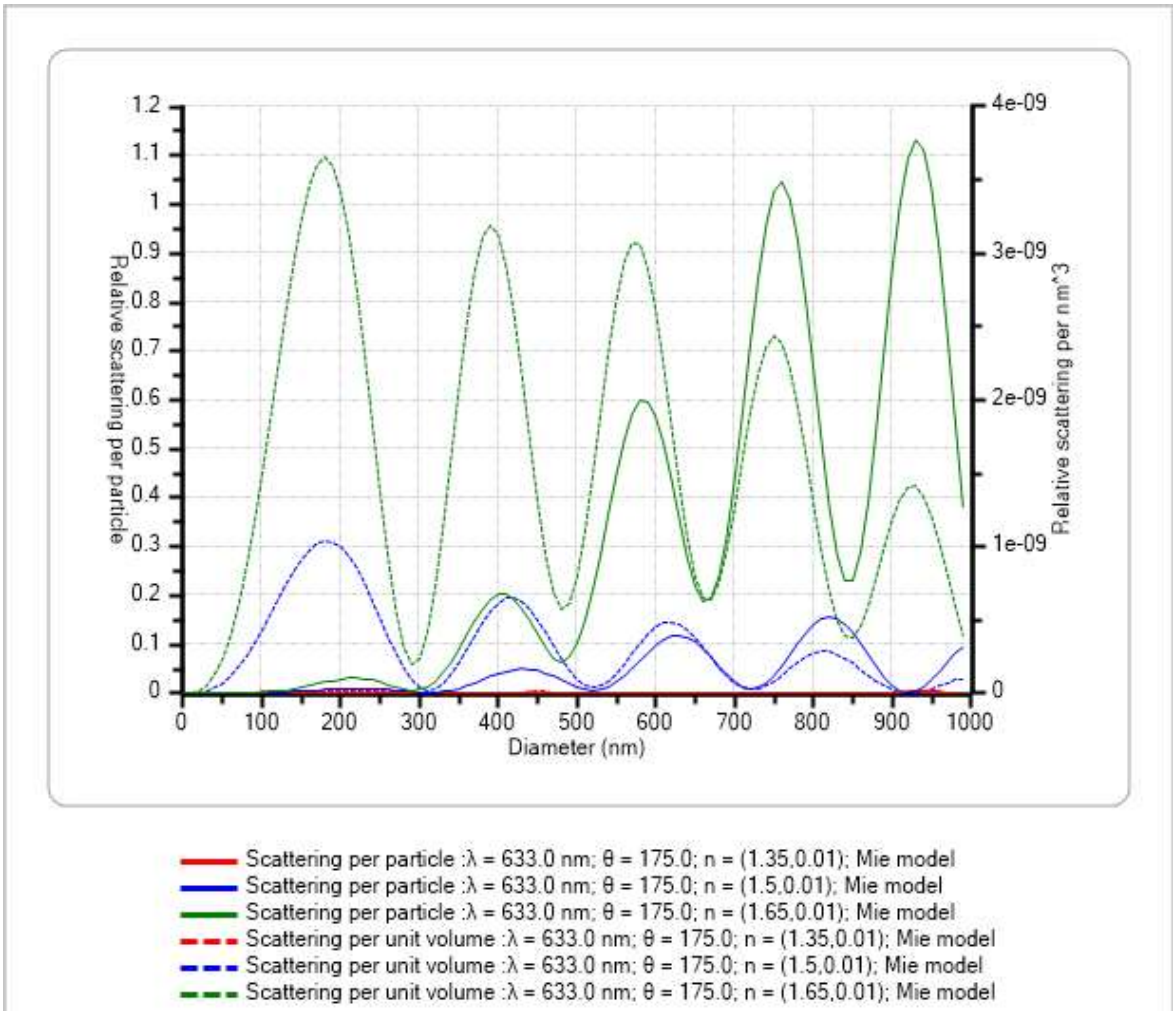

Figure B.1.3 Calculated size and refractive index dependent scattering efficiency for colloids in the BSA-ACP-HAp system.

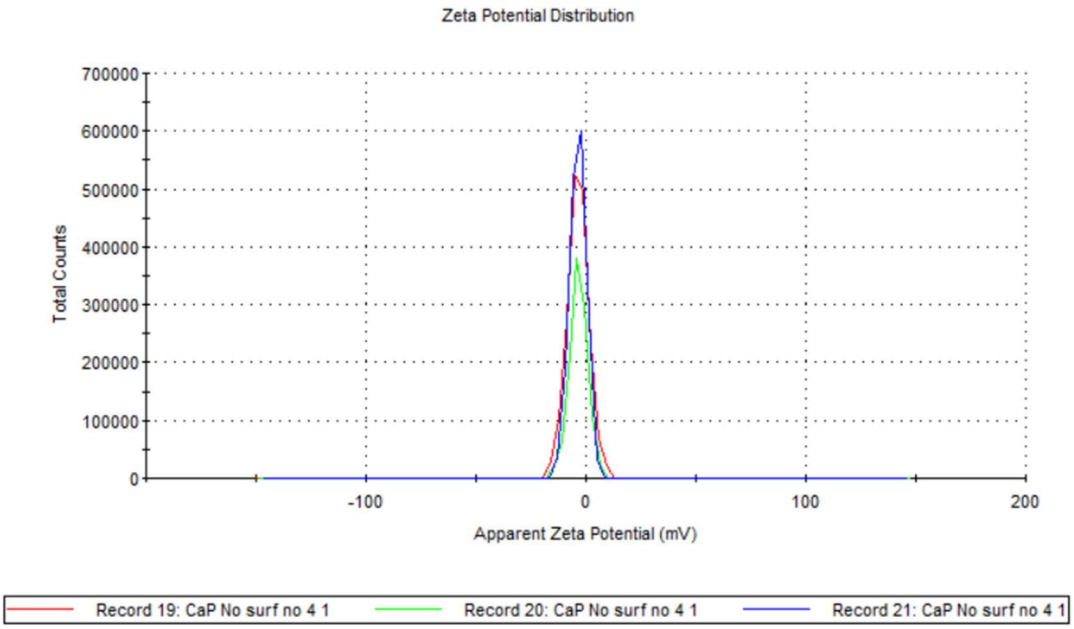

Figure B.1.4 Zeta potential data for uncoated ACP particles Data were collected at 20°C with a Zetasizer Nano ZSP (Malvern Instruments Limited) and disposable folded capillary cells (Malvern Instruments Limited) after a 10 second thermal equilibration period. Three measurements are shown, each of which comprises a minimum of 10 and a maximum of 100 runs. Attenuation and voltage were automatically selected by the instrument. The Smolochowski approximation was used. The dispersant was water, with a dielectric constant of 80.4. Optical parameters for the dispersant and the calcium phosphate particles were as detailed in the Dynamic Light Scattering general method.

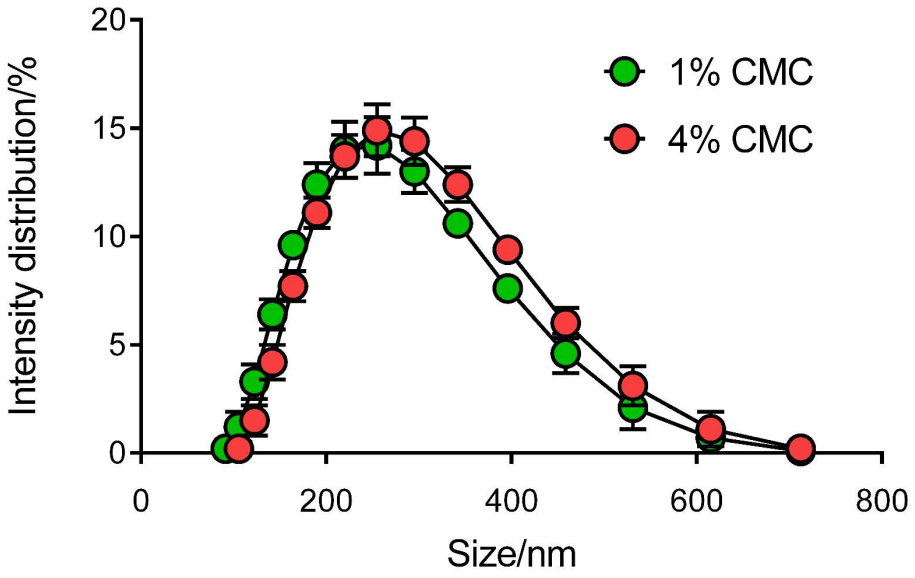

Figure B.1.5 DLS particle sizing of CMC-ACP colloids produced by impinging jet reactor, employing different concentrations of dispersant.

Appendix C Physicochemical characterisation

C.1 Size stability and surface charge in simple solution

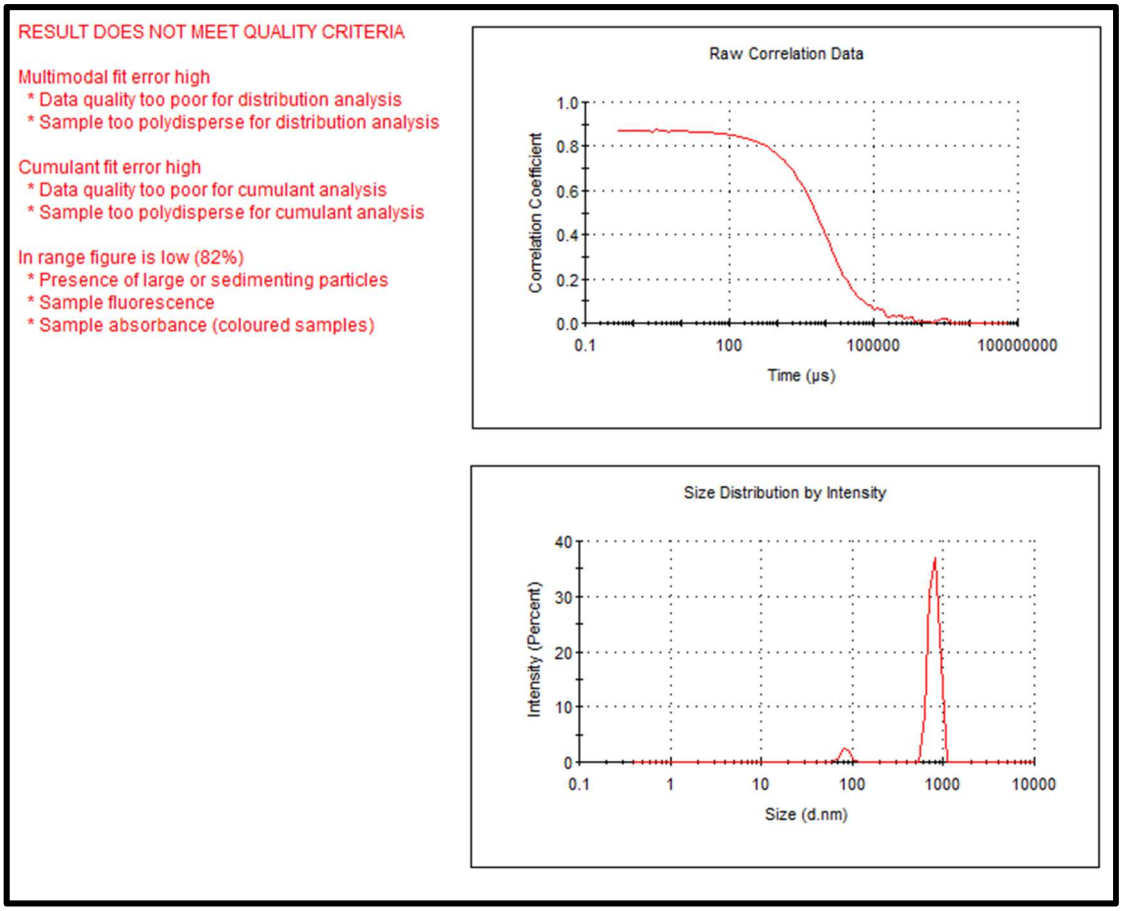

Figure C.1.1 Attempted DLS particle sizing of STPP-ACP colloids in pH 7 buffer. Material synthesis was carried out according to the optimum conditions described in section 3.23 except that resuspension was into 20 mMol/L pH 7 tris buffer. Attenuator and measurement position settings were automatically optimised by the instrument. Three measurements of 12 runs were attempted but in every case, the sample was too large and polydisperse for a viable measurement, as can be seen by the shape of the correlation function.

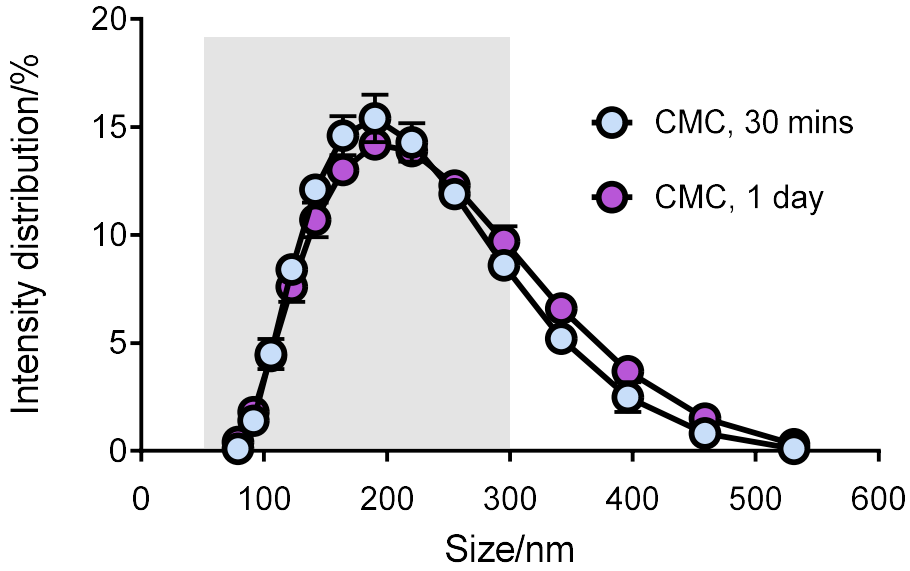

Figure C.1.2 Dynamic light scattering particle size results for the CMC stabilised ACP particles presented in Figure 4.1 with dispersant viscosity set to 1.0031 cP.

C.2 Transmission electron microscopy

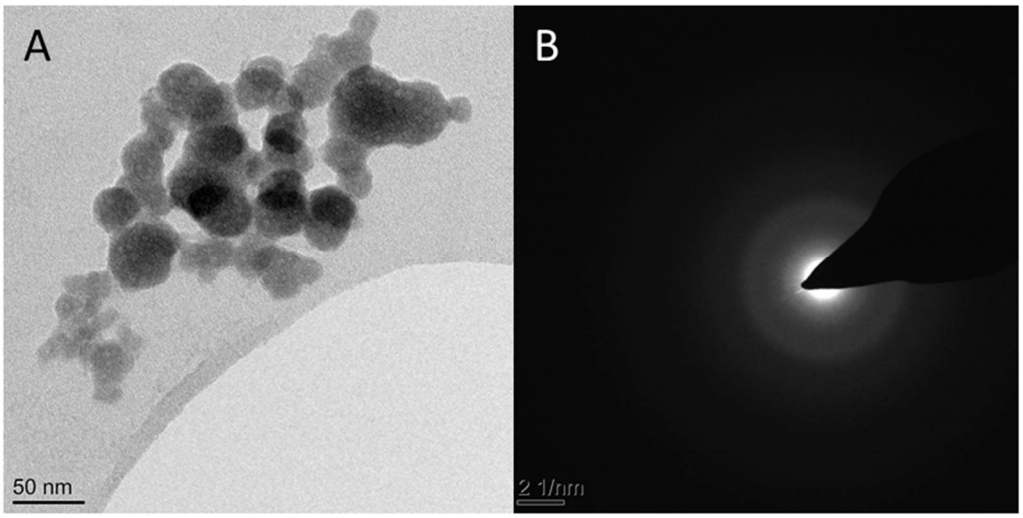

Figure C.2.1 Transmission electron microscopy characterisation of a carboxymethylcellulose functionalised ACP material after 1 week in pH 9 water. A fractal-like structure of agglomerated spheroids can be seen in bright field (**A**). By electron diffraction (**B**) the material had remained amorphous.

C.3 Particle sizing in complex solution

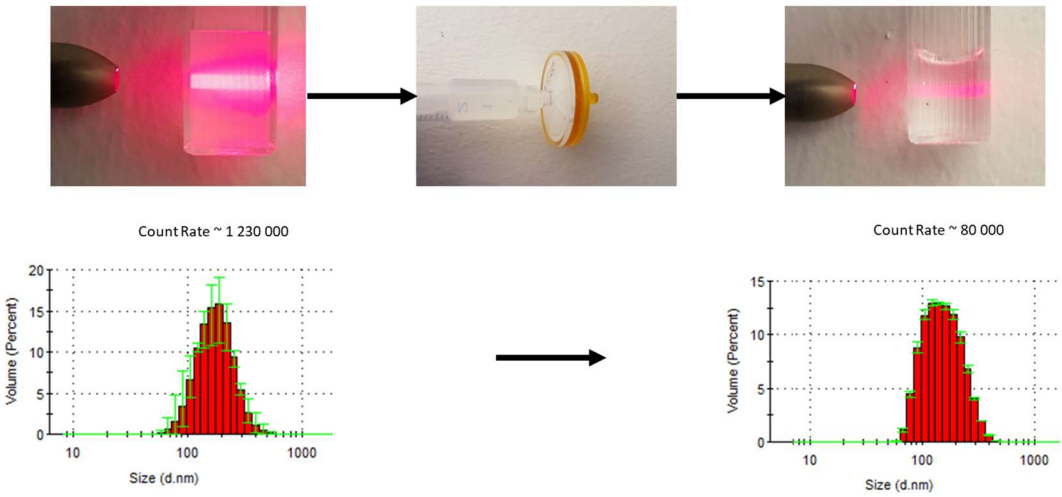

Figure C.3.1 Filtration failure. Laser refraction (upper, left) and particle sizing results (lower, left) are shown for a moderately concentrated solution of CMC stabilised ACP nanoparticles. The vast majority of the particle size distribution is below 450 nm in size, however upon passing the sample through a 450 nm syringe filter (upper, centre), most of the particles were retained by the filter, as evidenced by the reduction in laser refraction (upper, right) and DLS count rate (middle, right). The filter did not even manage to shift the particle size distribution to a lower size range (lower right vs lower left).

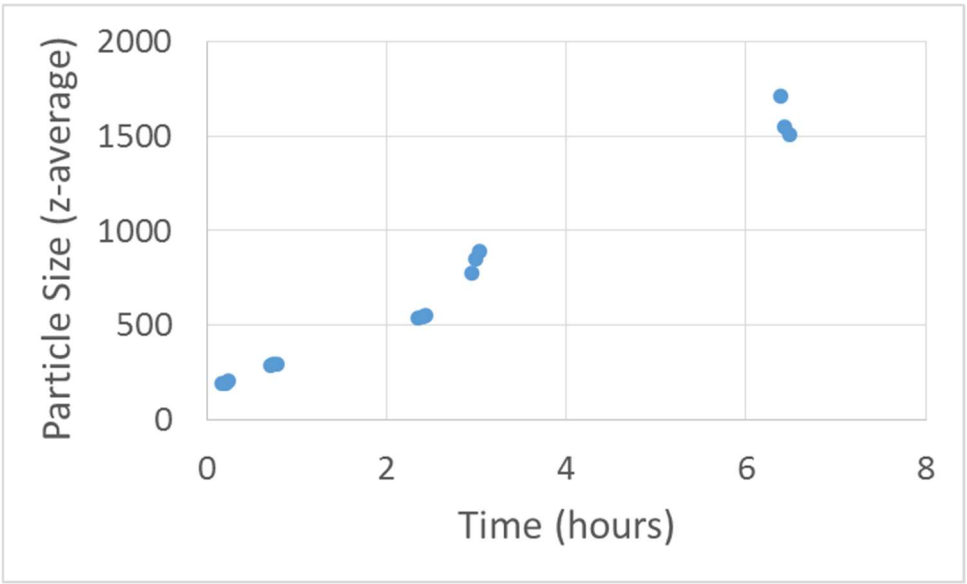

Figure C.3.2 Progressive agglomeration of QS-ACP particles produced from an inferior batch of quillaja saponin. The particles were produced via impinging jet reactor, resuspended in pH 9 water and then analysed via dynamic light scattering.

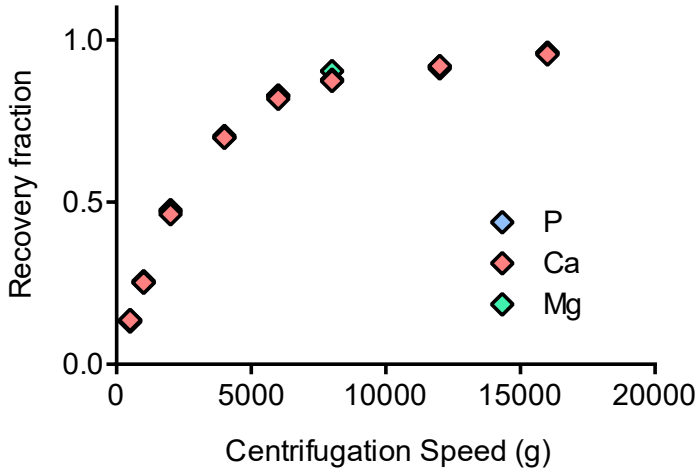

Figure C.3.3 Individual ion recovery curves for ACP particles in pH 9 water as quantified by ICP-OES.

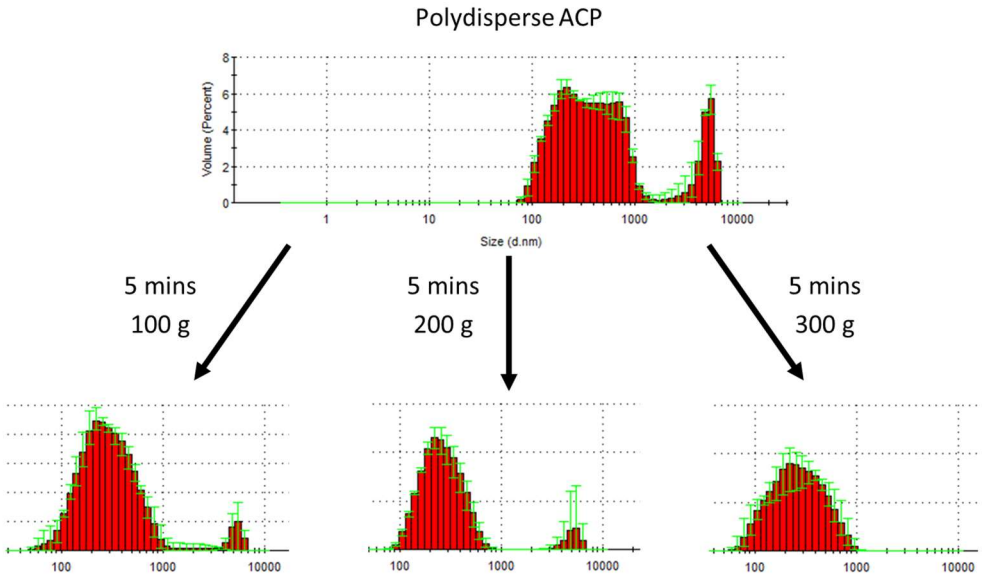

Figure C.3.4 Volume weighted particle sizing data obtained by dynamic light scattering for a polydisperse ACP material before and after centrifugation.

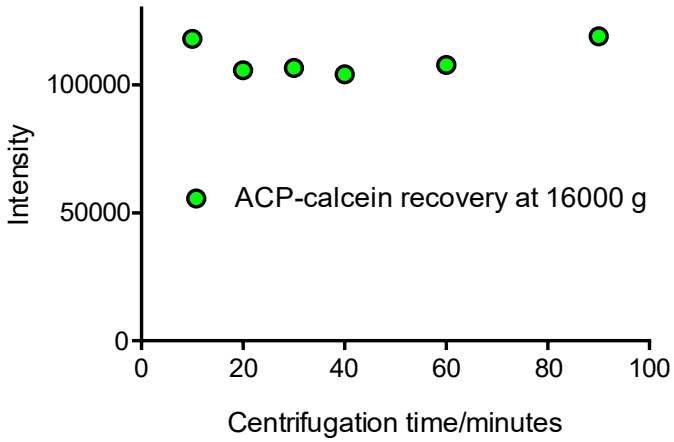

Figure C.3.5 Calcein loaded ACP particles were recovered effectively by 10 minutes at 16 000g

C.4 In vitro cargo incorporation, delivery and imaging

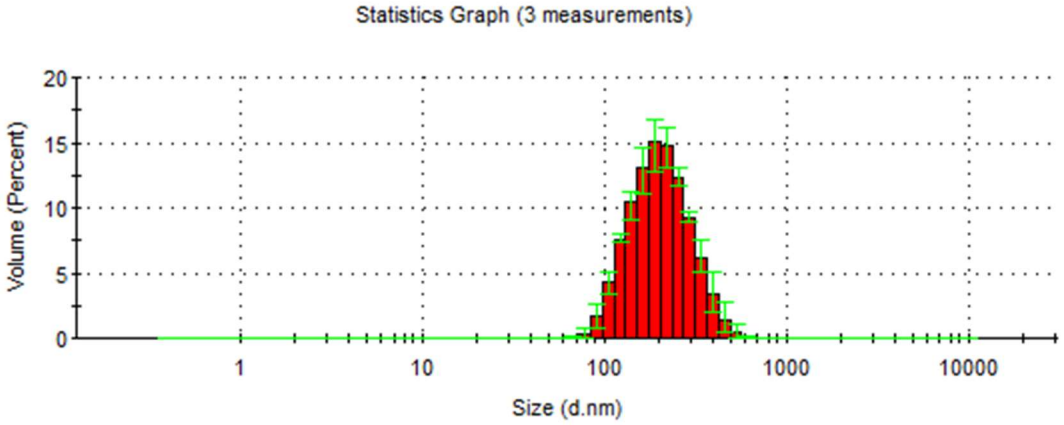

Figure C.4.1 Particle size data for CMC-ACP colloids prepared with 0.4mg/mL TRITC-BSA

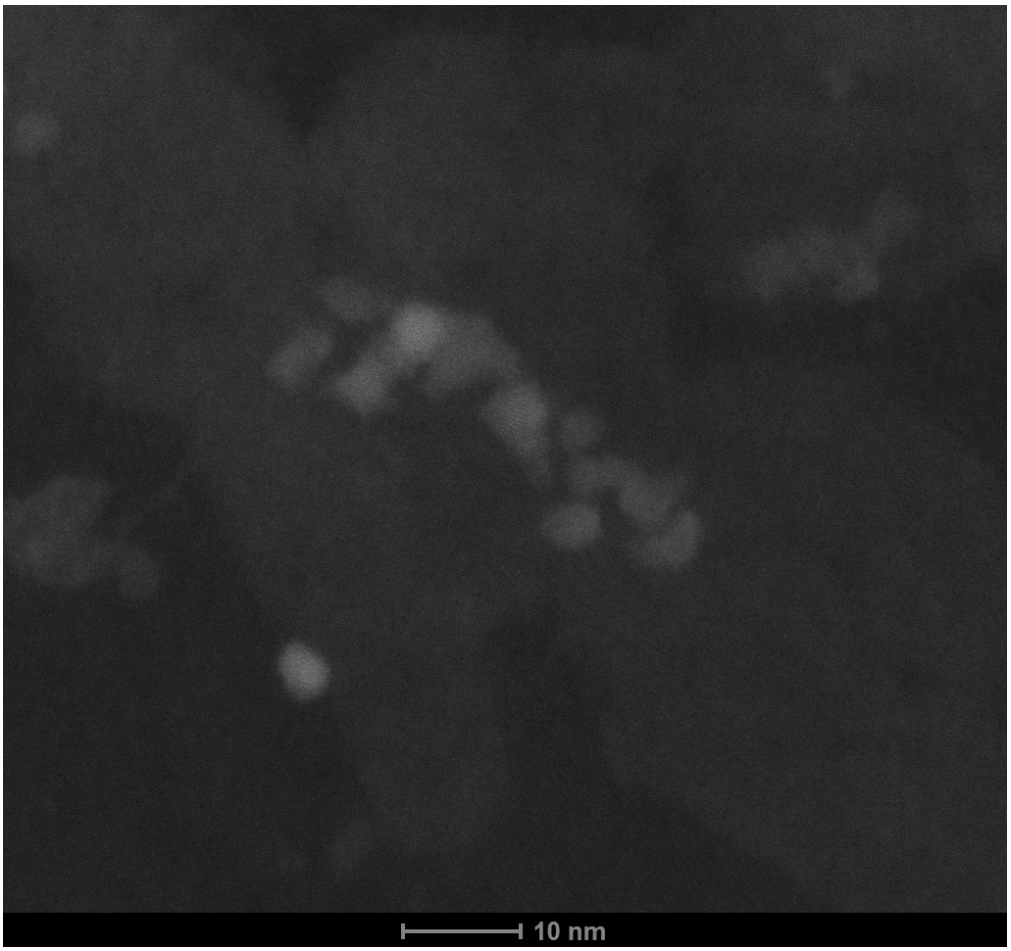

Figure C.4.2 High magnification HAADF TEM image of ACP embedded quantum dots. The quantum dots can be distinguished from the surrounding mineral by their higher contrast.

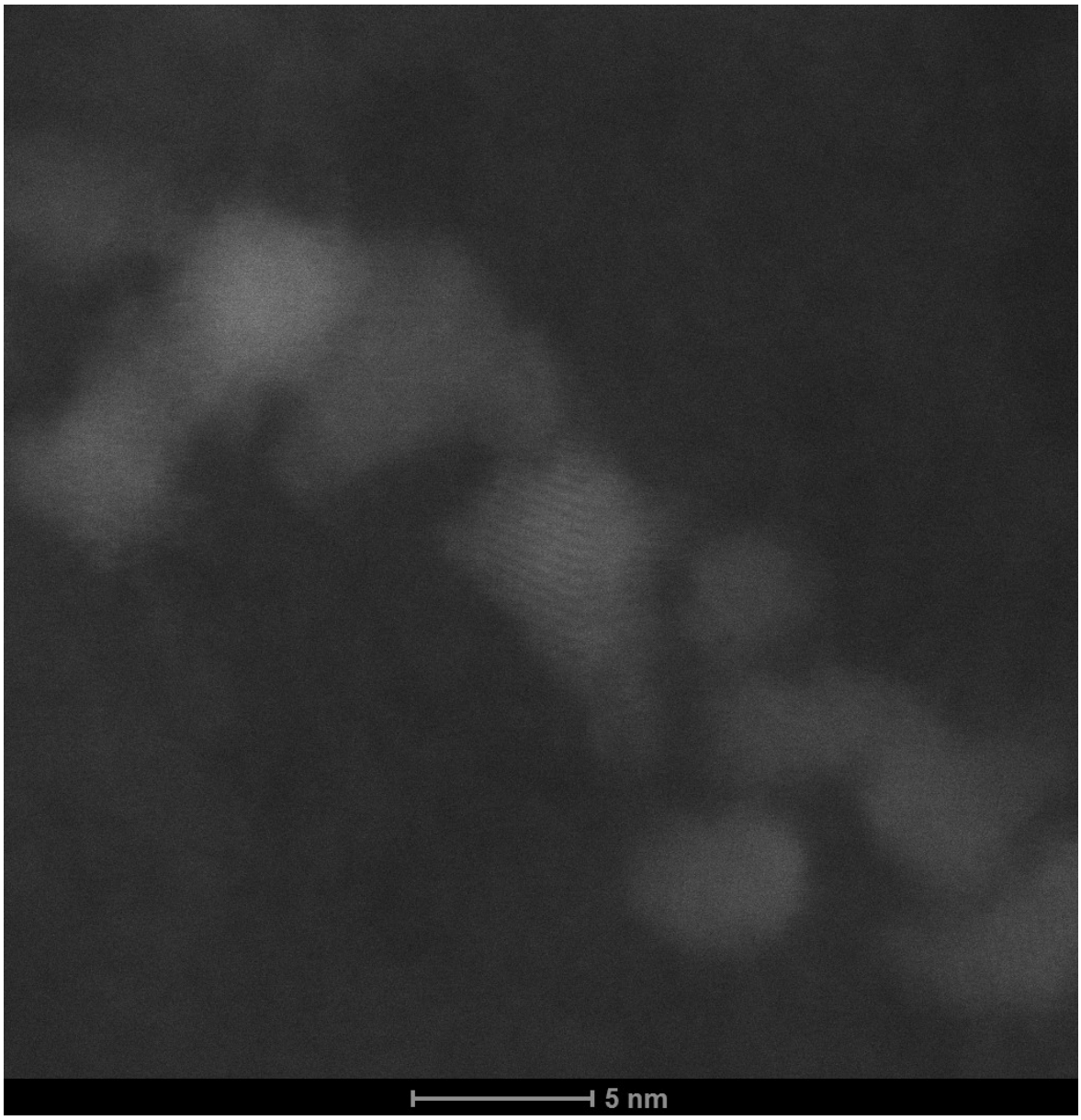

Figure C.4.3 Ultra high magnification HAADF TEM image of ACP embedded quantum dots. The quantum dots can be distinguished from the surrounding mineral by their higher contrast. Lattice fringes, indicative of crystallinity, are apparent for the central quantum dot.

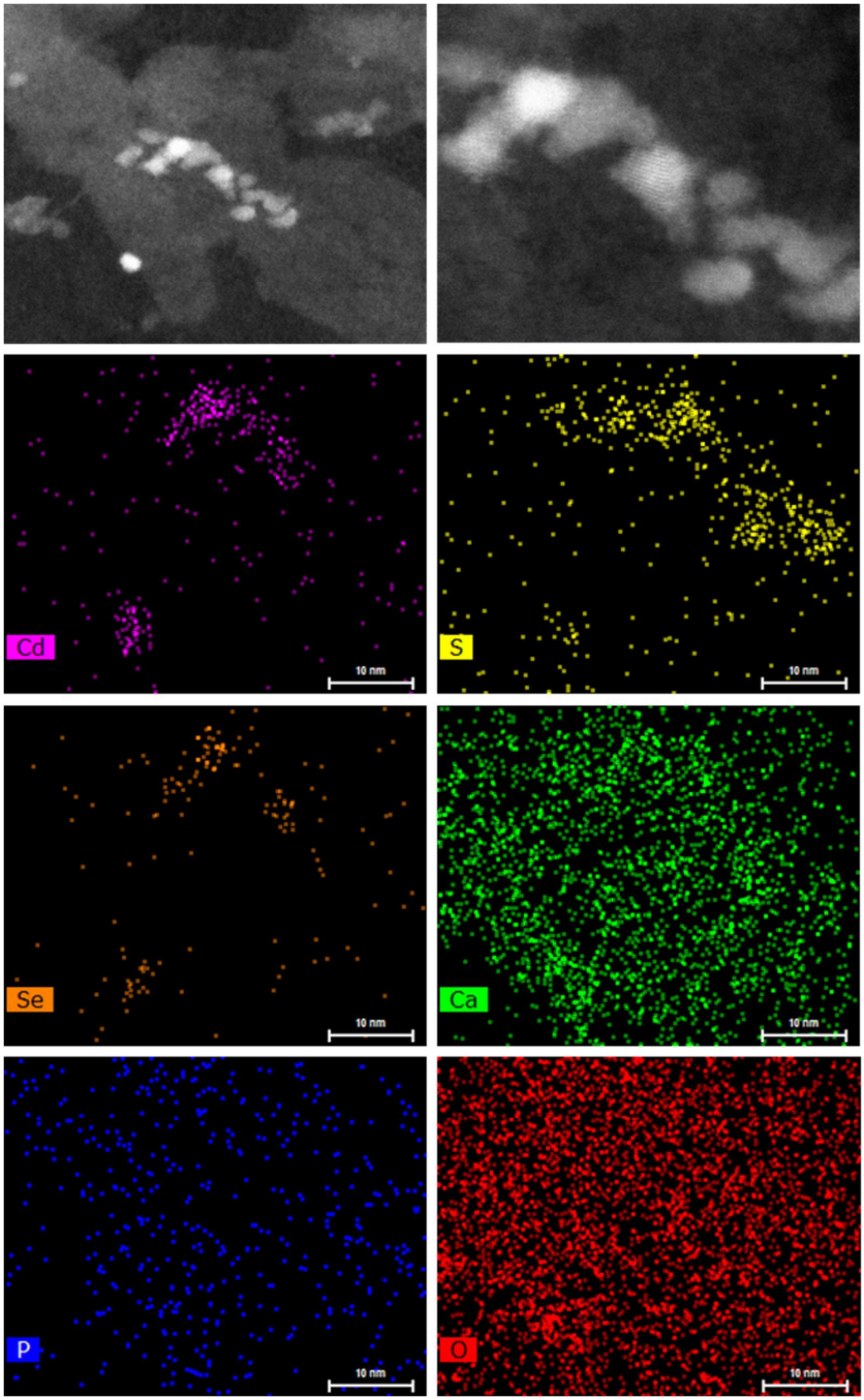

Figure C.4.4 Characterisation of quantum-dot loaded carboxymethylcellulose stabilised ACP via transmission electron microscopy and energy dispersive X-ray spectroscopy. A single particle is shown in dark field alongside accompanying EDX maps.

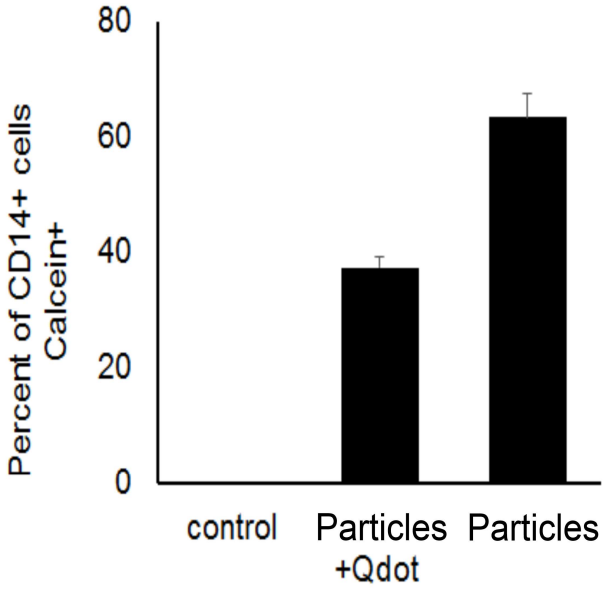

Figure C.4.5 In vitro delivery efficiency of calcein to gated $CD14^{+}$ cells. Data are shown for cells without any particles, for cells exposed to dual-labelled calcein-quantum-dot ACP particles and for cells exposed to singly calcein-labelled ACP particles

Appendix D MATLAB and Python Code

D.1 FTIR spectra smoothing

Data import

```
% clear the memory and command window,
clear
close all
clc
format long

datafiles = dir('**/*.txt');
index = contains({datafiles.name}, 'smooth');
datafiles(index)=[];
clear index

% format filenames for import
filenames = {datafiles(:).name};
filenames = filenames';
filenames = strrep(filenames,'.txt','');

% Batch import of data
for i = 1:numel(datafiles(:,1))
   name = char(filenames(i,:));
   data(:,:,i) = readmatrix(name);
end


% Remove NaN columns
for i = 1:numel(datafiles(:,1))
dat(:,:,i) = data(:,~all(isnan(data(:,:,1))),i);
end
data = dat; clear dat
```

Data Smoothing

```
datacols = size(data,2);
for i = 1:numel(datafiles(:,1))
   data(:,datacols+1,i) = sgolayfilt(data(:,2,i),2,35);
end

clear i datacols
```

Export data

```
for i = 1:numel(datafiles(:,1))
  txt1(i) = strcat(string(filenames(i)),'-smoothed.txt');
  writematrix(data(:,:,i),txt1(i));
end

clear i
```

Plot and save spectra

```
for i = 1:numel(datafiles(:,1))
    figure
    plot(data(:,1,i),data(:,3,i))
    xlabel('Wavenumber/cm^{-1}')
    ylabel('Transmittance')
    xlim([500 4000])
    ylim([0 120])
    box off;
    set(gca,'TickLength',[0.015 0.015]);
    set(gca,'TickDir','out');
    set(gca,'LineWidth',1);
    set(gca,'xdir','reverse');
    txt2(i) = strcat(string(filenames(i)),'-smoothed');
    %an1 = annotation('textbox',[0.58, 0.8, 0.1, 0.1],'string',txt2(i),'Fitl
    export_fig(txt2(i),'-tif','-q101')
end
```

D.2 Centrifugal size analysis

```
clear
clc
```

Section 1 Experimental Parameters

```
%Input the experimental conditions here

%fluid_volume = 1                  ;   %fluid volume per vessel (cm^3)
spin_time = 600                    ;   %centrifuge run time (seconds)
fluid_viscosity = 0.01             ;   %viscosity of assay fluid (g/cm*s)
fluid_density = 1                  ;   %density of assay fluid (g/cm^3)
particle_density = 1.5             ;   %density of centrifuged particles (g/cm^3)
distance_travelled = 2.65          ;   %distance between r0 and r1 (cm)

gravitational_field = 980.665      ;   %gravitational acceleration per g (cm/s^2)
```

Section 2 Single Phase Association Fit Parameters

```
%
y0 = 0.0;
plateau = 0.9516;
k = 0.0003299;
```

Section 3 Size Bins

```
% Input the particle sizes (nm) calculated in excel (column H)

particle_diameter = [600 500 400 300 200 100 50]; % vector truncated for clarity
```

Section 4 Calculations

```
spinspeeds= [SL_g_force(spin_time, fluid_viscosity, fluid_density, particle_density, gravitational_field, particle_diameter, distance_travelled)];

gross_efficiency = 100.*(y0 + (plateau - y0).*(1-exp(-k.*spinspeeds)));
```

```
% This function uses Stokes Law to approximate the sedimentation behaviour
% of particles under gravity. It computes the g force required to ensure
% that the given particle size is the largest size which may remain in the
% supernatant. The required inputs are time, viscosity, density of the fluid
% and solid, particle size and the distance travelled


function[g] = SLK(spin_time, fluid_viscosity, fluid_density, particle_density, gravitational_field, particle_diameter, distance_travelled)

velocity = distance_travelled./spin_time;

drag_coefficient = velocity ./((particle_diameter.*(10.^-7)).^2);

g = (18.*fluid_viscosity.*drag_coefficient)./((particle_density-fluid_density).*gravitational_field);

end
```

Python Script

```
import numpy as np
import matplotlib.pyplot as plt
for a in [1.04504332705836]:
    x = np.linspace(0,10,1001)
    k = 2*a*np.exp(a)*np.exp(-2*x-a*np.exp(-2*x))
    dx = x[1]-x[0]
    h = np.zeros(x.shape)
    h[0] = 2*a
    k[0] = 2*a
    for i in range(len(h)):
        khsum = 0
        for j in range(0,i-1):
            khsum = khsum + k[i-j]*h[j]

        h[i] = (k[i] - dx*(0.5*k[i]*h[0] + khsum))/(1+0.5*dx*k[0])

    plt.plot(x,h,label="a = "+str(a))
 #   plt.plot(x,k,label="a = "+str(a))
axes = plt.gca()
axes.set_xlim([0,2])
axes.set_ylim([-1,5])
plt.xlabel("x")
plt.ylabel("h(x)")
plt.legend()
plt.show()
np.savetxt('resolvent_kernel_output.csv',(x,h),delimiter=',')
```

References

A. Azab, H. and M. Anwar, Z. (2012) 'Coordination Tendency of Some Biologically Important Zwitterionic Buffers toward Metal Ion Nucleotide Complexes at Different Temperatures', *Journal of Chemical & Engineering Data*. American Chemical Society, 57(10), pp. 2890–2895. doi: 10.1021/je300830k.

Abbona, F. and Baronnet, A. (1996) 'A XRD and TEM study on the transformation of amorphous calcium phosphate in the presence of magnesium', *Journal of Crystal Growth*, 165(1–2), pp. 98–105. doi: 10.1016/0022-0248(96)00156-X.

Abramson, A. *et al.* (2019) 'A luminal unfolding microneedle injector for oral delivery of macromolecules', *Nature Medicine*. Nature Publishing Group, 25(10), pp. 1512–1518. doi: 10.1038/s41591-019-0598-9.

Adel, A. *et al.* (2008) 'Study of thermally and chemically unfolded conformations of bovine serum albumin by means of dynamic light scattering', *Materials Science and Engineering C*. Elsevier BV, 28(5–6), pp. 594–600. doi: 10.1016/j.msec.2007.10.004.

Ageno, M., Dore, E. and Frontali, C. (1969) 'The Alkaline Denaturation of DNA', *Biophysical Journal*. The Biophysical Society, 9(11), pp. 1281–1311. doi: 10.1016/S0006-3495(69)86452-0.

Ahmad, B., Kamal, M. and Khan, R. (2005) 'Alkali-Induced Conformational Transition in Different Domains of Bovine Serum Albumin', *Protein & Peptide Letters*. Bentham Science Publishers Ltd., 11(4), pp. 307–315. doi: 10.2174/0929866043406887.

Allen, T. (1997) *Particle Size Measurement*. Chapman & Hall.

Altinoğlu, E. I. *et al.* (2008) 'Near-Infrared Emitting Fluorophore- Doped Calcium Phosphate Nanoparticles for In Vivo Imaging of Human Breast Cancer', *ACS Nano*, 2(10), pp. 2075–2084.

Anselmo, A. C., Gokarn, Y. and Mitragotri, S. (2018) 'Non-invasive delivery strategies for biologics', *Nature Reviews Drug Discovery*. Nature Publishing Group, pp. 19–40. doi: 10.1038/nrd.2018.183.

Attard, P., Antelmi, D. and Larson, I. (2000) 'Comparison of the Zeta Potential with the Diffuse Layer Potential from Charge Titration', *Langmuir*, 16(4), pp. 1542–1552. doi: 10.1021/la990487t.

Awaad, A., Nakamura, M. and Ishimura, K. (2012) 'Imaging of size-dependent uptake and identification of novel pathways in mouse Peyer's patches using fluorescent organosilica particles', *Nanomedicine: Nanotechnology, Biology, and Medicine*. Elsevier Inc., 8(5), pp. 627–636. doi: 10.1016/j.nano.2011.08.009.

Babič, M. *et al.* (2008) 'Poly(L-lysine)-modified iron oxide nanoparticles for stem cell labeling', *Bioconjugate Chemistry*. American Chemical Society, 19(3), pp. 740–750. doi: 10.1021/bc700410z.

Bar-Yosef Ofir, P. *et al.* (2004) 'The Influence of Polyelectrolytes on the Formation and Phase Transformation of Amorphous Calcium Phosphate', *Crystal Growth and Design*, 4(1), pp. 177–183. doi: 10.1021/cg034148g.

Bernhardt, C. (2000) *Sedimentation in Particle Size Analysis*, *Encyclopedia of Analytical Chemistry*. doi: 10.1002/9780470027318.a1513.

Bhandari, S. *et al.* (2018) 'Intravenous irons: From basic science to clinical practice', *Pharmaceuticals*. MDPI AG. doi: 10.3390/ph11030082.

Blaubrand (2015) *Volumetric Instruments and Density Bottles Testing Instructions (SOP)*.

Borchard, G. (2001) 'Chitosans for gene delivery.', *Advanced drug delivery reviews*, 52(2), pp. 145–50. doi: 10.1016/s0169-409x(01)00198-3.

Boskey, A. L. and Posner, A. S. (1973) 'Conversion of amorphous calcium phosphate to microcrystalline hydroxyapatite. A pH-dependent, solution-mediated, solid-solid conversion', *Journal of Physical Chemistry*, 77(19), pp. 2313–2317. doi: 10.1021/j100638a011.

Boskey, A. L. and Posner, A. S. (1974) 'MAGNESIUM STABILIZATION OF AMORPHOUS CALCIUM PHOSPHATE: A KINETIC STUDY', *Materials Research Bulletin*, I(907), pp. 11–30.

Boussif, O. *et al.* (1995) 'A versatile vector for gene and oligonucleotide transfer into cells in culture and in vivo: Polyethylenimine', *Proceedings of the National Academy of Sciences of the United States of America*, 92(16), pp. 7297–7301. doi: 10.1073/pnas.92.16.7297.

Brody, S. (1934) *Basal metabolism, endogenous nitrogen, creatinine, and sulphur excretions as functions of body weight*, *Univ. Mo. Agric. Exp. Sta. Res. Bull.*

Buda, A., Sands, C. and Jepson, M. (2005) 'Use of fluorescence imaging to investigate the structure and function of intestinal M cells', *Advanced Drug Delivery Reviews*. Elsevier B.V., 57(1), pp. 123–134. doi: 10.1016/j.addr.2004.07.014.

Butler, M. *et al.* (2007) 'Dietary microparticles implicated in Crohn's disease can impair macrophage phagocytic activity and act as adjuvants in the presence of bacterial stimuli', *Inflammation Research*. Springer, 56(9), pp. 353–361. doi: 10.1007/s00011-007-7068-4.

Cai, G. Bin *et al.* (2010) 'Synthesis of polyacrylic acid stabilized amorphous calcium carbonate nanoparticles and their application for removal of toxic heavy metal ions in water', *Journal of Physical Chemistry C*, 114(30), pp. 12948–12954. doi: 10.1021/jp103464p.

Caruso, F. (ed.) (2003) *Colloids and Colloid Assemblies*, *Colloids and Colloid Assemblies*. Wiley. doi: 10.1002/3527602100.

Chen, F. *et al.* (2011) 'Europium-doped amorphous calcium phosphate porous nanospheres: Preparation and application as luminescent drug carriers', *Nanoscale Research Letters*. Springer New York LLC, 6(1), pp. 1–9. doi: 10.1186/1556-276X-6-67.

Cheroutre, H. and Madakamutil, L. (2004) 'Acquired and natural memory T cells join forces at the mucosal front line', *Nature Reviews Immunology*, 4(4), pp. 290–300. doi: 10.1038/nri1333.

Christoffersen, J. *et al.* (1989) 'A contribution to the understanding of the formation of calcium phosphates', *Journal of Crystal Growth*, 94(3), pp. 767–777. doi: 10.1016/0022-0248(89)90102-4.

Christoffersen, M. R., Christoffersen, J. and Kibalczyc, W. (1990) 'Apparent solubilities of two

amorphous calcium phosphates and of octacalcium phosphate in the temperature range 30-42°C', *Journal of Crystal Growth*, 106(2–3), pp. 349–354. doi: 10.1016/0022-0248(90)90079-Z.

Clark, M. A., Jepson, M. A. and Hirst, B. H. (2001) 'Exploiting M cells for drug and vaccine delivery', *Advanced Drug Delivery Reviews*, 50(1–2), pp. 81–106. doi: 10.1016/S0169-409X(01)00149-1.

Cole, E. T. *et al.* (2002) 'Enteric coated {HPMC} capsules designed to achieve intestinal targeting', *International Journal of Pharmaceutics*, 231(1), pp. 83–95. doi: http://dx.doi.org/10.1016/S0378-5173(01)00871-7.

Combes, C. and Rey, C. (2010) 'Amorphous calcium phosphates: Synthesis, properties and uses in biomaterials', *Acta Biomaterialia*. Acta Materialia Inc., 6(9), pp. 3362–3378. doi: 10.1016/j.actbio.2010.02.017.

Cornell, R. M. and Schwertmann, U. (2003) *The iron oxides: structure, properties, reactions, occurrences and uses*. John Wiley & Sons.

Curry, N. A. and Jones, D. W. (1971) 'Crystal structure of Brushite, Calcium Hydrogen Orthophosphate Di-hydrate: A Neutron-diffraction Investigation', *Journal of the Chemical Society A: Inorganic, Physical, Theoretical*, (0), pp. 3725–3729.

Delgado, A. V. *et al.* (2007) 'Measurement and interpretation of electrokinetic phenomena', *Journal of Colloid and Interface Science*. Academic Press, 309(2), pp. 194–224. doi: 10.1016/j.jcis.2006.12.075.

Demyanovich, R. J. and Bourne, J. R. (1989) 'Rapid Micromixing by the Impingement of Thin Liquid Sheets. 2. Mixing Study', *Industrial and Engineering Chemistry Research*, 28(6), pp. 830–839. doi: 10.1021/ie00090a027.

Dey, A. *et al.* (2010) 'The role of prenucleation clusters in surface-induced calcium phosphate crystallization', *Nature Materials*. Nature Publishing Group, 9(12), pp. 1010–1014. doi: 10.1038/nmat2900.

Ding, H. *et al.* (2014) 'Toward a detailed understanding of magnesium ions on hydroxyapatite crystallization inhibition', *Crystal Growth and Design*, 14(2), pp. 763–769. doi: 10.1021/cg401619s.

Dirkse, T. P. (1986) 'Gold, and Zinc, Cadmium, Mercury Oxides and Hydroxides, IUPAC Solubility Data Series, Vol. 23, TP Dirkse, Ed'. Pergamon Press, New York.

Dorozhkin, S. V (2010) 'Amorphous calcium (ortho)phosphates', *Acta Biomaterialia*, 6(12), pp. 4457–4475. doi: http://dx.doi.org/10.1016/j.actbio.2010.06.031.

Dorozhkin, S. V (2012) 'Calcium orthophosphates: applications in nature, biology, and medicine', in *Calcium orthophosphates: applications in nature, biology, and medicine*. CRC Press, pp. 169–170.

Drucker, D. J. (2020) 'Advances in oral peptide therapeutics', *Nature Reviews Drug Discovery*. Nature Research, pp. 277–289. doi: 10.1038/s41573-019-0053-0.

E. Robison, H. and W. Martin, S. (1948) 'Beaker-Type Centrifugal Sedimentation of Subsieve Solid–Liquid Dispersions. I. Theory', *The Journal of Physical and Colloid Chemistry*, 52(5), pp. 854–881. doi: 10.1021/j150461a010.

Eanes, E. D. (1998) 'Amorphous Calcium Phosphate: Thermodynamic and Kinetic Considerations', in Amjad, Z. (ed.) *Calcium Phosphates in Biological and Industrial Systems*. Boston, MA: Springer US, pp. 21–39. doi: 10.1007/978-1-4615-5517-9_2.

EFSA (2006) 'Tolerable Upper Intake Levels for Vitamins and Minerals by the Scientific Panel on Dietetic products, nutrition and allergies (NDA) and Scientific Committee on Food (SCF)'.

Elliott, J. C., Mackie, P. E. and Young, R. A. (1973) 'Monoclinic hydroxyapatite', *Science*, 180(4090), pp. 1055–1057. doi: 10.1126/science.180.4090.1055.

Erni, P. and Elabbadi, A. (2013) 'Free Impinging Jet Microreactors: Controlling Reactive Flows via Surface Tension and Fluid Viscoelasticity', *Langmuir*, 29(25), pp. 7812–7824. doi: 10.1021/la401017z.

Fanale, M. A. and Younes, A. (2007) 'Monoclonal antibodies in the treatment of non-Hodgkin's lymphoma', *Drugs*. Springer, 67(3), pp. 333–350.

Faria, A. M. C. and Weiner, H. L. (2005) 'Oral tolerance', *Immunological Reviews*. Munksgaard International Publishers, 206(1), pp. 232–259. doi: 10.1111/j.0105-2896.2005.00280.x.

FDA (2019) *FDA Food Additive Status List*. Available at: https://www.fda.gov/food/food-additives-petitions/food-additive-status-list.

Feiler, A., Jenkins, P. and Ralston, J. (2000) 'Metal oxide surfaces separated by aqueous solutions of linear polyphosphates: DLVO and non-DLVO interaction forces', *Physical Chemistry Chemical Physics*. Royal Society of Chemistry, 2(24), pp. 5678–5683.

Field, J. E., Farhat, M. and Walley, S. M. (2014) 'Comminution limit (CL) of particles and possible implications for pumped storage reservoirs', *Journal of Materials Science*, 49(10), pp. 3780–3784. doi: 10.1007/s10853-014-8089-3.

Frédéric, C. J. *et al.* (2010) 'Infliximab, Azathioprine, or Combination Therapy for Crohn's Disease', *New England Journal of Medicine*, 362(15), pp. 1383–1395. doi: 10.1056/NEJMoa0904492.

Fujihashi, K. *et al.* (2001) 'Peyer's patches are required for oral tolerance to proteins', *Proceedings of the National Academy of Sciences*, 98(6), pp. 3310–3315. doi: 10.1073/pnas.061412598.

G. Bastús, N. *et al.* (2014) 'Synthesis of Highly Monodisperse Citrate-Stabilized Silver Nanoparticles of up to 200 nm: Kinetic Control and Catalytic Properties', *Chemistry of Materials*. American Chemical Society, 26(9), pp. 2836–2846. doi: 10.1021/cm500316k.

Ganesh, S. *et al.* (2006) 'Cytokine Storm in a Phase 1 Trial of the Anti-CD28 Monoclonal Antibody TGN1412', *New England Journal of Medicine*, 355(10), pp. 1018–1028. doi: 10.1056/NEJMoa063842.

Gebauer, D. *et al.* (2014) 'Pre-nucleation clusters as solute precursors in crystallisation', *Chemical Society Reviews*, 43(7), pp. 2348–2371. doi: 10.1039/c3cs60451a.

Gelli, R. *et al.* (2018) 'Effect of pH and Mg 2+ on Amorphous Magnesium-Calcium Phosphate (AMCP) stability', *Journal of Colloid and Interface Science*. Elsevier Inc., 531, pp. 681–692. doi: 10.1016/j.jcis.2018.07.102.

van Ginneken, V. *et al.* (2007) 'Metabolomics (liver and blood profiling) in a mouse model in response to fasting: A study of hepatic steatosis', *Biochimica et Biophysica Acta - Molecular and Cell Biology of Lipids*. Elsevier, 1771(10), pp. 1263–1270. doi: 10.1016/j.bbalip.2007.07.007.

Green, S. J. and Brendsel, J. (2006) 'Could the GI tract be a better portal for antibody therapy?', *Gut*. BMJ Publishing Group, 55(11), p. 1681.

Gregorio, D. S. *et al.* (2018) 'A universal curve of apatite crystallinity for the assessment of bone integrity and preservation', *Scientific Reports*, 8(1), pp. 1–13. doi: 10.1038/s41598-018-30642-z.

Gustafsson, J. P. *et al.* (2008) 'Phosphate removal by mineral-based sorbents used in filters for small-scale wastewater treatment', *Water Research*. doi: 10.1016/j.watres.2007.06.058.

Habraken, W. J. E. M. *et al.* (2013) 'Ion-association complexes unite classical and non-classical theories for the biomimetic nucleation of calcium phosphate', *Nature Communications*. Nature Publishing Group, 4, pp. 1507–1512. doi: 10.1038/ncomms2490.

Halberg, I. B. *et al.* (2019) 'Efficacy and safety of oral basal insulin versus subcutaneous insulin glargine in type 2 diabetes: a randomised, double-blind, phase 2 trial', *The Lancet Diabetes and Endocrinology*. Lancet Publishing Group, 7(3), pp. 179–188. doi: 10.1016/S2213-8587(18)30372-3.

Hanifi, A., Fathi, M. H. and Sadeghi, H. M. M. (2010) 'Effect of strontium ions substitution on gene delivery related properties of calcium phosphate nanoparticles', *Journal of Materials Science: Materials in Medicine*, 21(9), pp. 2601–2609. doi: 10.1007/s10856-010-4123-4.

Hansel, T. T. *et al.* (2010) 'The safety and side effects of monoclonal antibodies', *Nature Reviews Drug Discovery*. Nature Publishing Group, 9(4), pp. 325–338. doi: 10.1038/nrd3003.

Hartono, S. *et al.* (2012) 'Poly-l-lysine Functionalized Large Pore Cubic Mesostructured Silica Nanoparticles as Biocompatible Carriers for Gene Delivery', *ACS Nano*, 6(3), pp. 2104–2117. doi: 10.1021/nn2039643.

Haynes, W. M. (ed.) (2010) *CRC Handbook of Chemistry and Physics*. 91st edn. CRC Press.

Heel, K. A. *et al.* (1997) 'REVIEW: Peyer's patches', *Journal of Gastroenterology and Hepatology*. Blackwell Publishing Ltd, 12(2), pp. 122–136. doi: 10.1111/j.1440-1746.1997.tb00395.x.

Heijboer, A. C. *et al.* (2005) 'Sixteen hours of fasting differentially affects hepatic and muscle insulin sensitivity in mice', *Journal of Lipid Research*. American Society for Biochemistry and Molecular Biology, 46(3), pp. 582–588. doi: 10.1194/jlr.M400440-JLR200.

Heine, M. C. and Pratsinis, S. E. (2007) 'Brownian Coagulation at High Concentration', *Langmuir*, 23(19), pp. 9882–9890. doi: 10.1021/la7012599.

Hermans, J. (1966) 'Experimental free energy and enthalpy of formation of the alpha-helix.', *The Journal of physical chemistry*. American Chemical Society, 70(2), pp. 510–515. doi: 10.1021/j100874a031.

Hesselink, F. T., Vrij, A. and Overbeek, J. T. G. (1971) 'On the theory of the stabilization of dispersions by adsorbed macromolecules. II. Interaction between two flat particles', *Journal of Physical Chemistry*, 75(14), pp. 2094–2103. doi: 10.1021/j100683a005.

Hewitt, R. E. *et al.* (2017) 'Imaging flow cytometry assays for quantifying pigment grade titanium dioxide particle internalization and interactions with immune cells in whole blood', *Cytometry Part A*, 91(10), pp. 1009–1020. doi: 10.1002/cyto.a.23245.

Hiemstra, T. and Van Riemsdijk, W. H. (1996) 'A surface structural approach to ion adsorption: The charge distribution (CD) model', *Journal of Colloid and Interface Science*. Academic Press Inc., 179(2), pp. 488–508. doi: 10.1006/jcis.1996.0242.

Hirayama, T. and Nagasawa, H. (2017) 'Chemical tools for detecting Fe ions', *Journal of Clinical Biochemistry and Nutrition*, 60(1), pp. 39–48. doi: 10.3164/jcbn.16.

Hirsch, A. *et al.* (2014) 'Infrared Absorption Spectrum of Brushite from First Principles', *Chemistry of Materials*, 26(9), pp. 2934–2942. doi: 10.1021/cm500650t.

Holt, L. E., Pierce, J. A. and Kajdi, C. N. (1954) 'The solubility of the phosphates of strontium, barium, and magnesium and their relation to the problem of calcification', *Journal of Colloid Science*. Academic Press, 9(5), pp. 409–426. doi: 10.1016/0095-8522(54)90029-X.

Holzwarth, U. and Gibson, N. (2011) 'The Scherrer equation versus the "Debye-Scherrer equation"', *Nature Nanotechnology*, 6(9), p. 534. doi: 10.1038/nnano.2011.145.

Hondow, N. *et al.* (2012) 'Quantitative characterization of nanoparticle agglomeration within biological media', *Journal of Nanoparticle Research*. Springer, 14(7), pp. 1–15. doi: 10.1007/s11051-012-0977-3.

Hsu, J. P. and Liu, B. T. (1999) 'Electrical interaction energy between two charged entities', *Journal of Chemical Physics*. American Institute of PhysicsAIP, 110(1), pp. 25–33. doi: 10.1063/1.478080.

Hu, Y. *et al.* (2007) 'Cytosolic Delivery of Membrane-Impermeable Molecules in Dendritic Cells Using pH-Responsive Core−Shell Nanoparticles', *Nano Letters*, 7(10), pp. 3056–3064. doi: 10.1021/nl071542i.

Hunter, T. (2012) 'Why nature chose phosphate to modify proteins', *Philosophical Transactions of the Royal Society B: Biological Sciences*, 367(1602), pp. 2513–2516. doi: 10.1098/rstb.2012.0013.

Israelachvili, J. (2011) *Intermolecular and Surface Forces*, *Intermolecular and Surface Forces*. Elsevier Inc. doi: 10.1016/C2009-0-21560-1.

Jafarbeglou, Maryam *et al.* (2016) 'Clay nanocomposites as engineered drug delivery systems', *RSC Advances*. Royal Society of Chemistry, pp. 50002–50016. doi: 10.1039/c6ra03942a.

Jeurissen, S. H. M., Wagenaar, F. and Janse, E. M. (1999) 'Further characterization of M cells in gut-associated lymphoid tissues of the chicken', *Poultry Science*, 78(7), pp. 965–972. doi: 10.1093/ps/78.7.965.

Jin, W. *et al.* (2018) 'Synergic Effect of Sr2+ and Mg2+ on the Stabilization of Amorphous Calcium Phosphate', *Crystal Growth & Design*. American Chemical Society (ACS), 18(10), pp. 6054–6060. doi: 10.1021/acs.cgd.8b00908.

Johnson, B. K. and Prud'homme, R. K. (2003) 'Mechanism for rapid self-assembly of block copolymer nanoparticles', *Physical Review Letters*, 91(11). doi: 10.1103/PhysRevLett.91.118302.

Jokerst, J. V *et al.* (2011) 'Nanoparticle PEGylation for imaging and therapy', *Nanomedicine*. Future Medicine, 6(4), pp. 715–728.

Jung, S. *et al.* (2010) 'Atomization patterns produced by the oblique collision of two Newtonian liquid jets', *Physics of Fluids*, 22(4), pp. 1–10. doi: 10.1063/1.3373513.

Kalinin, V. V and Radke, C. J. (1996) 'An ion-binding model for ionic surfactant adsorption at aqueous-fluid interfaces', *Colloids and Surfaces A: Physicochemical and Engineering Aspects*, 114, pp. 337–350. doi: http://dx.doi.org/10.1016/0927-7757(96)03592-3.

Kamack, H. J. (1951) 'Particle Size Determination by Centrifugal Pipet Sedimentation', *Analytical Chemistry*. American Chemical Society, 23(6), pp. 844–850. doi: 10.1021/ac60054a006.

Kamack, H. J. (1972) *A note on centrifugal particle size analysis*, *J. Phys. D: Appl. Phys*.

Kanzaki, N. *et al.* (2001) 'Calcium phosphate clusters', *Biomaterials*, 22(21), pp. 2921–2929. doi: 10.1016/S0142-9612(01)00039-4.

Karimi, M. *et al.* (2016) 'A facile and sustainable method based on deep eutectic solvents toward synthesis of amorphous calcium phosphate nanoparticles: The effect of using various solvents and precursors on physical characteristics', *Journal of Non-Crystalline Solids*. Elsevier B.V., 443, pp. 59–64. doi: 10.1016/j.jnoncrysol.2016.04.026.

van Kemenade, M. J. J. M. and de Bruyn, P. L. (1987) 'A kinetic study of precipitation from supersaturated calcium phosphate solutions', *Journal of Colloid And Interface Science*. Academic Press, 118(2), pp. 564–585. doi: 10.1016/0021-9797(87)90490-5.

Kendall, R. A. *et al.* (2009) 'Fabrication and in vivo evaluation of highly pH-responsive acrylic microparticles for targeted gastrointestinal delivery', *European Journal of Pharmaceutical Sciences*. Elsevier, 37(3–4), pp. 284–290. doi: 10.1016/j.ejps.2009.02.015.

Kim, S. *et al.* (2004) 'Influence of Ca/P ratios of starting solutions on the crystallization of amorphous calcium phosphate to hydroxyapatite', *Metals and Materials International*. Korean Institute of Metals and Materials, 10(2), pp. 171–175. doi: 10.1007/BF03027322.

Kim, S. and Lee, J. (2010) 'Effective polymeric dispersants for vacuum, convection and freeze drying of drug nanosuspensions', *International Journal of Pharmaceutics*. Elsevier B.V., 397(1–2), pp. 218–224. doi: 10.1016/j.ijpharm.2010.07.010.

Kovtun, A. *et al.* (2012) 'Chlorhexidine-loaded calcium phosphate nanoparticles for dental maintenance treatment: Combination of mineralising and antibacterial effects', *RSC Advances*, 2(3), pp. 870–875. doi: 10.1039/c1ra00955a.

Krogstad, D. V., Wang, D. and Lin-Gibson, S. (2017) 'Polyaspartic Acid Concentration Controls the Rate of Calcium Phosphate Nanorod Formation in High Concentration Systems', *Biomacromolecules*. American Chemical Society, 18(10), pp. 3106–3113. doi: 10.1021/acs.biomac.7b00772.

Kumar, C. S. S. R. (2007) 'Nanomaterials for Medical Applications', in *Kirk-Othmer Encyclopedia of Chemical Technology*. Hoboken, NJ, USA: John Wiley & Sons, Inc. doi: 10.1002/0471238961.nanokuma.a01.

Kumar, D. V. R., Prasad, B. L. V. and Kulkarni, A. A. (2013) 'Impinging jet micromixer for flow synthesis of nanocrystalline MgO: Role of mixing/impingement zone', *Industrial and Engineering Chemistry Research*, 52(49), pp. 17376–17382. doi: 10.1021/ie402012x.

Lambert, I. and Clever, H. L. (1992) 'IUPAC Solubility Data Series, vol. 52: Alkaline Earth hydroxides in water and aqueous electrolytes'. Pergamon Press, Oxford.

Latt, S. A., Cheung, H. T. and Blout, E. R. (1965) 'Energy Transfer. A System with Relatively Fixed Donor-Acceptor Separation', *Journal of the American Chemical Society*, 87(5), pp. 995–1003. doi: 10.1021/ja01083a011.

Laue, T. (1996) 'Analytical Ultracentrifugation', *Current Protocols in Protein Science*, 4(1).

Layrolle, P., Ito, A. and Tetsuya, T. (1998) 'Sol – Gel Synthesis of Amorphous Calcium Phosphate and Sintering into Bioceramics, Microporous Hydroxyapatite', *J. Am. Ceram. Soc.*, 28.

Lee, T. C. *et al.* (2003) 'Detecting microdamage in bone', *Journal of Anatomy*, 203(2), pp. 161–172. doi: 10.1046/j.1469-7580.2003.00211.x.

Lelouard, H. *et al.* (2012) 'Peyer's Patch Dendritic Cells Sample Antigens by Extending Dendrites Through M Cell-Specific Transcellular Pores', *Gastroenterology*, 142(3), pp. 592-601.e3. doi: http://dx.doi.org/10.1053/j.gastro.2011.11.039.

Li, R. and Ashgriz, N. (2006) 'Characteristics of liquid sheets formed by two impinging jets', *Physics of Fluids*, 18(8). doi: 10.1063/1.2338064.

Lin, D. and Xing, B. (2008) 'Tannic acid adsorption and its role for stabilizing carbon nanotube suspensions', *Environmental Science and Technology*, 42(16), pp. 5917–5923. doi: 10.1021/es800329c.

Liu, F. *et al.* (2011) 'Evolution of a physiological pH 6.8 bicarbonate buffer system: Application to the dissolution testing of enteric coated products', *European Journal of Pharmaceutics and Biopharmaceutics*. Elsevier, 78(1), pp. 151–157. doi: 10.1016/j.ejpb.2011.01.001.

Liu, L., Moreno, L. and Neretnieks, I. (2008) 'A Novel Approach to Determine the Critical Coagulation Concentration of a Colloidal Dispersion with Plate-like Particles', *Langmuir*, 25(2), pp. 688–697. doi: 10.1021/la802658g.

Liu, Z. *et al.* (2014) 'Calcium phosphate nanoparticles primarily induce cell necrosis through lysosomal rupture: The origination of material cytotoxicity', *Journal of Materials Chemistry B*, 2(22), pp. 3480–3489. doi: 10.1039/c4tb00056k.

Lomer, M. C. E. *et al.* (2004) 'Dietary sources of inorganic microparticles and their intake in healthy subjects and patients with Crohn's disease', *British Journal of Nutrition*. Cambridge University Press (CUP), 92(6), pp. 947–955. doi: 10.1079/bjn20041276.

Lu, X. and Leng, Y. (2005) 'Theoretical analysis of calcium phosphate precipitation in simulated body fluid', *Biomaterials*, 26(10), pp. 1097–1108. doi: 10.1016/j.biomaterials.2004.05.034.

Lyklema, J. (1989) 'Discrimination between physical and chemical adsorption of ions on oxides', *Colloids and Surfaces*, 37, pp. 197–204. doi: http://dx.doi.org/10.1016/0166-6622(89)80118-0.

Mancardi, G. *et al.* (2017) 'Detection of Posner's clusters during calcium phosphate nucleation: A molecular dynamics study', *Journal of Materials Chemistry B*. Royal Society of Chemistry, 5(35), pp. 7274–7284. doi: 10.1039/c7tb01199g.

McConnell, E. L., Basit, A. W. and Murdan, S. (2008) 'Measurements of rat and mouse gastrointestinal pH, fluid and lymphoid tissue, and implications for in-vivo experiments', *Journal of Pharmacy and Pharmacology*, 60(1), pp. 63–70. doi: 10.1211/jpp.60.1.0008.

McNaught, A. D., Wilkinson, A. and others (1997) *Compendium of chemical terminology*. Blackwell Science Oxford.

Melmed, S. *et al.* (2015) 'Safety and efficacy of oral octreotide in acromegaly: Results of a multicenter phase III trial', *Journal of Clinical Endocrinology and Metabolism*. Endocrine Society, 100(4), pp. 1699–1708. doi: 10.1210/jc.2014-4113.

Ménard, S., Cerf-Bensussan, N. and Heyman, M. (2010) 'Multiple facets of intestinal permeability and epithelial handling of dietary antigens', *Mucosal Immunology*, pp. 247–259. doi: 10.1038/mi.2010.5.

Meyer, J. L. and Eanes, E. D. (1978) 'a thermodynamic analysis of the amorphous to crystalline calcium phosphate transformation', *Calcif. Tiss. Res.*, 25, pp. 59–68.

Mikolajczyk, A. E. *et al.* (2015) 'Assessment of tandem measurements of pH and total gut transit time in healthy volunteers', *Clinical and Translational Gastroenterology*. Nature Publishing Group, 6(7), pp. e100-8. doi: 10.1038/ctg.2015.22.

Miles, F. L. *et al.* (2015) 'Cell-based assays using calcein acetoxymethyl ester show Variation in Fluorescence With Treatment Conditions', 2(3). doi: 10.14440/jbm.2015.73.Cell-based.

Mitra, S. and Dungan, S. R. (1997) 'Micellar Properties of Quillaja Saponin. 1. Effects of Temperature, Salt, and pH on Solution Properties', *Journal of Agricultural and Food Chemistry*, 45(5), pp. 1587–1595. doi: 10.1021/jf960349z.

Mitragotri, S., Burke, P. A. and Langer, R. (2014) 'Overcoming the challenges in administering biopharmaceuticals: Formulation and delivery strategies', *Nature Reviews Drug Discovery*. Nature Publishing Group, 13(9), pp. 655–672. doi: 10.1038/nrd4363.

Morgan, T. T. *et al.* (2008) 'Encapsulation of organic molecules in calcium phosphate nanocomposite particles for intracellular imaging and drug delivery', *Nano Letters*, 8(12), pp. 4108–4115. doi: 10.1021/nl8019888.

Morgan, T. T., Goff, T. M. and Adair, J. H. (2011) 'The colloidal stability of fluorescent calcium phosphosilicate nanoparticles: The effects of evaporation and redispersion on particle size distribution', *Nanoscale*, 3(5), pp. 2044–2053. doi: 10.1039/c0nr00995d.

Morishita, M. and Peppas, N. A. (2006) 'Is the oral route possible for peptide and protein drug delivery?', *Drug Discovery Today*, 11(19–20), pp. 905–910. doi: http://dx.doi.org/10.1016/j.drudis.2006.08.005.

Mowat, A. M. I. (2003) 'Anatomical basis of tolerance and immunity to intestinal antigens', *Nature Reviews Immunology*. European Association for Cardio-Thoracic Surgery, pp. 331–341. doi:

10.1038/nri1057.

Mudunkotuwa, I. A. and Grassian, V. H. (2011) 'The devil is in the details (or the surface): Impact of surface structure and surface energetics on understanding the behavior of nanomaterials in the environment', *Journal of Environmental Monitoring*, 13(5), pp. 1135–1144. doi: 10.1039/c1em00002k.

Napper, D. H. (1983) 'The Role of Polymers in the Stabilization of Disperse Systems', in *Chemistry and Technology of Water-Soluble Polymers*. Boston, MA: Springer US, pp. 233–248. doi: 10.1007/978-1-4757-9661-2_14.

Navrotsky, A. (2001) 'Thermochemistry of nanomaterials', *Reviews in Mineralogy and Geochemistry*, 44(1997), pp. 73–103. doi: 10.2138/rmg.2001.44.03.

Neutra, M. R., Frey, A. and Kraehenbuhl, J. P. (1996) 'Epithelial M cells: Gateways for mucosal infection and immunization', *Cell*. Cell Press, pp. 345–348. doi: 10.1016/S0092-8674(00)80106-3.

Nightingale, A. M. *et al.* (2014) 'Controlled multistep synthesis in a three-phase droplet reactor', *Nature Communications*. Nature Publishing Group, 5(May), pp. 1–8. doi: 10.1038/ncomms4777.

Ninham, B. W. (1999) 'On progress in forces since the DLVO theory', *Advances in Colloid and Interface Science*. Elsevier Science Publishers B.V., pp. 1–17. doi: 10.1016/S0001-8686(99)00008-1.

Nisbet, A. D. *et al.* (1981) 'The Complete Amino-Acid Sequence of Hen Ovalbumin', *European Journal of Biochemistry*, 115(2), pp. 335–345. doi: 10.1111/j.1432-1033.1981.tb05243.x.

Nollet, L. M. L. and De Gelder, L. S. P. (2013) *Handbook of Water Analysis, Third Edition*. Taylor & Francis. Available at: https://books.google.co.uk/books?id=tZEAAAAAQBAJ.

O'Brien, F. J., Taylor, D. and Lee, T. C. (2002) 'An improved labelling technique for monitoring microcrack growth in compact bone', *Journal of Biomechanics*, 35(4), pp. 523–526. doi: 10.1016/S0021-9290(01)00200-7.

Oakenfull, D. and Sidhu, G. S. (1989) 'Toxicants of plant origin', *Glycosides*. CRC Press Inc Boca Raton, FL, 11, pp. 97–141.

Ochi, H. *et al.* (2006) 'Oral CD3-specific antibody suppresses autoimmune encephalomyelitis by inducing CD4+CD25-LAP+ T cells', *Nature Medicine*, 12(6), pp. 627–635. doi: 10.1038/nm1408.

Okamoto, Y. and Hidaka, S. (1994) 'Studies on calcium phosphate precipitation: Effects of metal ions used in dental materials', *Journal of Biomedical Materials Research*, 28(12), pp. 1403–1410. doi: 10.1002/jbm.820281204.

Olton, D. *et al.* (2007) 'Nanostructured calcium phosphates (NanoCaPs) for non-viral gene delivery: Influence of the synthesis parameters on transfection efficiency', *Biomaterials*, 28(6), pp. 1267–1279. doi: 10.1016/j.biomaterials.2006.10.026.

Ostwald, W. (1897) 'Studien über die Bildung und Umwandlung fester Körper', *Zeitschrift für Physikalische Chemie*, p. 289. doi: 10.1515/zpch-1897-2233.

P. Johnson, C., Li, X. and E. Logan, B. (1996) 'Settling Velocities of Fractal Aggregates', *Environmental*

Science & Technology, 30(6), pp. 1911–1918. doi: 10.1021/es950604g.

Pan, H. *et al.* (2010) 'Mystery of the transformation from amorphous calcium phosphate to hydroxyapatite', *Chemical Communications*, 46(39), pp. 7415–7417. doi: 10.1039/c0cc00971g.

Pan, H. B. and Darvell, B. W. (2009) 'Calcium phosphate solubility: The need for re-evaluation', *Crystal Growth and Design*, 9(2), pp. 639–645. doi: 10.1021/cg801118v.

Parkhurst, D. L. and Apello, C. A. (2013) 'Description of Input and Examples for Phreeqc Version 3: A Computer Program for Speciation, Batch-reaction, One-dimensional Transport, and Inverse Geochemical Calculations', in *Techniques and Methods: book 6*. U.S. Geological Survey. Available at: http://pubs.usgs.gov/tm/06/a43.

Past, W. L. (1974) 'Microinterferometry of developing bone mineral', *Calcified Tissue Research*, 15(1), pp. 315–324. doi: 10.1007/BF02059066.

Pastre, J. C., Browne, D. L. and Ley, S. V. (2013) 'Flow chemistry syntheses of natural products', *Chemical Society Reviews*. Royal Society of Chemistry, pp. 8849–8869. doi: 10.1039/c3cs60246j.

Peetsch, A. *et al.* (2013) 'Silver-doped calcium phosphate nanoparticles: Synthesis, characterization, and toxic effects toward mammalian and prokaryotic cells', *Colloids and Surfaces B: Biointerfaces*. Elsevier B.V., 102, pp. 724–729. doi: 10.1016/j.colsurfb.2012.09.040.

Pele, L. *et al.* (2015) 'Artefactual nanoparticle activation of the inflammasome platform: In vitro evidence with a nano-formed calcium phosphate', *Nanomedicine*, 10(9), pp. 1379–1390. doi: 10.2217/nnm.14.58.

Pele, L. C. *et al.* (2017) 'Synthetic mimetics of the endogenous gastrointestinal nanomineral: Silent constructs that trap macromolecules for intracellular delivery', *Nanomedicine: Nanotechnology, Biology and Medicine*. Elsevier, 13(2), pp. 619–630. doi: 10.1016/J.NANO.2016.07.008.

Powell, J. J. *et al.* (2015) 'An endogenous nanomineral chaperones luminal antigen and peptidoglycan to intestinal immune cells', *Nature Nanotechnology*. Nature Publishing Group, 10(4), pp. 361–369. doi: 10.1038/nnano.2015.19.

Powell, J. J., Thoree, V. and Pele, L. C. (2007) 'Dietary microparticles and their impact on tolerance and immune responsiveness of the gastrointestinal tract', in *British Journal of Nutrition*. Cambridge University Press. doi: 10.1017/S0007114507832922.

Raghuvanshi, R. S. *et al.* (1998) 'Stabilization of Dichloromethane-Induced Protein Denaturation During Microencapsulation', *Pharmaceutical Development and Technology*. Informa Healthcare, 3(2), pp. 269–276. doi: 10.3109/10837459809028504.

Reynolds, E. C. (1997) 'Remineralization of enamel subsurface lesions by casein phosphopeptide-stabilized calcium phosphate solutions', *Journal of Dental Research*, 76(9), pp. 1587–1595. doi: 10.1177/00220345970760091101.

Reynolds, E. C. (2004) 'US 6,780,844 B1: CALCIUM PHOSPHOPEPTIDE COMPLEXES'.

Riedle, S. *et al.* (2020) 'A Murine Oral-Exposure Model for Nano and Micro Particulates: Demonstrating Human Relevance with Food-Grade Titanium Dioxide', 2000486, pp. 1–8. doi:

10.1002/smll.202000486.

Root, M. J. (1990) ‘Inhibition of the amorphous calcium phosphate phase transformation reaction by polyphosphates and metal ions’, *Calcified Tissue International*, 47(2), pp. 112–116. doi: 10.1007/BF02555994.

Saber-Samandari, S. and Gross, K. A. (2011) ‘Amorphous calcium phosphate offers improved crack resistance: A design feature from nature?’, *Acta Biomaterialia*. Acta Materialia Inc., 7(12), pp. 4235–4241. doi: 10.1016/j.actbio.2011.06.048.

Schwarz, J. A., Contescu, C. I. and Putyera, K. (2004) *Dekker Encyclopedia of Nanoscience and Nanotechnology*. M. Dekker (Dekker Encyclopedia of Nanoscience and Nanotechnology). Available at: https://books.google.co.uk/books?id=hKpm9mEWbsYC.

Shakweh, M. *et al.* (2005) ‘Poly (lactide-co-glycolide) particles of different physicochemical properties and their uptake by peyer’s patches in mice’, *European Journal of Pharmaceutics and Biopharmaceutics*. Elsevier, 61(1–2), pp. 1–13. doi: 10.1016/j.ejpb.2005.04.006.

Shepherd, N. A. *et al.* (1987) ‘Exogenous pigment in Peyer’s patches’, *Human Pathology*. W.B. Saunders, 18(1), pp. 50–54. doi: 10.1016/S0046-8177(87)80193-4.

da Silva, A. B. *et al.* (2020) ‘Gastrointestinal absorption and toxicity of nanoparticles and microparticles: Myth, reality and pitfalls explored through titanium dioxide’, *Current Opinion in Toxicology*. Elsevier B.V., pp. 112–120. doi: 10.1016/j.cotox.2020.02.007.

Škalko-Basnet, N. (2014) ‘Biologics: Targets and Therapy Dovepress Biologics: the role of delivery systems in improved therapy’, *Biologics: Targets and Therapy*, 8, pp. 107–114. doi: 10.2147/BTT.S38387.

Slater, C. and Cohen, L. (1962) ‘A centrifugal particle size analyser’, *Journal of Scientific Instruments*. IOP Publishing, 39(12), p. 614. doi: 10.1088/0950-7671/39/12/327.

Sokolova, V. V. *et al.* (2006) ‘Effective transfection of cells with multi-shell calcium phosphate-DNA nanoparticles’, *Biomaterials*, 27(16), pp. 3147–3153. doi: 10.1016/j.biomaterials.2005.12.030.

Studart, A. R., Amstad, E. and Gauckler, L. J. (2007) ‘Colloidal stabilization of nanoparticles in concentrated suspensions’, *Langmuir*, 23(3), pp. 1081–1090. doi: 10.1021/la062042s.

Sun, L. *et al.* (2010) ‘Preparation and Properties of Nanoparticles of Calcium Phosphates With Various Ca/P Ratios’, *Journal of Research of the National Institute of Standards and Technology*, 115(4), pp. 243–255. doi: 10.6028/jres.115.018.

Sun, X. *et al.* (2009) ‘Size-Controlled Synthesis of Magnetite (Fe3O4) Nanoparticles Coated with Glucose and Gluconic Acid from a Single Fe(III) Precursor by a Sucrose Bifunctional Hydrothermal Method’, *The Journal of Physical Chemistry C*, 113(36), pp. 16002–16008. doi: 10.1021/jp9038682.

Tarcha, P. J. (1990) *Polymers for Controlled Drug Delivery*. CRC Press. Available at: https://books.google.co.uk/books?id=A73NI1TmS7wC.

Tenhuisen, K. S. and Brown, P. W. (1997) ‘Variations in solution chemistry during calcium-deficient and stolchiometric hydroxyapatite formation from CaHPO4 · 2H2O and Ca4(PO4)2O’, *Journal of*

Biomedical Materials Research, 36(2), pp. 233–241. doi: 10.1002/(SICI)1097-4636(199708)36:2<233::AID-JBM12>3.0.CO;2-H.

Terao, T., Matsuda, K. and Shouji, H. (2001) 'Improvement in site-specific intestinal absorption of furosemide by Eudragit L100-55', *Journal of Pharmacy and Pharmacology*. Wiley-Blackwell, 53(4), pp. 433–440. doi: 10.1211/0022357011775721.

Termine, J. D. and Eanes, E. D. (1972) 'Comparative chemistry of amorphous and apatitic calcium phosphate preparations', *Calcified Tissue Research*, 10(1), pp. 171–197. doi: 10.1007/BF02012548.

Tessari, R. K. and De Carvalho, M. A. (2015) 'Compilation of heuristics for inventive problem solving', in *Procedia Engineering*. doi: 10.1016/j.proeng.2015.12.347.

Treboux, G. *et al.* (2000) 'Existence of posner's cluster in vacuum', *Journal of Physical Chemistry A*, 104(21), pp. 5111–5114. doi: 10.1021/jp994399t.

Treuel, L. *et al.* (2014) 'Physicochemical characterization of nanoparticles and their behavior in the biological environment', *Physical Chemistry Chemical Physics*, 16(29), pp. 15053–15067. doi: 10.1039/c4cp00058g.

Truong-Le, V., Lovalenti, P. M. and Abdul-Fattah, A. M. (2015) 'Stabilization Challenges and Formulation Strategies Associated with Oral Biologic Drug Delivery Systems', *Advanced Drug Delivery Reviews*. Elsevier B.V., 93, pp. 95–108. doi: 10.1016/j.addr.2015.08.001.

Twarog, C. *et al.* (2019) 'Intestinal Permeation Enhancers for Oral Delivery of Macromolecules: A Comparison between Salcaprozate Sodium (SNAC) and Sodium Caprate (C10)', *Pharmaceutics*. MDPI AG, 11(2), p. 78. doi: 10.3390/pharmaceutics11020078.

Twu, Y.-K., Chen, Y.-W. and Shih, C.-M. (2008) 'Preparation of silver nanoparticles using chitosan suspensions', *Powder Technology*. Elsevier, 185(3), pp. 251–257.

Tye, R. J. (1989) 'Industrial and non-food uses for carrageenan', *Carbohydrate Polymers*, 10(4), pp. 259–280. doi: http://dx.doi.org/10.1016/0144-8617(89)90066-0.

US Department of Health (2004) 'Toxicological profile for strontium', *Public Health Service, Agency for Toxic Substances and Disease Registry*.

Viseras, C. *et al.* (2010) 'Current challenges in clay minerals for drug delivery', *Applied Clay Science*. Elsevier, pp. 291–295. doi: 10.1016/j.clay.2010.01.007.

Wang, C. G. *et al.* (2009) 'Crystallization at multiple sites inside particles of amorphous calcium phosphate', *Crystal Growth and Design*, 9(6), pp. 2620–2626. doi: 10.1021/cg801069t.

Wang, J. *et al.* (2015) 'Toward oral delivery of biopharmaceuticals: An assessment of the gastrointestinal stability of 17 peptide drugs', *Molecular Pharmaceutics*. American Chemical Society, 12(3), pp. 966–973. doi: 10.1021/mp500809f.

Wang, L. and Nancollas, G. (2001) 'Calcium Orthophosphates: Crystallization and Dissolution', *Chemical Reviews*, 108(11), pp. 4628–4669. doi: 10.1021/cr0782574.Calcium.

Welzel, T., Meyer-Zaika, W. and Epple, M. (2004) 'Continuous preparation of functionalised calcium

phosphate nanoparticles with adjustable crystallinity', *Chemical Communications*, 4(10), pp. 1204–1205. doi: 10.1039/b402521k.

Whitaker, J. R. (1980) 'Changes Occuring in Proteins in Alkaline Solution', in *Chemical Deterioration of Proteins*. American Chemical Society (ACS), pp. 145–163. doi: 10.1021/bk-1980-0123.ch007.

White, H. D., Walker, M. L. and Trinick, J. (1998) 'A computer-controlled spraying-freezing apparatus for millisecond time- resolution electron cryomicroscopy', *Journal of Structural Biology*. Academic Press Inc., 121(3), pp. 306–313. doi: 10.1006/jsbi.1998.3968.

Winge, R. K., Peterson, V. J. and Fassel, V. A. (1979) 'Inductively coupled plasma-atomic emission spectroscopy: prominent lines', *Applied Spectroscopy*. Society for Applied Spectroscopy, 33(3), pp. 206–219.

Wuthier, R. E. and Eanes, E. D. (1975) 'Effect of phospholipids on the transformation of amorphous calcium phosphate to hydroxyapatite in vitro', *Calcified Tissue Research*. Springer-Verlag, 19(1), pp. 197–210. doi: 10.1007/BF02564004.

Yang, Y. *et al.* (2015) 'The effect of amorphous calcium phosphate on protein protection against thermal denaturation', *Chemical Communications*. Royal Society of Chemistry, 51(41), pp. 8705–8707. doi: 10.1039/c5cc01420d.

Yang, Z., Best, S. M. and Cameron, R. E. (2009) 'The Influence of α-Tricalcium Phosphate Nanoparticles and Microparticles on the Degradation of Poly(D,L-lactide-co-glycolide)', *Advanced Materials*. WILEY-VCH Verlag, 21(38–39), pp. 3900–3904. doi: 10.1002/adma.200901093.

Yukioka, H. *et al.* (1987) 'Gastric emptying and small bowel transit times in volunteers after intravenous morphine and nalbuphine', *Anaesthesia*. John Wiley & Sons, Ltd, 42(7), pp. 704–710. doi: 10.1111/j.1365-2044.1987.tb05314.x.

Zhang, J. *et al.* (2016) 'Flow characteristics in free impinging jet reactor by particle image velocimetry (PIV) investigation', *Fluid Dynamics Research*, 48(4), p. 045505. doi: 10.1088/0169-5983/48/4/045505.

Zhang, L. (2011) 'Voluntary oral administration of drugs in mice', *Protocol Exchange*. Springer Nature. doi: 10.1038/protex.2011.236.

Zhang, Z. J. *et al.* (1991) 'Suppression of diabetes in nonobese diabetic mice by oral administration of porcine insulin', *Proceedings of the National Academy of Sciences*, 88(22), pp. 10252–10256. Available at: http://www.pnas.org/content/88/22/10252.abstract.

Zhao, J. *et al.* (2014) 'Microwave-assisted hydrothermal rapid synthesis of amorphous calcium phosphate nanoparticles and hydroxyapatite microspheres using cytidine 5'-triphosphate disodium salt as a phosphate source', *Materials Letters*. North-Holland, 124, pp. 208–211. doi: 10.1016/j.matlet.2014.03.054.

Zhong, Q. and Jin, M. (2009) 'Zein nanoparticles produced by liquid-liquid dispersion', *Food Hydrocolloids*. Elsevier Ltd, 23(8), pp. 2380–2387. doi: 10.1016/j.foodhyd.2009.06.015.